

# Search for Solar Axions with the CCD Detector and X-ray Telescope at CAST Experiment

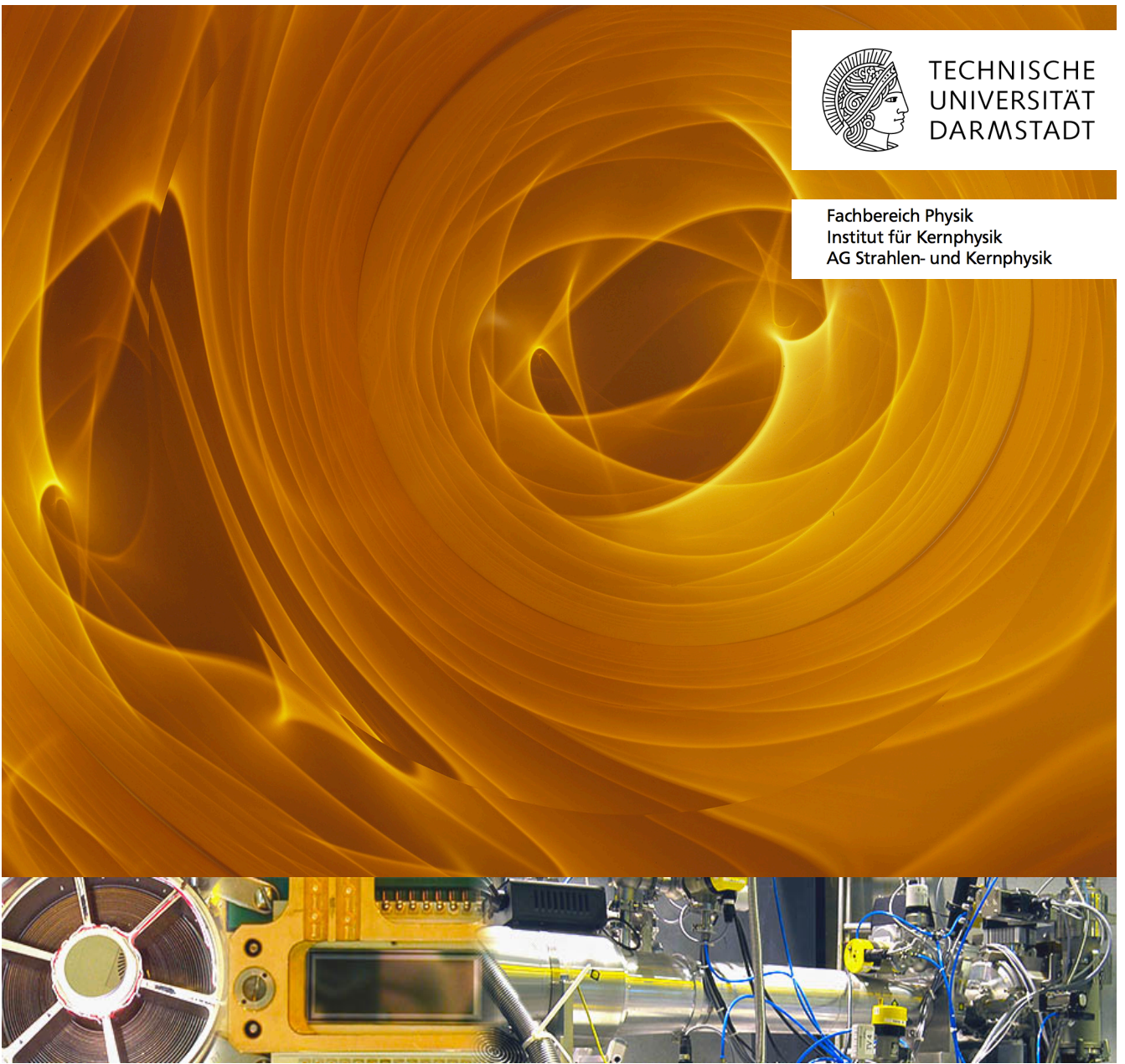
Zur Erlangung des Grades eines Doktors der Naturwissenschaften (Dr. rer. nat)  
Genehmigte Dissertation von Dipl. Ing. Madalin-Mihai Rosu aus Roman, Rumänien  
Juni 2015 – Darmstadt – D 17



TECHNISCHE  
UNIVERSITÄT  
DARMSTADT

Fachbereich Physik  
Institut für Kernphysik  
AG Strahlen- und Kernphysik

CERN-THESIS-2015-061  
03/06/2015



---

Search for Solar Axions with the CCD Detector and X-ray telescope at CAST Experiment  
Suche nach Solaren Axionen mit einem Röntgenteleskop und CCD Detektor am CAST Experiment

Genehmigte Dissertation von Dipl. Ing. Madalin-Mihai Rosu aus Roman, Rumänien

1. Gutachten: Prof. Dr. Dr. h.c./RUS Dieter H.H. Hoffmann
2. Gutachten: Prof. Dr. Konstantin Zioutas

Tag der Einreichung: 13.04.2015

Tag der Prüfung: 03.06.2015

Darmstadt – D 17



---

*Dedicated to the memory of my grandmother Maria Galavan  
and my high school Physics teacher Mircea Gligor.*





Cover picture represents reflection patterns of one of the gold-plated spare mirrors of ESA's XMM-Newton X-Ray space telescope.

[http://www.esa.int/spaceinimages/Images/2012/12/Reflecting\\_on\\_XMM-Newton](http://www.esa.int/spaceinimages/Images/2012/12/Reflecting_on_XMM-Newton)





---

## Zusammenfassung

---

Am CERN Axion Solar Telescope (CAST) Experiment wird das weltweit empfindlichste Helioskop zum Nachweis von Axionen eingesetzt. Axionen sind schwach wechselwirkende pseudoskalare Teilchen, die zur Lösung des sogenannten starken Charge-Parity Problems des Standardmodells vorgeschlagen wurden.

Das Detektionsprinzip basiert auf dem inversen Primakoff Effekt, ein Mechanismus, der zur Umwandlung der Axionen in leicht nachweisbare Röntgenstrahlung in Anwesenheit eines starken transversalen magnetischen Feldes führt. Die solaren Axionen werden aufgrund des Primakoff Effekts im heißen und dichten Sonnenkern aus der Kopplung eines realen mit einem virtuellen Photon erzeugt. Die Sonnen-Modelle sagen eine maximale Axionenleuchtkraft bei einer Energie von 3 keV voraus. Der Ursprung dieser Axionen befindet sich hauptsächlich innerhalb von 20% des Sonnenradiuses. Infolgedessen wird auch ein Maximum der Intensität der entsprechenden Röntgenstrahlung bei etwa 3 keV erwartet.

CAST verwendet einen Magneten mit einer Länge von 9.26 m und einem Feld von 9 Tesla. An den vier Öffnungen des Magneten befinden sich Röntgendetektoren zum Nachweis der Photonen, die aus der Konversion der Axionen resultieren. Zur Berücksichtigung verschiedener Axion Massen wurden  $^3\text{He}$  beziehungsweise  $^4\text{He}$  als Puffergase im Inneren des Magneten eingesetzt. Sie dienen der Wiederherstellung der Kohärenzbedingung, die für die Axion-Photon-Umwandlung notwendig ist. Somit wurden bisher unerforschte Regionen des Wertebereiches der Axionmasse untersucht, die von QCD Axion-Modellen begünstigt werden. Diese Experimentstrategie ermöglichte in der Zeit von 2003 bis 2013 die Suche nach Axionen mit Massen zwischen 0.02 und 1.17 eV.

Einer der CAST Detektoren ist ein pn-CCD Chip, der sich in der Brennebene eines Röntgenteleskops befindet. In dieser Arbeit wird ein Überblick über die Daten, die in den Jahren 2009, 2010 und 2011 mit diesem Detektor erfasst wurden, gegeben. Die gewonnenen Signal- und Hintergrundwerte weisen auf eine fehlende Konversionssignatur hin. Die analysierten Daten werden im Rahmen der Experimentkooperation dazu verwendet, um durch Zusammenführung mit den Daten der anderen Detektoren die kombinierten Obergrenzen des Parameterbereiches der Axion-Photon-Kopplungskonstante  $g_{a\gamma} \lesssim 3.3 \times 10^{-10} \text{ GeV}^{-1}$  at 95% C.L. innerhalb eines Massenbereiches von 0.65 eV bis 1.17 eV zu verfeinern.

Darüber hinaus wurden das Reflexionsvermögen des Röntgenteleskops überprüft, die Ausrichtung des Spiegelmoduls kontrolliert und korrigiert und Detektorkalibrierungen zusammen mit einer langfristigen Detektorüberwachung und entsprechende Stabilitätsstudien in der Zeit von 2009 bis 2014 durchgeführt. Um ein maximales Entdeckungspotenzial und die beste Empfindlichkeit des Experimentaufbaus zu gewährleisten, wurde das Spiegelmodul an der Panter Röntgentestanlage in München überprüft. Dabei wurde festgestellt, dass die Leistungsmerkmale des Moduls innerhalb der nach einem elfjährigen Einsatz erwarteten Grenzen liegen.





---

## Abstract

---

The CERN Axion Solar Telescope (CAST) is an experiment that uses the world's highest sensitivity Helioscope to date for solar Axions searches. Axions are weakly interacting pseudoscalar particles proposed to solve the so-called Strong Charge-Parity Problem of the Standard Model.

The principle of detection is the inverse Primakoff Effect, which is a mechanism for converting the Axions into easily detectable X-ray photons in a strong transverse magnetic field. The solar Axions are produced due to the Primakoff effect in the hot and dense core of from the coupling of a real and a virtual photon. The solar models predict a peak Axion luminosity at an energy of 3 keV originating mostly from the inner 20% of the solar radius. Thus an intensity peak at an energy of 3 keV is also expected in the case of the X-ray radiation resulting from Axion conversion.

CAST uses a high precision movement system for tracking the Sun twice a day with a LHC dipole twin aperture prototype magnet, 9.26 meters long and with a field of 9 Tesla. On the four apertures of the magnet, X-ray detectors look for photons resulted from Axion conversion. For investigating different Axion masses,  $^3\text{He}$  and  $^4\text{He}$  buffer gas was injected in the magnetic region, restoring the coherence for Axion-to-photon conversion into mass regions so far unexplored, favoured by QCD Axion models. Using this scanning strategy, Axion masses were investigated in the range 0.02 eV to 1.17 eV between 2003 and 2013.

One of CAST Detectors is a pn-CCD chip placed in the focal plane of an X-ray Telescope. In this thesis an overview of 2009, 2010 and 2011 data taken with this detector is presented. Signal and background levels were extracted, indicating that no conversion signature was detected. The analysed data is being used within the collaboration for improving the combined upper limits on the Axion-to-photon coupling constant parameter space ( $g_{a\gamma} \lesssim 3.3 \times 10^{-10} \text{ GeV}^{-1}$  at 95% C.L.), for the mass range 0.65 eV to 1.17 eV, by merging it with the results from the other detectors.

Besides this, X-ray Telescope mirror module reflectivity checks and alignment were performed, together with long-term detector system monitoring, stability studies and calibrations, spanning the interval 2009-2014. In order to ensure the highest discovery potential and the best sensitivity of the setup, the mirror module was tested at the Panter X-ray test facility in Munich, and the performance was found to be within the expected margins after 11 years operation of.



---

## Table of contents

---

<b>ZUSAMMENFASSUNG .....</b>	<b>I</b>
<b>ABSTRACT .....</b>	<b>III</b>
<b>TABLE OF CONTENTS .....</b>	<b>V</b>
<b>ABBREVIATIONS AND SYMBOLS USED .....</b>	<b>VII</b>
<b>1. INTRODUCTION.....</b>	<b>1</b>
<b>2. THE STANDARD MODEL .....</b>	<b>4</b>
2.1. THE STANDARD MODEL OF PARTICLE PHYSICS, SYMMETRIES AND GAUGE THEORIES .....	4
2.2. CPT SYMMETRY AND CP-VIOLATION .....	5
2.2.1. Parity Transformation: <i>P</i> -Symmetry.....	5
2.2.2. Charge Conjugation: <i>C</i> -Symmetry .....	6
2.2.3. Time Reversal: <i>T</i> -Symmetry.....	6
2.2.4. CPT-Theorem and the Neutral Kaon System .....	6
2.3. THE $U(1)_A$ PROBLEM .....	9
2.4. THE STRONG CP-PROBLEM .....	11
2.5. THE PECCEI-QUINN MECHANISM .....	12
<b>3. THE AXION PHYSICS .....</b>	<b>13</b>
3.1. COUPLING OF AXIONS .....	13
3.2. COUPLING WITH GLUONS .....	14
3.3. COUPLING WITH PHOTONS.....	14
3.4. COUPLING WITH ELECTRONS .....	15
3.5. COUPLING WITH NUCLEONS .....	15
3.6. OTHER PROCESSES .....	16
3.7. THE VISIBLE AXION .....	17
3.8. THE INVISIBLE AXION MODELS.....	18
3.9. AXIONS AS DARK MATTER CANDIDATES .....	21
3.10. ASTROPHYSICAL CONSTRAINTS.....	23
3.10.1. <i>Stellar evolution of Low-Mass Stars</i> .....	24
3.10.2. <i>Globular Clusters limits</i> .....	25
3.10.3. <i>White Dwarf cooling</i> .....	26
3.10.4. <i>Supernova 1987A</i> .....	27
3.11. COSMOLOGICAL CONSTRAINTS.....	29
3.12. DETECTING THE INVISIBLE AXION.....	30
3.12.1. <i>Telescope Searches</i> .....	31
3.12.2. <i>Haloscope Searches</i> .....	31
3.12.3. <i>Helioscopes</i> .....	32
3.12.4. <i>Bragg diffraction experiments</i> .....	33
3.12.5. <i>Laboratory experiments</i> .....	33
3.12.6. <i>Polarisation experiments</i> .....	34
<b>4. THE SOLAR AXION .....</b>	<b>36</b>
4.1. THE SOLAR MODEL AND THE AXION PRODUCTION.....	36
4.2. AXION-PHOTON CONVERSION PROBABILITY .....	39
4.2.1. <i>The Conversion Probability in Vacuum</i> .....	40
4.2.2. <i>Conversion Probability in a buffer gas</i> .....	41
4.3. EXPECTED NUMBER OF PHOTONS .....	43
<b>5. CERN AXION SOLAR TELESCOPE .....</b>	<b>44</b>
5.1. HISTORY .....	46



5.2.	THE MAGNET .....	47
5.3.	THE CRYOGENIC SYSTEM .....	48
5.4.	THE TRACKING SYSTEM .....	50
5.5.	SOLAR FILMING .....	53
5.6.	THE SLOW CONTROL SYSTEM .....	55
5.7.	THE VACUUM SYSTEMS .....	55
5.8.	THE BUFFER GAS SYSTEM .....	56
5.8.1.	<i>Thin cryogenic cold windows</i> .....	57
5.8.2.	<i>He<sup>3</sup> storage and metering</i> .....	58
<b>6.</b>	<b>X-RAY DETECTORS .....</b>	<b>59</b>
6.1.	TIME PROJECTION CHAMBER .....	60
6.2.	THE MICROMEGAS DETECTOR .....	61
6.3.	THE X-RAY TELESCOPE MIRROR SYSTEM .....	62
6.4.	THE PN-CCD .....	67
6.4.1.	<i>The pn-Junction and the Depletion Region</i> .....	67
6.4.2.	<i>Fully Depleted Back-side Illuminated pn-CCD</i> .....	69
6.4.3.	<i>Implementation in CAST</i> .....	73
6.4.4.	<i>Quantum Efficiency and Energy Resolution</i> .....	75
<b>7.</b>	<b>X-RAY TELESCOPE ALIGNMENT .....</b>	<b>78</b>
<b>8.</b>	<b>CCD ALIGNMENT ANALYSIS .....</b>	<b>82</b>
8.1.	THE LASER RUNS .....	82
8.2.	X-RAY FINGER MEASUREMENTS .....	83
<b>9.</b>	<b>CCD DATA ANALYSIS .....</b>	<b>86</b>
9.1.	2009 .....	89
9.2.	2010 .....	94
9.3.	2011 .....	98
<b>10.</b>	<b>CONCLUSIONS AND OUTLOOK .....</b>	<b>102</b>
<b>11.</b>	<b>ANNEX 1 .....</b>	<b>104</b>
<b>12.</b>	<b>ANNEX 2 .....</b>	<b>108</b>
<b>13.</b>	<b>ANNEX 3 .....</b>	<b>112</b>
<b>14.</b>	<b>ANNEX 4 .....</b>	<b>115</b>
<b>15.</b>	<b>LIST OF EQUATIONS .....</b>	<b>120</b>
<b>16.</b>	<b>LIST OF FIGURES .....</b>	<b>122</b>
<b>17.</b>	<b>LIST OF TABLES .....</b>	<b>126</b>
<b>18.</b>	<b>BIBLIOGRAPHY .....</b>	<b>127</b>
<b>19.</b>	<b>ACKNOWLEDGEMENTS .....</b>	<b>132</b>
	<b>CURRICULUM VITAE .....</b>	<b>134</b>
	<b>ERKLÄRUNG ZUR DISSERTATION .....</b>	<b>135</b>

## Abbreviations and symbols used

<b>QCD</b>	Quantum Chromodynamics
<b>CMB</b>	Cosmic Microwave Background
<b>WMAP</b>	Wilkinson Microwave Anisotropy Probe
<b>PQ</b>	Peccei and Quinn
<b>CERN</b>	Conseil Européen pour la Recherche Nulcléaire
<b>LHC</b>	Large Hadron Collider (CERN)
<b>CAST</b>	CERN Axion Solar Telescope
<b>CCD</b>	Charge Coupled Device
<b>MICROMEGAS</b>	MICROMesh Gaseous Structure
<b>SM</b>	Standard Model
<b>CPT</b>	Charge Parity Time (operators)
<b>CMS</b>	Compact Muon Solenoid (CERN)
<b>ATLAS</b>	CERN Experiment
<b>CKM</b>	Cabibbo-Kobayashi-Maskawa-Matrix
<b>SN 1987A</b>	Supernova explosion observed in 1987
<b>DFSZ</b>	Dine-Fischler-Srednicki-Zhitnitskii Model
<b>KSVZ</b>	Kim-Shiftman-Vainshtein-Zakharov Model
<b>ALPs</b>	Axion like particles
<b>WISPs</b>	Weakly Interacting Sub-eV Particles
<b>HDM</b>	Hot Dark Matter
<b>CDM</b>	Cold Dark Matter
<b>RGB</b>	Red Giant Branch
<b>SGB</b>	Sub Giant Branch
<b>AGB</b>	Asymptotic Giant Branch
<b>HB</b>	Helium Burning Stars
<b><math>M_{\odot}</math></b>	Solar Mass
<b>CL</b>	Confidence Level
<b>ADMX</b>	Axion Dark Matter Experiment
<b>DESY</b>	The Deutsches Elektronen-Synchrotron
<b>PVLAS</b>	Polarizzazione del Vuoto con LASer experiment
<b>NIST</b>	National Institute of Standards and Technology
<b>LEP2</b>	Large Epectron Positron (CERN)
<b>MRB</b>	Magnet Return Box
<b>MFB</b>	Magnet Feed Box
<b>NOVAS</b>	U.S. Naval Observatory Vector Astronomy Software
<b>FOV</b>	Field Of View
<b>XRT</b>	X-ray Telescope
<b>TPC</b>	Time Projection Chambre
<b>ABRIXAS</b>	A Broadband Imaging X-ray All-sky Survey space mission
<b>PANTER</b>	X-ray test facility located in Neuried Munich
<b>MPE</b>	Max-Plank Institut für Extraterrestrische Physik
<b>HEW</b>	Half energy width
<b>XMM-Newton</b>	X-ray Multi-Mirror Mission space mission (ESA)
<b>CAMEX64</b>	CMOS Amplifier and Multiplexer chip
<b>ADC</b>	Analog-to-Digital Converter
<b>SDD</b>	Silicone Drift Detector
<b>ADU</b>	Analogue to Digital Unit
<b>DAQ</b>	Data Acquisition System
<b>FWHM</b>	Full Width Half Maximum
<b>OSQAR</b>	Optical Search of QED Vacuum Magnetic Birefringence





---

## 1. Introduction

---

*“Given enough time, Hydrogen starts to wonder where it came from,  
and where it is going.”*

**Edward R. Harrison**

The Standard Model of particle Physics is at the moment humanity’s best and most complete and widely accepted theory that explains the behaviour of the observable Universe. Since its inception it was tested countless times against observations and experiments, it has been quite successful in providing explanations to numerous problems, however it is unlikely to be the final theory, since it falls short of answering many important questions. A first notable flaw is the omission of gravity from the four fundamental interactions, the force that we as macroscopic nonrelativistic beings are most in touch with. Moreover there are more than 19 arbitrary parameters required for the model to fit the available data.

For the purpose of this thesis one of the most relevant and puzzling shortfall of the SM is its inability to answer to the so-called strong CP-problem in Quantum Chromodynamics (QCD), the theory that deals with the study of strong interactions. This problem is the baffling question as to why the strong force in nature does not appear to break the combination of charge conjugation and parity transformation as the theory leads us to expect.

In 1977 Roberto Peccei and Helen Quinn formulated a possible solution to this strong CP-problem. They were not the only ones pursuing an explanation to this open question, but they were the only ones to come up with an elegant mechanism to explain the apparent conservation of CP in strong interactions by introducing just one additional symmetry, which is now referred as Peccei-Quinn-symmetry (PQ-symmetry).

When this new symmetry is spontaneously broken at a yet unknown scale  $f_a$ , it gives rise to a Goldstone Boson, as Steven Weinberg and Frank Wilczek pointed out independently in 1978 thus giving birth to a new light pseudo-scalar particle call the Axion.

Wilczek fit the name with a dose of humour after the well-known washing detergent since this hypothetical particle would tidy up efficiently a problem of Physics.

Axions are of increasingly great interest in the context of our growing awareness about the abundance of Dark Energy and Dark Matter relative to regular baryonic matter. Most recent CMB measurements of the cosmic background fluctuations are most disconcerting and at the same time exciting for physicists because surprises have always played an important role in scientific research being an indication of where to look for new Physics in general.

WMAP measures the relative density of baryonic and non-baryonic matter to an accuracy of better than a few percent of the overall density.

As of January 2013 we know that the composition of the Universe is

- 4.6% Atoms (actual density of about 1 proton per 4 cubic meters);
- 24% Cold Dark Matter;
- 71.4% Dark Energy (necessary to explain both the flatness of the Universe, the observed accelerated expansion, and the evolution of the clusters of Galaxies);

Axions, if they exist could play an important role in the history of the Universe. They might have been produced shortly after the Big Bang, and could still be generated today in the core of Stars for example the Sun. Relic Axions produced in the early Universe could contribute significantly to that 24% about which we know nothing at the moment.

---

In its initial form proposed by Peccei and Quinn, the Axion theory that assumes the spontaneous breaking of the PQ-symmetry around the electroweak scale, can be ruled out rather quickly but the search for the so called *invisible* Axions still continues.

These Axions of masses below 1 eV would couple very weakly to fundamental particles, property that makes them really challenging to detect. Various bounds from cosmology and astrophysics have been derived for roughly constraining the possible parameter space of the Axions. This resulted in a window in mass terms between 1 eV and  $\mu\text{eV}$ .

Various experiments have been searching for this elusive particle surrounding this mass range employing different methods. One of the methods which is also used in this thesis is the so called Primakoff effect. This effect allows for the conversion of the Axions into photons and vice versa in the presence of strong electromagnetic fields. This makes from our Sun the closest and most intense available celestial source (laboratory/factory) of Axions.

Experiments attempting to detect solar Axions are generally referred as *Helioscopes*. The most sensitive Helioscope to date is the CERN Axion Solar Telescope (CAST). Its main advantage is that it uses a fantastic LHC superconductive prototype dipole magnet cooled at 1.4 K capable of providing 9T over a length of 10m. Moreover CAST is able to precisely point and track the sun with this magnet twice a day, at sunrise and sunset for a total of 3 hours. Being a LHC bending dipole, the magnet has 2 bores thus providing 4 apertures for installing detectors. At both ends of these 2x10 m long bores 4 X-ray Detectors have been mounted for detecting photons from Primakoff conversion.

Installed at one end of the magnet two low background MICROMesh Gaseous Structure (MICROMEGAS, MM) detectors are searching for solar Axions signature during the sunset tracking run. The sunrise ports are populated with another MICROMEGAS and an X-ray telescope consisting of X-ray optics with a Charged Coupled Device (CCD) placed in the focal plane.

For scanning different Axion mass ranges CAST experiment consisted of two phases. During the first one data was taken with vacuum in the magnetic volume, thus investigating with very high sensitivity masses up to 0.02 eV.

To increase the sensitivity for higher masses helium was injected in a finely dosed controlled manner in the magnetic region thus restoring the coherence for Axion-to-photon conversion.

The Helium run consisting of both isotopes  $^4\text{He}$  and  $^3\text{He}$  will be referred as Phase 2. Because of the fact that the LHC dipole had to be operated at 1.8 K to maintain superconductivity,  $^4\text{He}$  could be used only up to a pressure of 16.4 mbar, point at which it liquefies. For reaching higher masses and pressures the much more rare and expensive  $^3\text{He}$  isotope was used, thus increasing the complexity of the experiment.

The most sensitive detector system used at CAST is the X-ray telescope coupled with the pn-CCD detector placed in its focal plane. Both components were originally built for satellite space missions.

Their combined use provides the X-ray telescope with the highest Axion discovery potential of all CAST detectors during both Phase I and II along with an excellent imaging capability. The implementation of the X-ray mirror optics suppresses background with a factor of 155 by the virtue of focusing the photons from the magnet aperture area of  $14.5\text{ cm}^2$  to a spot of roughly  $9.3\text{ mm}^2$  on the CCD chip.

The first phase of CAST was in 2003-2004 with two years of data yielding an upper limit on the Axion-to-photon coupling of  $g_{a\gamma} < 8.8 \times 10^{-11}\text{ GeV}^{-1}$  (95% C.L) for Axion masses  $m_a \leq 0.02\text{ eV}$ .

During the first part of the Phase II in 2005 and 2006 the magnet was filled with  $^4\text{He}$  gas. CAST measured a total of 162 different pressure settings, out of which 149 were covered by the CCD detector. The range 0.08 -> 13.42 mbar was covered in steps of 0.08-0.09 mbar.

Using this method Axion masses up to 0.4 eV were scanned for the first time with high sensitivity, extending the Axion search deep into formerly unexplored regions preferred by theoretical models.

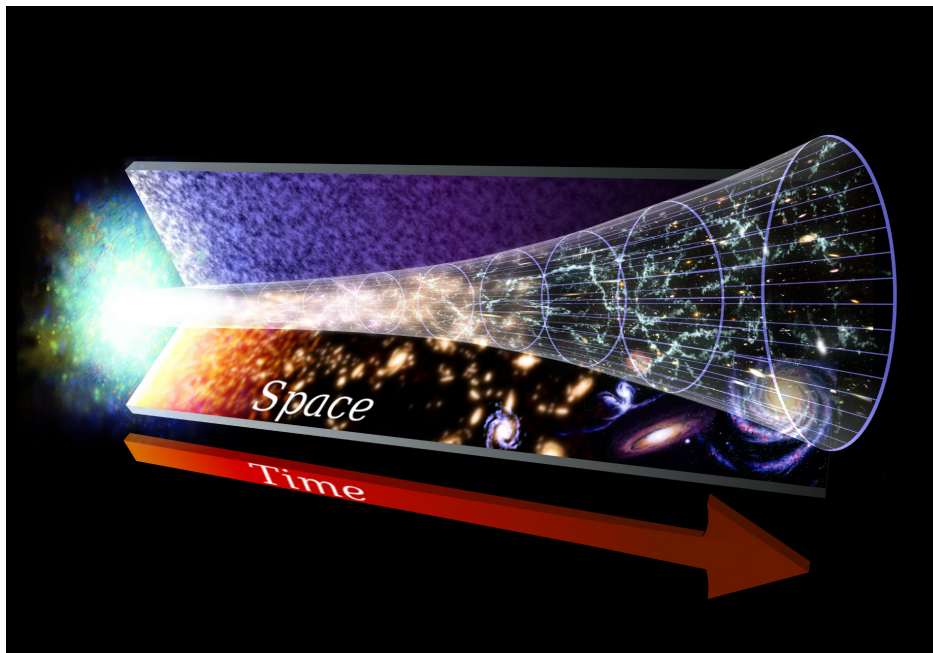
---

Since 2007, CAST has been acquiring data with  $^3\text{He}$  until the end of 2012.

This thesis is devoted to the analysis of the  $^3\text{He}$  data acquired with the CCD detector and CAST experiment during the years 2009, 2010, and 2011. As a final result of this analysis, an upper limit on the Axion-to-photon coupling constant  $g_{a\gamma}$  will be determined, since no significant signal above background was observed.

I would like to stress that the Axion parameter space that CAST explored in Phase II is especially interesting, since theoretical Axion models favour it and no other experiments so far have been able to investigate this promising mass range with sensitivity comparable to the one of CAST.

This aside CAST is pushing the limits of the fundamental Physics research and human knowledge also through it's campaigns from 2013 and 2014 trying to shed some light into the hidden sector by scanning for paraphotons and chameleons.



Evolution of the Universe Starting with the Big Bang [1]

INGREDIENTS:  
HYDROGEN, TIME

---

## 2. The Standard Model

---

Although the Standard Model's validity has been verified to great extent by many experiments, being a well-established theory, it is also generating some unresolved puzzles such as the strong CP problem. QCD, the non-abelian gauge theory of strong interactions, predicts a violation of the strong CP symmetry that has never yet been verified or observed. One solution to this strong CP problem was introduced by Peccei and Quinn in 1977 [2], who proposed the conservation of the CP symmetry in the presence of a pseudoscalar particle called the Axion, expanding on the idea of Hooft [3] [4] who stressed that the Physics of a theory with non-trivial vacuum topology, such as QCD, requires an additional parameter  $\theta$  in its Lagrangian.

---

### 2.1. The Standard Model of Particle Physics, Symmetries and Gauge Theories

---

The Standard Model of particle Physics provides a framework for the elementary particles and three of the four known interactions between them as mentioned in the introduction (Figure 2-2). It is a quantum field theory and it includes the electroweak theory as well as Quantum Chromodynamics (QCD) in the frame of the structure

$$SU(3)_C \times SU(2)_L \times U(1)_Y$$

Equation 2-1

Here the gauge group  $SU(3)_C$  forces the existence of the gluon fields responsible for the strong interactions between quarks the corresponding charge in this case being the colour. The two other symmetry groups,  $SU(2)_L$  and  $U(1)_Y$  represent the electroweak interaction theory with the corresponding weak charge isospin  $L$  and respectively the weak hypercharge  $Y$ .

The elementary particles in the SM are fermions, for instance quarks and leptons, and vector Bosons that are mediating the fundamental forces like the photons do for the electromagnetic interactions,  $W$  and  $Z$  Bosons for the weak interactions and the gluons for the strong interactions. The infamous Higgs Boson, the remainder of the Higgs field has famously been confirmed on 4 July 2012 with a mass of approx. 125 GeV by ATLAS and CMS groups at CERN<sup>1</sup> - LHC<sup>2</sup> yielding the Nobel Prize on December 10 2013 for two of the original researchers, Peter Higgs and Francois Englert.

The major drawback of the SM is that it does not include the fourth fundamental interaction (gravity) and that it relies on 19 free parameters (the nine fermion masses, three coupling constants, four CKM – quark mixing angles, the Higgs doublet and the  $\theta$  parameter) that have to be determined experimentally since they can not be derived directly from the theory.

It is obvious that symmetries play an essential role in Physics. They are connected with conservation laws via Noether's theorem, which states that there is a correspondence of a conservation law (for instance conserved current and charge) with the invariance of the Lagrangian under a continuous symmetry. [5]

Symmetries can be classified in two major groups, local and global symmetries. If symmetry holds in all points in space-time, then it is referred to as global, while a local one is valid only for a certain subset of space-time. These local symmetries are of special interest in Physics since they provide the basis for gauge theories. In general the transformations can be either continuous or discrete, giving rise to continuous and discrete symmetries, respectively. In order to characterize continuous symmetries, Lie groups are applied, while for discrete ones finite groups are usable.

---

<sup>1</sup>Conseil Européen pour la Recherche Nucléaire

<sup>2</sup>Large Hadron Collider

Some examples of continuous symmetries are translations in time and space as well as rotations. Invariance under translations in time leads to energy conservation, translations in space produce linear momentum conservation and rotations in space conserve the angular momentum *if the theory is invariant under this symmetry*.

These groups are Lorentz, and more generally Poincaré groups.

In the SM one can find also symmetries describing non-continuous changes in a system, discrete symmetries for example in the form of charge conjugation (C-symmetry), parity transformation (P-symmetry) and time inversion (T-symmetry). Particles and antiparticles are exchanged under charge transformations, while parity transformations just reverse the space coordinates. One can imagine the time reversal as if the direction of time is inverted.

The local symmetries, which are often referred as to gauge symmetries, form the basis of the Standard Model. Symmetries as U(1), SU(2), and SU(3) are internal symmetries which do not depend on space-time coordinates. I would like to mention that the invariance under U(1) gauge transformation leads to conservation of electric charge, lepton number and hypercharge, SU(2) insures the conservation of isospin, and SU(3) invariance conserves baryon number and quark colour.

As for the quark flavour conservation, it is only governed approximately by SU(3) invariance.

---

## 2.2. CPT Symmetry and CP-Violation

---

### 2.2.1. Parity Transformation: P-Symmetry

---

This is one important example of discrete symmetry transformation and the action of this transformation refers to the inversion of all spatial coordinates,  $(x, y, z) \rightarrow (x', y', z')$  having the operator parity  $P$ . It follows that for a scalar wave function the parity transformation is defined by

$$P\psi(\vec{r}, t) = \pi\psi(-\vec{r}, t)$$

Equation 2-2

The possible eigenvalues of  $P$  are either  $\pi = +1$  (even parity) or  $\pi = -1$  (odd parity), and applying  $P$  twice yields the original system ( $P^2 = 1$ ). Scalars have a parity of 1, pseudoscalars of  $-1$ , while vectors (i.e. polar vectors) have  $P = -1$  and pseudovectors (i.e. axial vectors) show  $P = 1$ .

If we consider for example the effect of spatial transformation on the electric and magnetic field  $E$  and  $B$ , we find that  $E$  is odd under  $P$  and  $B$  is even.

In the SM, P-symmetry is conserved in electromagnetic and strong interactions with the condition that it is possible to assign an intrinsic parity to the particles. The value of the intrinsic parity is opposite for particles and their corresponding antiparticles.

In weak interactions the parity is not conserved but even maximally violated for charged current weak interactions. This violation can be seen in the so called  $\tau - \theta -$  puzzle, where two decays for charged strange mesons were found as it follows:

$$\theta^+ \rightarrow \pi^+ + \pi^0$$

$$\tau^+ \rightarrow \pi^+ + \pi^+ + \pi^-$$

Equation 2-3

---

They have parity in the final state and were expected to also have different parity in the initial state (being two different particles). Now we know that  $\tau$  and  $\theta$  are the same particle known under the name of the positive kaon  $K^+$ . The explanation for these observations is that in weak interactions the parity is not conserved.

Another more striking way to see maximal parity violation is that there exist only left-Neutrinos (spin aligned opposite to the direction of flight) and right-handed antineutrinos (spin along the direction of flight) [6].

---

### 2.2.2. Charge Conjugation: C-Symmetry

---

Charge conjugation operation changes the sign of the inner quantum numbers of the particle transforming the particles into its corresponding antiparticle and vice versa but this discrete symmetry leaves all other coordinates unchanged. Both strong and electromagnetic forces conserve this C-symmetry, while in weak interactions, invariance under  $C$  is not given. This is caused by the fact that this symmetry does not change the chirality, which would transform a left-handed Neutrino into a left-handed antineutrino, particle that is not present in the Standard Model. In weak interactions C-symmetry is maximally violated.

---

### 2.2.3. Time Reversal: T-Symmetry

---

In this operation of time reversal  $t$  is replaced by  $-t$  which causes the directions of the spin and momenta to be reversed. Interestingly the operator  $T$  replaces all the complex numbers with their complex conjugate. In electromagnetic and strong interactions  $T$ -symmetry is conserved.

---

### 2.2.4. CPT-Theorem and the Neutral Kaon System

---

In Physics, a combined operation made from C, P and T in any order plays a special role. As the Pauli-Lüders theorem [7] states, any quantum field theorem constructed from fields of spin 0,  $\frac{1}{2}$  and 1 by local interactions that are invariant under proper Lorentz group, is invariant under CPT transformations also. The SM is one example of such a theory and given T invariance, CP invariance follows directly from the CPT theorem.

The combination of parity transformation and charge conjugation known as CP-symmetry implies basically that a process in which all participants are exchanged with their antiparticles is equivalent to the mirror image of the original process and it seems to be conserved in strong and electromagnetic interactions. Also for weak interactions it appeared at first that despite the fact that neither C nor P symmetries are conserved separately, the theory was invariant under their combination.

However CP-violation was first observed experimentally in the decay of neutral Kaons. Actually in this process are two different types of violations of the symmetry: indirect and direct violation.

Direct violations indicate that it occurs due to mixing of the neutral kaon  $K^0$  with its antiparticle  $\bar{K}^0$  ( $\Delta S = 2$ , see Figure 2-1) while the indirect violations actually occur in the decay process ( $\Delta S = 1$ )

The neutral kaon  $K^0$  and its antiparticle  $\bar{K}^0$  are produced as two clearly distinguishable states in strong interaction processes and the  $K^0$  cannot be its own antiparticle due to the fact that kaons carry strangeness which is conserved in strong interactions thus as a possible consequence two neutral kaons must exist. If one assumes that CP-symmetry is conserved in weak interactions, then the physically observable states should be given by the CP-eigenstates. But being particle and antiparticle, the strong eigenstates cannot be the CP-eigenstates in question.

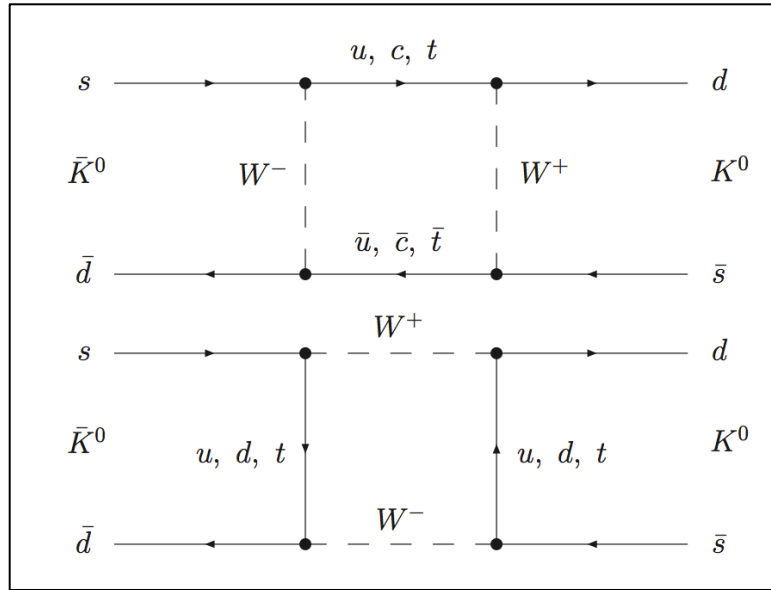


Figure 2-1 Box diagram for neutral kaon oscillations.

But a linear combination of the neutral kaons provides what it is needed:

$$K_1 = \frac{(K^0 - \bar{K}^0)}{\sqrt{2}}, CP = +1$$

$$K_2 = \frac{(K^0 + \bar{K}^0)}{\sqrt{2}}, CP = -1$$

Equation 2-4

Since we assume CP invariance, these states can only decay in a CP-conserving way that implies two different decay modes.  $K_1$  can only decay into a two pions final state which has  $CP=1$ , while  $K_2$  must decay into three pions with  $CP=-1$ .

Since the mass of  $K_2$  is only a little larger than the mass of three pions, one expects the process to be slow in comparison with  $K_1$  by a factor of 600 [8] and indeed the presence of two neutral kaons having very different lifetimes was confirmed experimentally, namely  $K_S$  and  $K_L$ .

An implication of CP-symmetry is that one should not be able to identify  $K_S=K_1$  and  $K_L=K_2$ . In this case  $K_L$  should decay exclusively into three pions this meaning that at a certain distance away from the source, one should not be able to observe any  $2-\pi$  decays.

Despite that, in 1964 Cronin and Fitch [9] found that a small part of  $K_L$  beam decays into two pions. This implies that the observed  $K_L$  and  $K_S$  are not identical with the pure CP-eigenstates but contain a small fraction  $\epsilon$  of the respective other eigenstates.

$$K_S = \frac{(K_1 - \epsilon K_2)}{\sqrt{1 + |\epsilon|^2}}$$

Equation 2-5

$$K_L = \frac{(K_2 + \epsilon K_1)}{\sqrt{1 + |\epsilon|^2}}$$

Equation 2-6



The value of  $\epsilon$  has been determined to be  $|\epsilon| = (2.229 \pm 0.01) \times 10^{-3}$  [10] [9]. This phenomenon is called indirect CP-violation, because it occurs in the mixing but is observed only in the decay process.

However direct CP-violation that occurs directly in the decay has also been observed, but in a smaller proportion by a factor of 1000 compared with the direct effect. Both are present since mixing and decay arise from the same interaction with the W Boson. The Cabibbo-Kobayashi-Maskawa-Matrix (CKM-Matrix) actually allows for CP-violation.

Another sector in which the CP-violation is observed is in the decay of B-mesons in experiment such as BaBar [11] at SLAC and Belle at KeK. [12]

In order to understand the CP-violation in general, it is necessary to take a closer look at its origin in the Standard Model. While in strong and electromagnetic interactions it is not allowed to have a change in quark flavour, in the weak interactions the family symmetry is broken and the mixing of quarks becomes possible. A complex phase in the CKM matrix includes the CP-violation into the SM. This is in principle a direct consequence of the fact that there three quark families as far as we know, all of them with different mass for each of the up-type quarks and each of the down-type quark. These families of particles would not mix and no CP-violation would occur if quarks were massless. In the SM, the mechanism of breaking the family symmetry and gain mass is the Higgs mechanism, and at the same time it is generating a violation of CP-symmetry via charged current interactions [13].

$$\begin{pmatrix} d' \\ s' \\ b' \end{pmatrix} = \begin{pmatrix} V_{ud} & V_{us} & V_{ub} \\ V_{cd} & V_{cs} & V_{cb} \\ V_{td} & V_{ts} & V_{tb} \end{pmatrix} \begin{pmatrix} d \\ s \\ b \end{pmatrix}$$

Equation 2-7 CKM matrix

To conclude, CP-violation in the Standard Model arises from quark to Higgs coupling and at least three families are needed. CKM-Matrix being complex coupled with the fact that no pair of quarks with the same charge is degenerate in mass results that CP-symmetry is violated. This leads to the conclusion that CP-violation in the electroweak sector of the SM is a natural consequence.

Perturbative approach to this sector conserves CP, but does not describe the strong interactions properly.

This so called  $U(1)_A$ -problem will be solved by introducing an additional term in the Lagrangian at the price of losing CP-invariance. This gives rise to the so-called Strong CP-problem that can be solved with different approaches.



### 2.3. The $U(1)_A$ Problem

In the framework of the QCD, the following Lagrangian describes the dynamics of the interactions of quarks and gluons:

$$\mathcal{L}_{QCD} = - \sum_f \bar{q} \left( \gamma^\mu \frac{1}{i} D_\mu + m_f \right) q_f - \frac{1}{4} G_a^{\mu\nu} \tilde{G}_{\mu\nu}^a$$

Equation 2-8

where  $q_f$  are the quark fields of  $f$  flavours of quarks,  $m_f$  are the quark masses and  $G_a^{\mu\nu}$  is the gluon field tensor with its respective dual  $\tilde{G}_{\mu\nu}^a$  ( $a$  being the gluon colour index) the analogous of the electromagnetic field tensor  $F^{\mu\nu}$ . In the limit of  $m_f \rightarrow 0$ , chiral rotations of the quark states into each others is a global symmetry:  $U(f)_R \times U(f)_L$ . However only  $m_u$  and  $m_d$  are small enough to be approximated to zero at the scale of  $\Lambda_{QCD}$ . In these conditions one has an approximate chiral symmetry  $U(2)_R \times U(2)_L$ .

There are two subgroups of this symmetry, one vectorial  $U(2)_V (V = R + L)$  and one axial  $U(2)_V (A = R - L)$ . The vectorial part is an exact symmetry that implies the conservation of baryon number, whilst the axial part is not yet observed.

However the axial subgroup  $U(1)_A$  (with  $A=L-R$  spin alignment) is not a symmetry in the QCD. As a consequence of the breaking of this symmetry, a pseudoscalar particle should exist with vanishing mass in the limit of  $m_u$  and  $m_d \rightarrow 0$  that corresponds to the Nambu-Goldstone Boson on the  $U(1)_A$  symmetry.

This is known as the  $U(1)_A$  problem, the solution of which created yet another one [14]. A detailed solution to this problem can be found in [15]

Another solution to this problem has been presented by Hooft [3] who introduced an anomalous symmetry breaking known as Adler-Bell-Jackiw anomaly, which means that the symmetry is broken in the quantum theory but not classically. The direct consequence in our case is the appearance of an additional term  $\mathcal{L}_\theta$  in the Lagrangian:

$$\mathcal{L}_\theta = \theta \frac{g^2}{32\pi^2} G_{\mu\nu}^a \tilde{G}_a^{\mu\nu}$$

Equation 2-9

where  $g$  is the coupling constant and  $G_{\mu\nu}^a$  the gluon field strength tensor together with its dual  $\tilde{G}_a^{\mu\nu}$  given by:

$$\tilde{G}_a^{\mu\nu} = \frac{1}{2} \epsilon^{\mu\nu\rho\sigma} G_{\rho\sigma}^a$$

Equation 2-10

The understanding of the origin of the additional term lies in the fact that the QCD is a non-Abelian field theory, and the vacuum reveals a complicated structure, thus one should take a closer look at  $\theta$  – vacuum. More precisely this means that the ground state is a superposition of an infinite number of degenerate vacua characterized by a winding number  $n$ . These vacua  $|n\rangle$  have the property of not being invariant under all possible gauge transformations and as a consequence they are not the proper vacuum. The ground state often referred as  $\theta$  – vacuum can be obtained as a superposition of the degenerate vacua and it is gauge-invariant, being expressed as:

$$|\theta\rangle = \sum_{n=-\infty}^{\infty} e^{-in\theta} |n\rangle$$

Equation 2-11

A new expression of the Lagrangian  $\mathcal{L}_\theta$  can be obtained by calculating the transition amplitude between  $\mathcal{L}_\theta - vacua$  with the according numbers  $n$  and  $n'$

$$\mathcal{L}_\theta = \theta q$$

Equation 2-12

where  $q$  is the so called Pontryagin index [16] :

$$q = n - n' = \frac{g^2}{32\pi^2} G_{\mu\nu}^a \tilde{G}_a^{\mu\nu}$$

Equation 2-13

taking into account the electroweak interactions:

$$\bar{\theta} = \theta + \theta_{weak} = \theta + \arg(\det M)$$

Equation 2-14

where  $M$  signifies the quark mass matrix, the additional term in the Lagrangian is becoming:

$$\mathcal{L}_{\bar{\theta}} = \bar{\theta} \frac{g^2}{32\pi^2} G_{\mu\nu}^a \tilde{G}_a^{\mu\nu}$$

Equation 2-15

thus the QCD Lagrangian can be written as:

$$\mathcal{L}_{QCD} = \mathcal{L}_{pert} + \mathcal{L}_{\bar{\theta}}$$

Equation 2-16

This new additional term is renormalized and gauge invariant, and it manages to solve the  $U(1)_A$ -Problem but at the cost of introducing a new term which is not invariant under CP, situation known as **CP-Problem**.

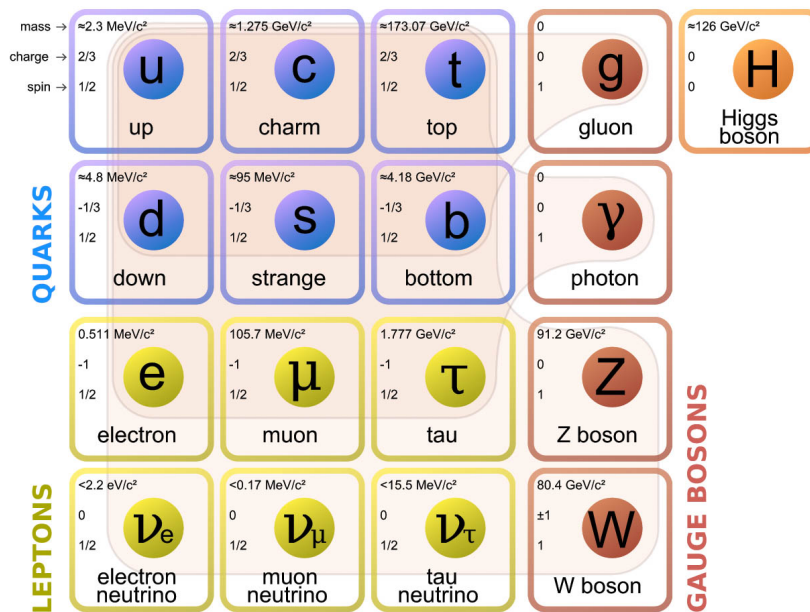


Figure 2-2 Updated diagram of the Standard Model - elementary particles with three generations of fermions, gauge Bosons on the fourth column, and the Higgs Boson in the fifth [17]

## 2.4. The Strong CP-Problem

To help us demonstrate that this new term introduced in the QCD Lagrangian violates CP, we will make a parallel with a similar term from QED, which contains the electromagnetic field tensor described by the following formula:

$$F_{\mu\nu}\tilde{F}^{\mu\nu} = 4\vec{E} \cdot \vec{B}$$

Equation 2-17

If we act with C transformation we get the following:

$$\begin{aligned} C(\vec{E}) &= -\vec{E} \\ C(\vec{B}) &= -\vec{B} \end{aligned}$$

Equation 2-18

And when applying P transformation:

$$\begin{aligned} P(\vec{E}) &= -\vec{E} \\ P(\vec{B}) &= +\vec{B} \end{aligned}$$

Equation 2-19

Because P is violated while C is conserved, it is clear CP-symmetry is violated overall but if we consider a term of the form  $F_{\mu\nu}\tilde{F}^{\mu\nu}$  the CP will be conserved since it is proportional with  $(B^2 - E^2)$ .

The CP-violating effects from one can expect from the term in the Equation 2-15 are large unless  $\bar{\theta}$  is extremely small.

If we look at the  $\bar{\theta}$ -dependence of the electric dipole moment of the neutron  $d_n$  predicted by MIT in the bag model [18] :

$$d_n = 32.7 \times 10^{-3} e \frac{3m_u m_d m_s}{m_u m_d + m_u m_s + m_d m_s} R^2 \bar{\theta}$$

Equation 2-20

If we use a bag radius of  $R \approx (140 \text{ MeV})^{-1}$  as well as  $m_d/m_u = 1.8$  ;  $m_s/m_d = 20$  and  $m_s \approx 300 \text{ MeV}$  one obtains:

$$d_n = 8.2 \times 10^{-16} \bar{\theta} e \text{ cm}$$

Equation 2-21

In literature can be found values of [19] [20] [21] :

$$d_n = 2.7 - 5.2 \times 10^{-16} \bar{\theta} e \text{ cm}$$

Equation 2-22

The latest experimental limit on the EDM of the neutron is [10] [21]:

$$|d_n| < 2.9 - 6.3 \times 10^{-26} e \text{ cm at } 90\% \text{ confidence level}$$

Equation 2-23

This implies a value for  $\bar{\theta} < 10^{-10}$  that is perfectly allowed (i.e it can take any value between 0 and  $2\pi$  with the same likelihood) but it needs an explanation since this would imply fine-tuning of the two contributions to  $\bar{\theta}$ . Either both QCD and electroweak contributions are in the order of  $\bar{\theta}$  or the two terms cancel each other resulting such a small value.

In essence the answer to the question *why is  $\bar{\theta}$  such a small quantity* is an equivalent formulation to the strong CP-Problem.

There are several solutions proposed for solving the strong CP-problem. The least likely solution involves zero quark masses, then a second one is called soft-CP and sets  $\theta = 0$ , while a third and most elegant uses the Axion solution as proposed by Peccei and Quinn [22] [23].

## 2.5. The Peccei-Quinn Mechanism

This mechanism is the preferred one from the three proposed solutions mainly because it is the most elegant and also because the other two are increasingly unlikely. At the moment the possibility of a massless quark is ruled out and the soft CP solution requires one-loop suppression to achieve compatibility with the experimental limits.

The fundamental concept that this mechanism relies on, is to make  $\bar{\theta}$  dynamically variable (i.e. a phase) with a minimum value at zero instead of having it under the form of a parameter or a coupling constant specific for this theory. In the case of a  $\bar{\theta}$  dynamically variable, different  $\bar{\theta}$ 's will distinguish different vacuum states in one given theory, and it has to be shown that  $\bar{\theta} = 0$  is the true vacuum.

For obtaining  $\bar{\theta} = 0$  Peccei and Quinn introduced a new global chiral symmetry called  $U(1)_{PQ}$  known as *Peccei-Quinn-Symmetry* (PQ-symmetry).

$U(1)_{PQ}$  is spontaneously broken at the energy scale of the symmetry,  $f_a$ , generating a Goldstone Boson which is massless at the classical level but acquires a small mass through the axial anomaly. This Pseudo-Goldstone Boson is called the **Axion** [24] [25].

The new field imposes a new term  $\mathcal{L}_{Axion}$  to the QCD Lagrangian  $\mathcal{L}_{QCD}$  as it follows:

$$\mathcal{L}_{QCD} = \mathcal{L}_{pert} + \mathcal{L}_{\bar{\theta}} + \mathcal{L}_{Axion} = \mathcal{L}_{pert} + \bar{\theta} \frac{g^2}{32\pi^2} G_{\mu\nu}^a \tilde{G}_a^{\mu\nu} + \mathcal{L}_{Axion}$$

Equation 2-24

The new term has the following structure:

$$\mathcal{L}_{Axion} = \mathcal{L}_{kin} + \mathcal{L}_{int} - V_{eff}$$

Equation 2-25

$$\mathcal{L}_{kin} = -\frac{1}{2}(\partial_\mu a)(\partial^\mu a)$$

Equation 2-26

The first term represents the kinetic energy  $\mathcal{L}_{kin}$ , the second accounts for the potential of interaction with the other Axions and the third term can be expanded as:

$$V_{eff}(a) = -C_a \frac{a}{f_a} \frac{g^2}{32\pi^2} G_{\mu\nu}^a \tilde{G}_a^{\mu\nu}$$

Equation 2-27

This term takes into account the interactions of the Axions with gluons.

$C_a$  is a model depending parameter,  $a$  is the Axion field,  $g$  is the strong coupling constant, and  $f_a$  is the scale of spontaneous PQ-symmetry breaking referred as SSB.

To obtain the vacuum expectation value of the Axion field one has to calculate the extreme of the potential:

$$\langle a \rangle = -\frac{f_a}{C_a} \bar{\theta}$$

Equation 2-28

Basically, the existence of the so far hypothetical Axions needs to be proven to explain why no CP violation is observed in the strong interactions, although initially it was expected.

### 3. The Axion Physics

In the previous chapter we have arrived at the conclusion that the existence of an Axion would solve the CP-problem through the Peccei-Quinn mechanism. This chapter will give an overview on general Axion Physics, properties of the Axions and coupling with fundamental Bosons and fermions. Different Axion models will also be discussed.

#### 3.1. Coupling of Axions

Coupling to fundamental particles is the symmetry breaking scale of the newly introduced PQ-Symmetry  $U(1)_{PQ}$ , so it is the most important parameter which determines the property of the Axion noted as  $f_a$ .

Before starting it should be noted that the breaking scale is arbitrary, since it just represents the curvature of the Axion potential which has a minimum for  $\bar{\theta} = 0$  so all the values are allowed for the breaking scale. The same holds true for the Axion mass and the coupling constants of Axions to various particles because both are inversely proportional to  $f_a$ .

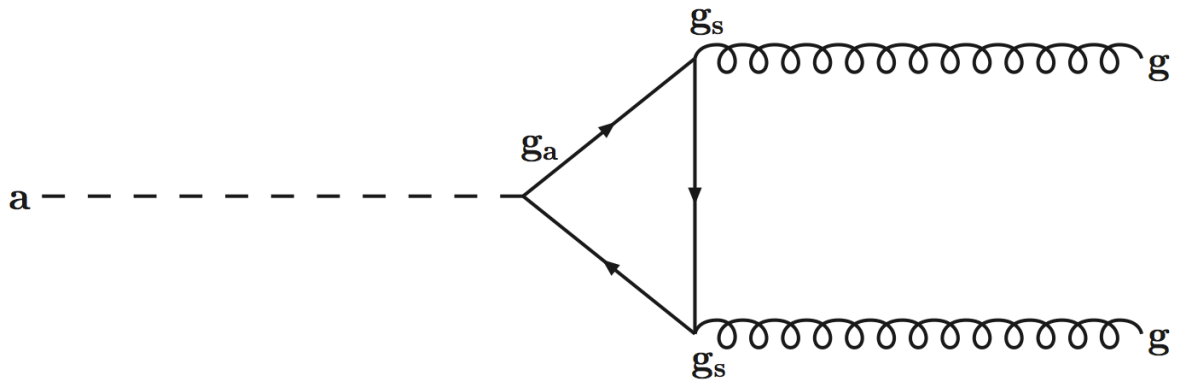


Figure 3-1 Triangle loop diagram for the Axion-to-gluon coupling.

In the above picture  $g_s$  is the strong coupling constant and  $g_a$  is the Axion to fermion Yukawa coupling.

Axions can couple to fundamental Bosons and fermions, their interaction contributing to the interaction term  $\mathcal{L}_{int}$ . More explicitly the interaction part can be written as:

$$\mathcal{L}_{int} = \mathcal{L}_{a\gamma} + \mathcal{L}_{af}$$

Equation 3-1

where  $\mathcal{L}_{a\gamma}$  describes the interaction of Axions with photons and  $\mathcal{L}_{af}$  the one with fermions.

$$\mathcal{L}_{a\gamma} = g_{a\gamma} a \vec{E} \cdot \vec{B}$$

Equation 3-2

### 3.2. Coupling with Gluons

As shown in the Figure 3-1 Axions can couple to gluons via a triangle loop due to chiral anomaly and this yields the following contribution:

$$\mathcal{L}_{aG} = \frac{\alpha_s}{8\pi f_a} a G_a^{\mu\nu} \tilde{G}_{\mu\nu}^a$$

Equation 3-3

where  $\alpha_s$  is the fine structure constant.

Due to the interaction with gluons they can also mix with pions acquiring this way mass [26] [27].

$$m_a = \frac{m_{\pi^0} f_{\pi}}{f_a} \left[ \frac{z}{(1+z+W)(1+z)} \right]^2 \approx 0.6 eV \frac{10^7 GeV}{f_a}$$

Equation 3-4

The coupling of gluons with Axions is present in all Axion models, and as a consequence also the coupling of Axions with photons is generic in all models.

### 3.3. Coupling with Photons

Thanks to the Axion mixing with pions, Axions also couple with photons. The following equation represents the contribution to the Lagrangian from Axion-photon interaction:

$$\mathcal{L}_{a\gamma} = -\frac{1}{4} g_{a\gamma} F_{\mu\nu} \tilde{F}^{\mu\nu} a = g_{a\gamma} \vec{E} \cdot \vec{B}_a$$

Equation 3-5

Where  $a$  denotes the Axion field and  $g_{a\gamma}$  represents the coupling constant of Axions to photons. Also  $\vec{E}$  and  $\vec{B}$  represent the electric and magnetic field.

Also in models in which fermions carry a PQ-charge in addition to the electric charge another contribution can appear. Then, the interaction can also take place via a fermionic triangle loop as shown in the following picture:

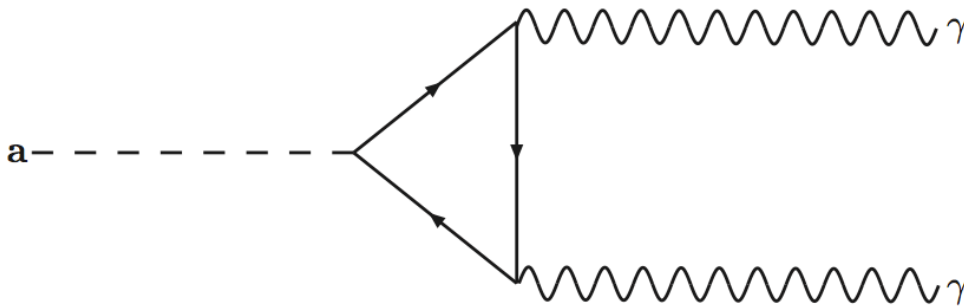


Figure 3-2 Additional contribution to the coupling of Axions to photons via a triangle loop through fermions carrying both PQ and electric charges.

### 3.4. Coupling with Electrons

The Lagrangian of interaction with the fermions is the following:

$$\mathcal{L}_{af} = \frac{g_{af}}{2m_f} (\bar{\psi}_f \gamma^\mu \gamma_5 \psi_f) \partial_\mu a$$

Equation 3-6

where  $m_f$  is the fermion mass and  $g_{af}$  the coupling constant explicitly written as:

$$g_{af} = \frac{C_f m_f}{f_a}$$

Equation 3-7 fermion coupling constant

Focusing on the coupling with electrons there are two possible important couplings with Axions shown in the following diagrams:

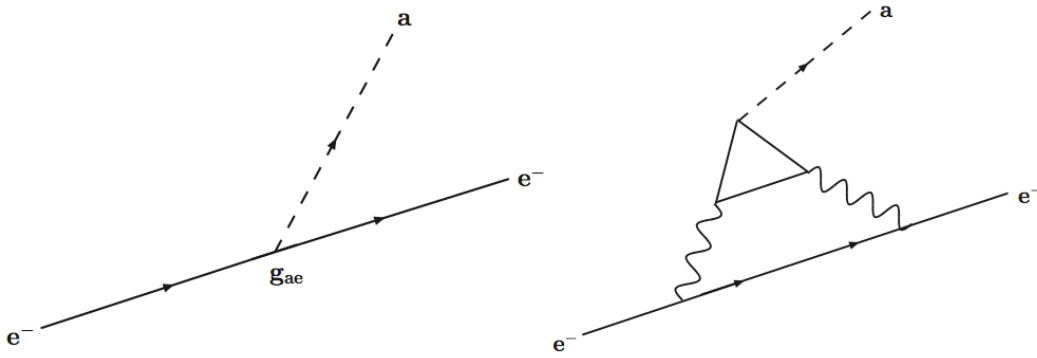


Figure 3-3 Axion-electron coupling. Left: Contributing Feynman diagram for direct Axion-electron coupling which is possible only in models in which fermions carry PQ-charge (see DFSZ Model). Right: Radiatively induced coupling of Axions to electrons at a one-loop level. This coupling is present even in models in which fermions do not carry PQ-charge (see KSVZ Model).

### 3.5. Coupling with Nucleons

There are two different and almost equal contributions in this case: the coupling to light quarks at tree-level and the mixing of the Axions with pions. This is important because even the so-called hadronic Axions still show a coupling to light quarks at tree level, but only to a heavy exotic quark species, and can be used for deriving bounds on Axion mass from the supernova SN 1987A case in which mainly the coupling with nucleons is dominant.

The coupling constant is given by [26]:

$$g_{aN} = \frac{C_N m_N}{f_a} = 1.56 \times 10^{-7} m_a C_N \text{eV}^{-1}$$

Equation 3-8

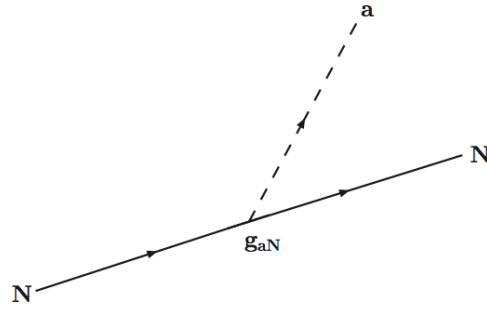


Figure 3-4 Feynman Diagram of direct Axion to nucleon coupling. Even Axions which do not couple to light quarks at tree-level still have a coupling to nucleons since the Axion nucleon coupling partly results from Axion-pion mixing and partly from the shown direct coupling of Axions to nucleons.

### 3.6. Other processes

There are some other processes involving Axions, which play a role in the frame of astro-physical picture. For Axions models with tree-level coupling to electrons, the dominant Axion emission process in main sequence Stars, white dwarfs and red giants are bremsstrahlung and Compton-like processes which have the following diagram:

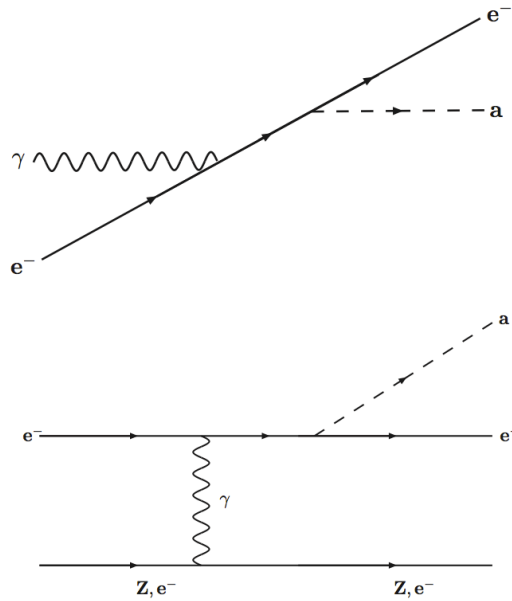


Figure 3-5 Upper image: Compton-like process for Axion models with Axion-electron coupling at tree-level. Together with the bremsstrahlung process shown in the lower part of this figure, Compton scattering is the main Axion emission process in main sequence Stars, white dwarfs and red giants. Lower image: Electron bremsstrahlung process for Axion models with Axion electron coupling at tree-level.

In the same Stars, the dominating emission process for hadronic Axions is the **Primakoff Effect** because the coupling to electrons is strongly suppressed. In the conditions found inside the Stars, with plasma and intense electric field a photon can be converted into an Axion via this Primakoff effect which is incidentally the discovery process on which Helioscopes rely on [28].



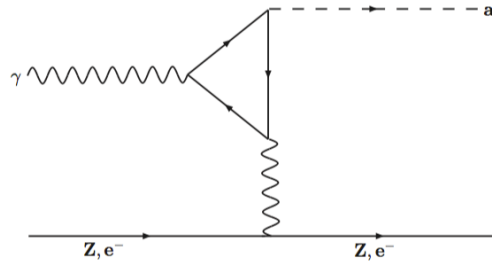


Figure 3-6 The Primakoff effect - the dominant Axion emission process in hadronic models for main sequence Stars, horizontal branch Stars, red giants and white dwarfs.

In the case of neutron Stars both models show the same dominant emission process: nucleon-Axion bremsstrahlung represented in the following Feynman diagram:

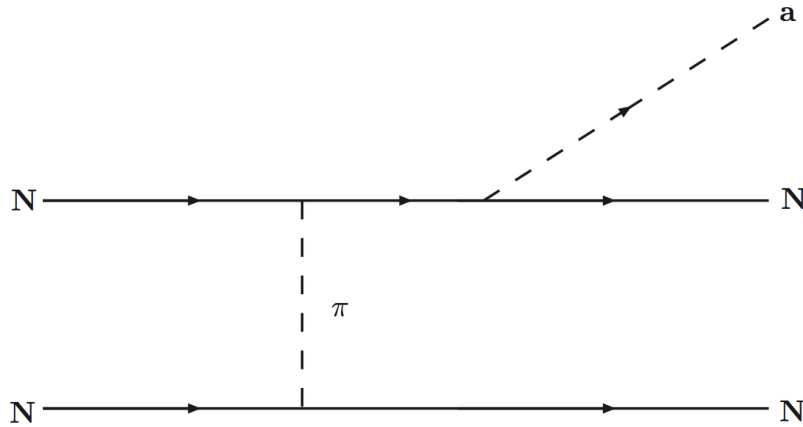


Figure 3-7 Axion Nucleon bremsstrahlung is the most important Axion emission process in neutron Stars.

### 3.7. The visible Axion

Also known as the Peccei-Quinn-Weinberg-Wilczek Axion, was born from the originally proposed additional symmetry by Peccei and Quinn [22] [24] [25], which assumed that the symmetry breaking scale of the PQ-symmetry was of the order of the electroweak scale  $f_{weak} \approx 250 \text{ GeV}$ . This would yield an Axion mass larger than 150 keV that was ruled out quickly.

A requirement for the visible models is the existence of two independent Higgs fields, which give mass to  $u$  and  $d$  quarks.

These standard Axion models were excluded by the following kaon decay:

$$K^+ \rightarrow \pi^+ a$$

Equation 3-9

The experimental limit for this decay is lower than the expected branching ratio resulting from the visible models [29].

Bardeen and Tye provided calculations for the lifetime of the visible Axion based on its decay into two photons which is about 0.1 sec for a 150 keV Axion. For Axions heavier than 1 MeV, the lifetime gets considerably shorter since the decay channel into electron-positron pair opens yielding a lifetime of:  $10^{-8} - 10^{-9} \text{ s}$  [27] [30].

### 3.8. The invisible Axion Models

The exclusion of the visible Axions gave a theoretical motivation for producing Axion models with a much weaker coupling and a smaller mass than initially expected from the PQWW Axion. Due to the fact that the breaking scale  $f_a$  is in principle arbitrary, it could be chosen much larger than the electroweak breaking scale.

One such model is the so-called Kim-Shiftman-Vainshtein-Zakharov Model (KSVZ). In this case, since the ordinary quarks, leptons and Higgs fields do not carry PQ-charge, an exotic heavy quark  $Q$  carrying PQ charge was introduced. The Axion interactions in this model occur mainly through the new exotic quark, thus Axions in this model are considered as “*hadronic Axions*” [31] [32].

Opposite to this the Dine-Fischler-Srednicki-Zhitnitskii Model (DFSZ) does not require any additional heavy quark but supplementary Higgs doublets are introduced.

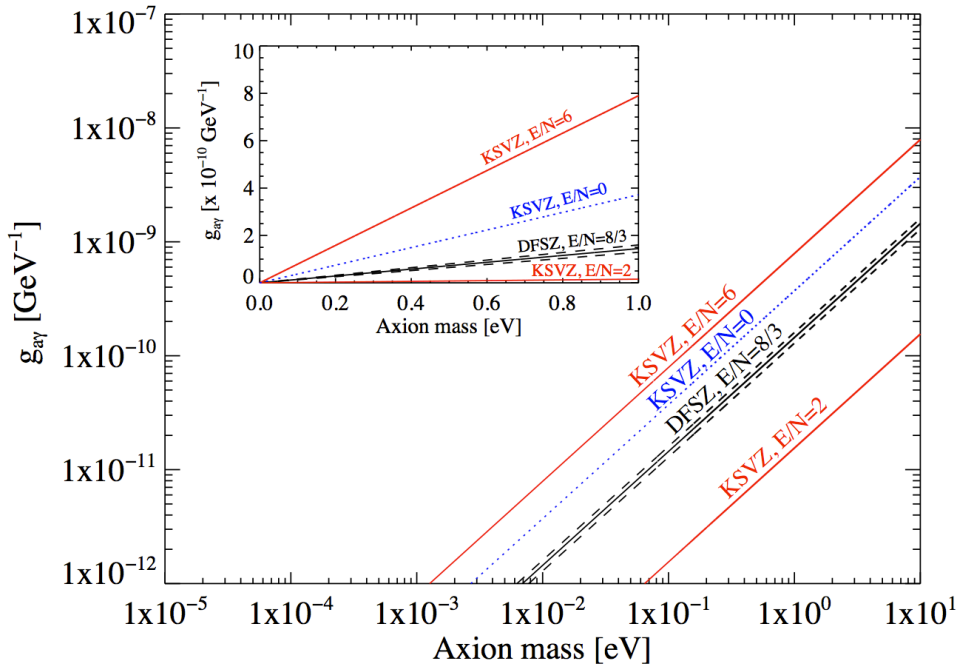


Figure 3-8 Plotted the two most common invisible Axion models KSVZ and DFSZ . The inserted plot shows the same plot but in linear scale. The error bars are inserted here under the form of black dashed lines.

The Axion-photon coupling constant is given by:

$$g_{a\gamma} = \frac{\alpha}{2\pi f_a} \left[ \frac{E}{N} - \frac{2(4+z+w)}{3(1+z+w)} \right]$$

Equation 3-10

where  $\alpha$  is the fine structure constant ( $e^2/4\pi \approx 1/137$ ),  $z$  and  $w$  are the quark mass ratios and  $E/N$  is a model dependent term.

$$g_{a\gamma} = \frac{\alpha}{2\pi f_a} \left( \frac{E}{N} - 1.92 \pm 0.08 \right) = \frac{\alpha}{2\pi f_a} C_\gamma$$

Equation 3-11

The ration  $\frac{E}{N}$  is the result of the electromagnetic anomaly  $E$  and colour anomaly  $N$  [33] [34]. As a consequence depending on the model,  $E/N$  can enhance the Axion-photon coupling if it takes higher values or it can suppress it otherwise.

$$E \equiv 2 \sum_f X_f Q_f^2 D_f$$

$$N \equiv \sum_f X_f$$

Equation 3-12

where  $X_f$  represents the PQ-charge of the fermion  $f$ , while  $Q_f$  is its electric charge in units of  $e$ .  $D_f = 1$  for colour singlets (charged leptons) and  $D_f = 3$  for quarks.

The case of  $E/N = 0$  is often referred as the standard KSVZ Model and in general for KSVZ  $E/N$  is calculated as:

$$\frac{E}{N} = 6Q_{heavy}^2$$

Equation 3-13

where  $Q_{heavy}$  is the electric charge of the heavy quark which can take the following values:  $\{2/3, -1/3, 1, 0\}$ . This implies that the ratio of anomalies can be between 0 and 6 [35] .

While the KSVZ Model decreased the Axion mass by decreasing its coupling to ordinary matter needing to introduce a supplementary quark which is neutral with respect to the electroweak sector, the DFSZ Model has a different philosophy. It makes use of two Higgs doublets  $\Phi_1$  and  $\Phi_2$ . One of them couples only to right-handed quarks of charge  $2/3$  and the other interacts only with right-handed quarks of charge  $-1/3$  and right handed charged leptons. In order to obtain a breaking scale higher than the electroweak scale some fine-tuning is necessary but its big advantage is that it does not require the introductions of a new exotic heavy quark. Also it can be relatively easily integrated into the Grand Unified Theories because in the supersymmetric extensions of the Standard Model, generally two Higgs doublets are preferable.

So in the grand unified model such as DFSZ (Dine-Fischler-Srednicki-Zhitiniskii) [36] [37], Axions couple with ordinary quarks and leptons thus giving  $E/N = 8/3$  and giving a value for  $g_{a\gamma}$ :

$$g_{a\gamma}^{DFSZ} \approx -0.75 \frac{\alpha}{2\pi f_a}$$

Equation 3-14

The ALP community (Axion Like Particles) is getting increasing interest and attention. It makes efforts to include quests for mini-charged particles from the hidden sector Physics involving paraphotons and chameleons. I would like to note that recent new models involving hypothetical pseudoscalar particles have been proposed [38].

Sometimes the invisible Axions are also referred as WISPs , acronym that stands for Weakly Interacting Sub-eV Particles [39].

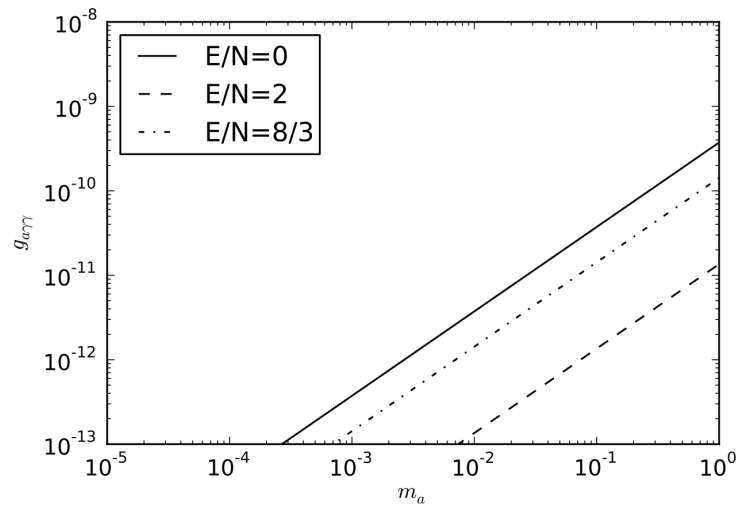
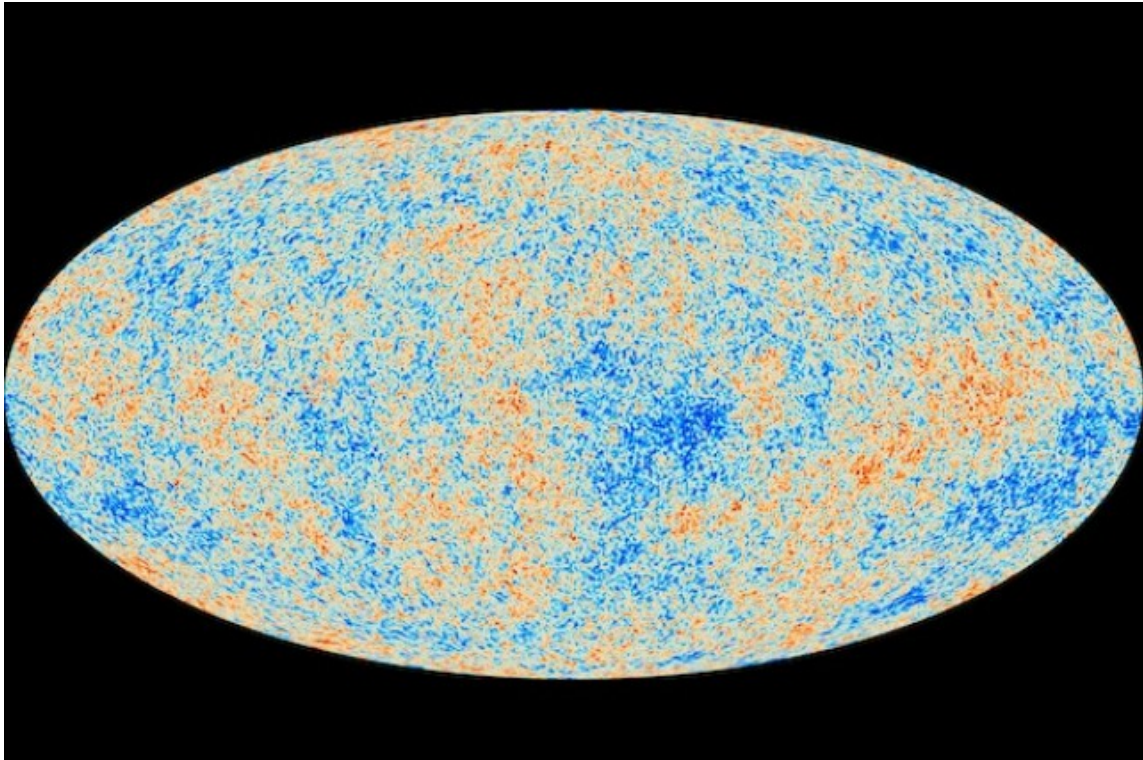


Figure 3-9 Axion mass versus coupling constant,  $E/N$  dependence for DFSZ Model



The cosmic microwave background (CMB) as observed by Planck / ESA and Planck Collaboration

---

### 3.9. Axions as Dark Matter Candidates

---

In Figure 3-10 are condensed four years of data from the European Space Agency's Planck spacecraft. The image was released in December 2014 at the conference in Ferrara Italy and will be published soon.

We live in a 13.8 billion years old Universe and these pictures show maybe the most precise map of the Universe as it was at 380000 years after the Big-Bang. You can think of this CMB as the hazy afterglow of the Big-Bang, a snapshot of the oldest light that illuminated the sky during the Universe's infancy.

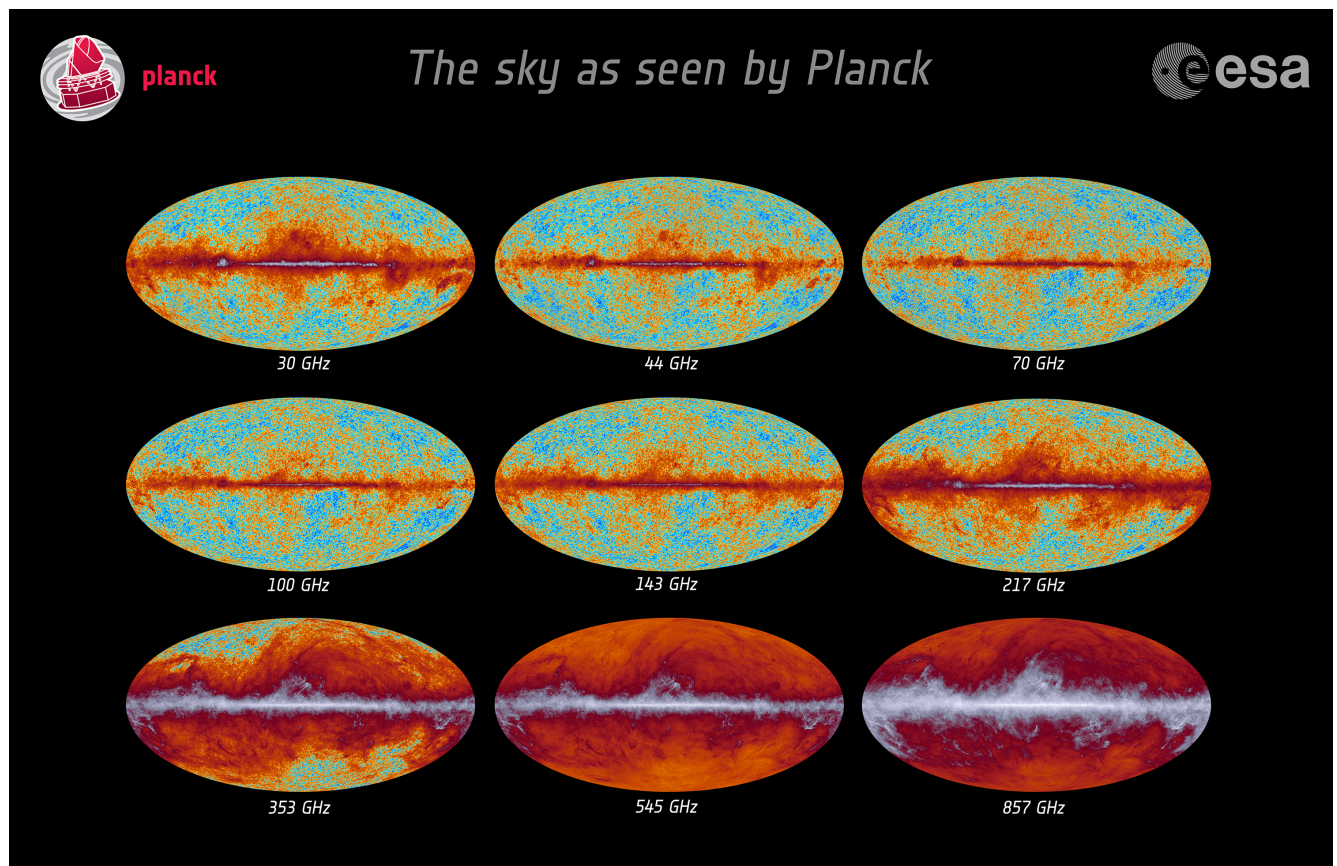


Figure 3-10 CMB as observed by Planck in 9 frequency channels – 12.2014

Planck was launched in 2009 and was designed to map the sky in nine different frequencies ranging from microwave to sub-millimetre wavelengths. Its mission was to observe the first light in the Universe. Immediately after the Big-Bang, radiation filled the Universe, and remnants of that radiation are observable by us today as the cosmic microwave background. As the Universe expanded, it cooled, and the radiation stretched to microwave wavelengths with minute temperature fluctuations. These correspond to the regions of slightly different densities, generated by quantum-mechanical fluctuations in the first microseconds after the Big Ban. These anisotropies represent the seeds of the Stars, galaxies and clusters of galaxies we have today.

Seven of Planck's nine frequency channels were equipped with polarisation sensitive detectors, and the new data in addition the temperature fluctuations has also polarisation information which is not yet published at the date I am writing this thesis. However the new data confirms and refines the earlier measurements: The Standard Model continues to fit very well only the 4.6% of the baryonic matter content of the Universe.

Dark Matter is estimated to account for 24% of the mass content of the Universe the rest of 71.4% being attributed to Dark Energy.



The problem is that the Standard Model does not account for Dark Matter and Dark Energy, and for the purpose of this thesis it does not predict a candidate that could be a Dark Matter candidate. On the other hand, the Axion, arising from the Peccei-Quinn solution to the Strong CP problem can be a *viable candidate*.

Axions satisfy the general criteria for becoming a cold Dark Matter candidate. Although Axions have a small mass, Axion Dark Matter is non-relativistic as they were produced in the early Universe from equilibrium through the following three mechanisms:

- Vacuum realignment [40] [41] [42];
- String decay [43] [44] [45];
- Domain wall decay [46] [47] [48].

Thermally produced Axions, which should have a mass in the eV range, can form a hot Dark Matter component.

The misalignment effect or the decay of the Axion strings would provide a very low mass Axion that can be a component of the cold Dark Matter.

Dark Matter can be *hot* (HDM) made from light relativistic particles or *cold* (CDM), made from heavier nonrelativistic particles. Axions are candidate for both, with certain limits imposed.

Axions with masses in the eV range can account for the HDM together with the Neutrinos. WMAP puts a limit for the HDM Axion mass to  $m_a < 1.02 \text{ eV}$  [49] produced in the thermalization process:

$$\pi + \pi \rightarrow \pi + a$$

*The Axions are long-lived, weakly interacting, colour and charge neutral particles.* If we consider that the lifetime of the Axions is governed by the following decay:  $a \rightarrow \gamma\gamma$  according to [50] we get:

$$\tau_a = 4.6 \times 10^{40} \text{ s} \left( \frac{E}{N} - 1.95 \right)^2 \left( \frac{f_a/N}{10^{10} \text{ GeV}} \right)^5$$

Equation 3-15

And by setting  $\frac{E}{N} = 0$  and  $\frac{f_a}{N} \geq 3 \times 10^5 \text{ GeV}$  which is a value favoured by the cosmological and astrophysical constraints one finds that  $\tau_a > t_0$ , where  $t_0$  is the age of the Universe.

### 3.10. Astrophysical constraints

The Axion mass  $m_a$  is in principle arbitrary once the CP-Problem is solvable for any value of the PQ breaking scale  $f_a$ . However we are able to exclude certain mass ranges based on astrophysical observations and cosmology. This is useful information for the experimental physicist who can concentrate on mass ranges where Axions are more likely to exist. The main source of constraint for the Axion parameter space is the *evolution of low-mass Stars*.

In the next image the main astrophysical and cosmological bounds are summarised and also some experimentally scanned regions are shown.

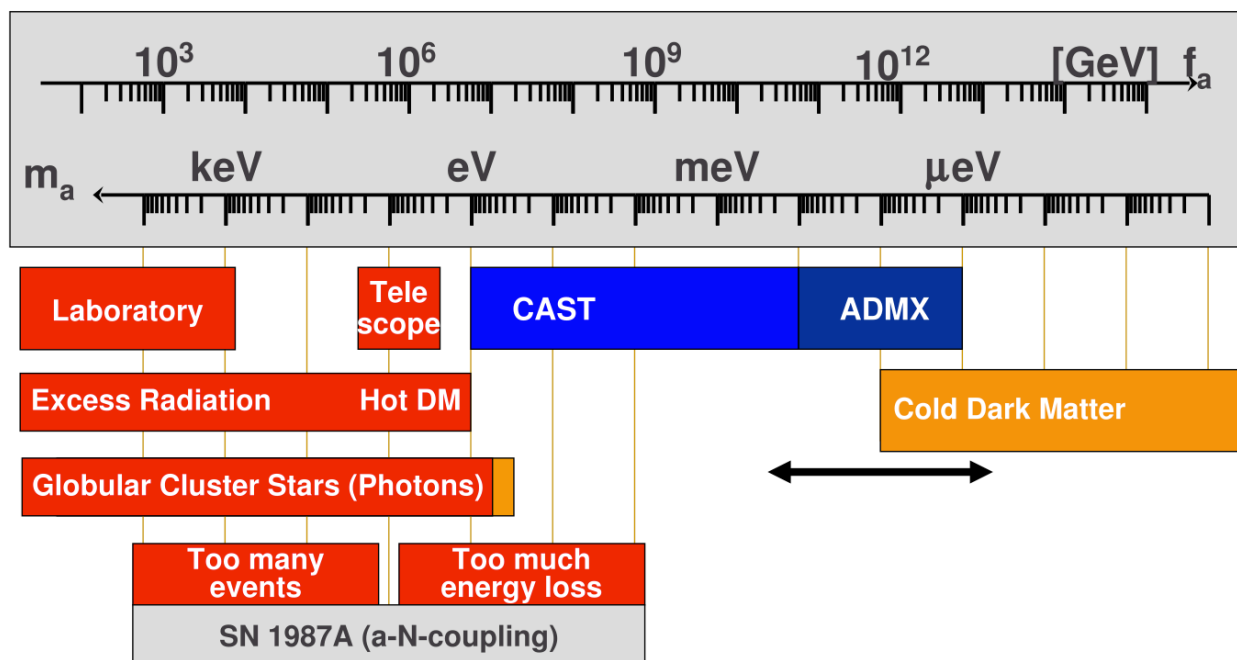


Figure 3-11 Astrophysical and cosmological exclusion ranges together with experimentally reachable mass-ranges. The orange bars indicate a strong model dependence. [51]

---

### 3.10.1. Stellar evolution of Low-Mass Stars

---

Having a good understanding of the life and evolution of Stars is essential for the Axion Physics mainly because one can deduce limits on the Axion mass thinking in framework of the energy loss channel. Though the details of stellar evolution are not yet fully understood. It is a well-known fact that the Stars are born in the globular clusters that lie within the disks of the spiral galaxies. Usually in these globular clusters, Stars tend to have the same chemical composition, age and generation. The main free parameter that separates them is their *initial mass*.

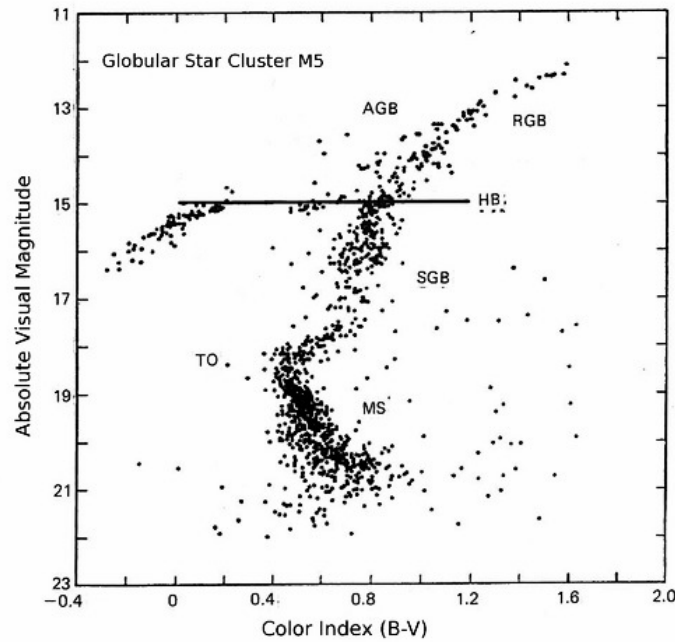


Figure 3-12 The Hertzsprung-Russell diagram for the globular Star cluster M5 - it is a good representative for a typical globular cluster of the same generation. Here the visual magnitude is plotted as a function of the colour index.

In the attached H-R diagram (Figure 3-12) the high mass Stars from this specific globular Star cluster have left the main sequence at a relatively low turn off point denoted TO illustrating a greater age than the open Star clusters and indicating the evolutionary tracks of these Stars into the red giant branch denoted as RGB as well as the other evolutionary stages like the sub-giant branch (SGB) and AGB, the asymptotic giant branch. As indicated in the figure by the line, the horizontal branch extends to the left [52].

The colour index is essentially the difference between the blueness  $B$  and the brightness  $V$ , the blueness being a measure of the colour of the surface temperature, blue hot Stars shifting towards the left.

The first stage in the life of a regular Star is the burning of the hydrogen from its core and is called the main sequence. The mass parameter impacts the position of the MS Stars in the diagram by shifting it and the more massive a Star is the brighter it shines and its lifetime is shorter.

The next stage in the evolution of a Star happens when all the hydrogen supply from the core is exhausted. The Star develops a degenerate helium core with a burning hydrogen shell the result of which is an increase in surface area and a decrease in surface temperature. This turns the Star into a red giant that starts climbing the red giant branch (RGB). When moving up the brightness is also increasing because the luminosity is determined by the gravitational potential at the outer zone of the helium core.



$$M_{\odot} \approx 1.988 \times 10^{30} \text{ kg}$$

Equation 3-16 The solar mass

The red giant continues to burn the hydrogen shell until the helium core reaches  $0.5 * M_{\odot}$  mass and it is dense and hot enough to start fusing helium. Two  $\alpha$  particles form an  ${}^8\text{Be}$  nucleus which is unstable thus the helium burning process must follow the triple  $\alpha$  reaction directly to carbon  $3\alpha \rightarrow {}^{12}\text{C}$ . Because the core expands further pushing the hydrogen shell outwards, the energy production rate goes down together with the brightness.

Once the entire supply of hydrogen is exhausted, a degenerate core of carbon-oxygen is formed and the Star climbs the asymptotic giant branch (AGB). [53]

Since the Stars in this category are not massive enough to ignite the new carbon-oxygen degenerate core, they become a white dwarf. [54]

### 3.10.2. Globular Clusters limits

A globular cluster is a gravitationally bound system of about  $10^6$  Stars of low metallicity, which were formed at the same time. They can provide a restrictive limit of the coupling constant  $g_{a\gamma}$  by making reasonable assumptions on their helium-burning lifetime and in addition to this another limit can be derived on the Axion-electron coupling by observing the helium ignition phase.

The Stars from the horizontal branch and the red giants are the most useful for obtaining bounds on the Axionic parameters (see Figure 3-12).

In both HB and RG Stars the photons can be converted into Axions via Primakoff effect by interacting with a virtual photon from the electromagnetic fields of the electron-proton plasma.

$$Ze + \gamma \rightarrow Ze + a$$

Equation 3-17

In HB Stars this mechanism would actually generate an energy loss channel much more so than in the RGB Stars where it is negligible. To be noted is that low mass Stars spent approx.  $10^{10}$  years on the main sequence while RGB and HB sequences have a duration of about  $10^8$  years so one should be able to observe that the number of helium burning Stars is reduced in comparison to red giants. A study conducted by A. Buzzoni et al. concludes that the HB to RGB Star ration observed in 15 clusters agrees within about 10% with the theoretical estimations [55]. This can be interpreted as the fact that the non standard energy loss rate should not exceed 10% of the standard helium burning luminosity:

$$L_x \leq 0.1 L_{3\alpha}$$

Equation 3-18 energy loss ratio

Considering a standard value for  $L_{3\alpha}$  of about  $20 L_{\odot}$  for the mass of a HB Star of about  $0.5 M_{\odot}$  the energy production rate can be calculated and an upper limit on the energy loss rate per unit of mass of the non standard channel can be estimated and then an upper limit on the Axion to photon coupling constant is obtained as:

$$g_{a\gamma} \leq 0.6 \times 10^{-10} \text{ GeV}^{-1}$$

Equation 3-19 coupling constant upper limit

which can be expressed in terms of Axion mass as:

$$m_a C_{\gamma} \leq 0.3 \text{ eV}$$

Equation 3-20 Axion mass upper limit

where  $C_\gamma \approx 0.75$  for DFSZ and  $C_\gamma \approx 0.08 - 4.08$  for the KSVZ Model.

Generally a reasonably conservative globular cluster limit from the analysis of the horizontal branch is:

$$g_{a\gamma} \lesssim 1.0 \times 10^{-10} \text{GeV}^{-1}$$

The Primakoff effect is suppressed in the degenerate helium cores of red giant Stars which have typically a temperature of  $10^8$  K and a density of about  $10^6$  g/cm<sup>3</sup>. At a critical combination of these two parameters the helium ignites, but the Axion cooling could shift this point and allow the core to grow larger. This would lead from the observational point of view to an increase in the brightness of red giants. However the theoretical expectations and the astronomical observations of the core mass at helium ignition match within 5 – 10 %. This argument of the helium ignition is especially helpful when the emission rates are larger for Stars on the red giant branch than on the HB.

If one applies the electron bremsstrahlung for the core conditions of a red giant we get the following coupling constant limit:

$$\begin{aligned} e + Ze &\rightarrow Ze + e + a \\ \epsilon_{brem} &\approx g_{ae}^2 \times 1.6 \times 10^{26} \text{erg g}^{-1} \text{s}^{-1} \\ g_{ae} &\leq 3 \times 10^{-13} \end{aligned}$$

Equation 3-21

### 3.10.3. White Dwarf cooling

White Dwarfs are the remnants of Stars with the original mass of several times the one of the Sun that cannot ignite their degenerate carbon-oxygen core.

They are a type of Stars that can remain in gravitational equilibrium indefinitely without any need of nuclear reactions or other power supply and like other types of Stars they are supported against gravitational collapse by the random motion of the particles they are made of. But unlike other Stars, these motions are not related to the internal temperature, so as white dwarfs radiate away their internal thermal energy cooling down, they do not lose pressure support, and contract.

The mechanism of the pressure that supports a white dwarf arises from the quantum mechanical effect called the Pauli exclusion principle, which states that two identical particles cannot have the same position and momentum.

When fermions are packed closely together, the exclusion principle forces most of them to have high velocities, and the more they get compressed, the faster they move. This motion gives rise to a pressure that resists compression.

The cooling process takes place first by Neutrino losses and later by surface emissions of photons. The Axion emission can be constrained by comparing the observed cooling speed with the theoretical estimates. This way one gets a result consistent with the one from the helium ignition in HB Stars:

$$g_{ae} \leq 3.5 \times 10^{-13}$$

Equation 3-22 White Dwarf limit

In the specific case of ZZ Ceti Stars cooling speed [51], the most restrictive limit on Axion-electron coupling was found to be:

$$g_{ae} \leq 1.3 \times 10^{-13} \text{ at } 95\% \text{ CL}$$

Equation 3-23 ZZ Ceti limit

---

### 3.10.4. Supernova 1987A

---

Computer models of stellar evolution indicate that the Sun will probably burn much of its core to carbon before settling down as a white dwarf. But for Stars five to eight times heavier than the Sun this process will continue all the way up the periodic table to iron. The ignition of each new element releases the necessary energy to resist the gravitational collapse, but iron is the end of the nuclear road for a Star.

What happens next is one of the most spectacular events in the astronomy, a Supernova. Any Star larger than eight solar masses will have at the end of its life an iron core that exceeds the Chandrasekhar limit of  $1.4M_{\odot}$ . This limit sets a bound on a mass consisting of nuclei in an electron gas and it basically is the maximum mass which can be supported by electron degeneracy pressure without suffering gravitational collapse.

The discovery on February 23 1987 of a nearby supernova was a wonderful stroke of luck for astronomers. SN 1987A exploded 170000 light years away (Figure 3-13) in the Large Magellanic Cloud that is a satellite galaxy of the Milky Way, and it is the first supernova for which the Star was observed before exploding, and in fact was the first detection of any Neutrinos from an astronomical object other than the Sun. In this type II supernova the Star (Sandulek-69202) collapsed into a neutron Star.

The Star being unable to ignite the iron core suffered a quick gravitational collapse stopped abruptly at the point where the equations of state stiffen when the nuclear density is reached ( $3 \times 10^{14} \text{ g/cm}^3$ ).

During this collapse the nuclear reactions that have built the iron core are undone, and the nuclei are broken into smaller pieces until a soup of subatomic particles remains. The energy necessary for this to happen comes from gravity, which releases 10 times more energy in this fast process than the Star in its entire life. 90% of that surplus is being carried away by Neutrinos resulted in the process of fusing protons and electrons into neutrons.

If one thinks about this, over the lifetime of a massive Star, gravity, and not nuclear reactions, provides most of the energy, and it does it most spectacularly almost entirely within the last second of the Star's life.

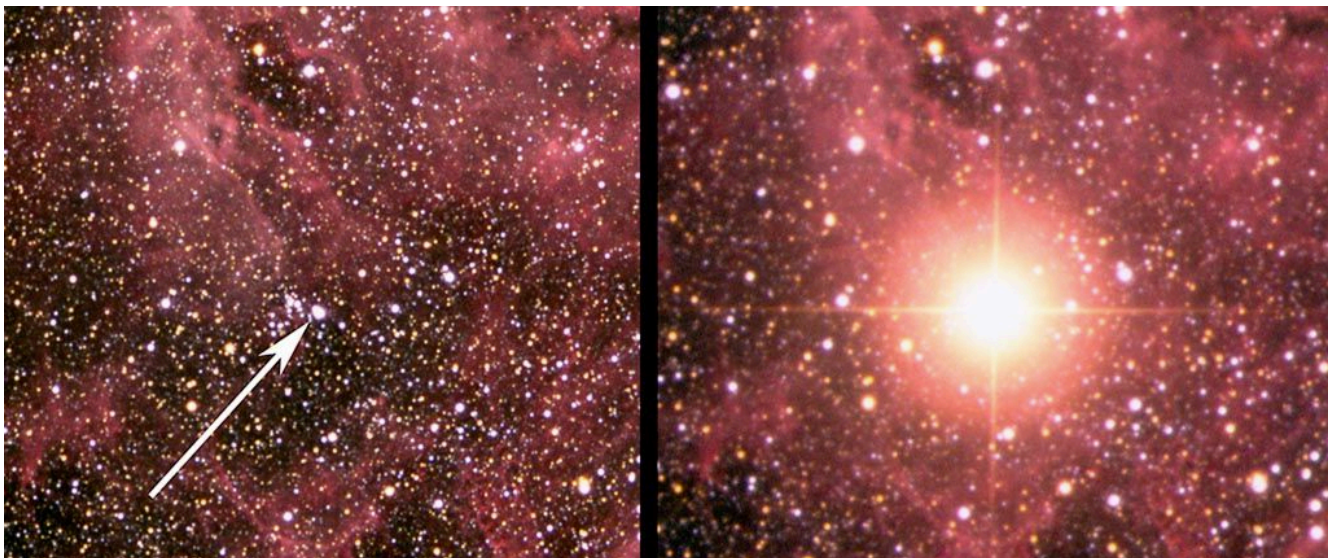


Figure 3-13 SN1987A before (left) and after.

In the resulting neutron Star even the weakly interacting Neutrinos are trapped. If Axions exist and if they interact more weakly they can provide another more efficient energy loss channel shortening the duration of the Neutrino burst. In principle, this reasoning can be used for deriving limits on other kinds of particles, like right-handed Neutrinos.

The dominant Axion process would be Axion-nucleon bremsstrahlung:

$$N + N \rightarrow N + N + a$$

resulting an Axion-nucleon coupling constant  $g_{aN}$  which for higher values would facilitate the energy loss thus shortening the Neutrino burst.

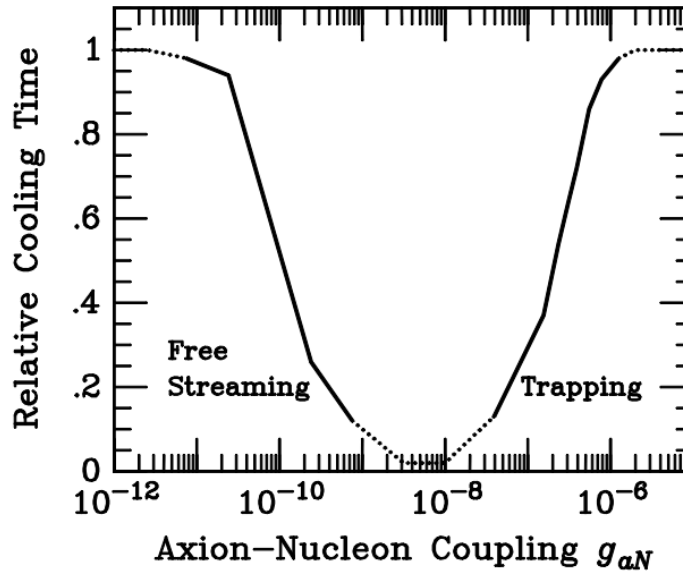


Figure 3-14 The duration of Neutrino cooling function of  $g_{aN}$  for SN 1987A [26]

For very small  $g_{aN}$ , the Neutrino burst is not affected and when increasing its value, the Neutrino burst decreases, reaching a minimum in the free streaming regime. If the coupling increases even more, the Axions are not able to escape any more in the trapping regime and the cooling can take place only by Axion diffusion, and emission from the Axion sphere, like in the initial case of Neutrino diffusion.

Once the Axion sphere moves beyond the Neutrino sphere the burst duration increases again and the Axions are unable to affect the signal duration, but if Axions were that interactive they should have left traces in the water Cherenkov detectors that provide the following limit on the coupling constant range for masses of  $20 \text{ eV} \rightarrow 20 \text{ keV}$ :

$$1 \times 10^{-6} \leq g_{aN} \leq 1 \times 10^{-3}$$

The Neutrino signal observed in 1987 both in IMB and Kamiokande Cherenkov detectors was of 19 Neutrinos in 10 seconds and it fitted the models. This yields a coupling constant in the range:

$$3 \times 10^{-10} \text{ GeV}^{-1} \leq g_{aN} \leq 3 \times 10^{-7} \text{ GeV}^{-1}$$

$$m_a < 16 \text{ meV}$$

Equation 3-24 SN1987A limit

---

### 3.11. Cosmological constraints

---

In the early Universe the Axions could have been produced through the interactions of quarks with gluons. The interaction  $\pi + \pi \leftrightarrow \pi + a$  is independent of the model thanks to  $a - \pi^0$  mixing [56]. Like the massive Neutrinos, these cosmic Axions can be constituent part of the hot Dark Matter. Based on the WMAP data a HDM limit [57] for the Axion mass range can be derived:

$$m_a < 0.4 - 1.2 \text{ eV}$$

On the other hand if the Axions were heavier than 20 eV they could have decayed in photons that could be detected as excess radiation, thus another limit can be imposed from this reasoning (Figure 3-12). This scenario would also decrease the Axion population.

### 3.12. Detecting the invisible Axion

Although being a prime candidate to elegantly solve many unanswered question, the Axions have yet to be confirmed. The first to propose a strategy for discovering the Axions was Pierre Sikivie in 1983. He came with the idea of using strong magnetic fields for converting the Axions into monoenergetic photons via the Primakoff effect. This is such a promising approach since the Axion-gluon interaction is a generic feature of all the models. He suggested the use of both haloscopes and Helioscope for investigating celestial Axion sources [58].

Because the momentum transfer is small the Primakoff could be pictured as an Axion to photon oscillation comparable to Neutrino flavour oscillations.

There are three main categories of experiments for detecting the invisible Axions, all employing the coupling with the magnetic field:

- Haloscopes for galactic Axions;
- Helioscopes for Solar Axions;
- Laser experiments for detecting laboratory Axions.

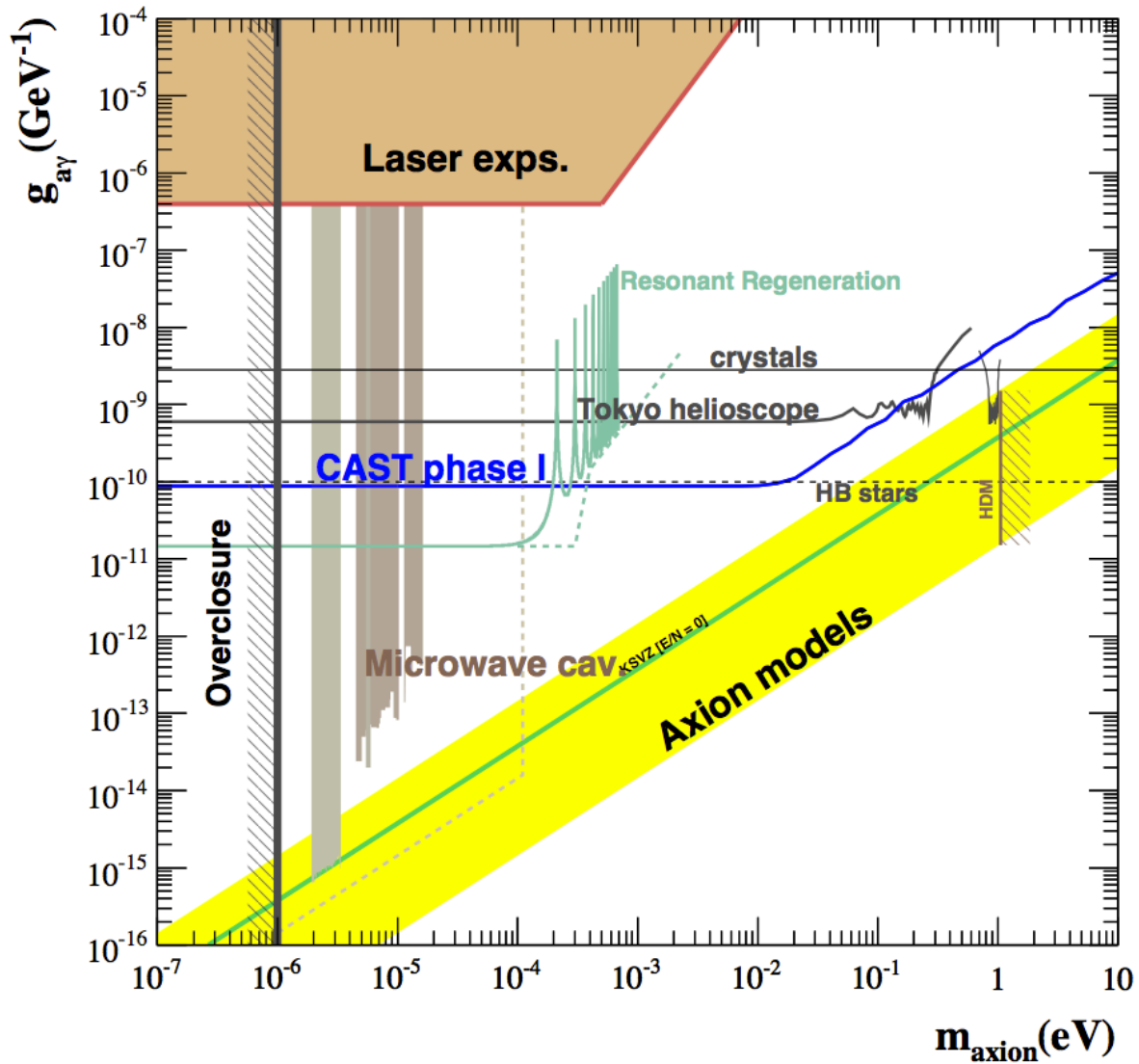


Figure 3-15 The Axion parameter space regions excluded by different experiments. [59]



### 3.12.1. Telescope searches

It is expected that the Axions decay extremely slowly into two photons with masses in the CDM regime, and this fact should be observable for the thermally produced heavy Axions. From the observational point of view an almost monochromatic emission line should be observable from the galaxies and the clusters of galaxies [60].

D. Grin et al. have derived the following bound on the Axion mass:

$$4.5 \text{ eV} < m_a < 7.7 \text{ eV}$$

Equation 3-25 Telescope bound

An observation made by the Haystack Observatory of the nearby dwarf galaxies yielded the following result:

$$g_{a\gamma} < 1 \times 10^{-9} \text{ GeV}^{-1} \text{ for axion masses } 298 \mu\text{eV} \leq m_a \leq 363 \mu\text{eV} \text{ at } 96\% \text{ CL}$$

Equation 3-26

### 3.12.2. Haloscope searches

The Haloscope experiments search for low mass ( $\mu\text{eV}$ ) CDM Axions that are gravitationally bound in the galactic halo.

Such a Haloscope basically consists in a electromagnetic cavity permeated by a strong static magnetic field. When encountering this field the light Axions should convert resonantly into nearly monochromatic microwave photons in the GHz range.

The first experiments of this kind were conducted in 1980 by Rochester-Brookhaven-Fermilab [61] and University of Florida and they covered Axion mass ranges:

$$4.5 \mu\text{eV} < m_a < 16.3 \mu\text{eV}$$

Most notable amongst this types of experiments is Axion Dark Matter Experiment (ADMX) [62] [63]. They have successfully probed the theoretical Axion models and excluded the mass range:

$$2.9 \mu\text{eV} < m_a < 3.5 \mu\text{eV}$$

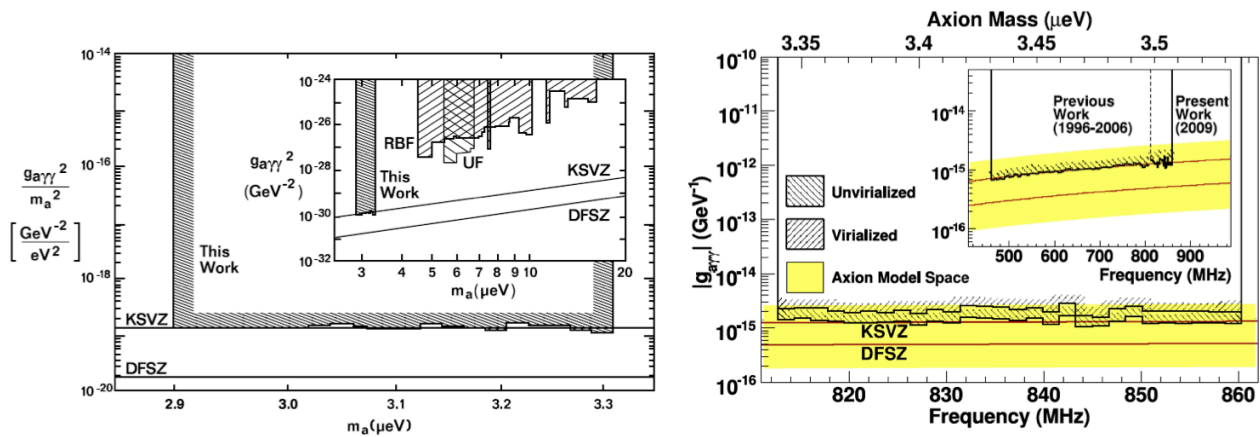


Figure 3-16 Left – the results of first generation ADMX , Right – recent results of ADMX.

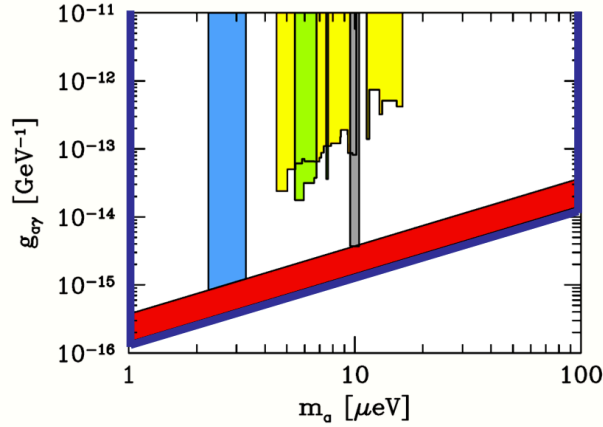


Figure 3-17 Combined exclusion plot for most important Haloscope experiments:

Yellow – RBF [64] , Green – UF [65], Blue – ADMX [66], Grey – CARRACK I [67]

### 3.12.3. Helioscopes

The Sun should be the closest and most intense Axion source that we can observe due to Primakoff conversion of photons in the high electric fields inside the solar core. The scope of an Helioscope is to convert back into photons those Axions in a strong transverse electric or magnetic field.

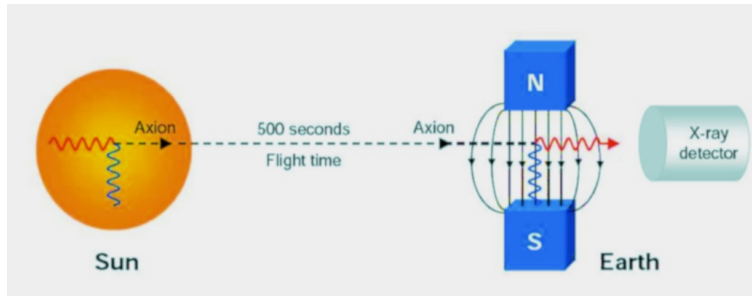


Figure 3-18 The principle of detection for an Helioscope.

The resulting photons have the same energy spectrum as the original Axions but scaled down by the conversion probability. They can be detected by placing an X-ray detector at the end of the magnetic field.

In the beginning of 90's Lazarus et al. [68] created the first Helioscope setting the following limits:

$$g_{a\gamma} \leq 3.6 \times 10^{-9} \text{GeV}^{-1} \text{ for } m_a \leq 0.03 \text{ eV}$$

$$g_{a\gamma} \leq 7.7 \times 10^{-9} \text{GeV}^{-1} \text{ for } 0.03 \text{ eV} \leq m_a \leq 0.11 \text{ eV}$$

These results were then surpassed by the Tokyo Axion Helioscope [69] with the following limit:

$$g_{a\gamma} \leq 6 \times 10^{-10} \text{GeV}^{-1} \text{ for } m_a \leq 0.03 \text{ eV}$$

CAST (CERN Axion Solar Telescope) is the implementation of this principle of detection with the highest sensitivity to date.



---

### 3.12.4. Bragg diffraction experiments

---

Axions could be coherently converted into photons in crystalline detectors that can provide the necessary Coulomb field from the nuclei in the crystal lattice, assuming that the incident Axions fulfil the Bragg condition with the plane of the crystal. The crystal can either be used as an Axion converter or as a focal optical device with a detector in its focal plane. This idea was originally proposed by E. A. Paschos and K. Zioutas [70].

There are three important experiments investigating these Bragg patterns:  
SOLAX using a germanium spectrometer with the following results [71]:

$$g_{a\gamma} \leq 2.7 \times 10^{-9} \text{GeV}^{-1} \text{ for } m_a \leq 1 \text{ KeV (95\% CL)}$$

Equation 3-27 SOLAX

COSME also with a Germanium detector [72]:

$$g_{a\gamma} \leq 2.78 \times 10^{-9} \text{GeV}^{-1} \text{ (95\% CL independent of } m_a)$$

Equation 3-28 COSME

DAMA with a NaI(Tl) crystal [73]:

$$g_{a\gamma} \leq 1.7 \times 10^{-9} \text{GeV}^{-1} \text{ (90\% CL independent of } m_a)$$

Equation 3-29 DAMA

Studies have revealed that detecting Axions with crystals is not feasible due to the low conversion probability. Because of this they are not able to compete with the globular cluster limit, unless very long exposure times are accepted.

---

### 3.12.5. Laboratory experiments

---

#### “Shining light through the wall” or “Photon regeneration” experiments

The basic principle of this experiment consists of a powerful laser beam shone through a strong transverse magnetic field that then hits a beam dump. A fraction of the laser photons should couple with the magnetic field and convert into weakly interacting Axions that can pass through the wall unlike the unconverted photons from the laser. On the other side of the wall there is another cavity with another transverse magnetic field that can convert back the Axions into detectable photons through the inverse-Primakoff effect.

The magnets were also fitted with locked resonating Fabry-Perot cavities on both sides for improving the sensitivity and suppressing the background.

An advantage of this pure laboratory approach is that it is independent of any model of Axion fluxes or densities because no cosmological or astrophysical Axion sources are needed.

The first experiment of this kind was done in 1990 with the following result [74]:

$$g_{a\gamma} \leq 6.7 \times 10^{-7} \text{GeV}^{-1} \text{ for } m_a \leq 10^{-3} \text{ eV (95\% CL)}$$

Equation 3-30

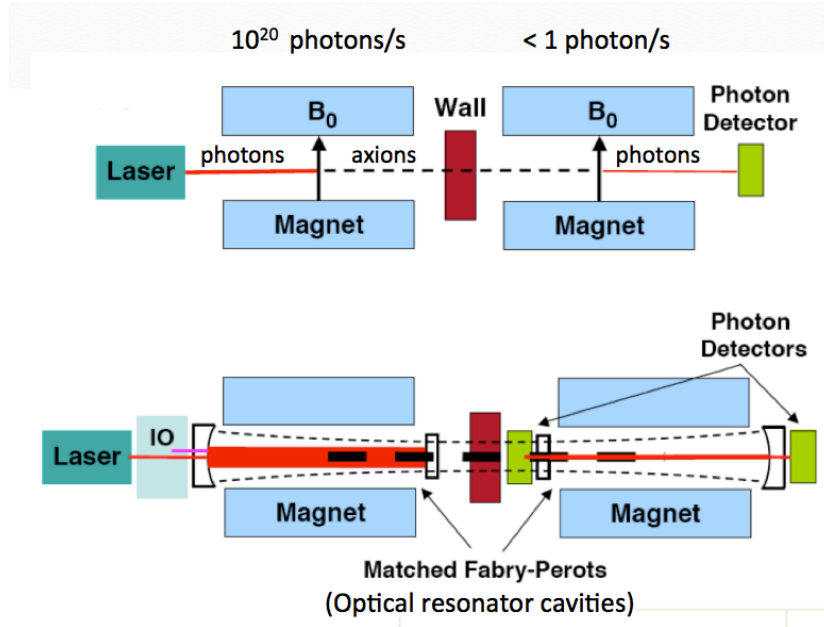


Figure 3-19 Principle of operation for “Shining light through the wall” or “Photon regeneration” experiments

There are a number of experiments that are running and taking data using this principle: ALPs at DESY using a HERA dipole magnet, Gammev at Fermilab using a Tevatron Magnet, and OSQAR experiment at CERN using a LHC superconductive dipole magnet.

### 3.12.6. Polarisation experiments

When a beam of polarised light passes through a transverse magnetic field it experiences dichroism and birefringence. The dichroism is basically a small rotation of the polarization vector (for linear polarized light) due to the fact that the electric field component  $E_{\parallel}$  parallel to the magnetic field  $B$  is suppressed by the Axion production, while  $E_{\perp}$  is unaffected. On the other hand, birefringence manifests itself by changing the polarization state from linear to elliptical. The mechanism by which this happens is the mixing of the virtual Axions in the  $E_{\parallel}$  and not in the  $E_{\perp}$  retarding one with respect to the other.

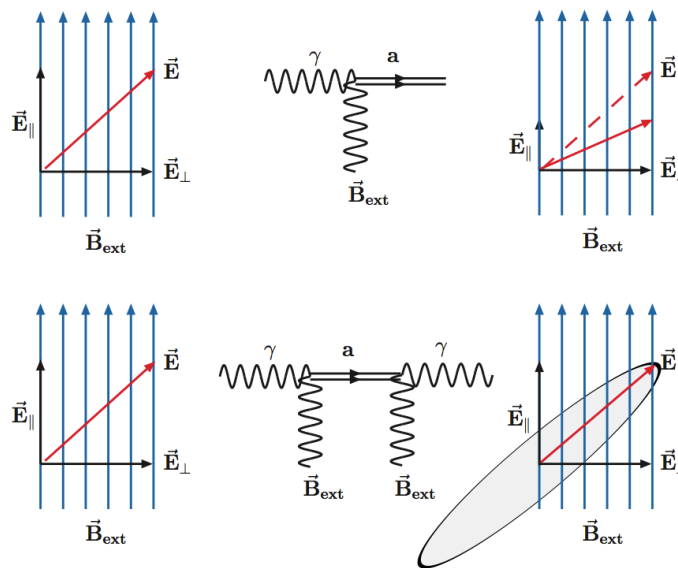


Figure 3-20 Top – the principle of dichroism, Bottom – the principle of birefringence.

---

BFRT has looked for these effects with their magnet with the following result [75]:

$$g_{a\gamma} \leq 3.6 \times 10^{-7} \text{GeV}^{-1} \text{ for } m_a \leq 5 \times 10^{-4} \text{ eV}$$

In 2006 PVLAS claimed to observe a rotation of the polarization plane of the light propagating through a magnetic field. This was later excluded by different experiments including PVLAS itself who claimed instrumental artefacts and retracted the previous results. This event excited the entire Axion community by raising the interest and the research activity in this field [76].

## 4. The Solar Axion

CAST experiment is the Helioscope with the highest discovery potential in the world to date. It looks at the Sun, the closest celestial source of Axions. In this chapter we will have a look at the Axion production in the core of the sun, the expected flux on the earth, the probability of conversion, the coherence condition, and the expected number of photons.

### 4.1. The Solar Model and the Axion production

The core of the Sun being extremely dense and hot facilitates the coupling of two photons for the conversion of black body photons with energies in the keV range into Axions. In this case the virtual photon is provided by the strong electromagnetic field originating from the charged particles in the plasma. This process is known as the Primakoff effect and has the following Feynman diagram:

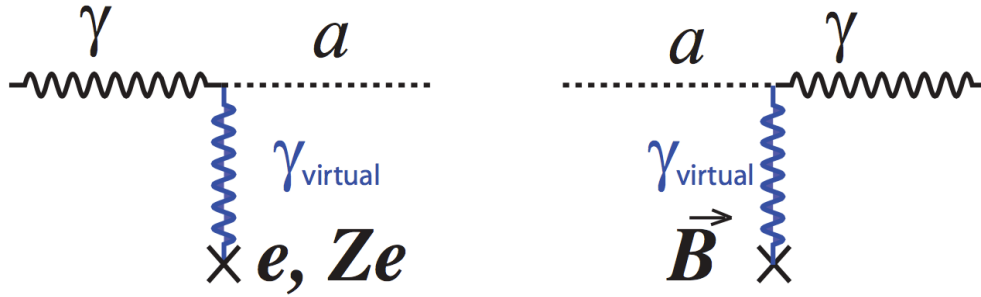


Figure 4-1 Feynman diagram of the direct and indirect Primakoff effect

$$\gamma + Ze \rightarrow Ze + a$$

In the case of the Sun the effective photon mass in the medium (the plasma frequency)  $\omega_p$  is rather small, usually around 0.3 keV and the solar core temperature is  $T_\odot \approx 15.6 \times 10^6 K \rightarrow 1.3 \text{ keV}$  giving the typical photon energies of  $3T_\odot \approx 4 \text{ keV}$ .

Raffelt estimated the total scattering cross section and assuming non-relativistic medium and neglecting recoil effects he derived an expression for the transition rate  $\Gamma_{\gamma \rightarrow a}$

$$\Gamma_{\gamma \rightarrow a} = \frac{T_\odot \kappa^2 g_{a\gamma}^2}{3\pi} \left[ \left( 1 + \frac{\kappa^2}{4E^2} \right) \ln \left( 1 + \frac{4E^2}{\kappa^2} \right) - 1 \right]$$

Equation 4-1

Near the centre of the Sun the Debye-Hückel scale  $\kappa$  is roughly 9 keV.

The total Axion flux can be calculated for  $\langle E_a \rangle = 4.2 \text{ keV}$  with the maximum at about 3keV:

$$\Phi_a = 3.54 \times 10^{11} \left( \frac{g_{a\gamma}}{10^{-10} \text{ GeV}^{-1}} \right)^2 \text{ cm}^{-2} \text{ s}^{-1}$$

Equation 4-2

Using the standard solar model, the Axion luminosity is:

$$L_a = 1.7 \times 10^{-3} \left( \frac{g_{a\gamma}}{10^{-10} \text{ GeV}^{-1}} \right)^2 L_\odot$$

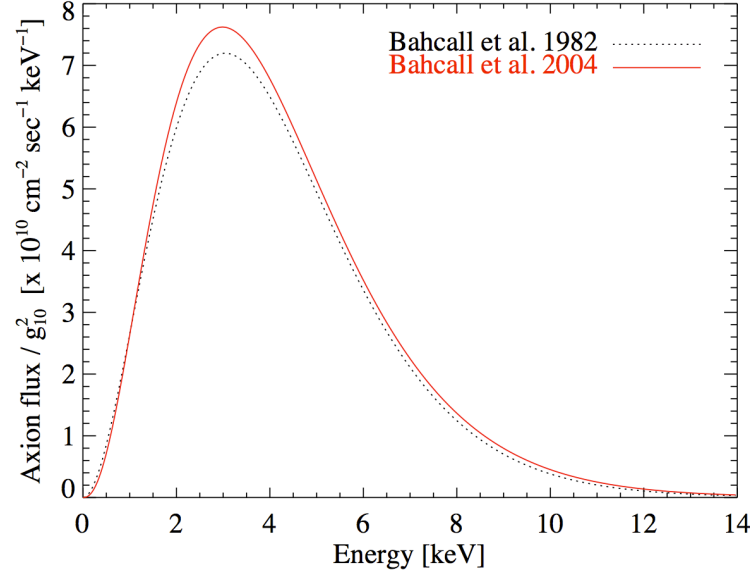


Figure 4-2 Differential Axion flux at Earth comparison for the old and revised model. [77]

Considering the fact that CAST uses a imaging device for detecting photons from the Axion-photon conversion it is better to transform the differential flux into the apparent surface luminosity of the two dimensional Solar disk  $\varphi_a(E_a, r)$

$$\varphi_a(E_a, r) = \frac{R_{\odot}^3}{2\pi^3 d_{\odot}^2} \int_r^1 ds \frac{s}{\sqrt{s^2 - r^2}} E_a k f_B \Gamma_{\gamma \rightarrow a}$$

Equation 4-3

The surface luminosity is basically a flux calculated per unit of surface area of the apparent bi-dimensional solar disk as a function of the coordinate. The unit is  $cm^{-2}s^{-1}keV^{-1}$  and  $d_{\odot}$  is the average distance Sun-Earth.

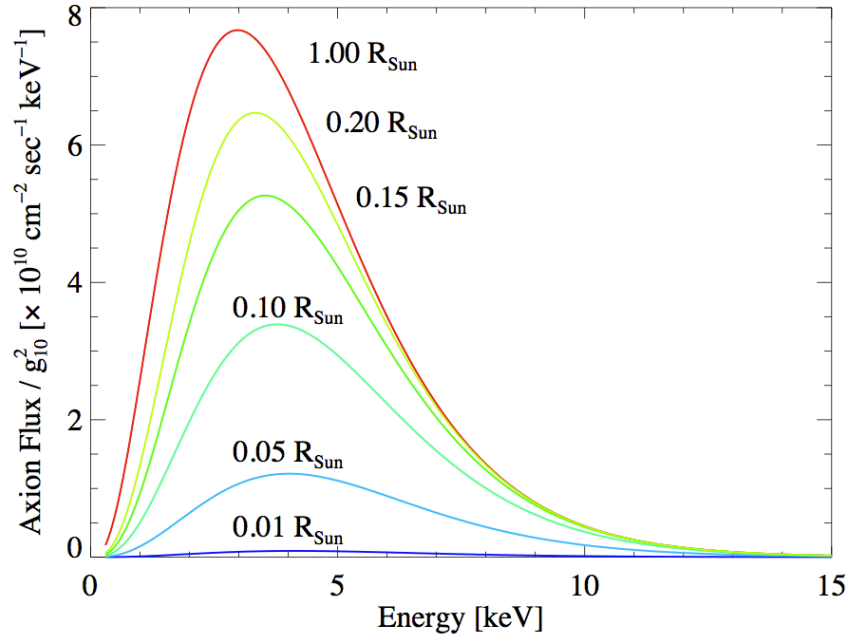


Figure 4-3 Axion surface luminosity of the Sun for different energies and radial coordinates. [59]

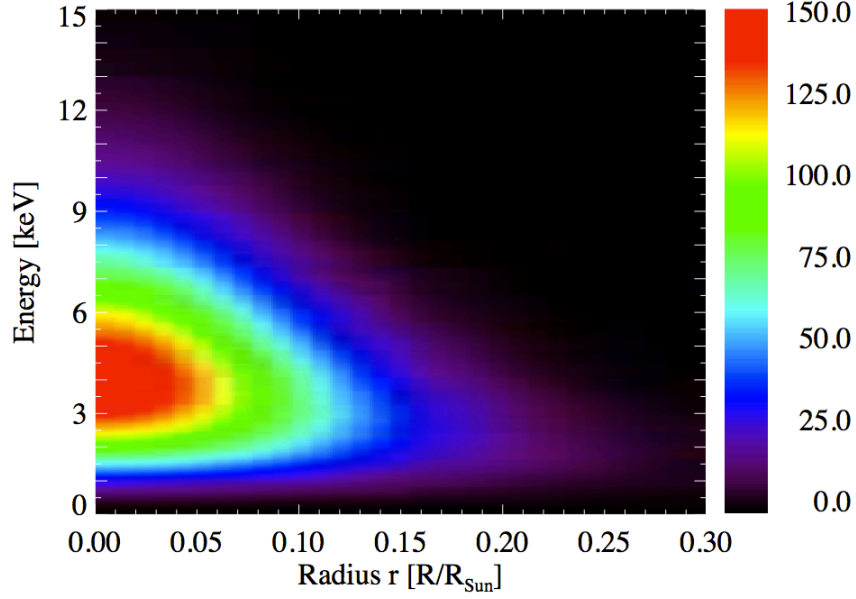


Figure 4-4 Solar surface Axion luminosity as a function of energy and dimensionless radial coordinate. The colour scale represents the flux in Axions/cm<sup>2</sup> s keV for unit surface area on the solar disk. [59]

One can obtain the total Axion flux on Earth by integrating the apparent surface luminosity over the entire solar disk:

$$\Phi_a = 2\pi \int_0^1 r dr \int_{\omega_p}^{\infty} \varphi_a(E_a, r) dE$$

Equation 4-4

where  $\omega_p$  represents the plasma frequency.

From precision helioseismology one can derive that a coupling constant of  $g_{a\gamma} > 10^{-9} \text{GeV}^{-1}$  is strongly disfavoured and that means that Axion luminosity  $L_a$  should not exceed 20% of the solar luminosity  $L_{\odot}$  [78].

Another constraint used for refuting the PVLAS claim of a signal is taking into account the fact that the Sun is at the middle of its helium burning phase, and an increased Axion luminosity like the one PVLAS reported, would have shortened the lifetime of the sun to 1000 years, which is obviously not in concordance with the observed reality.

Another parameter that can be used to constrain the coupling constant is the solar Neutrino flux, which could increase in the case of a high Axion luminosity. The mechanism is the heating of the solar core.

Base on the uncertainties in the solar Neutrino flux the following bounds can be derived:

$$g_{a\gamma} > 5 \times 10^{-10} \text{GeV}^{-1} \rightarrow L_a \leq 0.04 L_{\odot}$$

Equation 4-5

It should be noted that the limits CAST has provided so far are in complete agreement with the standard solar models, and the corresponding Axion flux is too small to affect the mechanisms we discussed so far.

## 4.2. Axion-Photon Conversion Probability

Through the inverse Primakoff effect in Helioscopes, the Axions can be converted into real detectable photons by coupling with a virtual photon provided by the intense magnetic field. Due to the fact that the photon has a spin one and the Axion is spinless, they can still mix provided that the mixing agent, namely the external field can provide the missing quantum numbers. In consequence a longitudinal field that provides an azimuthal symmetry because it can't change the angular momentum  $J_z$  of the photon is required. From here it derives [79] the condition that the mixing field must be transversal to the Axion's direction of flight.

$$\left[ \begin{pmatrix} \omega - \frac{m_\gamma^2}{2\omega} - i\frac{\Gamma}{2} & g_{a\gamma} \frac{B}{2} \\ g_{a\gamma} \frac{B}{2} & \omega - \frac{m_a^2}{2\omega} \end{pmatrix} - i\partial_z \right] \begin{pmatrix} A_{\parallel} \\ a \end{pmatrix} = 0$$

Equation 4-6 The wave equation for particles propagating in the z axis through a perpendicular magnetic field

where  $A_{\parallel}$  is the amplitude of the photon field parallel with B,  $\omega$  denotes the frequency,  $a$  is the Axion field and  $\Gamma$  is a dampening factor represented by the inverse of the photon absorption length.

Solving this in a perturbative approach, one gets the Axion photon conversion probability in a magnetic field of a specific length:

$$P_{a \rightarrow \gamma} = |\langle A_{\parallel}(z) | a(0) \rangle|^2 = \left( \frac{B g_{a\gamma}}{2} \right) \frac{1}{q^2 + \Gamma^2/4} [1 + e^{-\Gamma L} - 2e^{-\Gamma L/2} \cos(qL)]^2$$

Equation 4-7 Conversion Probability

The absolute momentum transfer between the Axion and the real photon is  $q$  and has the following relation:

$$q = \left| \frac{m_\gamma^2 - m_a^2}{2E_a} \right|$$

Equation 4-8 Momentum Transfer

where  $m_a$  and  $m_\gamma$  are the Axion mass and the effective photon mass in that medium while  $E_a$  is the Axion energy.

$$p_a = E_a \sqrt{1 - \frac{m_a^2}{E_a^2}}$$

Equation 4-9 Axion Momentum

If one considers  $m_a \ll E_a$  then:

$$p_a \approx E_a - \frac{m_a^2}{2E_a} \text{ and } p_\gamma \approx E_\gamma - \frac{m_\gamma^2}{2E_\gamma}$$

$$q = |p_a - p_\gamma| = \left| \frac{m_a^2}{2E_a} - \frac{m_\gamma^2}{2E_\gamma} \right|$$

Equation 4-10 Photon-Axion Momentum transfer

### 4.2.1. The Conversion Probability in Vacuum

To get the conversion probability of Axions into photons in vacuum and in the presence of a transversal magnetic field in Equation 4-7 one has to consider  $m_\gamma \rightarrow 0$  and the dampening factor to be also zero and the result is:

$$P_{a \rightarrow \gamma} = \left( \frac{BLg_{a\gamma}}{2} \right)^2 \left[ \frac{\sin(qL/2)}{qL/2} \right]^2$$

Equation 4-11

In vacuum the momentum transfer transforms to:

$$q = \frac{m_a^2}{2E_a}$$

This satisfies that the coherence is significantly different from zero because  $qL/2 < \pi$ . This is clear if one looks at the plot of the function  $\left( \frac{\sin x}{x} \right)^2$  as a function of  $x$  (Figure 4-5) (the main contributions are for values of  $x < \pi$ ) which results:

$$m_a < \sqrt{\frac{4\pi E_a}{L}}$$

Equation 4-12

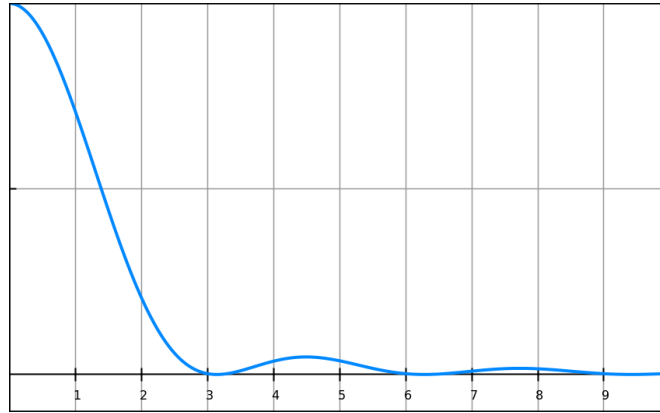


Figure 4-5 The function that dictates the conversion probability

If we consider the magnetic length is 10 m the coherence condition is satisfied for an Axion mass smaller than 0.02 eV and the probability of conversion takes the simpler form known as the simplified probability of conversion in vacuum:

$$P_{a \rightarrow \gamma} = \left( \frac{BLg_{a\gamma}}{2} \right)^2$$

Equation 4-13 Conversion Probability in Vacuum



---

#### 4.2.2. Conversion Probability in a buffer gas

---

The presence of a buffer gas in the conversion volume is necessary for gaining sensitivity to heavier Axion masses. The gas must be one with low atomic mass such as helium and hydrogen.

However in this case the formulas from the vacuum case must be modified because the photon masses are function of the density of the medium and the full formula for the momentum transfer needs to be considered.

The key aspect in this new situation is to have the photon mass in buffer gas. In vacuum the photons are massless and travel at speed of light while in an optically transparent medium they slow down and acquire an effective mass. In the classical treatment the slowing down is interpreted as interference of the incident photons with polarised photons coming from the matter while in the particle interpretation it is considered the mixing of the photons with the quantum excitations of the medium.

The photon energy can be written as:

$$E_\gamma^2 = m_\gamma^2 = \hbar^2 \omega_p^2$$

And the plasma frequency can be derived as [80]:

$$\omega_p^2 = 4\pi n_e \frac{e^2}{m} = 4\pi n_e r_0$$

Where  $r_0$  is the classical electron radius and  $n_e$  is the electron density which can be written as  $n_e = \frac{N_e}{V}$   $N_e$  meaning the number of electrons in the volume unit. Then the effective photon mass can be written as:

$$m_\gamma^2 = 4\pi \frac{N_e}{V} r_0 = 8\pi \frac{r_0 N_a p}{R T} \frac{K}{\text{mbar m}^2}$$

Considering that  $\hbar c = 0.197 \text{ GeV fm}$  the effective photon mass in helium is:

$$m_\gamma = \sqrt{0.01997 \frac{p/\text{mbar}}{T/K}} \text{ eV}$$

Equation 4-14 Effective photon mass in Helium

Now that we have the photon mass, we can determine the *momentum transfer* that is useful for determining the Axion mass sensitivity for a specific gas pressure imposing the condition of a small momentum transfer to fulfil the coherence condition.

For this purpose it is useful to study Figure 4-6 that shows clearly the minima of the momentum transfer for a narrow mass range of the Axion. This effect is useful for implementing a scanning strategy in the experimental setups where if the gas pressure is controlled precisely in the magnetic conversion volume the coherence condition imposed by the minima of the momentum transfer is satisfied correspondingly for the respective Axion masses thus only a narrow Axion mass range can be studied at a specific helium gas pressure with high sensitivity.

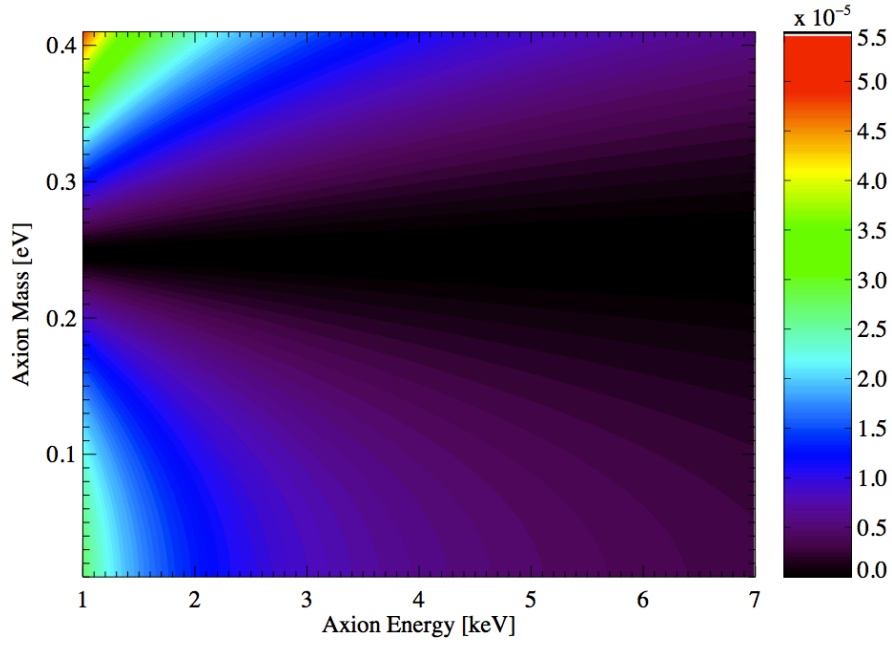


Figure 4-6 Colour coded plot of the momentum transfer in eV superimposed over Axion mass and energy dependence for a pressure of 5.5 mbar at 1.8K. [59]

However when implementing a scanning strategy the absorption of photons in the buffer gas must be taken into account. This effect is already included in the conversion probability formula through the dampening factor  $\Gamma$  that represents the inverse absorption length that depends on the gas type, pressure and photon energy.

If we consider a monoenergetic photon beam of intensity  $I_0$  that passes through a transparent medium of length  $L$  and inverse absorption length  $\Gamma$  its output intensity follows the following equation:

$$I = I_0 e^{-\Gamma L}$$

Equation 4-15

Because all the NIST [81] database values are given for the mass attenuation coefficient  $\mu/\rho$ ,  $\Gamma = (\mu/\rho)\rho_{gass}$  and the gas length path  $x = \rho_{gass}L$  the previous equation becomes:

$$\frac{I}{I_0} = e^{-\left(\frac{\mu}{\rho}\right)x}$$

Equation 4-16 Absorption length

If we take the values for He<sup>3</sup> from the NIST database ( $\mu/\rho$  in  $g/cm^3$ ) and we parameterize it for the photon energy range of 1-15 keV we get (Figure 4-7):

$$\frac{\mu}{\rho} = \exp(-1.5832 + 5.9195e^{-0.353808E} + 4.03598e^{-0.970557E})$$

$\Gamma$  as a function of energy and gas pressure can be obtained in  $cm^{-1}$ :

$$\Gamma(E, \rho) = (\rho_{gass}) \cdot \exp(-1.5832 + 5.9195e^{-0.353808E} + 4.03598e^{-0.970557E})$$

Equation 4-17

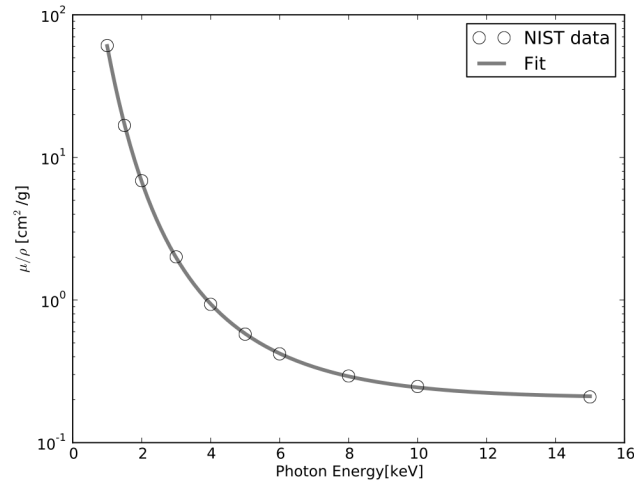


Figure 4-7 Best fit of the NIST data on He<sup>3</sup> mass attenuation coefficient

He<sup>4</sup> at 1.8K reaches saturation vapour pressure at 16.405 mbar, pressure that satisfies the coherence condition for an Axion mass of 0.43 eV. For higher masses He<sup>3</sup> must be used to re-establish the coherence condition.

#### 4.3. Expected number of photons

Theoretically the expected number of photons can be calculated for a specific gas density, Axion mass, Axion energy and coupling constant and has the following formula:

$$N_{\gamma} = \int \frac{d\Phi(E_a)}{dE_a} P_{a \rightarrow \gamma}(E_a) \epsilon(E_a) \Delta t A dE_a$$

Equation 4-18

- $\frac{d\Phi(E_a)}{dE_a}$  is the differential Axion flux at Earth, normalised in energy, time and area;
- $P_{a \rightarrow \gamma}$  probability of Axion-photon conversion;
- $A$  is the detector area;
- $\epsilon(E_a)$  the detector efficiency;
- $\Delta t$  exposure time

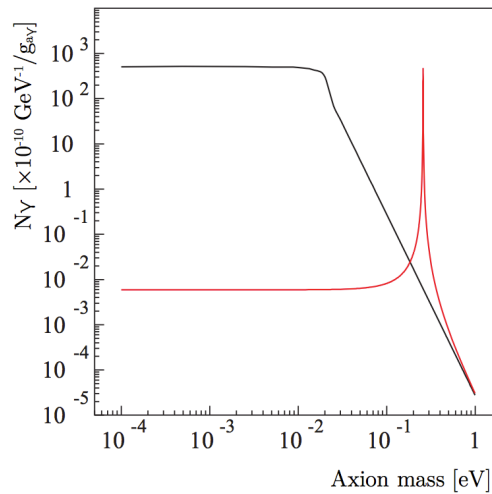


Figure 4-8 Black line – expected number of photons with vacuum in the conversion volume, Red line – coherence restored for a small Axion mass range with 6.08 mbar He<sup>4</sup> in the conversion volume. [59]

## 5. CERN Axion Solar Telescope

CAST is one of the 26 official experiments endorsed, supported and hosted by CERN. It is placed in a technical surface building at LHC Point 8, right across the border in France near Geneva Airport close to LHCb experiment.

CAST benefits from CERN's excellent infrastructure and expertise since it was approved in mid 2000 and Started taking data in 2003 aiming to shed light on a 36 year old riddle of Particle Physics by looking for Axions originating from the 16 million degree plasma in the Sun's core.

The international collaboration running the experiment was roughly 50 members from 20 institutions from across the globe.

CAST is the Helioscope with the highest sensitivity and discovery potential to date and has probed deep into previously uncharted Axion/ALP parameter space being a strong pillar in the European Strategy for Particle Physics.

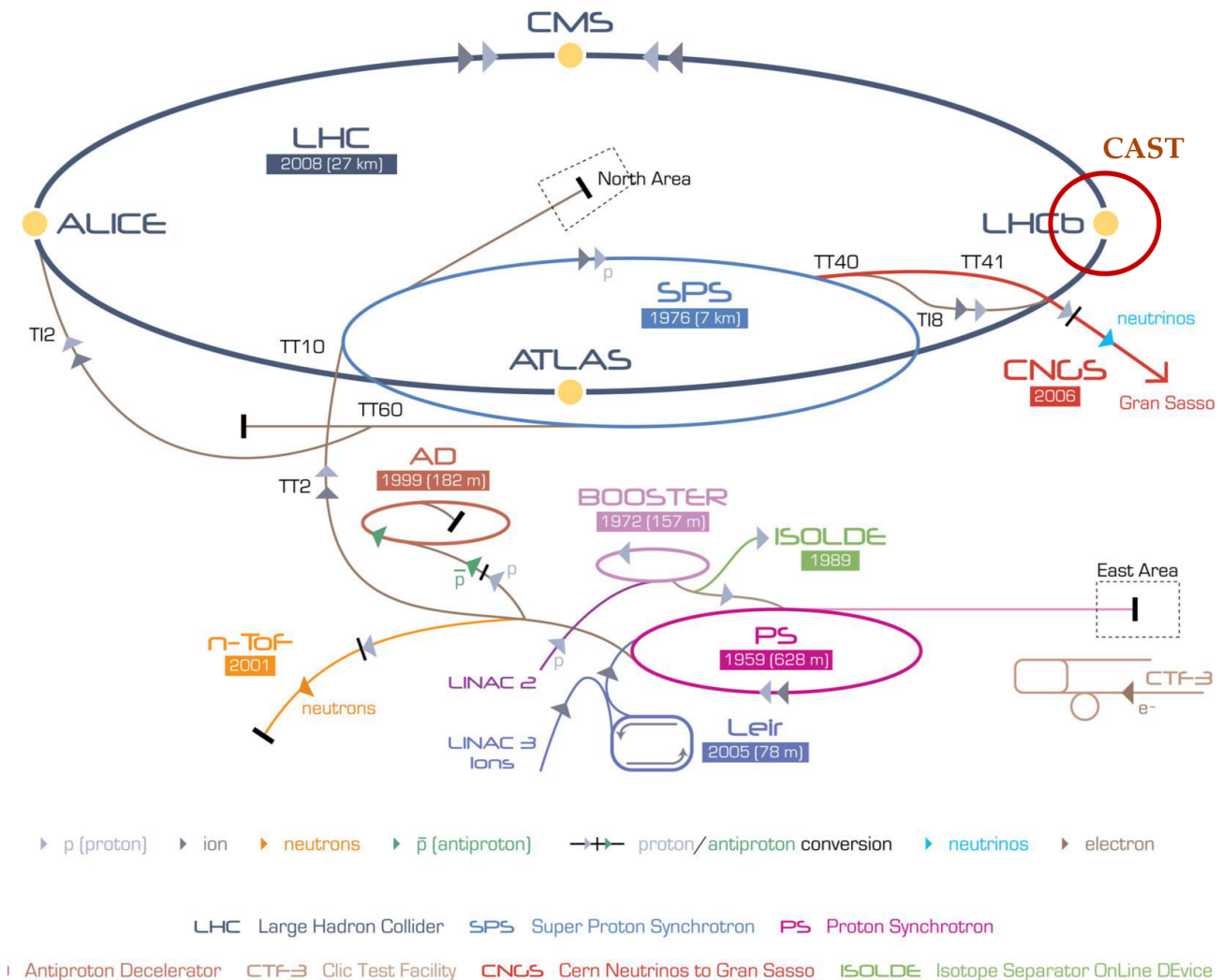


Figure 5-1 CERN's accelerator complex, experimental areas and test facilities [82]

In CAST experiment, the LHC prototype magnet is mounted on a mobile platform that allows movement in the vertical plane from  $-8^\circ$  to  $+8^\circ$  and in the horizontal from  $-40^\circ$  to  $+40^\circ$ . This way the axis of the magnet can be maintained pointed at the centre of the Sun for approximately 1.5 hours at sunrise and 1.5 hours at sunset.

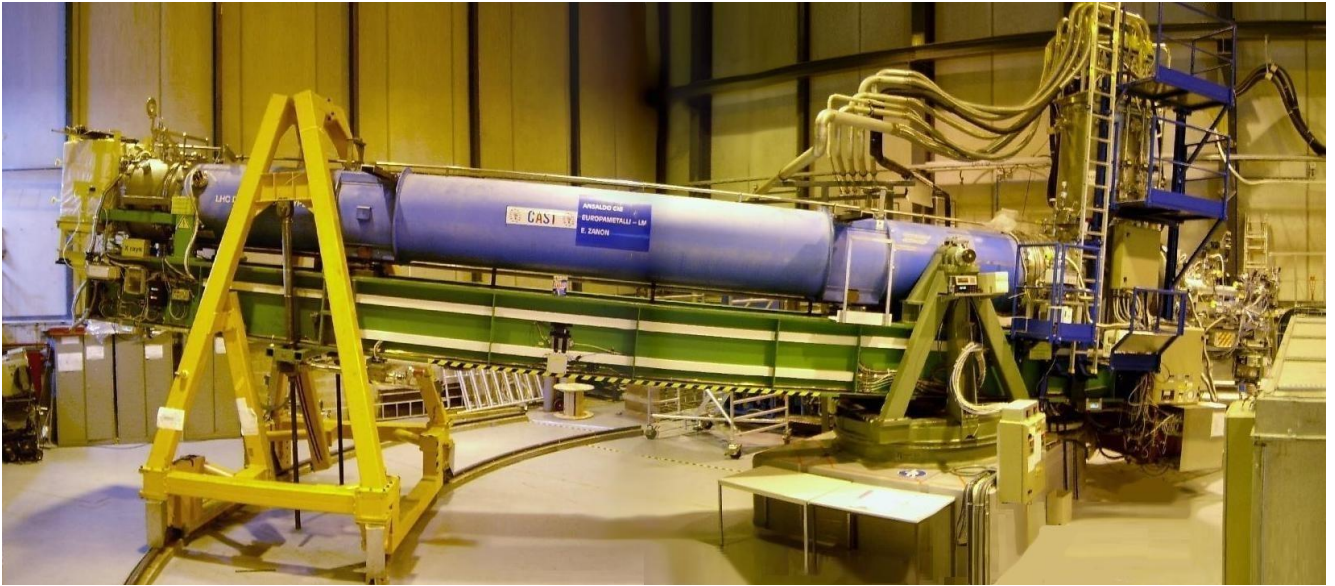


Figure 5-2 CAST experiment tracking the Sun in the morning run

Four low background detectors were installed, one at each aperture of the magnet (three Micromegas and one pn-CCD) looking for x-ray photons, signature of Axion to photon conversion in the cold bore. During the rest of the day, the magnet stays horizontal with the field on, taking background data.

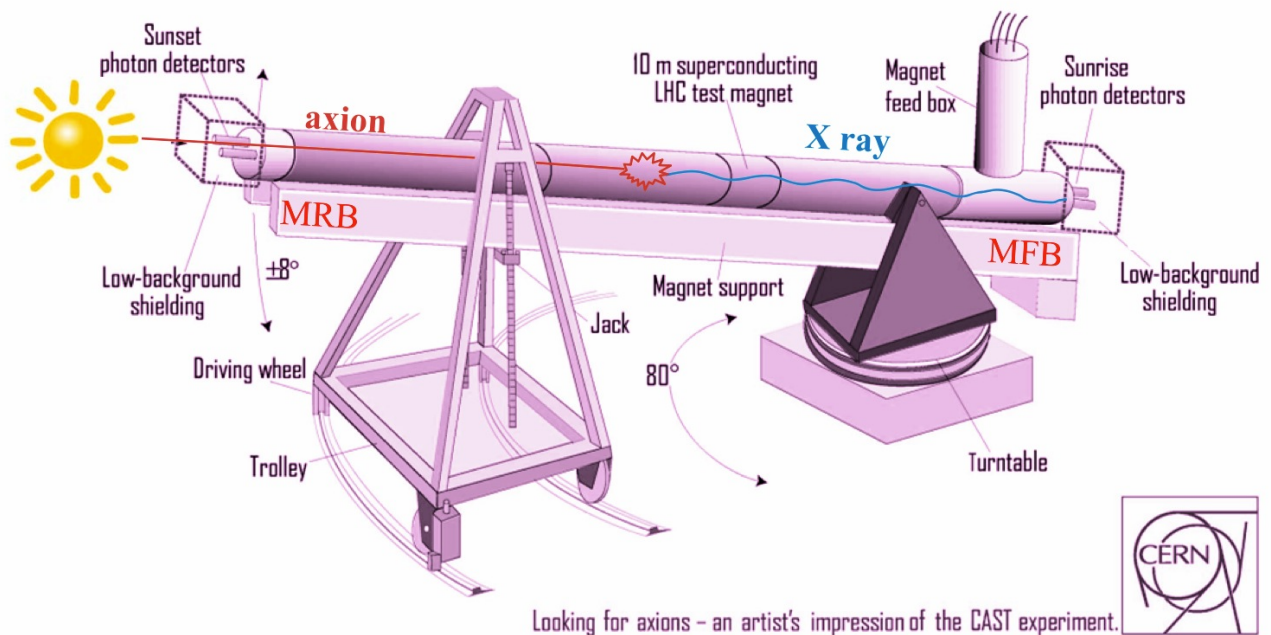


Figure 5-3 Schematic drawing explaining the principle of operation for the CERN Axion Solar Telescope. [83]

---

## 5.1. History

---

CAST experiment was proposed in 1999 [84] and commissioned between 2000-2003.

In 2003 it started taking the first data in vacuum phase that ended in 2004 with an upper Axion mass of 0.02 eV.

The experimental setup was then upgraded to allow the controlled and precise injection of buffer gas in the cold bore. In the first stage of Phase II (2006)  $\text{He}^4$  was used and Axion masses of up to 0.4 eV were scanned.

$\text{He}^4$  at 1.8K reaches saturation vapour pressure at 16.405 mbar pressure that satisfies the coherence condition for an maximum Axion mass of 0.43 eV. For higher masses  $\text{He}^3$  must be used to re-establish the coherence condition.

In the second stage of Phase II  $\text{He}^3$  was used to continue scanning for higher Axion masses Starting with 2008.

In 2012  $\text{He}^4$  pressures were revisited with higher sensitivity detectors.

Year	Phase	Sensitivity Range
2000 – 2003	Commissioning	–
2003 – 2004	Phase I (Vacuum)	< 0.02 eV
2006 – 2007	Phase II ( $\text{He}^4$ )	0.02 eV – 0.4 eV
2008 – 2011	Phase II ( $\text{He}^3$ )	0.4 eV – 1.15 eV
2012	Phase II ( $\text{He}^4$ - revisit)	0.02 eV – 0.4 eV

Table 5-1 Run History of CAST.



## 5.2. The magnet

Being a Helioscope, CAST relies on inverse Primakoff effect for converting solar Axions in a transverse magnetic field. The heart of the experiment is a fantastic 9.26 meter long, twin aperture, superconductive magnet capable of generating a field of 9 Tesla, from 13000 A flowing at 5 Volts. To stay superconductive, the magnet is cryogenically cooled at 1.8K with superfluid helium.

The magnet is a LHC prototype dipole for the bending magnets in the tunnel, but it was designed to be straight so no field of view is lost due to bending.

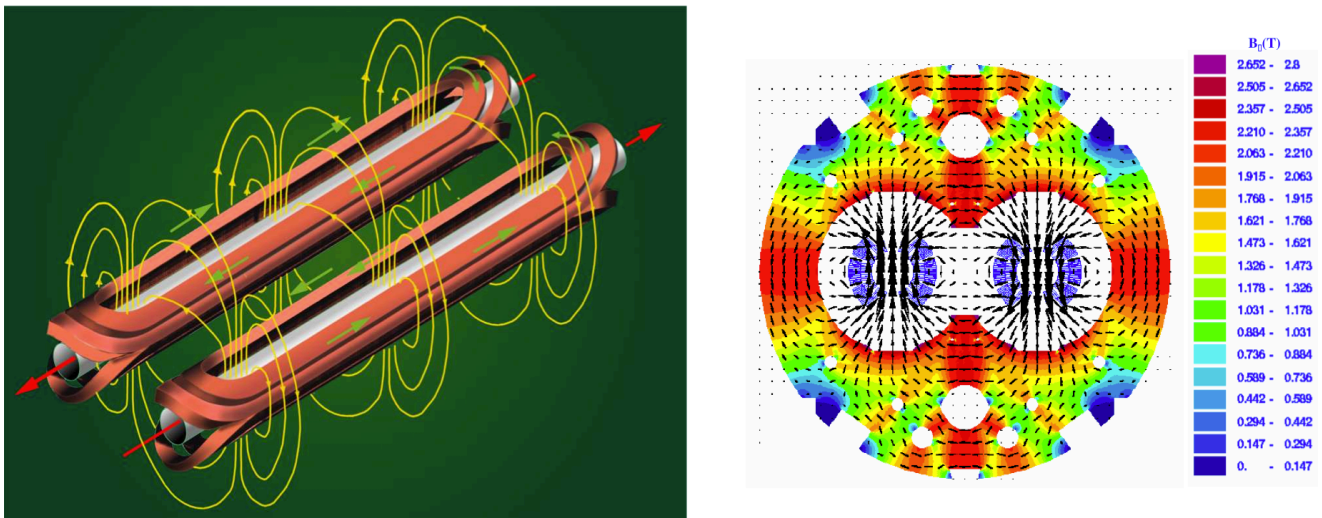


Figure 5-4 The magnetic field structure of the CAST dipole magnet at a maximum of 2.4T [83].

### LHC DIPOLE : STANDARD CROSS-SECTION

CERN AC/DI/MM - HE107 - 30.04.1999

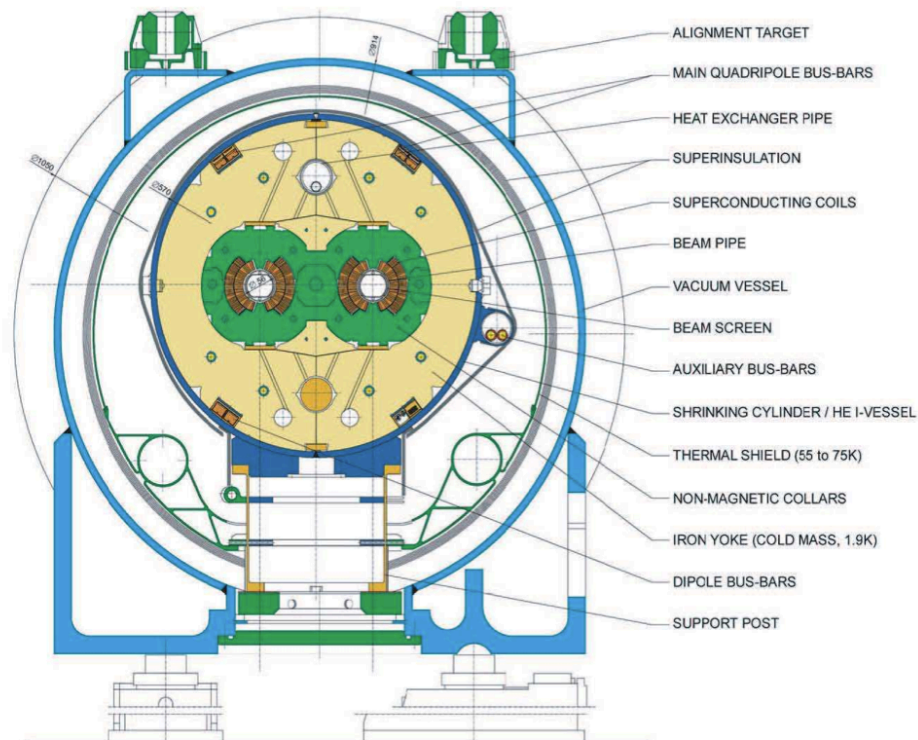


Figure 5-5 Standard cross section of a twin aperture LHC dipole prototype magnet [83]

The two beam pipes have a diameter of 43 mm, resulting in a total aperture to detectors of  $4 \times 14.52 \text{ cm}^2$ . This prototype magnet can provide a field of up to 9T over the full length of the two of the beam pipes, while the nominal field required for LHC operation at designed energy of 7 TeV per beam is 8.4T.

Current / A	Magnetic field / T
0	0
4988	3.4
10977	6.12
12000	7.46
12808	8.66
13330	9

Table 5-2 Current – Magnetic Field dependence for the CAST magnet

The superconductive compound in this magnet is Niobium-Titanium (NbTi) and since it was the original prototype, is the same as in the 1232 bending dipoles of the LHC. To ensure a reliable setup, during Phase II the magnet was operated at 13000 A.

### 5.3. The cryogenic system

The operation of any superconductive magnet requires cryogenic cooling. The CAST magnet is cooled by a superfluid helium system decommissioned from the former Large Electron Positron collider and DELPHI experiment.

It has been a major engineering challenge to integrate so many systems originally designed with other specifications, into a mobile platform type experiment capable of pointing at the centre of the Sun and track it with high accuracy. All the transfer lines for the liquid helium, gaseous helium, quench recovery system, as well as the magnet current supply had to be constructed very flexible to allow for enough degrees of movement.



Figure 5-6 Cryo flexibles condensing atmospheric oxygen and water during a Quench.



---

The cooling of the magnet is done in 2 stages. In the first stage the magnet is cooled down from ambient temperature to 4.5 K with the reconditioned LEP2/DELPHI compressor. Then the second stage takes over and a ROOTS pumping group cools down the circuit to 1.8 K.

The Magnet Feed Box (MFB) is placed on the end of the magnet closest to the pivoting point (Figure 5-6). All the electrical and cryogenic feed to the magnet is done in the MFB, already used with the cryogenic LHC test benches. The other end of the magnet is closed with the Magnet Return Box (MRB).

During operation it can happen that a small portion of the magnet spontaneously loses the superconductive state due to the magnitude of the field in static state or during ramping up and down. By virtue of Joule effect due to the high current, that small domain can overheat and start a rapid chain reaction in which the entire magnet flips into resistive state. The temperature increases by a factor of 20 in less than 5 seconds, a phenomenon known as *Quench*. This can be dangerous for the coil, and to prevent damage, a quench protection system is deployed when an increase in resistivity is detected in the magnet. This consists in discharging a bank of heaters inside the magnet to uniformly heat up the coil in a controlled way, together with the closing of the helium supply valve.

Due to the sharp increase in temperature the superfluid helium will boil and expand, and to prevent over-pressurising the system, when the internal pressure reaches a preset safety threshold, the helium is released.

These natural quenches are quite rare (one every few months). More frequent are the fake quenches triggered by external safety signals like power line/transformer glitches, compressed air and water pressure drops.



Figure 5-7 Safety release of cryogenic hydrogen during a Magnet Quench in 2010

---

## 5.4. The tracking system

---

In order to maintain the magnetic field transversal to the incoming solar Axions/photons, the axis of the magnet needs to be aligned with the centre of the Sun. CAST is able to track the Sun with an accuracy better than  $0.01^\circ$  which is a good engineering accomplishment considering that the entire moving mass is greater than 50 tons.

The magnet is mechanically supported by a large green metallic platform (Figure 5-2) that sits on the MFB side on a turntable which gives the necessary degrees of movement horizontally while in the MRB side it is attached with two lifting jacks by a yellow triangular structure.

This girder structure houses both motors for horizontal and vertical movement as well as the encoder units and runs on two rails.

The stress on the lifting screws is roughly 5 tons each, the rest of the weight being supported by the turntable.

In the horizontal plane the surrounding structure limits the movement to a range of  $80^\circ$  while in the vertical plane the limit is  $\pm 8^\circ$  mainly derived from the difficulty of cryogenically cooling and reliably operating a 10 m long magnet at that angle considerably increasing the risk of quenches.

There are two encoder units for horizontal and vertical movement that are responsible for keeping track of the pointing vector in the local coordinate system linking the motors to the guidance software.

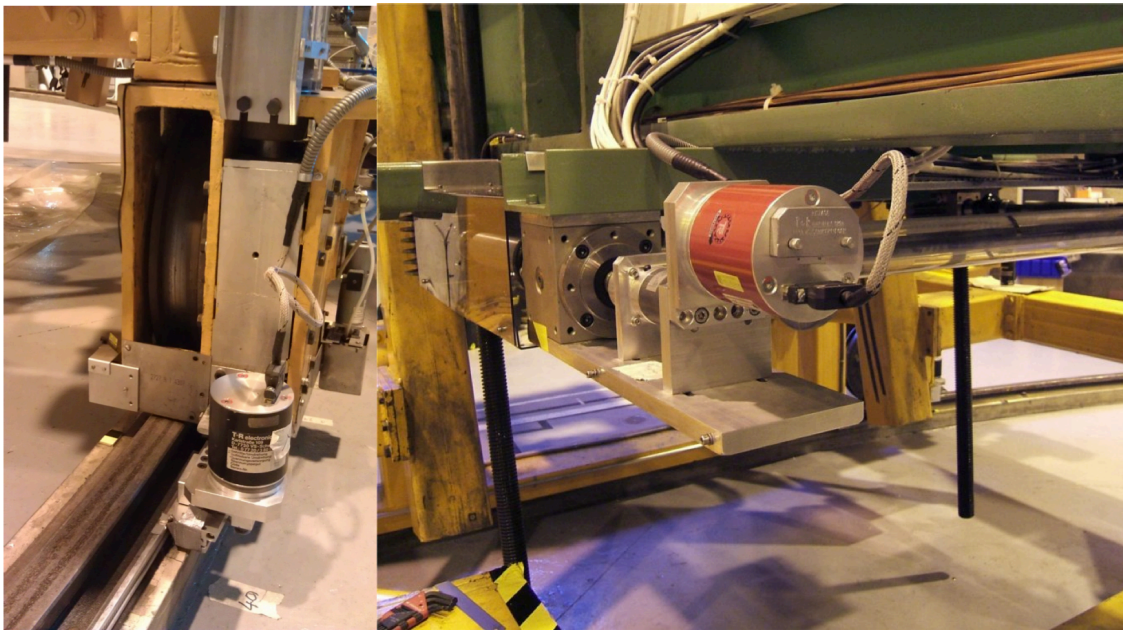


Figure 5-8 Driving mechanisms: Left – horizontal motor encoder and a driving wheel;  
Right – vertical motor encoder, with the transmission system and lifting jacks.

The total range of movement is sliced and integrated into the encoder systems as it follows: the vertical encoder values ranges from 0 to 53000 (1 unit =  $30\ \mu\text{m}$ ) and the horizontal encoder from 0 to 33000 (1 unit =  $35\ \mu\text{m}$  of magnet movement). The horizontal motor frequencies range from 1 to 150 Hz while the vertical from 1 to 70 Hz.

To get the correspondence between the encoder values and the inclination and azimuth angles a reference grid measurement was done in 2002 in which both angles were measured by a team of geometers for a grid of encoder values.

Then these measurements were used to make a two-dimensional Hardy's multiquadratic interpolation [85] to the entire encoder space so that each motor encoder pair ( $HE$ ,  $VE$ ) corresponds to an angle pair ( $\theta$ ,  $\phi$ ).

However due to irregularities in the rails, mechanical stresses are induced in some intervals and it is to be expected that the interpolation sometime diverts from the linear behaviour as it can be seen in Figure 5-9.

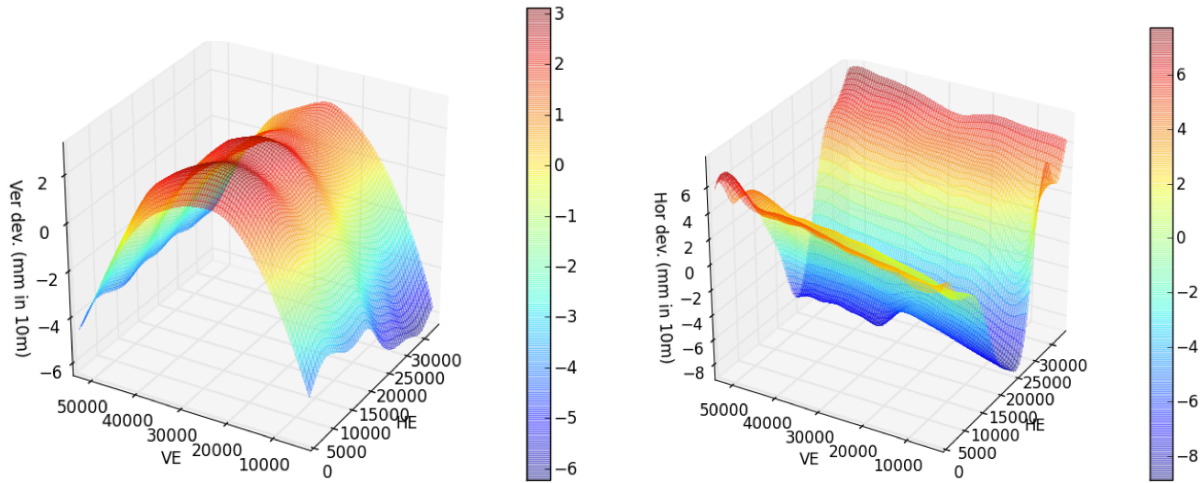


Figure 5-9 Deviation from standard linear interpolation in the encoder-angle relation

For each tracking, the full range of vertical movement is covered while the initial azimuth coordinate varies from astronomical reasons every day, so different coordinate subspaces will be covered in different months of the year and are consistent from year to year as seen in the following plot:

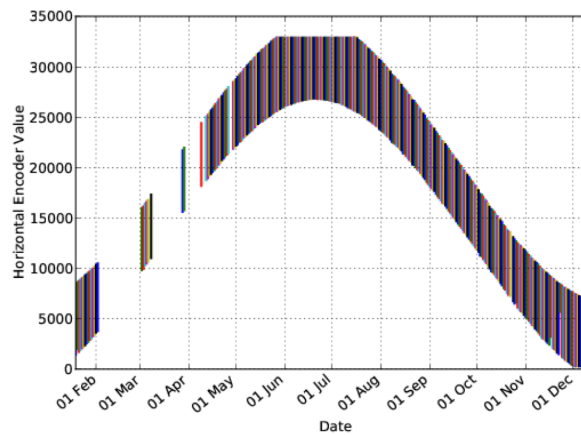


Figure 5-10 Cumulative tracking coverage of the grid coordinate space for 2005-2011

The magnet's movement control is done by a tracking program developed in the LabVIEW system design software. The software is synchronised with the timeservers at CERN to achieve precise timing. In manual mode the magnet is pointed at the encoder values selected by the user. When in tracking mode, the program dynamically aligns the reference axis of the magnet to the centre of the Sun, only if it is within a reachable window ( $-7.2^\circ < V < 7.95^\circ$  and  $46.8^\circ < H < 133.1^\circ$ ) working in a feedback loop of one minute.

It initially calculates where the Sun will be at the end of the current cycle using the U.S. Naval Observatory Vector Astronomy Software (NOVAS) subroutine package [86] specially implemented for Geneva's coordinates<sup>3</sup>, altitude and local time. Based on the relative position of the Sun in one minute in the future and the current one of the magnet, it sets the speed of the motors in order to most efficiently reach it.

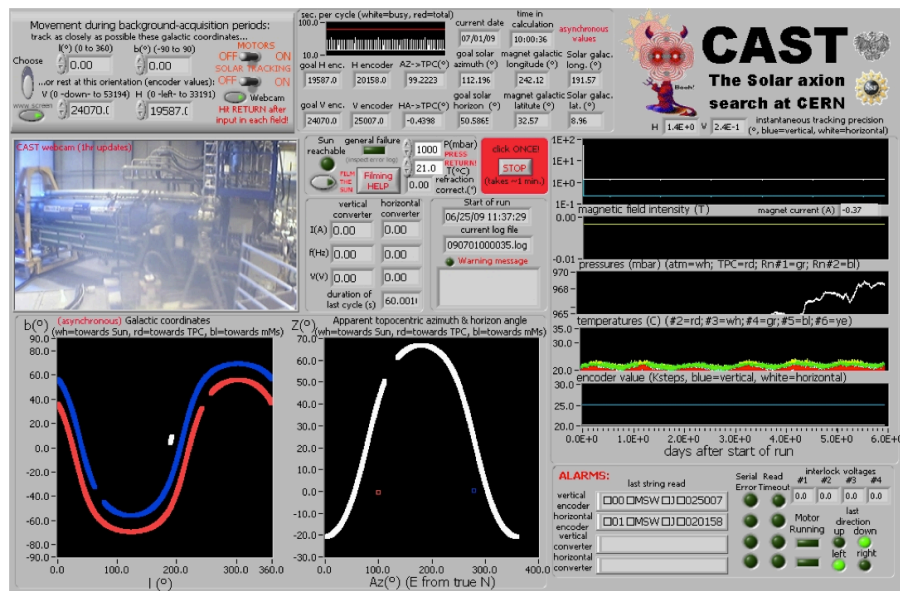


Figure 5-11 User Interface of the tracking program displaying the trajectory of the Sun, position of the magnet, precision of the tracking, atmospheric conditions and many other parameters

Source of error	Expected error	Maximal error
Astronomical calculations	0.002°	0.006°
Uncertainty of coordinates	0.001°	
Timing uncertainty	-	
GRID measurement (0.02 theodolite precision)	0.001°	
GRID interpolation	0.002°	< 0.01°
H encoder precision	0.0014°	
V encoder precision	0.0003°	
Deviation of Motor Speeds from linearity	< 0.002°	
Hysteresis	0.0034°	
<b>TOTAL</b>	<b>0,01°</b>	

Table 5-3 Error sources in the Sun Tracking System.

The accuracy of the tracking is maintained and crosschecked with regular Sun Filming and additional GRID measurements.

Overall, an accuracy better than 0.01° is achieved.

<sup>3</sup> 46° 15'N, 6° 5'E, 435 m above sea level



## 5.5. Solar filming

Twice a year, in March and September for about two weeks, CAST is able to directly track the Sun through a small window cut in the east-facing wall. The experiment uses this opportunity as an optical crosscheck to the magnet movement when tracking the Sun.

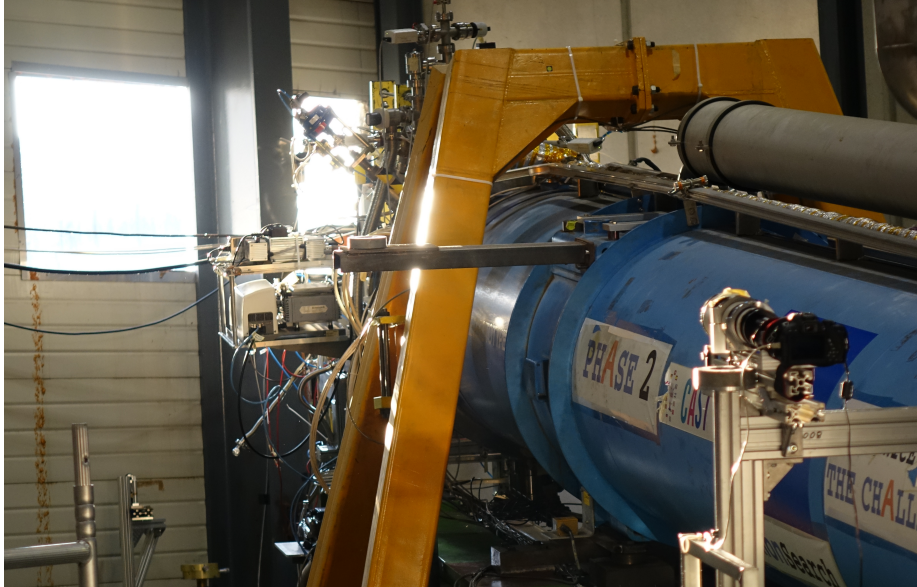


Figure 5-12 Sun filming in March 2014 with aligned DSLR camera

The tracking accuracy is critical for an imaging detector like the CCD that is in the focal plane of the Abrixas optics, especially in the context that as we have already seen in Figure 4-3, most of the Axions come from the inner 20% of the Sun.

It is useful to understand the field of view (FOV) provided by the magnet bore which is the fundamental limitation of any detector system mounted on CAST. This can be understood as the opening angle  $\alpha$ .

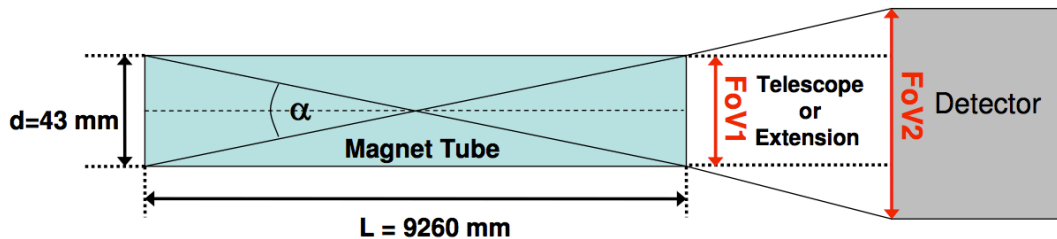


Figure 5-13 The FOV  $\alpha$  of the magnet. FOV1 is the fully illuminated view, while FOV2 is what actually the detectors see due to the distance between the bore and the sensitive part

$$\alpha = 2 \arctan \frac{d}{L} = 0.53^\circ$$

Equation 5-1 FOV of the magnet

However since it is impossible to directly couple any of the detectors directly to the opening port of the magnet due to technical reasons like cryogenic and vacuum isolation, all the detectors will suffer from a vignetting effect.

For instance the actual FOV for the CCD chip due to inherent geometric restrictions is  $0.34^\circ \times 1.06^\circ$  which is approx. 64% of the entire Sun. This is acceptable since the X-ray telescope focuses the signal

in a spot of 23 pixels in diameter, covering the 20% of the Sun from where the model predicts that 82.6% of the Axions are coming.

But this limiting of the field of view raises the bar on the pointing accuracy if one is aiming to detect Axions from the solar core (10%-20% of solar radius).

Another effect that has to be corrected during the Sun Filming is the fact that optical light suffers refraction while passing through the atmosphere that has a strong temperature gradient over its thickness. The refraction  $R$  can be defined as the difference between the true and the apparent zenith angle:

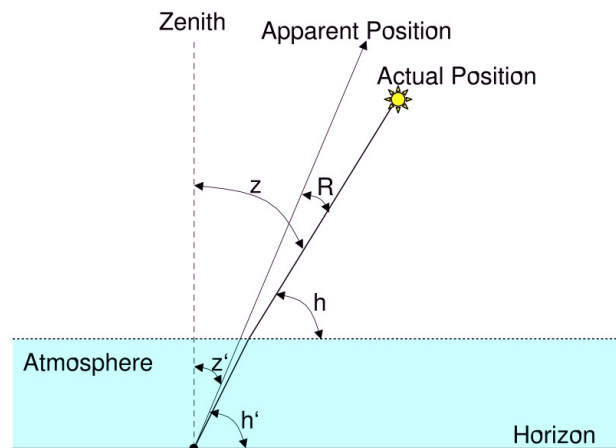


Figure 5-14 Atmospheric refraction scheme

This is of special importance for the Sun filming since the refraction depends on the distance the ray travels in the atmosphere so it is the largest for objects close to horizon ( $\approx 0.6^\circ$ ) and decreases to zero for the zenith position.

The tracking program has a special sun filming mode that accepts values of the local pressure and temperature, and applies the necessary corrections in real time so that the magnet tracks the apparent position of the Sun instead of the real one given by the NOVAS.

The experimental setup for the filming consists of a SLR camera with special filters and a 800 mm telephoto lens. The camera is aligned to the tracking axis with a laser and can be controlled remotely via software. This setup is capable of a precision of  $0.002^\circ$ .

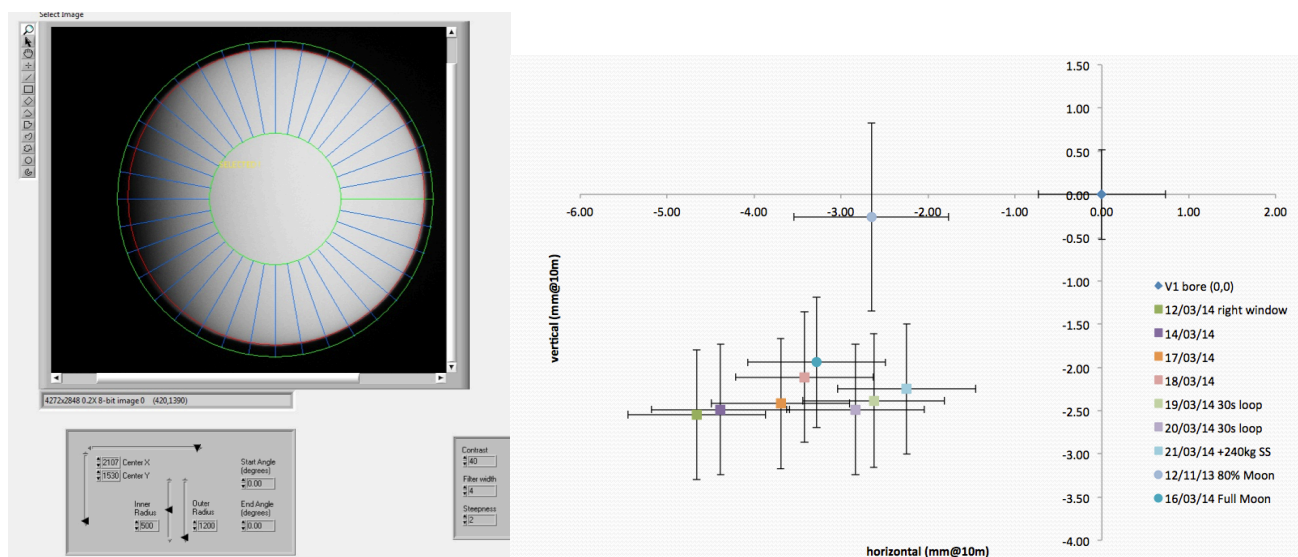


Figure 5-15 Solar filming campaign of March 2014.

## 5.6. The Slow Control System

This LabVIEW program centralises most of the sensors installed on the experiment, logs them and can also plot important parameters as:

- Position and inclination of the magnet;
- Loads on the lifting jacks;
- Pressures in different parts of the vacuum system;
- Environmental temperature pressure and humidity;
- Temperatures;
- Status of compressed air, water supply, gas flow, magnet current, etc.

The Slow Control takes the data from the sensors in analogue and digital form from the Slow Control rack where the National Instruments readout cards are and does periodic logging and managing of the data. This system also performs the important task of sending automatic SMS alarms to system responsables when preset threshold values are crossed by critical signals.

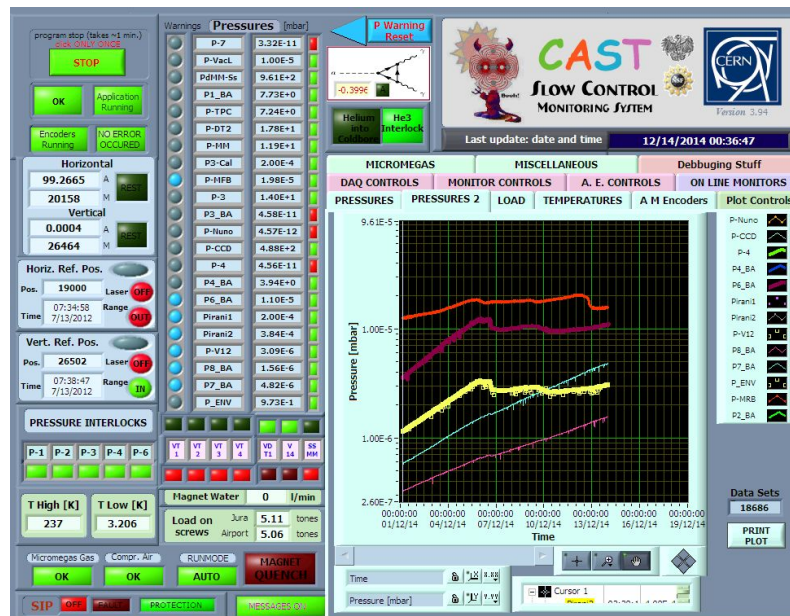


Figure 5-16 CAST Slow Control snapshot

## 5.7. The Vacuum systems

In Phase I (2003-2004) the conversion volume was pumped to  $10^{-7}$  mbar for scanning in low Axion mass domain. For maximising the conversion probability for higher masses in Phase II  $\text{He}^4$  and  $\text{He}^3$  buffer gas had to be precisely injected into the conversion volume. This required upgrading the original setup with additional pumps, valves, windows and safety interlocks especially for  $\text{He}^3$  phase because it is an extremely rare and expensive isotope.

The vacuum system is separated into three main subsystems, each with its own pumping group (Figure 5-17). With blue is marked the cryostat that works trough the principle of vacuum isolation to separate the superfluid helium from the ambient temperature.

The general CAST vacuum is separated from the conversion volume by the 4 cold windows and from the 4 detector systems by the gate-valves  $VT1 \rightarrow VT4$ . In normal data taking these valves are kept open and they can be manually or automatically closed by a PLC controlled interlock system in case of power failure, compressed air failure, quench, degradation of the vacuum or detector maintenance. The interlocks are designed for safety reasons to prevent mainly the contamination of the XRT-CCD

system. The CCD is cooled by a cold finger at 115 K and is capable of cryo-pumping gases through the X-ray optics if VT4 is opened, contaminating this way the mirrors leading to a decreased efficiency by condensing a layer of impurities.

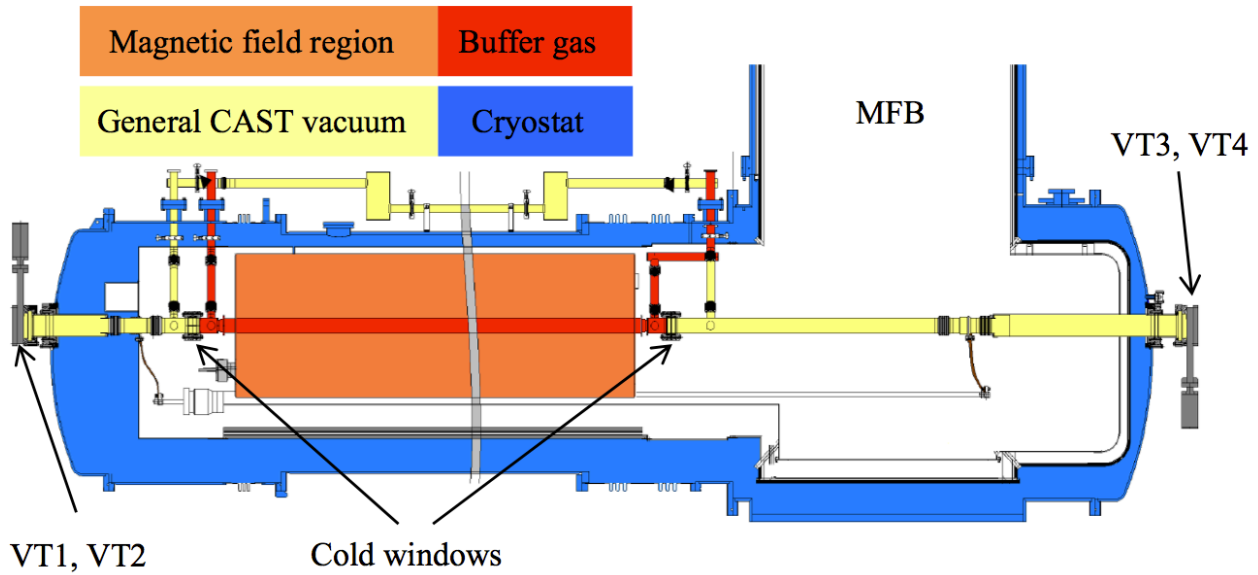


Figure 5-17 Subsystems of the magnet. Cold windows are used for separating the buffer gas in the conversion volume [83]

Another major purpose of the interlock system is to avoid losing  $\text{He}^3$  in the case of a cold window failure. In this case the rise in pressure would trigger the closing of the gate-valves preventing the detector systems from pumping out the  $\text{He}^3$ .

The interlock system also provides protection for each detector subsystem from problems of the other subsystems such as leaks and erroneous manipulations.

The cryostat and general cast vacuum are each permanently monitored by two Residual Gas analysers capable of detecting leaks and contaminations. They work on the principle of mass spectrometry and allow in real time the identification of the constituent gasses pumped from that volume.

## 5.8. The buffer gas system

As explained in the previous chapters, Axion Helioscopes usually make use of low absorption buffer gas to detect Axions of a specific mass. At first CAST used  $\text{He}^4$  that reaches vapour saturation pressure at 16.405 mbar at 1.8 K. In the second stage of Phase II  $\text{He}^3$  was used to restore the coherence for Axion masses up to 1.16 eV because this isotope liquefies at 135.8 mbar at 1.8 K. The existing system had to be upgraded to perform safely at these higher pressures and also to prevent losses and contaminations of the rare and expensive isotope.

In normal Data Taking and background mode all the gate-valves are opened to prevent signal losses through X-ray photons absorption into the windows of the valves. However it is obvious that the buffer gas must be contained in the conversion volume in the magnetic field region and to be isolated from the CAST general vacuum and the detectors pumping systems. Here come into play the cryogenic cold windows.



---

### 5.8.1. Thin cryogenic cold windows

---

In total there are 4 of these windows installed in CAST serving the main purpose of closing the cold bore tubes. Their position is marked in Figure 5-17.

The main design specifications are:

- Operation at low temperatures (1-120 K);
- Mechanical robustness for withstanding sharp pressure differential of up to 2.5 bars during quenches and in normal operation under 130 mbar;
- High transparency to X-ray photons in 1-7 keV range;
- Good transparency to visible photons for alignment purposes;
- Low permeability to Helium.

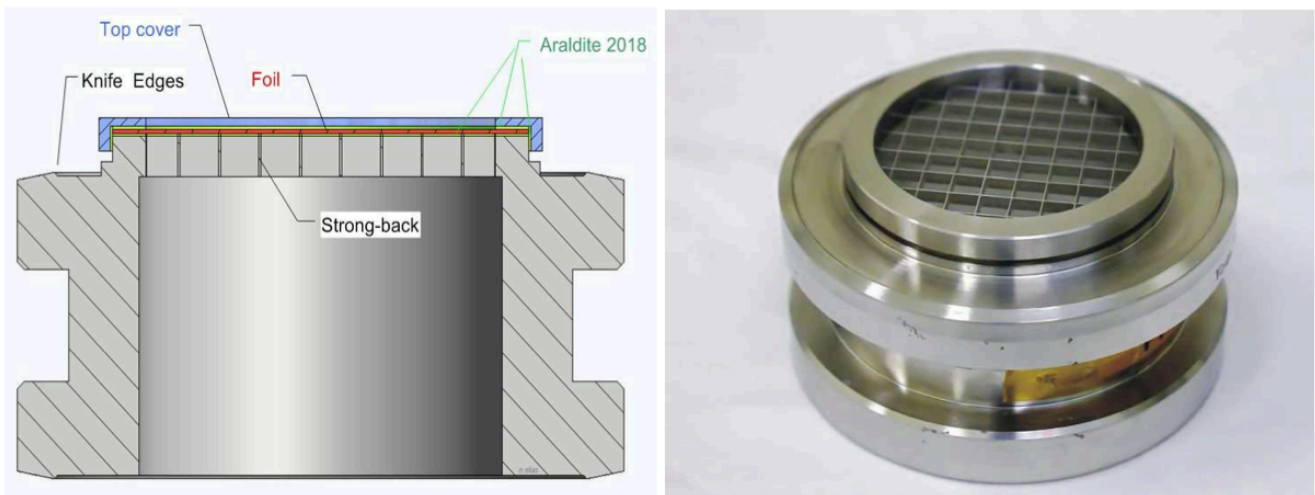


Figure 5-18 Left – cross section of a cold window , Right – Cold window mounted on a CF63 flange

The research and development phase for these windows was conducted at CERN [87] and the final construction followed the original design from CEA-Saclay.

The membrane is a  $15\ \mu\text{m}$  foil of polypropylene glued to a stainless steel strongback support. The supporting structure has a blocking geometric factor of 12.6 % and the overall transmission of the photons in the energy range 1 to 7 keV is  $\approx 87\%$ . The windows were tested to assure their reliability in the case of a Quench and the leak rate was determined to be below  $1 \times 10^{-7}\ \text{mbar liter/sec}$ .

The cold windows have also to endure the thermal differential between the conversion volume and the general vacuum. In these conditions the foil surface facing the exterior is the coldest surface of the general CAST vacuum, thus cryo-pumping gases on the surface. This condensation reduces the X-ray transmission of the windows and a heater system was installed in the flanges of the windows so that they can be backed out regularly at 200 K .

Extensive computational fluid dynamics (CFD) simulations were conducted over the years to completely understand the buffer gas dynamics inside the cold bores while tilting the magnet during the tracking. The conclusions are that the flow inside the CAST magnet is a transitional one. In most of the volume the velocity is very low, and the flow is laminar, but close to the ends the simulations show a laminar-to-turbulent flow due to the warmer windows.

This knowledge is essential in estimating the density distribution of the gas column under hydrostatic and thermal influences.

The finality of all this is determining the actual coherence length for the specific Axion mass of the respective pressure step.

### 5.8.2. He<sup>3</sup> storage and metering

For minimising the risk of losing any amount of this rare isotope, it is stored in a 1000 litre under-pressurised storage tank. In the case of a leak, atmosphere would go inside instead of vice-versa.

The main functionalities that the system has are:

- The precise transfer of the metered amount of He<sup>3</sup> inside the cold bores;
- The recovery of the buffer gas in the case of a quench;
- The purification of the gas during the injection procedure;
- The safe storage and gas transfer.

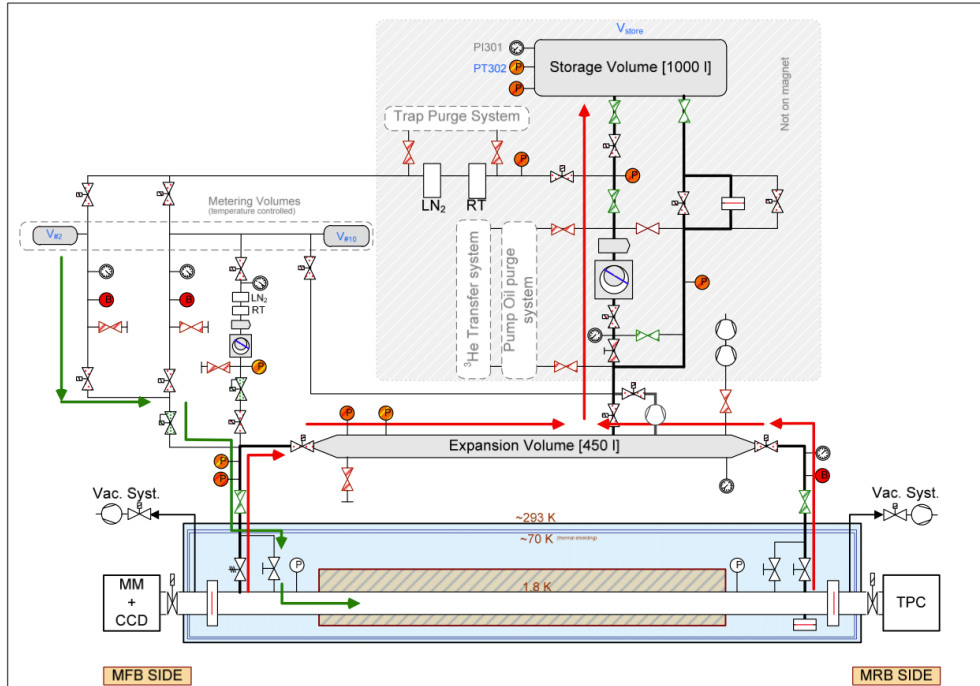


Figure 5-19 Schematic drawing of the He<sup>3</sup> gas system. With green arrows is indicated the standard filling procedure. With red arrows is represented the recovery procedure in the storage volume. [88]

The purification of the buffer gas is ensured by the use of two charcoal traps. One is at room temperature and it filters water vapours and oil contaminants from the pumps. The second one is a cold trap, and it is immersed in a liquid nitrogen bath that condenses the rest of the impurities at 77 K. The charcoal traps are being regenerated periodically.

In the event of a quench, the pressure rises in the conversion volume due to heat dissipation in the magnet. This produces the expansion of the buffer gas, and to protect the cold windows two electro-pneumatic valves, one at each side of the magnet, open and connect the conversion volume to a 10 meter long, 450 litre expansion volume found on top of the magnet. Then the gas is recovered with a hermetic pump from the cold bore, expansion volume and the connecting pipes in the storage volume.

In order to systematically scan for Axion masses we need to know exactly how much gas we put in the conversion volume. This is achieved by using a metering volume of 1.63 litres found in a thermostatic bath with a stability of  $\pm 0.01$  K. Having that known volume at 309 K and at a known pressure it is easy to calculate how many moles are injected for a certain pressure drop.

The filling is done in the middle of each morning and evening tracking run when the magnet is horizontal.

---

## 6. X-Ray Detectors

---

In order to detect the X-ray photons that should result from the Axion conversion in the buffer gas found in the transversal magnetic field, X-ray detectors are mounted at the 4 apertures of the cord bore. CAST tracks the Sun twice a day with a total solar exposure of 3 hours.

The sunrise tracking run Starts almost 2 hours before the sunrise. First the magnet is moved from the parking position to the proper position at the rendezvous point with the Sun found at  $-8^\circ$  vertical angle below the horizon. The tracking program takes the magnet there and waits for the Sun, then both the horizontal and vertical movement Start at the correct speed to track the Sun's trajectory.

In this situation the Axions escape the Sun's core and after a flight time of approx. 500 seconds pass without interacting trough the atmosphere, Earth's crust, sunset shielding, sunset detectors and end up in the conversion volume. Here they interact with a virtual photon provided by the strong transversal magnetic field, and convert into a real X-ray photon detected by the sunrise detectors found at the other end of the magnet. In the middle of the shift when the magnet is horizontal, a new pressure step is injected in the conversion volume changing the conversion probability for a slightly higher Axion mass. The morning tracking run continues until the magnet points upwards at  $+8^\circ$  horizon when the mechanical limitations of the experimental setup are reached. The tracking program takes the magnet in the parking position and the detectors take background data until the evening shift when the same method of detection is repeated but this time Starting at  $+8^\circ$  and ending at  $-8^\circ$  and taking Axion sensitive data with sunset detectors.

During the morning tracking the evening sunset detectors take background data, and vice versa.

If one assumes a coupling constant of  $10^{-10} GeV^{-1}$  then the conversion probability is expected to be quite small, yielding a mean number of photons expected per tracking less than one at the figure of merit that CAST magnet has. This imposes a design requirement for extremely low intrinsic background for the X-ray detectors used so that they are able to detect any excess of photons during the tracking compared with background.

To achieve this the following methods were used:

- Passive shielding to block external X-rays and gammas;
- Active veto shielding for filtering out the incoming muons;
- Use as much as possible radio-pure materials in and around the detectors;
- Use of X-ray optics to improve the signal to noise ratio by concentrating the signal in the focal spot tacking this way signal and background at the same time.

During the first 10 years of CAST data taking, three types of detectors were used for looking at X-rays photons from Inverse Primakoff effect:

- Conventional Time Projection Chamber detectors (TPC);
- MICROMesh Gaseous Structure detectors (MICROMEGAS);
- X-ray telescope with a Charged Couple Device (CCD) in the focal plane.

Up until now no excess signal has been observed above background:

$$g_{a\gamma} \leq 8.8 \times 10^{-11} GeV^{-1} \text{ at } 95\% CL \text{ for } m_a \leq 0.02 eV/c^2 [89]$$

$$g_{a\gamma} \leq 2.2 \times 10^{-10} GeV^{-1} \text{ at } 95\% CL \text{ for } 0.02 eV/c^2 \leq m_a \leq 0.39 eV/c^2 [90]$$

$$g_{a\gamma} \leq 2.7 \times 10^{-10} GeV^{-1} \text{ at } 95\% CL \text{ for } 0.39 eV/c^2 \leq m_a \leq 0.64 eV/c^2 [91]$$

Equation 6-1

## 6.1. Time Projection Chamber

This type of detector has been operated as a sunset detector from the beginning of the data taking up until 2007 covering the vacuum phase and first stage of Phase II.

As a detector it is from the family of gas filled drift chambers and multiwire proportional chambers (MWPC) that use high voltage levels on the opposite sides to guide the electrons towards the readout wires.

Chronologically MWPC was developed first then the drift chambers. The principle of detection is that the incident particle ionizes the atoms from the gas mixture and the resulting free electrons move towards the readout wires under the influence of the intense electric field ionizing on the way there in an avalanche effect more atoms. The resulting charge is accumulated on the readout wires and the position of the interaction and the energy can be derived from these signals. In addition to this the drift chambers can also derive timing information from the arrival time of the electrons to the wires.

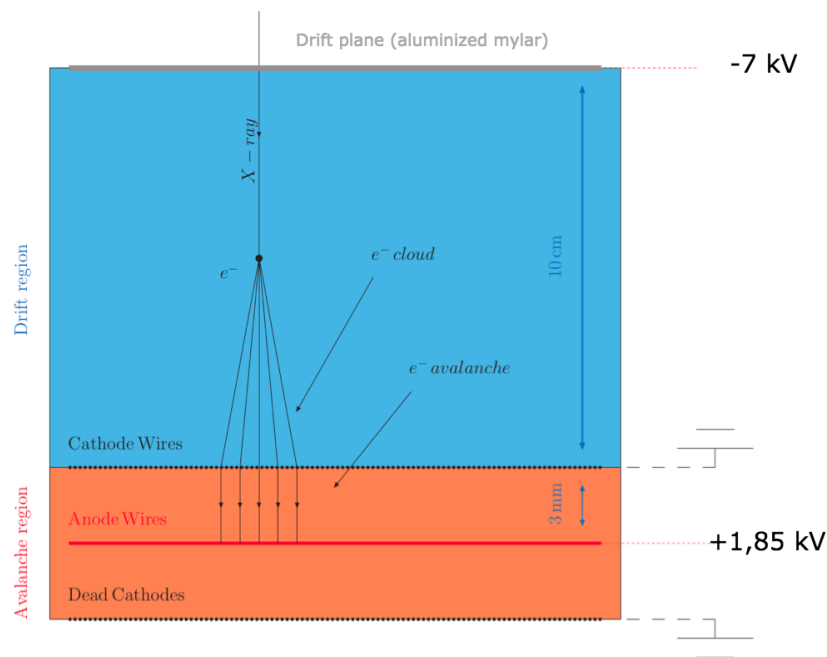


Figure 6-1 CAST TPC schematics

CAST TPC works on the same principle and it is the third generation from that family of detectors. It has a drift volume of  $10\text{cm} \times 15\text{cm} \times 30\text{cm}$  filled with a mixture of 95% Ar and 5%  $\text{CH}_4$  operating at a voltage of -7kV on the incident plane. There is an anode wire at 1.85 kV sandwiched between two grounded cathode wires.

The drift volume operates with an electric field of 700 V/cm while in the amplification region the field increases to 5 kV/cm in order to produce the avalanche effect for an amplified signal on the anode wires. The position of the event can be obtained from the activated anode and cathode wires as well as the drift time.

The separation of the gas chamber and the detector vacuum system is done by a  $3\text{ }\mu\text{m}$  aluminized mylar stretched and glued to a strongback. As a precaution and better vacuum performance a differential pumping system is used. A differential window further separates the vacuum system in two regions. The bad vacuum is contained between the drift window and the differential window while the good vacuum is on the other side of the differential window, directly connected to the cold bore.

The main reason for this differential system is to prevent the cryo-pumping of the diffused detector gas in the cold bore/cold windows thus increasing the X-ray photon absorption.

---

## 6.2. The Micromegas Detector

---

Starting with the  $\text{He}^3$  stage of the second phase, the TCP detectors were upgraded to three MICROMesh Gaseous Structure detectors covering the two sunset ports and one of the sunrise magnet apertures. They were developed rather recently with a more compact design and using a micromesh to separate the conversion from the amplification region instead of the wires used by the TCP detector.

However the basic working principle remains the same: the photon coming from the conversion volume traverses the isolation vacuum between the two windows, then is converted into a photoelectron in the conversion-drift region then can drift more for a short distance creating further ion-electron pairs. This is enabled by the photoelectric effect in the gas mixture of 95% argon and 5% isobutane. The ions are neutralised by the micromesh and the electrons carry on into the amplification region where an avalanche process happens under the influence of the intense field.

The actual detector signal is composed from the ions on the mesh used to estimate the energy of the incoming particle and the electron signal on the strips used for determining both energy and position of the incoming particles.

The shape of the field close to the micromesh is an important parameter for the transparency to electrons and the evacuation of positive ions. The voltages are applied such that the amplification field is one order of magnitude higher than the drift field thus ensuring the quick and efficient collection of ions. The timing of the signal is usually within 100 ns, depending on the width of the amplification gap and the gas mixture employed.

In the CAST Microbulk detectors the anode has a 2D readout scheme with the strips interconnected diagonally through vias in one or two extra layers [92]. The detector has a spatial resolution better than  $100\ \mu\text{m}$  due to the diffusion in the  $350\ \mu\text{m}$  pitch of the strips that are nested in a 192 X-Y pattern covering a total active area of  $45\ \text{cm}^2$ .

The detector was constructed as much as possible with radiopure materials like plexiglas and kapton, and low radioactivity soldering technique was used to minimise its internal radioactivity.

A notable upgrade to Phase II was the gold plating of the amplification mesh. This has considerably reduced the Cu-fluorescence line originating from the detector materials.

A passive shielding was implemented in the sunrise Micromegas line with the scope of reducing the environmental radiation like gammas and neutrons. The first layer is a 2 mm cadmium foil for absorbing thermal neutrons, then 25 mm archaeological lead and a 5 mm copper layer that also acts as a Faraday cage. The outer layer consists of 25 cm of polypropylene to thermalize neutrons. The air gaps in the shielding are continuously flushed with dry Nitrogen to reduce the concentration of air, thus reducing the Radon radioactivity and the unwanted effects of humidity in the air.

The MM detectors also use the concept of differential pumping for better vacuum performance. The first  $4\ \mu\text{m}$  window separates the vacuum of the magnet bore that is usually in the range of  $5 \times 10^{-7}\text{ mbar}$  from the buffer vacuum of  $5 \times 10^{-4}\text{ mbar}$ . The second window separates the buffer vacuum from the gas filled conversion region usually found at 1 bar. To support this pressure differential the  $4\ \mu\text{m}$  thick window needs a glued steel strong-back for mechanical support. The window was designed to provide a leak rate as low as possible having at the same time a transparency of 94.6% to low energy X-ray photons.

Daily detector calibrations were performed using a  $^{55}\text{Fe}$  source mounted on a mechanical manipulator that can be moved from a parking shielded position into the detector line of sight. The isotope decays by electron capture to  $^{55}\text{Mn}$  that further emits fluorescence photons  $K_\alpha = 5.9\ \text{keV}$  and  $K_\beta = 6.49\ \text{keV}$  with a ratio of 8.5:1 and a half-life of 2.73 years.



---

### 6.3. The X-Ray Telescope Mirror System

---

The CAST X-ray Telescope Mirror System is the focusing part of the most sensitive detector system from the CAST experiment having in the focal plane a Charge Coupled Device that will be covered in the next chapter.

The main advantage of this fantastic telescope is provided by the virtue of its focusing ability, concentrating the entire magnet bore aperture of 43 mm diameter in a spot of about 1.7 mm radius. If a detector with high spatial resolution is used in the focal plane, a background suppression by a factor of approx. 154 is achieved by focusing any possible signal from an area of 14.5 cm<sup>2</sup> to a small spot of 9.4 mm<sup>2</sup>. Also this approach enables the reduction of systematic effects by measuring Axion sensitive data in the focal spot and background data with the rest of the CCD chip at the same time.

The CAST X-ray mirror system is based on the concept of a Wolter Type I mirror optics (Wolter 1952), a well-known and tested technology in X-ray astronomy in the Einstein, Exosat, Rosat, Chandra and XMM-Newton X-ray observatories.

This specific telescope is a spare module originally built for ABRIXAS X-ray space mission launched in April 1999 with the scope of extending the mapping of the sky provided by ROSAT at higher energies of 0.5 keV and 15 keV [93].

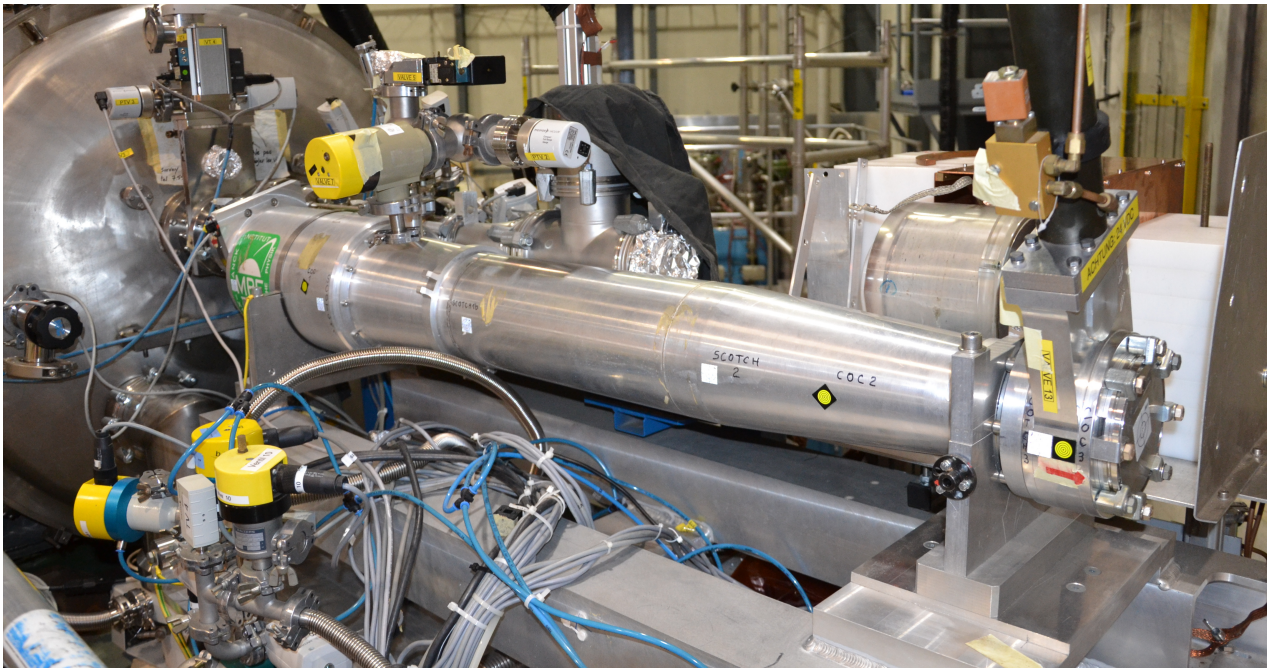


Figure 6-2 CAST X-ray Telescope Mirror System mounted on Sun-Rise platform with vacuum and electro-pneumatic systems disconnected. Survey targets are visible.

The internal structure of this module consists of 27 nested nickel shells, gold coated and arranged confocally in parabolic-hyperbolic succession with a total focal length of 1600 mm. The diameter of the outermost shell is 163 mm while the innermost has a diameter of 76 mm. For mechanical support the individual shells are nested in a spoke like structure that subdivides the mirror module in six azimuthal sectors. The telescope was integrated on the CAST platform in an off-axis arrangement since the CAST magnetic bore of 43 mm diameter can be completely covered by one of the 6 sectors (Figure 6-3). This has the added advantage that the shadowing effect of the support structure has no influence on the imaging of the Sun trough the CAST magnet.

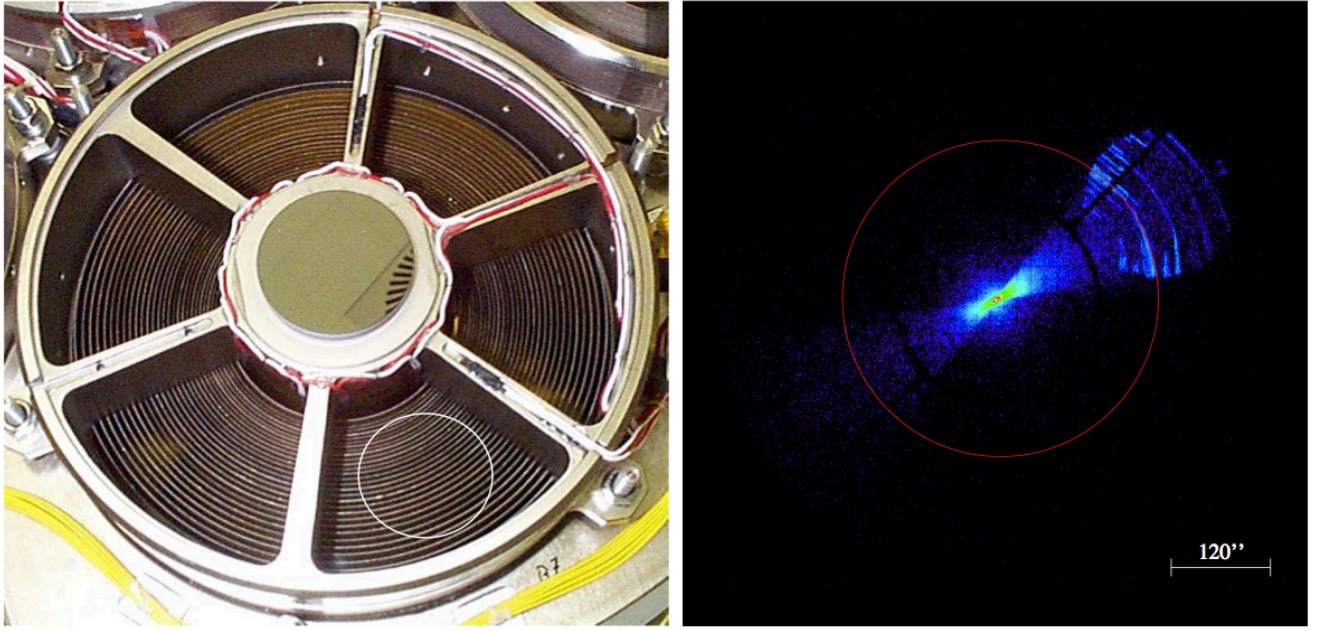


Figure 6-3 Left: Front view of ABRIXAS mirror system showing the 27 nested mirrors in 6 sectors. CAST magnet bore aperture is marked in one of the sectors justifying the off-axis use of the module. Right: Logarithmic intensity image of the Point Spread Function obtained at PANTER X-ray test facility in Munich by illuminating one sector with a beam of 1.5 keV. The red circle depicts the expected solar Axion image, and the top right reflexion is explained by single reflections on the shells due to finite distance to the source. [94]

X-rays obey the principle of total reflection when the incident angle  $\theta_1$  is larger than the critical angle  $\theta_c$  and the rays are traveling from an optical denser medium towards a medium with smaller index of refraction.

$$\frac{\sin \theta_1}{\sin \theta_2} = \frac{n_2}{n_1} \xrightarrow{\text{yields}} \theta_c = \arcsin\left(\frac{n_2}{n_1}\right)$$

$$\theta_c^2 \approx \lambda^2 r_0 N_e \xrightarrow{\text{yields}} \theta_c \approx \sqrt{N_e} \approx \sqrt{Z}$$

Equation 6-2

With the condition of being far from any absorption edges, the critical angle is proportional to the wavelength of the incident light,  $r_0$  is the classical electron radius and  $N_e$  is the electron density. From here it results that the critical angle is proportional to the square root of  $Z$  and that is the reason the mirrors were plated with gold.

Wolter type I optics it is mechanically the simplest from the family of three configurations and it creates a sharp image for the off-axis objects if the Abbe sine condition is satisfied by first reflecting the X-rays on the inside surface of a parabolic mirror and then on the inside of a hyperbolic one (Figure 6-4). Also this design is preferred for X-ray optics because at grazing incidence multiple mirrors can be nested one into another thus increasing the light collecting area and the efficiency of the module, property useful for observing low luminosity X-ray sources.

Type II Wolter optics has poorer performances for off axis objects and Type III is completely not suitable/efficient for X-ray Astronomy.

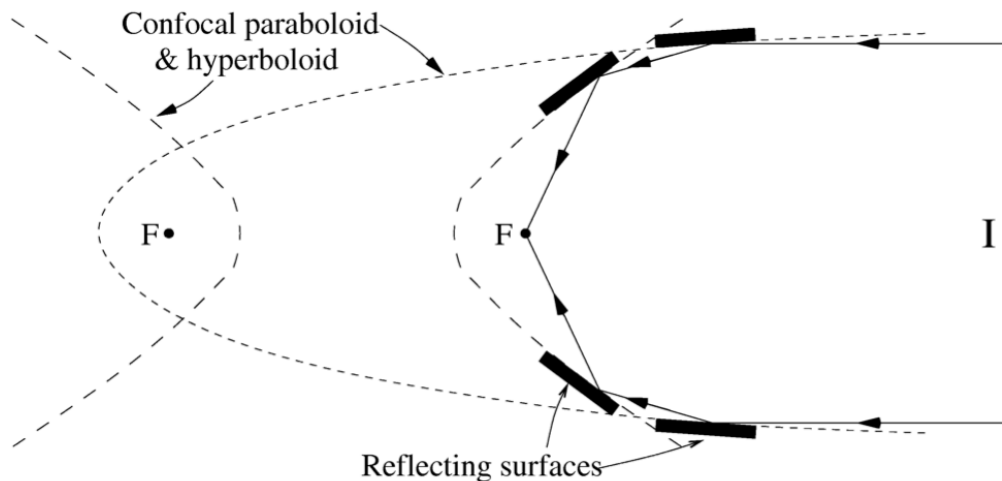


Figure 6-4 Wolter-type I optics schematics [95]

For a typical X-ray focusing system of a given focal length, the overall performance has a strong dependence of the effective area and the spatial resolution given by the Point Spread Function of the system (PSF).

The effective area of a mirror system depends on the photon energy, off axis angle dependence and the micro-roughness of the coating layer of the mirror in the sense that it decreases with the increase of micro-roughness and incidence angle due to the decrease of reflectivity and the increase of geometric effects due to vignetting.

A typical value for the ABRIXAS mirror system for the micro-roughness of the mirror surface is 0.5 nm (rms). Ray tracing algorithms have been used for estimating the effective area and the point spread function as a function of photon energy and off axis angles. The influences of the scattering effects due to micro-roughness features on the mirror surface were negligible in these simulations.

Furthermore the CAST mirror module was tested multiple times at the PANTER test facility of the Max-Planck-Institut für Extraterrestrische Physik (MPE) [96]. The measurements were conducted using monoenergetic X-ray sources of different energies to achieve a full illumination of the mirror system. The angular resolution of the mirror system was found to be of 34.5 arcsec half energy width (HEW) at 1.5 keV and 44.9 arcsec at 8 keV thus providing an oversampling of a factor of 10 in spatial resolution compared to the expected size of the Axion image coming from the sun.

Sector	Effective area – cm <sup>2</sup>			
	0.93 keV	1.49 keV	4.5 keV	8.04 keV
1	13.5	13.4	8.2	3.9
2	13.5	13.4	8.2	3.8
3	8.9	13.6	8.3	3.9
4	13.9	13.9	8.4	4.0
5	12.6	12.8	7.9	3.4
6	13.1	13.4	8.5	4.0

Table 6-1 Effective area measurement for all the sectors of CAST telescope at PANTER, sector nr. 4 had the best performances and is used at CAST.



At the beginning of 2013 the mirror module was returned to MPE in Garching for a new reflectivity check at PANTER facility. Previous reflectivity measurements were done in 2001, 2003 and 2008.

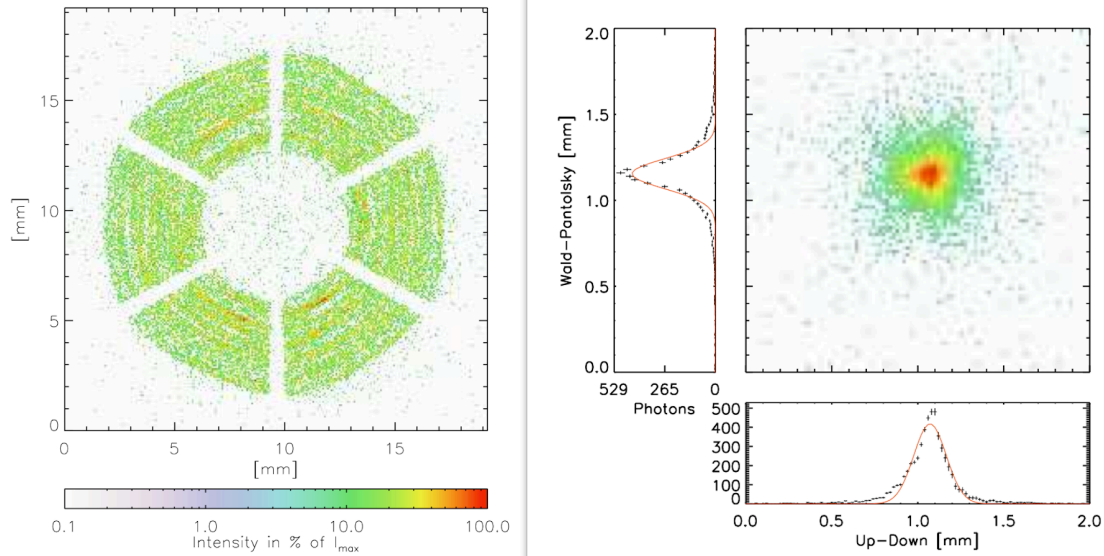


Figure 6-5 Left: Effective area – general view with all 6 sectors of the CAST Telescope with the out of focus transmitted intensity (shadowing effect of the support structure visible);  
Right: Point Spread Function of the CAST Telescope measured at 1.49 keV, HEW: 33.4'', W90: 123''.

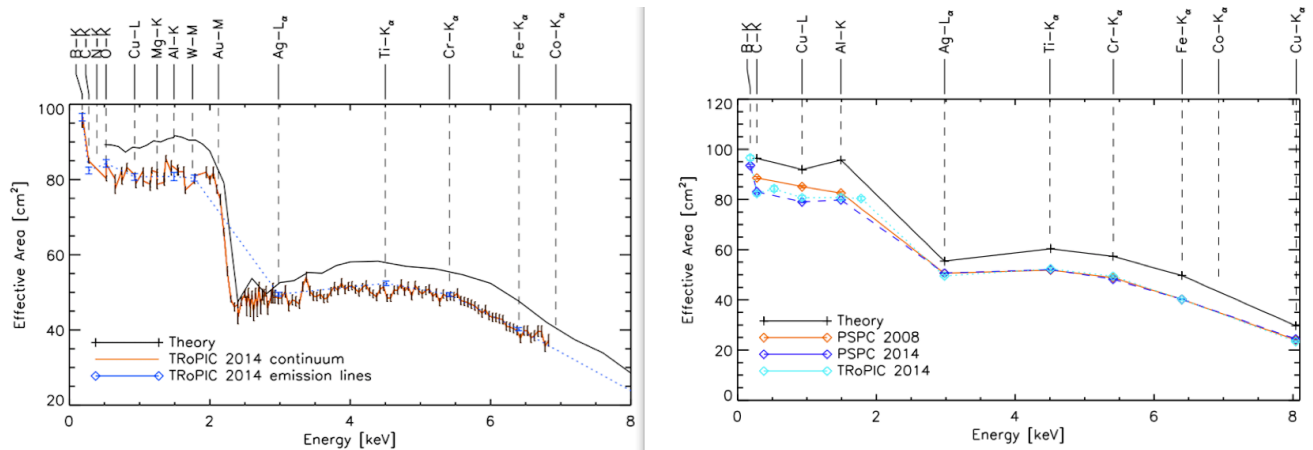


Figure 6-6 Left: Effective area of CAST Telescope measured at PANTER, extended for the first time below 2 keV with TRoPIC setup also for other energies beside the characteristic emission lines;  
Right: Comparison with 2008 measurements done in PSpC setup.

These measurements confirmed no significant changes of the Point Spread Function compared with the ones done in 2000-2001.

The effective area suffered no changes for energies above 2 keV. A 5% loss for energies below 2 keV was observed that is to be expected due to surface contamination of the mirrors during the 12 year long exploitation. However is remarkable the low degree of contamination crosschecked in 2014 trough a FTIR spectroscopy wipe test of the internal aluminium housing and the shell of the external mirror which yielded a contamination lower than  $16 \times 10^{-8} \text{ g/cm}^2$ .

Also the effective area was extended down to lower energies (B-K 0.18keV) and measuring more energy points besides the characteristic energy lines increased the fidelity of the estimation.

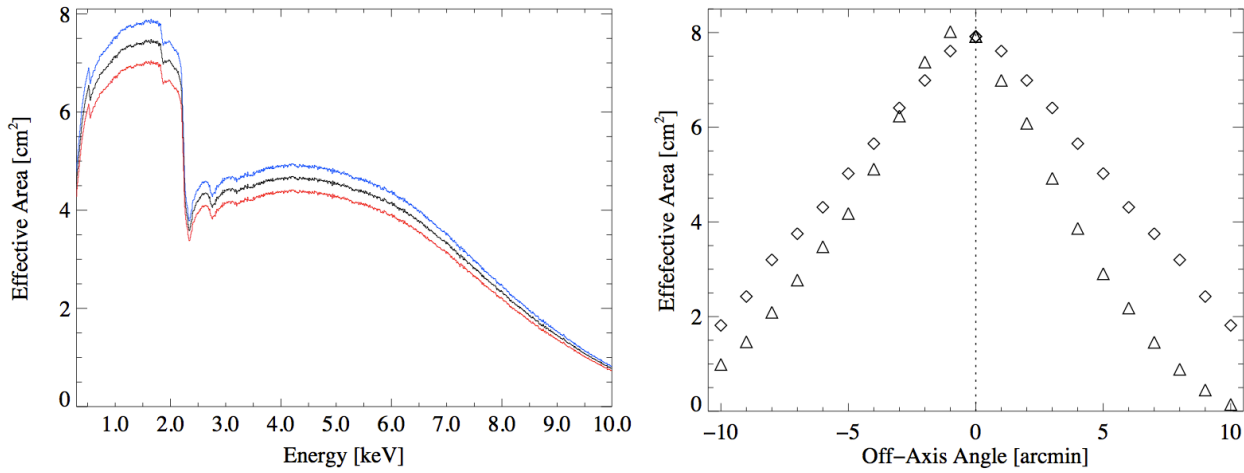


Figure 6-7 Left: Effective area of Sector nr. 4 of the CAST Telescope taking into account the magnet bore aperture of  $d=43\text{mm}$ , and the quantum efficiency of pn-CCD detector in three cases: Blue line – point source case, Black line – point source located at infinity, Red line – for a source of roughly the same angular size as the Axion image of the Sun;  
Right: Off-axis dependence of effective area for Sector nr. 4 shown for radial angles with triangles and tangential angles with diamonds. [97]

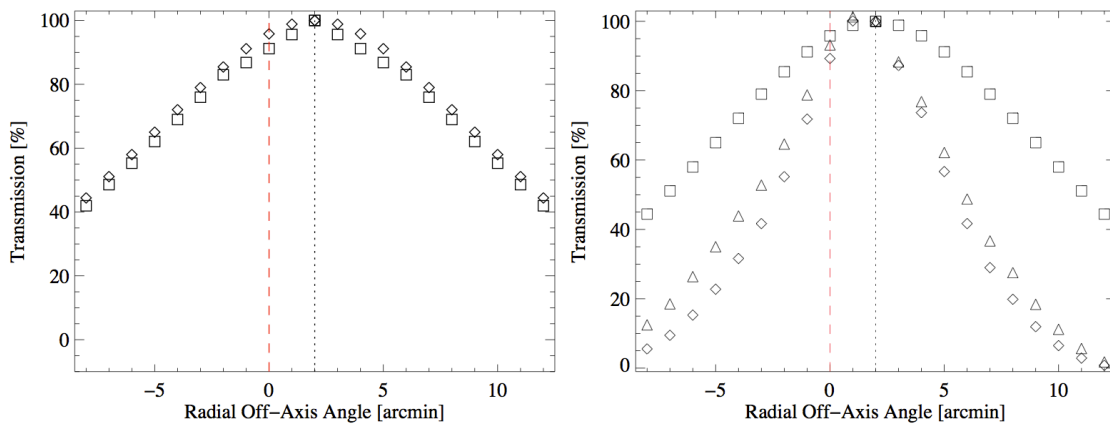


Figure 6-8 Left: Off-axis transmission penalty due to the geometric vignetting effects of the CAST setup plotted with triangles for the case of radial off-axis angles and with diamonds for the tangential off-axis angles;  
Right: The off-axis transmission dependence of individual components of radial off-axis angles: Rectangles – vignetting losses due to the magnet bore, Triangles – transmission of the mirror module, Diamonds – The total transmission of the system (Mirror Module coupled with the Magnetic Bore.) [97]

The overall combined efficiency of the CAST mirror module with the PN-CCD detector in the focal plane varies between 25% and 46%, depending on the X-ray photon energy resulted from the Axion conversion in the Magnetic Bore.

The radial off-axis dependence shows a slight asymmetry due to the fact that CAST uses only sector no. 4 of the mirror module for imaging the photons and this breaks the radial symmetry of the entire mirror module.

Analysing Figure 6-8 Right it is to be noted that introducing a slight misalignment of just 2 arcmin can induce a total system efficiency lose of 10% corresponding to the Red dashed line. This shows how critical is the alignment process of the telescope relative to the Magnet optical axis due to geometrical vignetting constraints.

A more detailed look at the CAST Telescope alignment I conducted at CERN will be presented in Chapter 7.

---

## 6.4. The pn-CCD

---

CAST used in the focal plane of the X-ray telescope a pn-CCD detector as an imaging device to detect any possible X-ray photons originating from inverse Primakoff Effect of solar Axions in the strong perpendicular magnetic field inside the magnet bore. This silicone drift detector has a size of  $3 \times 1 \text{ cm}$  and a resolution of  $200 \times 64$  pixels with  $150 \times 150 \mu\text{m}$  each.

The chip itself is the same as the one installed on board ESA's XMM-Newton satellite space mission and it is a fully depleted pn-CCD  $280 \mu\text{m}$  thick back side illuminated. It has a thin entrance window of  $20 \text{ nm}$  and a thick depletion region that enabled the detector to have outstanding quantum efficiency in the energy range of 1-7 keV higher than 95%.

This is the energy range particularly interesting for Axion searches (see Figure 4-3) and couples extremely well with the capabilities of the mirror module (Figure 6-7).

---

### 6.4.1. The pn-Junction and the Depletion Region

---

PN-Junctions lay at the foundation of all semiconductor detectors and for that matter at the foundation of any transistor. This junction is made by joining a p-type semiconductor with an n-type semiconductor material between which a space charge region forms where because of the natural initial difference in electron and hole concentration in the original materials a diffusion phenomena arises. Holes in the p-side are filled up with electrons from the other side and vice-versa happens in the n-side.

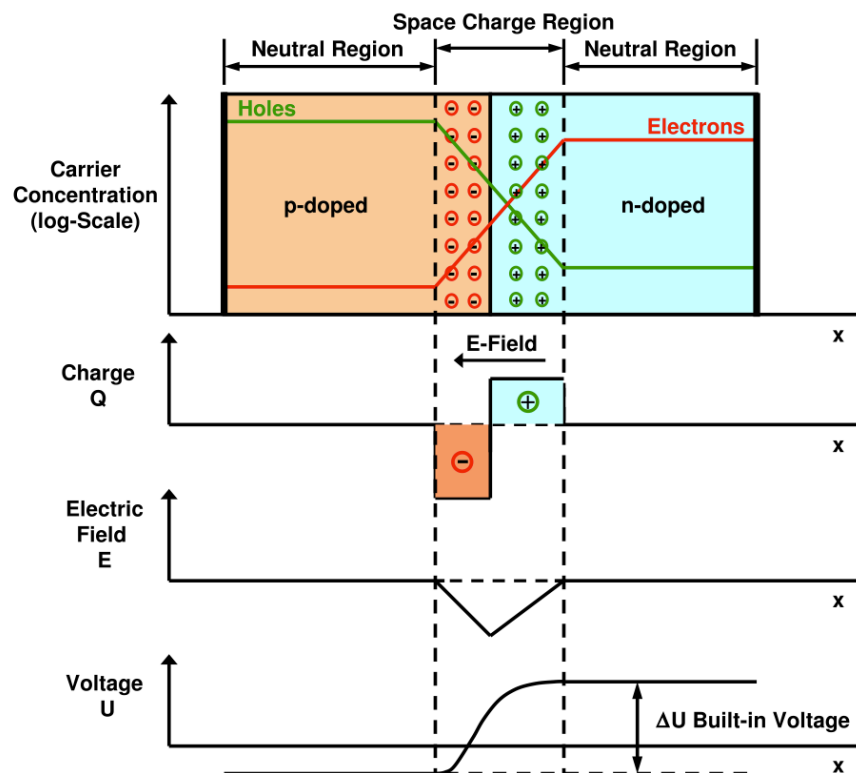


Figure 6-9 Schematic of a pn-Junction [59]

This build up of charge in the Space Charge Region creates an electric field that at some point balances this diffusion tendency. The potential difference across the junction is of the order of 1 V and leads to the deformation of local band structure inside the material.

The consequence is that in the space charge region or depletion region there are almost no free electrons or holes and the naturally arising electric field acts as a carrier for any mobile charge in that volume which is guided towards the exterior of the junction.

Now let us imagine an incoming ionization radiation that will create electron-hole pairs when it enters this space charged volume. These charge carriers will be naturally guided outside of the junction and can be collected by some electrical contacts by a readout system. This is indeed the working principle of the pn-CCD detector used at CAST.

To be noted is that the depletion depth is dependant on temperature and can also be varied with an external voltage.

$$d = x_n + x_p = \sqrt{\frac{2\epsilon\Delta U}{e} \frac{(N_A + N_D)}{N_A N_D}}$$

Equation 6-3

The width of the depletion region  $d$  is equal with the sum of the diffusion depths in the  $n$  side and  $p$  side and has the relation 6-3 where  $N_A$  and  $N_D$  are the acceptor and donor concentrations while  $\epsilon$  is the dielectric constant of the medium.

Choosing the right type of semiconductors is crucial for the photon absorption length and for the interaction of the radiation with the material. The combination of these two parameters largely determines the quantum efficiency of the detector for a given energy range.

The creation of electron-hole pairs as a result of radiation absorption inside the junction is critical because this actually gives the readout signal.

Incident charged particles will have low-recoil collisions with electrons along the flight path resulting in ionization while photons will interact via the photon or Compton effect with a target electron.

A fraction of the energy will certainly be used for ionization processes while exciting the lattice will absorb the rest [98]. This ratio largely depends on the detector material as follows:

$$N = \frac{E}{E'} ; \quad \langle (\Delta N)^2 \rangle = F \frac{E}{E'}$$

Equation 6-4

where  $N$  is the number of counts given by the detector for a specific dose of incoming radiation,  $E$  is the energy absorbed in the semiconductor and  $E'$  the total energy needed to create a electron-hole pair.  $F$  is the Fano factor, a material specific constant dependent on energy and temperature. As a physical interpretation the Fano factor accounts for all fundamental mechanisms of absorbing energy inside the junction, including those that do not lead to ionization.

Another critical parameter to consider is the photon absorption length which if it is too small can lead to signal degradation and low efficiencies because the charges generated can be lost on the surface of the detector. If the absorption length is too large the detector is basically transparent to the incident radiation and the pair production has low probability.

In the case of silicone the absorption has high efficiency around the M, L and K edges at energies of 20, 100-115 and 1830 eV (Figure 6-10) [99].

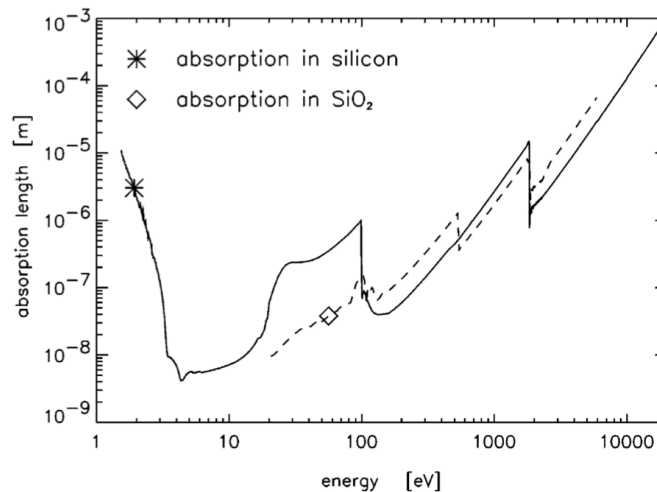


Figure 6-10 Energy dependence of absorption length in Si and SiO<sub>2</sub> [99]

#### 6.4.2. Fully Depleted Back-side Illuminated pn-CCD

The principle of operation for such a detector is the removal of mobile carriers through sideward depletion. The N-type silicon wafer is depleted via a small n<sup>+</sup> ohmic contact that is positively biased relative to the p<sup>+</sup> contacts implanted on both sides of the wafer. By applying a voltage on the terminals the electron channel in the middle of the substrate can be suppressed in the process of depletion.

The electronic potential has a parabolic shape when viewed from a plane perpendicular to the wafer with the minimum centred in the middle. This minimum can be manipulated with the voltages on the p<sup>+</sup> contacts, thus shifting it towards one plate or the other.

In Figure 6-11 the upper most sketch is with no reverse voltage applied thus only the intrinsic depletion zones are present, the in the middle full depletion is achieved closing the electron channel and in the lower most diagram the state of overdepletion is presented if the bias potential is pushed to higher levels. [99]

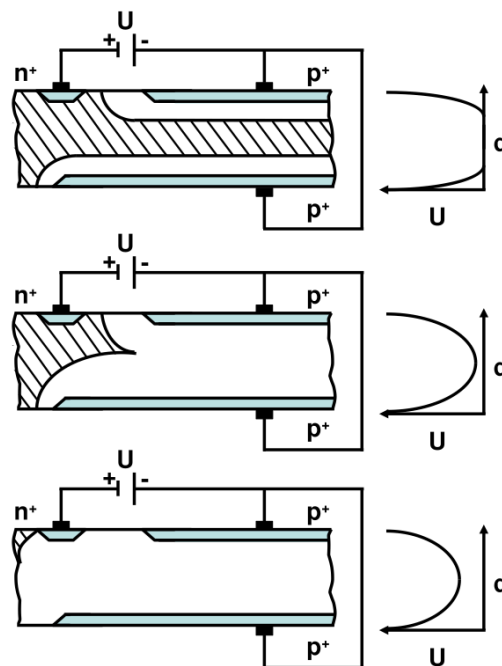


Figure 6-11 The Principle of sideward depletion [99]

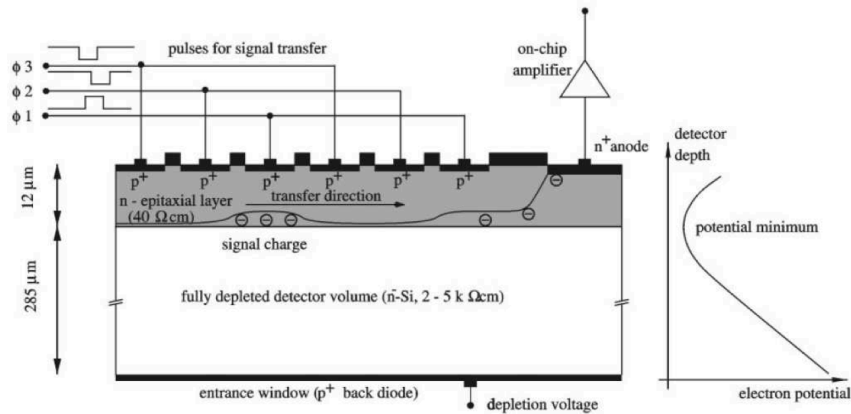


Figure 6-12 Cross section along a transfer channel trough a pn-CCD [99]

The practical implementation of the sideward depletion in the CCD detector from CAST is displayed in Figure 6-12. By boosting the voltages on the  $p^+$  implants readout can be achieved on  $\Phi_1\Phi_2\Phi_3$  transfer registers.

These three shift registers form the pixel structure of the chip (Figure 6-13) by being divided from the neighbouring pixels (the next three shift registers) on all sides by regions where the doping is increased forming strips perpendicular to the gate direction. These doped regions provide a box like potential barrier for the charge carriers thus forming the structure of a pixel.

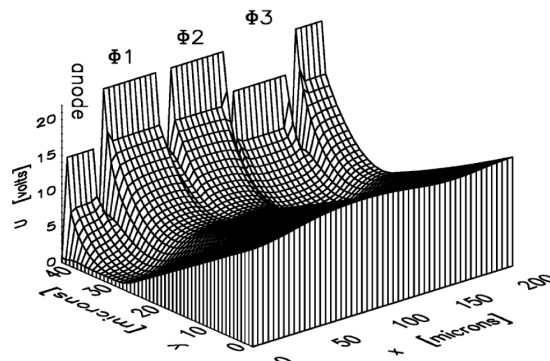


Figure 6-13 Pixel structure formed from the shift registers each of  $50\ \mu m$  resulting a pixel of  $150 \times 150\ \mu m^2$  [99]

The chip is structurally divided into 200 pixels in the direction of the signal transfer lines and 64 pixel columns. There are 64 output anodes where each signal is preamplified on the chip via a JFET source follower. The resulting 64 analogue signals are bonded to a CAMEX64 (CMOS Amplifier and Multiplexer chip) readout chip that amplifies, shapes, samples and multiplexes all the channels in parallel (Figure 6-14).

If the entire sensitive area is used a full readout cycle is approx. 70 ms long. Then the signals are handed over by the multiplexer to the Analog-to-Digital Converter (ADC) unit that can handle and digitise the 64 channels in parallel.

The TIMEX chip handles the timing controls of the CAMEX switches.

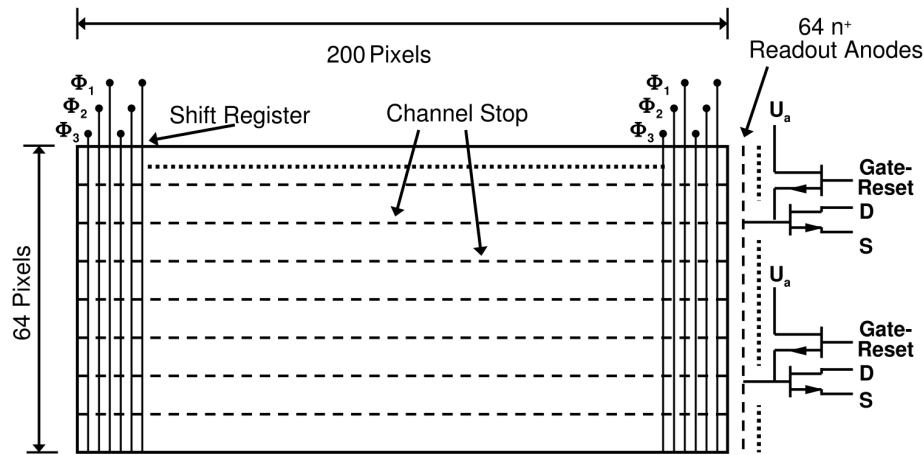


Figure 6-14 Schematics of the pn-CCD readout (64x200 pixels) [99]

From the point of view of the readout method, the pn-CCD and the general class of silicon drift detectors (SDD) are closely related, the main distinction being that the process of reading a SDD is a continuous one while the CCD integrates the charge for a set controllable exposure and shifts the packets of charge to the readout in a discrete time interval. This is the reason why a CCD can be also named a discrete SDD.

In the Physics of pn-CCD detectors there are a number of parameters that are critical for understanding and interpreting the data they provide. I will explain some of them below.

**Partial events** – at low energies below 500 eV for the incident photons, the absorption length is rather shallow and the charges are generated close to the surface of the detector. In this case the probability of recombination is significant. Charge collection efficiency is the ratio of deposited electrons as a function of absorption length and the number of generated electrons. This parameter is specific for each detector, and can be corrected.

**Pile-Up events** – this describes the situation when a pixel is stimulated by more than one photon during an exposure cycle. In this case the detector will read a single event with one timestamp. Shortening the exposure time per cycle reduces the chances of this to happen.

**Split events** – are a direct consequence of back side illuminated detectors. The charge generated by the absorption of one photon can disperse in the drift volume under the influence of coulomb repulsion and diffusion. This cloud of charge can be collected by more than one pixel. In general the splitting ratio is strongly dependent on the energy and the geometry of the drift layer.

Event type	Percentage
Single events	80%
Double events	19%
Triple and Quadruple events	1%

Table 6-2 Approximate distribution of split events for a pixel size of  $150 \times 150 \mu\text{m}^2$ .

In this case the generated charge can be collected by up to 4 pixels. The possible patterns are presented in Figure 6-15 and the charge deposited is colour coded in intensity.



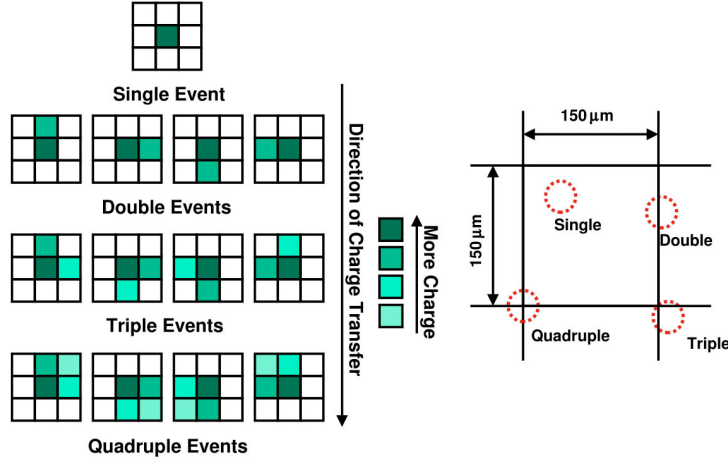


Figure 6-15 Examples of signal patterns for split events in a pn-CCD detector

**Out of Time events** – The CCD detector at CAST was operated with an integration time of 72 ms and a read out time of 6 ms during which the charge is shifted towards the CAMEX chip. However there is no shutter during the readout so the chip itself stays sensitive also during the readout phase. Any incoming photons during the readout cycle will be registered with a wrong line number since the shifting for readout is done along columns. For the expected Axion signal spot of 11.5 pixels in radius, the out of time event fraction is 8.1% while for an ideal point source it is of 9.2%.

**Offset** – It is the signal given by the detector without any incident signal. Since its origins are the thermally generated electrons in the semiconductor material it is strongly dependent on the temperature of the chip. In practice at CAST the chip is cooled by a cold finger/Stirling Cooler at 115K, for minimising the dark current.

**Energy resolution** – To have an estimation of the total energy resolution of the detector, all noise sources have to be considered as it follows:

$$\Delta E_{total} = \sqrt{\Delta E_{Fano}^2 + \Delta E_{ADC}^2 + \Delta E_{CAMEX}^2 + \Delta E_{CM}^2 + \Delta E_{Offset}^2}$$

Equation 6-5

For energie range of interest in CAST (1-7 keV) the typical energy resolution is about 170-180 eV while the MicroMegas detectors have ~14% *FWHM* for a 5.9 keV  $Fe^{55}$ .

**Noise** – For CAST CCD detector the noise has two main components:

*Intrinsic noise* – is a function of the purity degree of the semiconductor used. The energy required to create an electron-hole pair in the semiconductor used at CAST is 3.65 eV. Considering that the Fano factor is about 0.12 the intrinsic Fano noise at a calibration run with  $Mn - K_{\alpha}$  at 5.9 keV is about 20% thus limiting the energy resolution to 120 eV.

*Electronic noise* – One component of this is the thermal noise originating from leakage current of the readout anode and the thermal fluctuations of the electrons in the CAMEX pipeline. The other component is a low frequency one attributed to ADC chips. Being thermal in nature, cooling down the chip greatly improves the performances.



### 6.4.3. Implementation in CAST

Installed in CAST the XMM-Newton chip has a sensitive area of  $2.88 \text{ cm}^2$  with a resolution of  $260 \times 64$  pixels and a pixel size of  $150 \times 150 \mu\text{m}^2$ . It has a quantum efficiency close to unity for the energy range of interest for solar Axion searches (1 to 7 keV).

Taking into account the focal length of the X-ray telescope (1600 mm), each pixel has an angular resolution of  $19.3 \times 19.3 \text{ arcsec}^2/\text{pixel}$  thus the 64 pixel width fully covering the solar core ( $\sim 0.2 R_{\odot}$ ) from where most of the Axion flux originates (Figure 3-3). In this frame a spot of 23 pixels in diameter covers 82.6% of the total Axion solar flux.

For minimising the noise the pn-CCD was operated in CAST at a temperature of 115 K being in thermal contact to a gold plated cooling mask, a cold finger and flexible copper heat pipes to a Stirling Cooler.

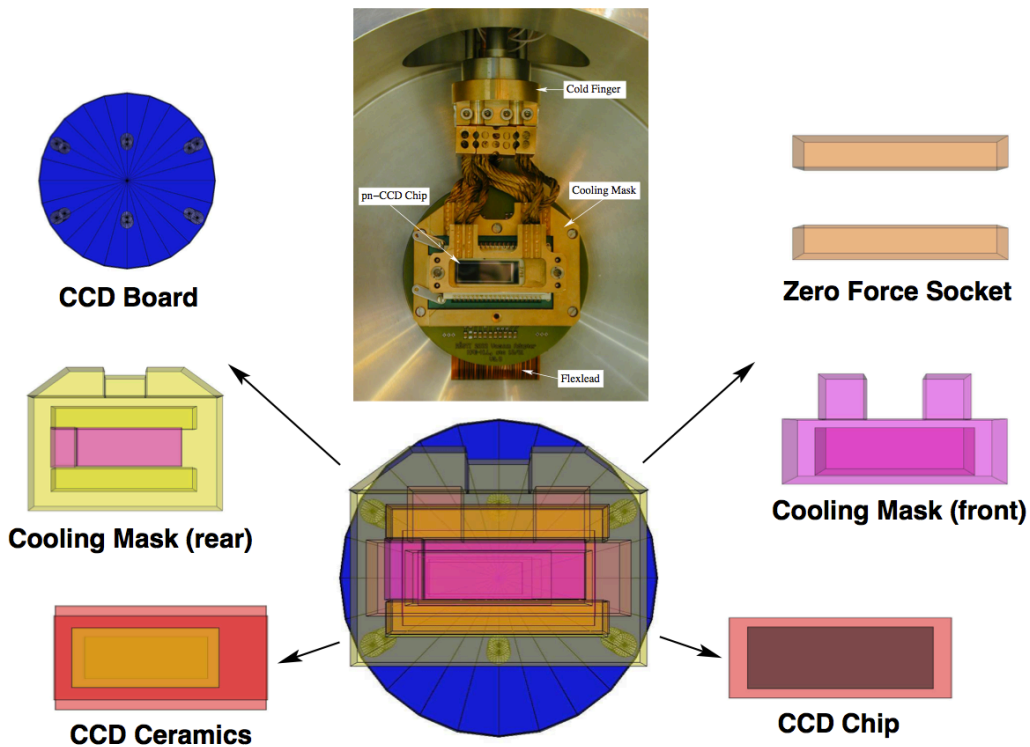


Figure 6-16 The pn-CCD chip implementation in CAST with the cooling system.  
Individual components are presented as they were modelled in GEANT4 during the implementation phase.

The chip itself is glued to an aluminium oxide substrate sandwiched by a copper cooling mask from the front and back that ensures a good thermal coupling. On the rear side an electronic board with various support electronic components is fixed. These components are housed inside a vacuum vessel that can be isolated from the rest of the systems with valves.

A passive shield made from oxygen free low activity copper of 10-40 mm in thickness found inside the vacuum vessel surrounds the detector. This copper box is then surrounded by a 22 mm thick lead layer depleted of  $^{210}\text{Pb}$  and another 250 mm layer placed outside the vacuum vessel.

Considering the general configuration of the system and the fact that the X-ray telescope is basically sandwiched on the input and output by two cold surfaces (the cold window of the cold bore and the CCD chip with the cooling mask), there is considerable potential for unwanted cryo-pumping that

could contaminate the detector, the window and the mirror module, thus decreasing the overall sensitivity of the detector system. In order to avoid this, the system is required to operate at pressures below  $5 \times 10^{-6}$  mbar.

The vacuum system is divided into a high vacuum region pumped with three turbo-pumps where the data taking pressure is usually around  $5 \times 10^{-7}$  mbar and a backing vacuum with an operating pressure of  $3 \times 10^{-2}$  mbar.

The low vacuum side is pumped with a Leybold EcoDry M15 Teflon piston pump upgraded in 2010 with an additional pumping stage by adding a membrane pump. The requirements of this backing stage are:

- oil free operation to avoid the chance of contaminating the high vacuum stage and the mirror module with oil droplets;
- operate at inclination angles of  $\pm 8^\circ$ ;
- have a pumping speed higher than 5 m<sup>3</sup>/h for properly sustaining the turbo-pumps when the CCD chip was thermally cycled, and when initially pumping down the mirror module. In that case the outgassing effect coming from the high internal surface required roughly 5-7 days of pumping to get into the  $10^{-6}$  mbar region.

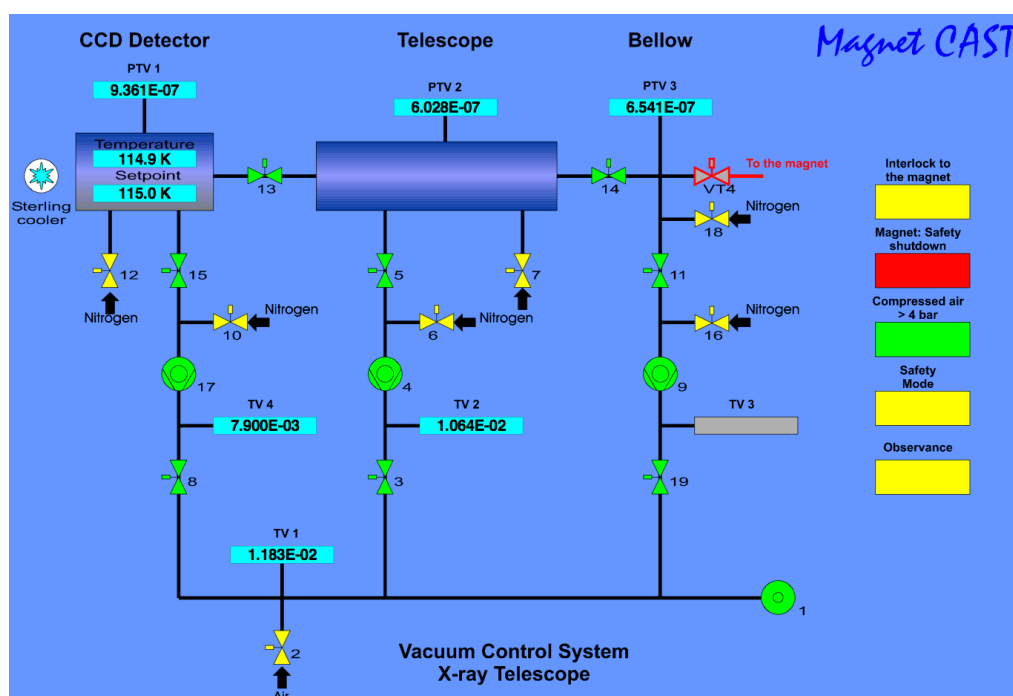


Figure 6-17 The Vacuum Control and Monitoring interface for the X-ray telescope – CCD detector system

The piston pump was isolated at the inlet for cleanliness reasons from the rest of the system by a DN25 fine molecular sleeve with filtering capabilities of 5 microns.

The high vacuum region is split in 3 volumes isolated with gate-valves and service valves. The CCD chamber, the telescope and the flexible bellow connecting the telescope to the magnet have each individual turbo pumps and dual stage PKR pressure sensors. Thanks to the modular design each volume can be isolated and serviced without breaking the vacuum in the entire system.

A Siemens Symatic S7-400 PLC unit handles the actual hardware and also checks that the safety interlock conditions are satisfied. In the event of a pressure fault, compressed air failure, power glitch,

magnet quench, VT4 gate-valve closure, the PLC will automatically bring the vacuum system into a safe state by closing all the valves and stopping the pumps.

Service Valve 7 is particularly useful because I have used it multiple times for injecting in a controlled way high purity dry nitrogen in the X-ray telescope before dismantling it for alignment/shipping to PANTER and between the data taking periods. This avoids contaminating the mirrors with normal atmospheric air and water vapour that would require long pumping times to get rid off.

#### 6.4.4. Quantum Efficiency and Energy Resolution

In general, the definition of Quantum Efficiency for most photon-sensitive devices is defined as the percentage of detected photons from the total number of incident photons. In other words this is a metric of the efficiency of the semiconductor material to convert photons into detectable electron-hole pairs, thus into a readable signal.

The EPIC pn-CCD chip used in CAST was calibrated for the XMM-Newton mission at synchrotron radiation facilities in Berlin and Orsay versus a reference solid state detector.

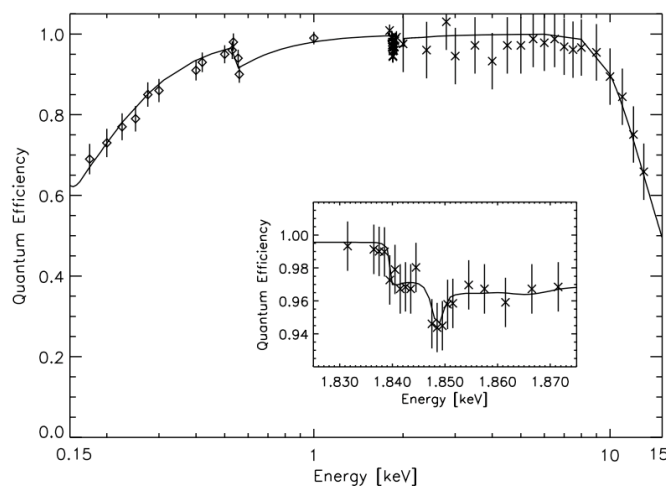


Figure 6-18 Quantum Efficiency of the pn-CCD chip used in CAST and in XMM-Newton function of incident photon energy [100]

A first drop in the Quantum Efficiency of the chip is observed at 0.525 keV due to absorption losses on the oxygen edge of the  $\text{SiO}_2$  layer that coats the surface of the detector.

The second notable drop showed in more detail in Figure 6-1 is the typical X-ray absorption fine structure (XAFS) in the region of the Si-K edge at 1.84 keV. Using photon absorption coefficients from atomic data tables the detector response was modelled by fitting the solid line.

However it is to be noted that for the entire energy range 0.3 keV to 10 keV the Quantum Efficiency of the CCD chip is above 90%.

Before being installed at CAST the CCD detector was also calibrated for its energy response at PUMA facility in Munich using an X-ray fluorescence generator. The purpose of this calibration is to find the factor correlating the electrons generated in the CCD detector by X-rays directed at different materials and the analogue to digital unit (ADU) collected at the readout.

The results are presented in Table 6-3 based on the Figure 6-19.

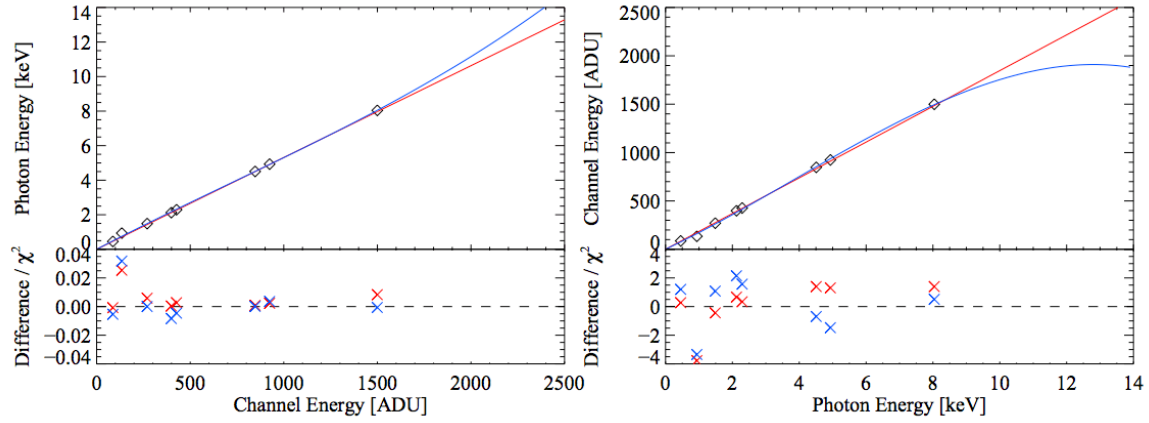


Figure 6-19 Left – Dependence ADU and the incident photon energy in keV based on calibration data. Red line is a linear fit and blue is a third order polynomial. Below is the deviation from the literature values in units of  $\chi^2$ ;  
Right – The same plot but with the axis inverted. [101]

	Parameter	Calibration	Calibration and Background
keV to ADU	a	184.69668	185.35991
	$\chi^2$	170.13183	1.3445306
	DOF	7	9
ADU to keV	a	0.0053142	0.0053136
	$\chi^2$	1.2498678	1.3996426
	DOF	7	9

Table 6-3 The relevant parameters of the response function.  
The linear fit function was chosen of the form  $f(x) = a \cdot x$

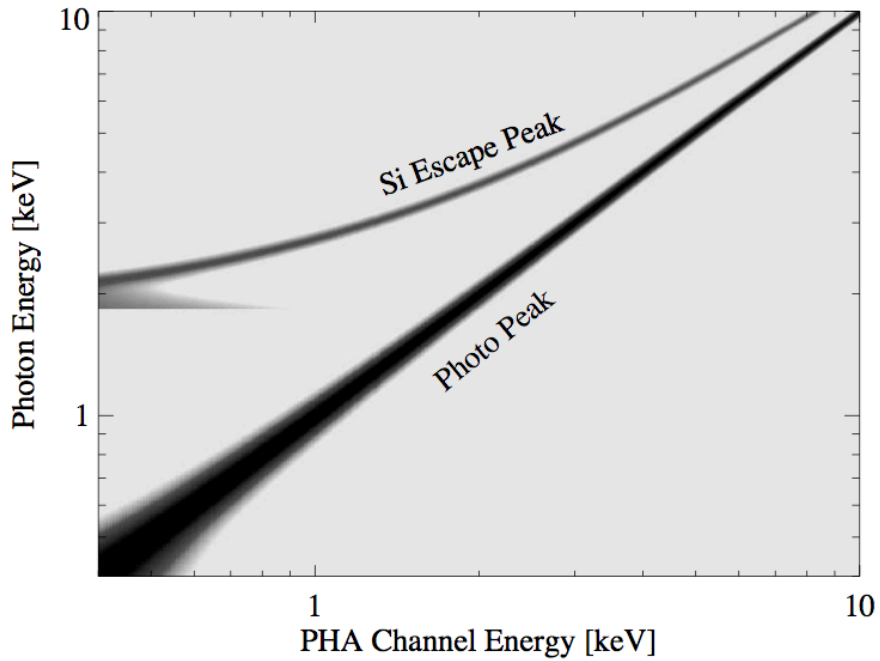


Figure 6-20 CAST pc-CCD detector Response Matrix in logarithmic grey scale.  
The width of the distribution correlates with the energy resolution. [100]

I would like to explain the appearance of the Si Escape Peak on the response matrix plot. When a incident photon is absorbed in the pn-CCD semiconductor material (silicone), an electron-hole pair is created. If the hole is placed in the inner shells, an electron populating the outer shells can fill it. This process happens with the emission of a photon. If this photon escapes the detector then this energy is missing from the incident signal and furthermore a new signal originating from this silicon escape peak can be registered at a lower energy:

$$E_{SiEscape} = E_{Mn-K_{\alpha}} - E_{Si-K_{\alpha}} \approx 4.15 \text{ keV}$$

Equation 6-6

To be noted is that this Si escape peak is at an energy with 1.74 keV lower than the photo peak.

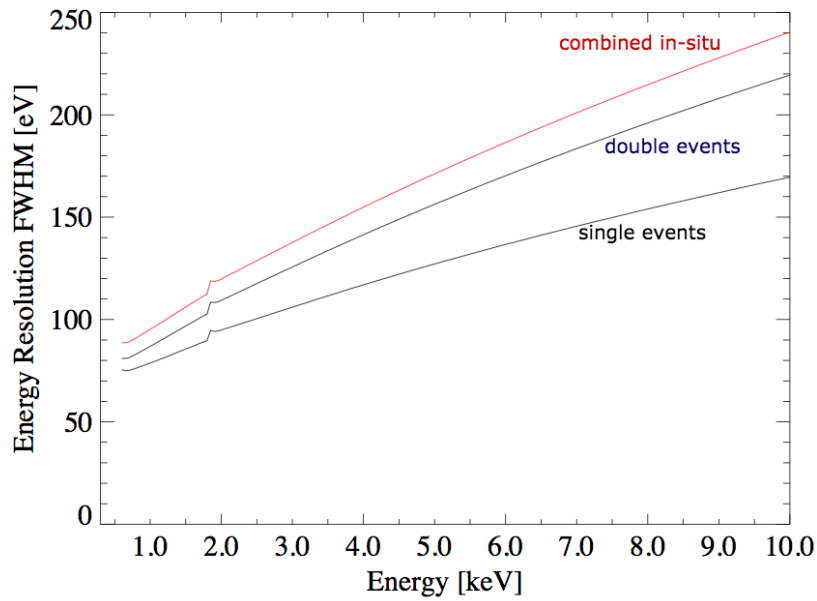


Figure 6-21 Energy Resolution of the CAST pn-CCD detector versus the incident photon energy

For a typical  $^{55}\text{Fe}$  calibration run the energy resolution of the CAST CCD detector is approx. 170 eV both  $Mn - K_{\alpha}$  and  $Mn - K_{\beta}$  peaks being visible.

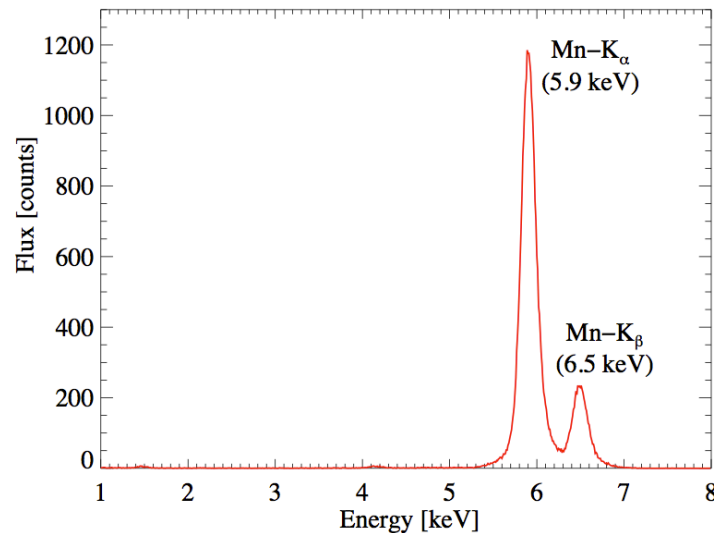


Figure 6-22 CAST CCD detector spectrum of  $^{55}\text{Fe}$  calibration source.

## 7. X-ray Telescope alignment

In June 2013 the pn-CCD detector was decommissioned and was replaced in 2014 with the InGrid detector developed at University of Bonn.

This new detector has better efficiency at lower energies favoured by the direction in which the CAST scientific program is heading. However the InGrid detector also makes use of the X-ray telescope used with the CCD detector. Extensive integration work has been done in 2014 to merge the vacuum systems and assure smooth and safe interoperation of the InGrid systems with CAST and XRT systems.

We took advantage of this opportunity to send the X-ray telescope back to PANTER for reflectivity and efficiency tests that were presented in Chapter 6.3 .

This meant that upon reinstallation the telescope had to be realigned with respect to the optical axis of the magnet bore.

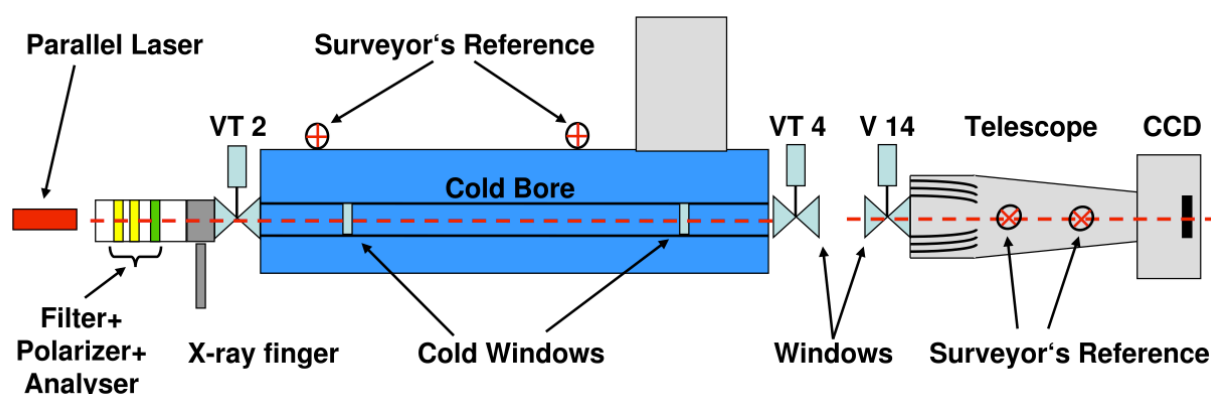


Figure 7-1 Schematic representation of the experimental setup for the XRT alignment

A schematic view of the experimental setup for aligning the X-ray telescope is presented in Figure 7-1. The alignment was conducted with the help of the CERN Survey group. For aligning the telescope one needs to shine a laser beam from the sunset side trough the optical axis of V1 beam line. This requires the sunset Micromegas detectors to be dismantled.

Then the magnet is levelled and parked in a standard horizontal and vertical coordinate where all the past alignments were done (H:20158 – V:26464).

The next step is for the geometers to align the T3000 theodolite with the optical axis of the V1 beam line using the magnet's coordinate system and the 2 crosshairs installed inside the beam pipe at both ends (see Figure 7-1 and Figure 7-2).

Then the ocular of the theodolite is replaced with a Wild GLO1 optical fibre mount used to inject a Thorlabs, 5 mW, linear polarised, 633 nm laser in the optics of the theodolite.

The advantage of this setup is that the laser can be projected and focused at specific planes using the optics of the theodolite. Then the XRT can be lifted with a crane and placed on its platform (Figure 7-2). Using a blind flange with crosshair target the XRT platform can be centred on the optical axis of the V1 beam by focusing the theodolite with the laser spot on that flange. After this step we know the upstream end of the telescope is on axis. Now the bellow can be installed and pumped down to simulate as much as possible the mechanical forces acting during normal data taking.

From the same considerations the entire XRT platform is loaded with 600-800 kg of lead plates to simulate the weight of the 2 detectors with shielding. This is important because I have determined using high precision digital inclinometers that the entire platform deforms with  $50\text{ }\mu\text{m}$  per each 100 kg of load added.



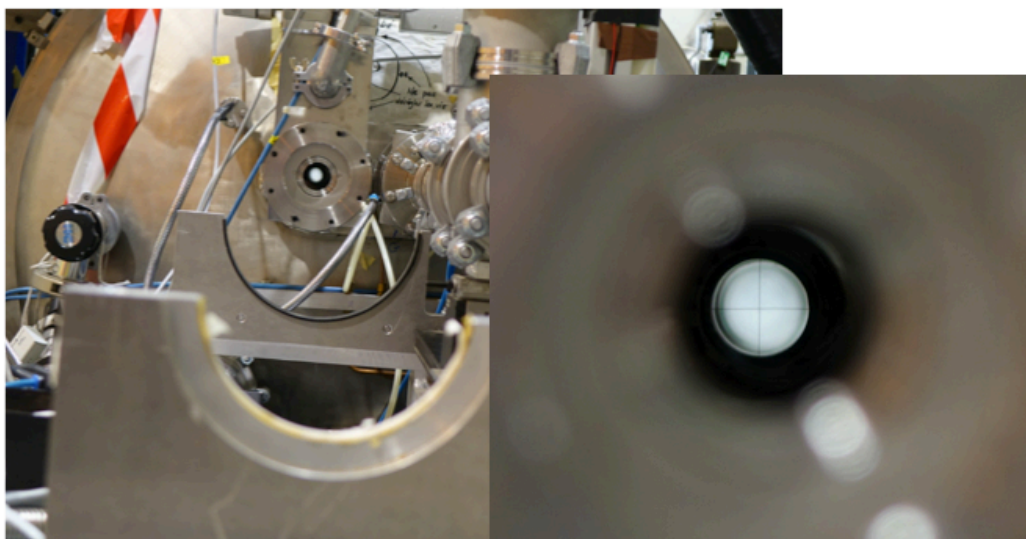


Figure 7-2 Left – View through the V1 Magnet bore from the point of view of the X-ray telescope dismantled at that time. The two mounting supports are visible in the lower part.  
Right – Zoomed view of the alignment crosshair found inside the V1 beam line of the magnet.

The next step is to install a self-centring precisely machined aluminium tube with a Plexiglas target with concentric rings placed in the focal plane of the telescope precisely where the detector would be (Figure 7-3). This tube is installed in the downstream of the XRT and before opening Gate-valve 13 (Figure 6-23) the tube needs to be cleaned, flushed with dry nitrogen and equalised in pressure with the telescope (PTV2).

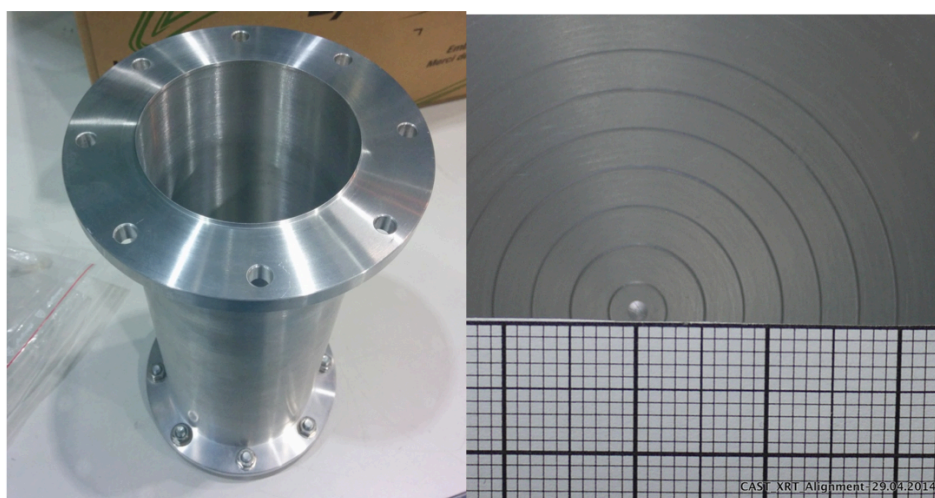


Figure 7-3 Left – The alignment tube used for aligning the XRT with the V1 beam line;  
Right – Plexiglas target found in the focal (detector) plane of the telescope, with mm paper for better reference.

Then the theodolite can be focused to infinity, thus expanding the laser spot to a diameter of 4 cm (the aperture of the theodolite) and filling the entire beam pipe. This collimated beam has the following path: the window of VT2 in sunset side, V1 magnet bore, window of VT4, bellow, window of V14, it enters the telescope and it is being focused on the Plexiglas target if the windowless V13 is opened.

The overall accuracy of this system taking into consideration the theodolite precision, and the mechanical tolerances ensures an alignment of the telescope with the magnet axis better than 40 arcsec.



If the telescope is on the same axis with the magnet and the theodolite one should get a symmetric spot in the centre of the target.

In April 2014 the spot was not centred and homogeneously distributed (Figure 7-4 Left) so the platform holding the XRT had to be tilted from the adjustment screws.

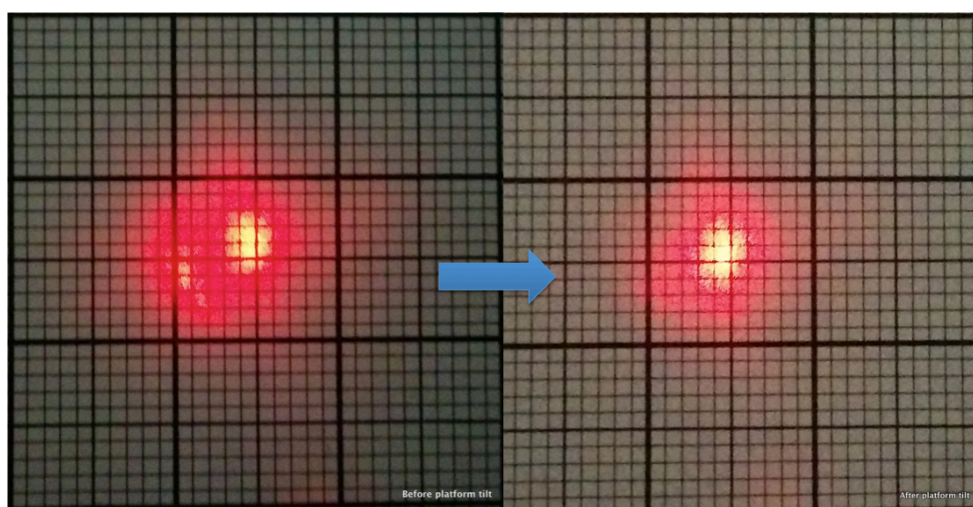


Figure 7-4 X-ray telescope laser alignment spot on the Plexiglas target overlaid with mm paper;  
Left – Spot before platform tilt;  
Right – Spot after the platform tilt.

The method I used to find the angle and the direction needed for the tilt was to systematically introduce an angle on the laser beam from the theodolite until I got a centred homogeneous spot on the alignment target (Figure 7-4 Right). In total 56 tilt points measurements were taken in steps of 0.005 degrees in  $x$  and  $y$  axis, positive and negative.

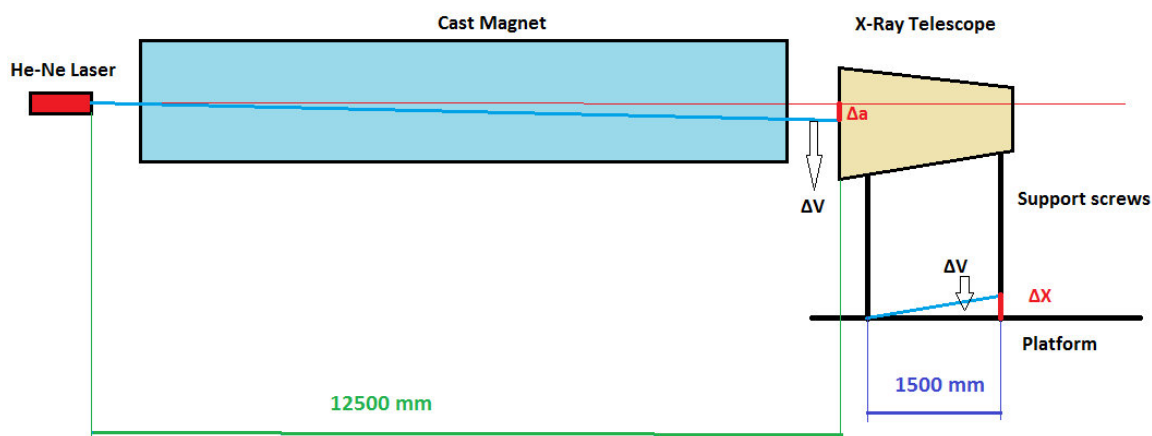


Figure 7-5 Principle of XRT alignment from 2014.

The best spot shape was obtained for a deflection of  $\Delta V = 0.0178^\circ = 0.311 \text{ mrad}$  introduced to the laser beam towards the floor of the experimental area. Applying tangent to this angle I got the value of  $\Delta X = 0.466 \text{ mm}$  needed to raise the telescope from the downstream end (Figure 7-5). After this tilt the spot was corrected as seen in Figure 7-4 from left to the right side.

In August 2014 after returning once more from PANTER where it was checked for silicone grease contamination of the vacuum system the telescope needed no tilt adjustment.

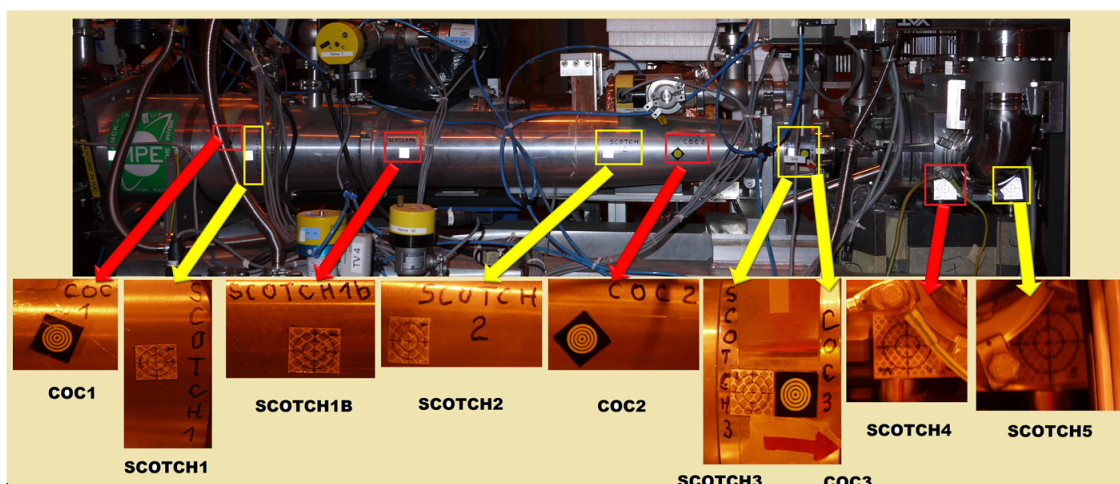


Figure 7-6 XRT survey targets for long-term alignment checks.

For long term stability check of the external shell of the CAST X-ray telescope, a series of survey targets glued on the aluminium housing are periodically surveyed and the position in three dimensional space is monitored with a precision of 0.3 mm.

Usually these measurements are taken twice a year and depending on the magnet temperature and position, pressure in the system and platform load, trends are visible (Figure 7-7).

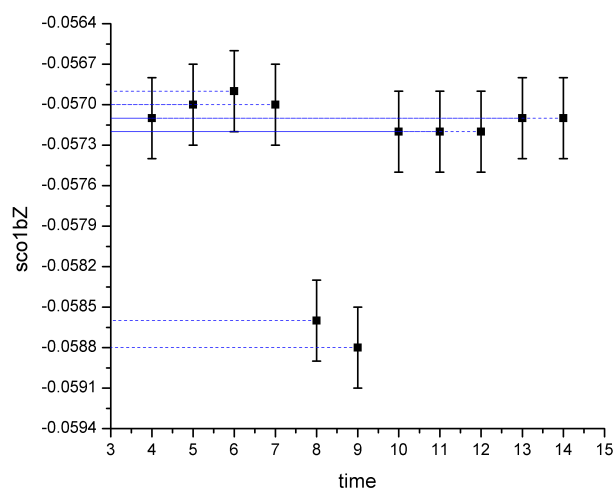


Figure 7-7 Z Coordinate variations of the SCOTCH1B survey target in mm.

Measurements 8 and 9 correspond to 12-02-2012 with the CCD-XRT vacuum system at atmospheric pressure and MRB side loaded with 450 kg of additional lead. A negative deflection in Z axis corresponds to a deformation in the platform towards the floor.

---

## 8. CCD alignment analysis

---

Following the same philosophy as for the X-ray telescope, in the case of the CCD chip the alignment process can be separated into the initial mechanical centring of the vacuum chamber and CCD chip on the focal spot of the telescope and then the long term monitoring of the alignment by checking the stability of the pixel coordinates from the focal spot.

The initial mechanical alignment I will not cover here since it was done before I Started my experimental work at CAST.

Long-term stability checks were done with laser illumination and with a pyroelectric X-ray source.

---

### 8.1. The Laser Runs

---

Laser runs are difficult to realise because they require the sunset detectors to be dismantled and were only conducted at the end of 2012 data taking season. The laser was aligned and injected in the same way as for the alignment of the telescope described in the previous chapter. The T3000 theodolite was aligned with the optical axis of V1 beam line and the laser was injected with the WILD GLO1 optical fibre ocular adaptor using the optics of the theodolite.

The main difference from the XRT alignment was the use of polariser filters to reduce the optical intensity reaching the CCD chip.

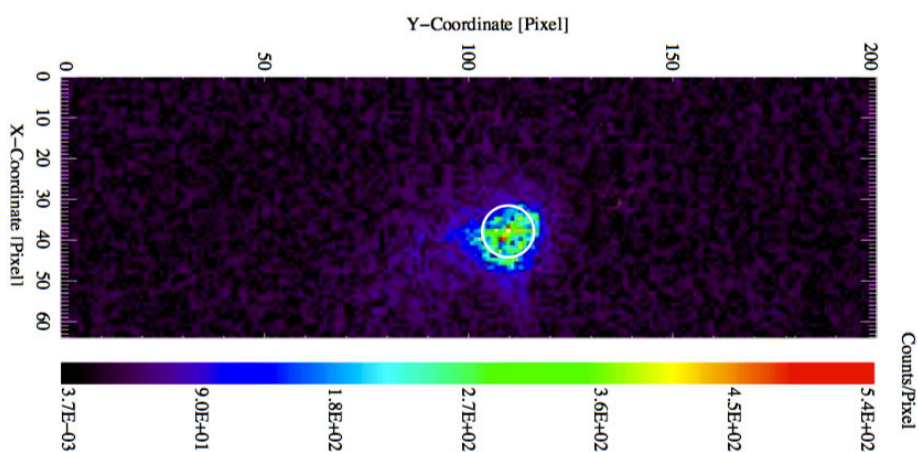


Figure 8-1 Laser run spot on the CCD chip;  
Spot coordinates must coincide with the X-ray finger runs.

Marked on the picture is the size of the projected footprint of 25% of the solar disk on the chip. The image was obtained by integrating 500 frames at a polarizer angle of  $10^\circ$  with ND5 filters. The laser was focused at infinity so that the collimated laser beam fill the entire cold bore and was focused by the mirror module on the CCD.

In the past studies were conducted for determining the effects of He gas inside the beam pipe and the effects of the cold windows by adding one additional window in place. The spot position was determined to be independent of the rotation and tilt of the extra window and the intensity of the laser as long as the entire magnet bore is illuminated.

Furthermore a linear behaviour of the X-ray optics was demonstrated between the observed laser spot on the chip and the off-axis angle of the laser in vertical and horizontal directions [102].

## 8.2. X-ray Finger Measurements

A pyroelectric X-ray source mounted on a manipulator retractable arm on the sunset platform (see Figure 7-1) is the main tool of checking the long-term alignment and stability of the spot coordinates on the pc-CCD detector of CAST experiment.

The main advantage of this setup is that it does not require the dismantling of the sunset detectors as the laser alignments do. Another benefit of using a pyroelectric source instead of a radioactive one is that it can be electrically switched off and parked off axis in a shielded position so that there is no impact on the background levels of sunset Micromegas detectors.

The stepper motor is controlled via a serial interface and has a precision of 0.01 mm. Repeatability of the movement relative to the V1 beam optical axis was confirmed by the geometers.

Since 2010 I had to replace twice the source due to low count rates originating from the limited life time of the sources. The interventions were complex due to complicated vacuum connections, cleanliness requirements, fragile and extremely toxic beryllium window of the source and tolerances of the mechanical assembly. After each intervention a new reference position was determined with the help of geometers by placing the source as close as possible to the V1 beam axis. However these adjustments can be done from the stepper motor only in horizontal directions. In the vertical axis and the rotation of the source must be aligned as close as possible when installing the source before tightening the mounting screws and the CF vacuum flanges.

The source used is a miniature Amptek Cool-X, X-ray generator which uses a pyroelectric crystal to generate energetic electrons that produce X-rays in a copper target. The source is a capsule 15 mm in diameter, hermetically sealed with a thin beryllium window transparent to X-ray photons.

Internally the crystal is thermally cycled and in the heating phase the crystal experiences a sudden decrease in polarization. The high surface positive potential attracts electrons from the low pressure gas inside the capsule, Ta and bremsstrahlung X-ray photons being generated by the crystal.

In the cooling phase the spontaneous polarization of the crystal increases, and the electrons are accelerated towards the copper target found at ground potential (Figure 8-1 - left).

The cycle period is about 3-4 minutes and the source can achieve a peak flux of  $10^8$  photons per second having a power requirement lower than 300 mW.

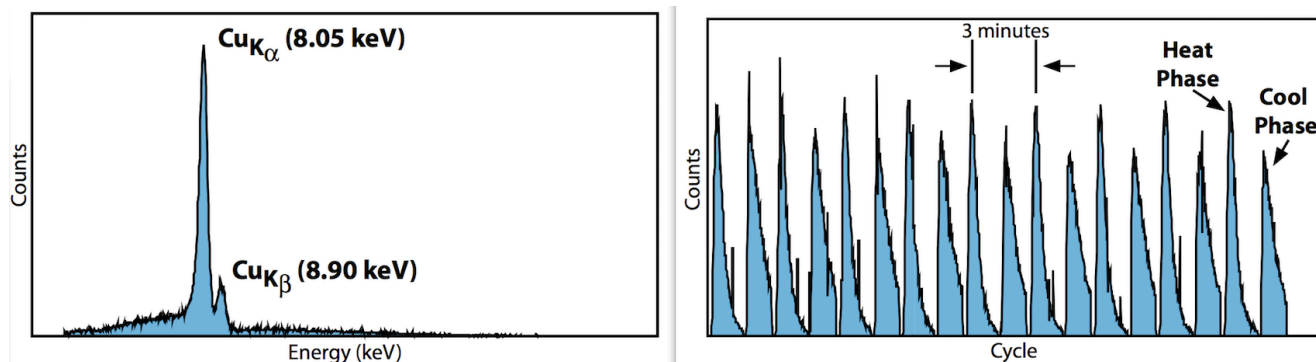


Figure 8-2 X-ray finger source from Amptek

Left- Cooling phase spectrum; Right- The output flux in cyclic emission during heating and cooling. [103]

The peak radiation at a distance of 10 cm is approximately 5 mSv/hour with 75% of the photons being below 10 keV. However one downside of this source is the limited lifetime. If used continuously the lifetime is approx. 200 hours and with 1-3 hours cycles can reach 1000 hours. In CAST the source was used in runs of 10 hours up to 6 times a year so they had to be replaced once every 2 years as a precautionary measure.

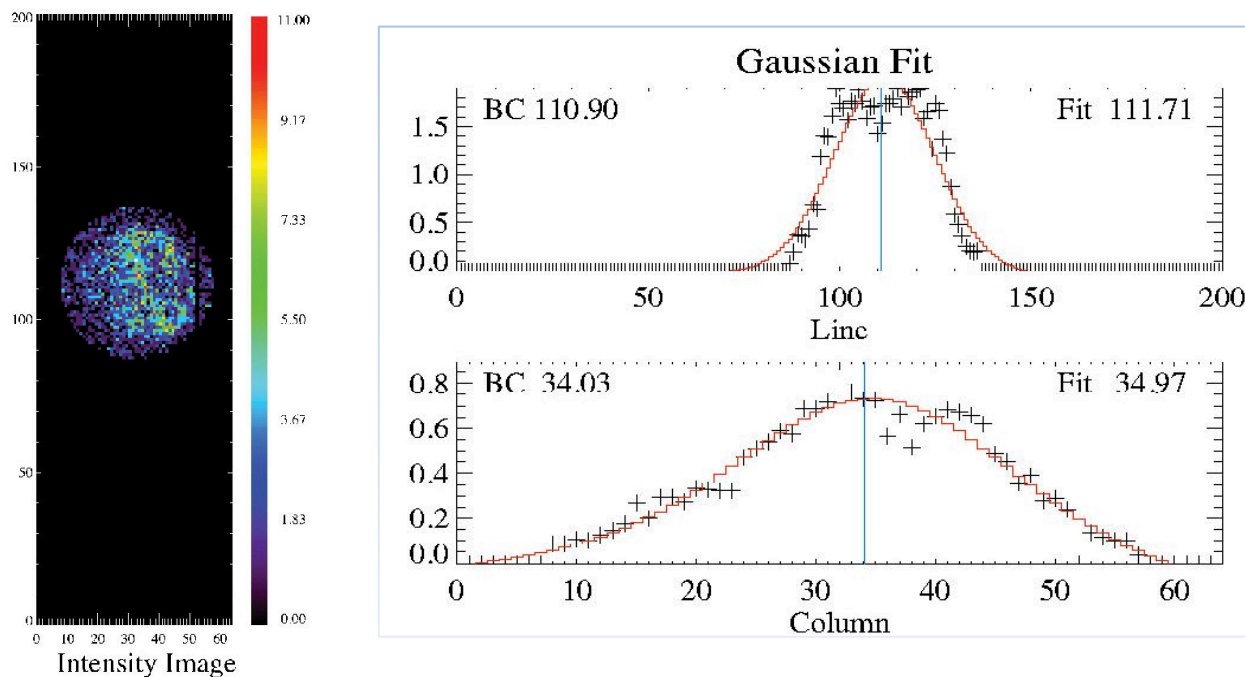


Figure 8-3 Left – CCD spot image of the X-ray Finger Run (05) from 03.12.2009;  
Right – Gaussian fit of the circular envelope of the intensity distribution for determining the spot coordinates.

The overall pointing precision of CAST's tracking system is considered to be better than 1 armin ( $\approx 0.017^\circ$ ) and the entire magnet bore allows a field of view of approx. 16 arcmin ( $\approx 0.27^\circ$ ).

The measurements made in 2009-2012 (and those made in 2005-2007) confirm that the experimental setup has a long term spot stability better than a pixel meaning better than 20 arcsec which is remarkable given the ever-changing mechanical vibration and stress the entire structure cycles through daily when tracking the Sun.

The final spot coordinates are extracted from the analysis of laser runs and X-ray finger runs. One might observe when comparing Figure 8-1 and Figure 8-2 significantly different spot sizes. This is due to the fact that the X-ray finger source is at a finite distance from the mirror module thus changing the grazing angle incidence. This results in the focusing of the 8 keV photons on a plane 30 cm behind the pn-CCD and forms a larger spot on the sensor.

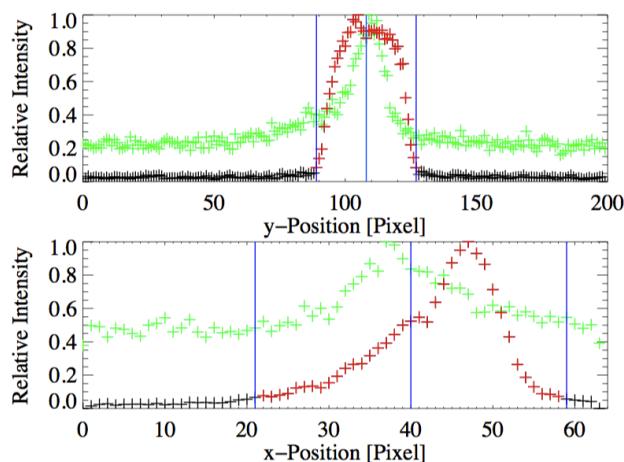


Figure 8-4 Typical demonstration of analysis for determining the centre coordinated of the Signal Area [102] by overlaying the laser alignment data (green crosses) and the X-ray finger data (red crosses for intensities higher than 7% of the maximum value). Blue lines indicate the circular envelope of the signal area.



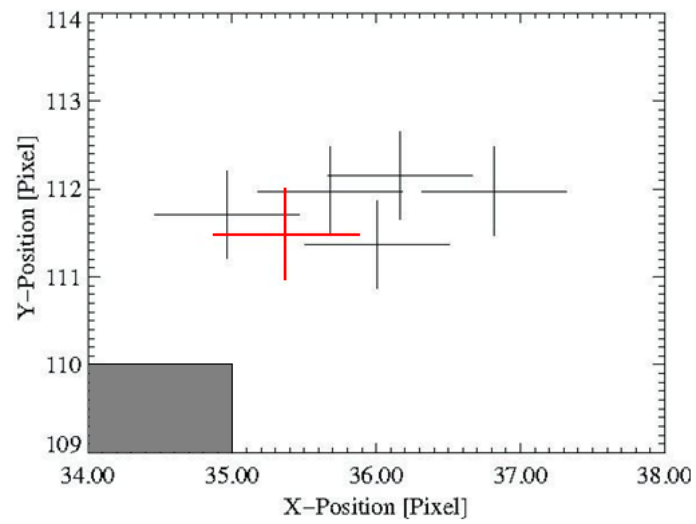


Figure 8-5 Coordinate stability of the Signal Area for 2009-2012.  
Red cross is the coordinate considered in the Data Analysis and it was stable within the tolerance of one pixel.



---

## 9. CCD data analysis

---

The CAST experiment has four main detectors coupled to the ports of the two magnetic cold bores. Two of them are sensitive to solar Axions in the morning up to 45 minutes before and 45 minutes after sunrise and the other two are sensitive 45 minutes before and 45 minutes after sunset. In the rest of the time the detectors take pedestral, calibration, background and dark-runs.

The pn-CCD detector was operated in the 2009-2012 interval by an autopilot that automatically did the following operations daily when the detector was not operated in manual mode:

- Based on a time table calculated for Geneva coordinates and altitude the Data Acquisition System (DAQ) Started a new acquisition run for that specific day 10 minutes before the Sun was at  $-8^\circ$  below the horizon;
- First run of the day was a Dark Run of 200 frames lasting about 14 seconds at the standard exposure and readout cycle of 72 ms is taken with valve V13 closed (Figure 6-17) and Run ID 00;
- Then the autopilot operating a compressed air manipulator, brings from a shielded position in the field of view of the CCD a  $^{55}\text{Fe}$  calibration source, and opens V13;
- A calibration run of 3500 frames (4 minutes) is taken with Run ID 01;
- The calibration source is retracted in the shielded position;
- Continuous data taking mode is engaged by taking 89 files each containing 12550 frames. This sums up to 15 minutes files and a total of 22 hours.
- After these 89 files the DAQ stops and waits for the Dark Run of the next morning.

Having this system in place in the days when a valid tracking took place the first six files of the day (90 min) covering all the tracing time were used for the Quick Look Analysis to provide the collaboration with almost real time feedback on the status of the data and the detector performance.

I have conducted these daily Quick Analysis reports from October 2009 until the end of the data taking with the CCD detector in 2012.

Each day with a successful morning tracking the Quick Look Analysis was done for the first 6 files of the day, together with the dark run and the calibration run. Important detector parameters like raw spectra, noise and offset maps, calibration spectra, light curves and event RGB images. Doing this one ensures the correct operation of the detector and can take measures to correct possible interferences like electrical noise and light leaks.

Also before the noon of each tracking day a report containing the counts inside the spot and the counts on the rest of the chip together with time stamp, energy and pixel coordinates was sent to an emailing list. These reports together with the reports from the other detectors were used in a protocol to determine if the pressure setting should be repeated. In the case of a number of events higher than expected the run coordinator can request the rescanning of that particular pressure setting. This protocol is based on Monte Carlo simulations to eliminate candidates and more details can be found in [104]. As general practice, CAST spends about 5% of the data taking period investigating pressure settings multiple times.

Moreover after checking of the tracking run which corresponds to the first six files of the current day, the entire previous day is checked (89 files each containing 15 min of data) for the same performance parameters and eventually if needed certain files are flagged and excluded from the analysis (Figure 9-1).

Data set(s): /archive/prc/cast/100510/C09\_32\_15\_100510\_02050/dark/cal.fits  
 2010-05-10T15:55:10.845 .. 2010-05-11T06:21:58.000  
 cast / 100510  
 Number of frames per image: 12570  
 Overall minimum .. maximum: 3.8 .. 12.1

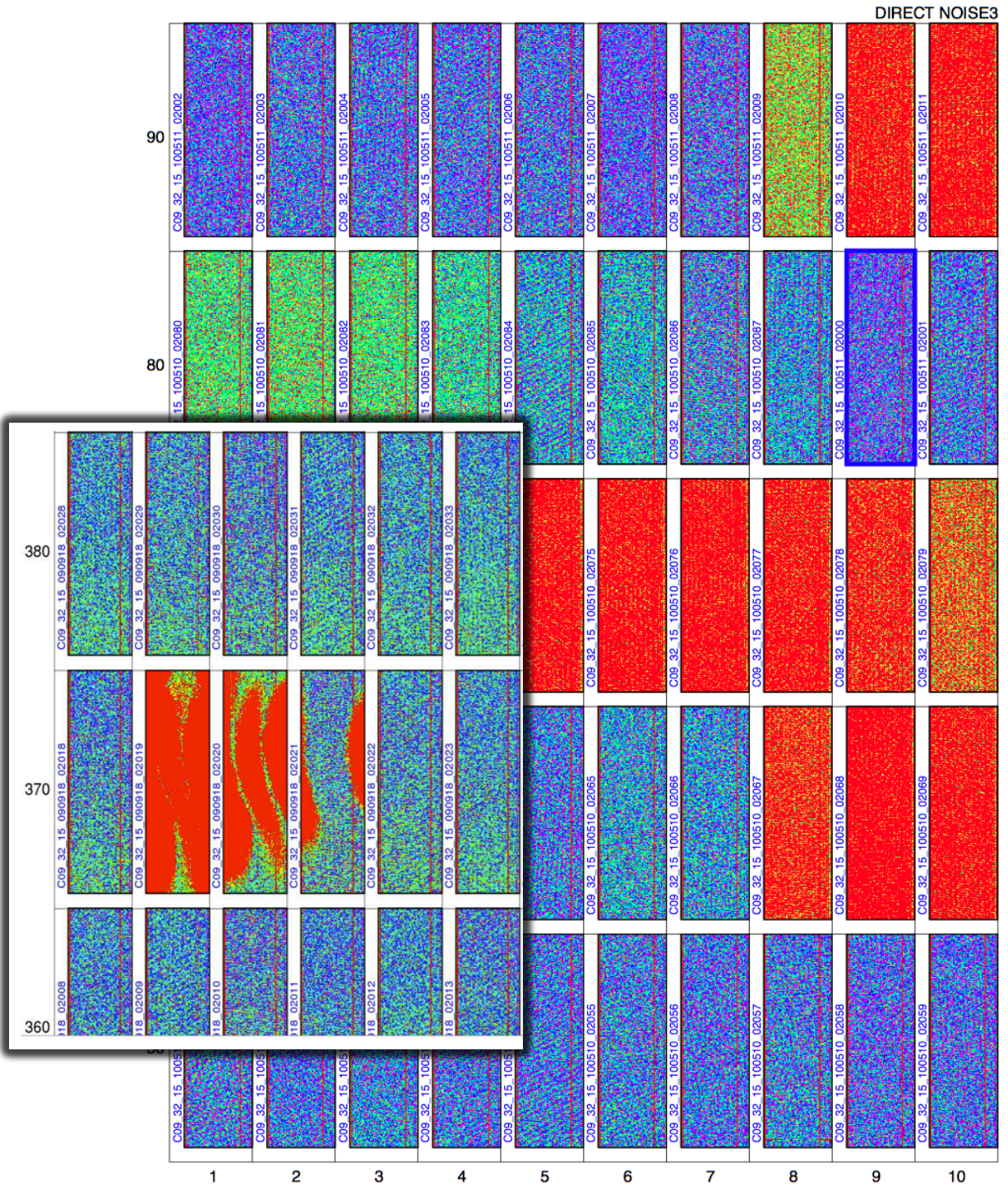
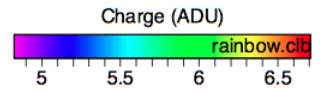


Figure 9-1 Left – Example of pn-CCD detector light contamination due to the angle the magnet did with the Sun light;  
 Right – Examples of electrical noise from May 2010.



# FITSUM

Fe55

Fit range (keV): 4.5000 7.0000

Number of data points: 781

Number of parameters: 15

Number of free parameters: 12

Chi Square (total/reduced): 825.038 1.077

Goodness of fit: 7.889E-02

Area: 2.88 cm\*\*2

Integration time: 251.2 s

Peak Position: 994.0 ADU / 1615.1 e1 / 5895.1 eV

FWHM: 32.3 ADU / 52.5 e1 / 191.8 eV ( -96.5 eV, 95.3 eV )

Peak-to-Valley-Ratio: 45.5 : 1

Peak-to-BGR-Ratio: 246.2 : 1

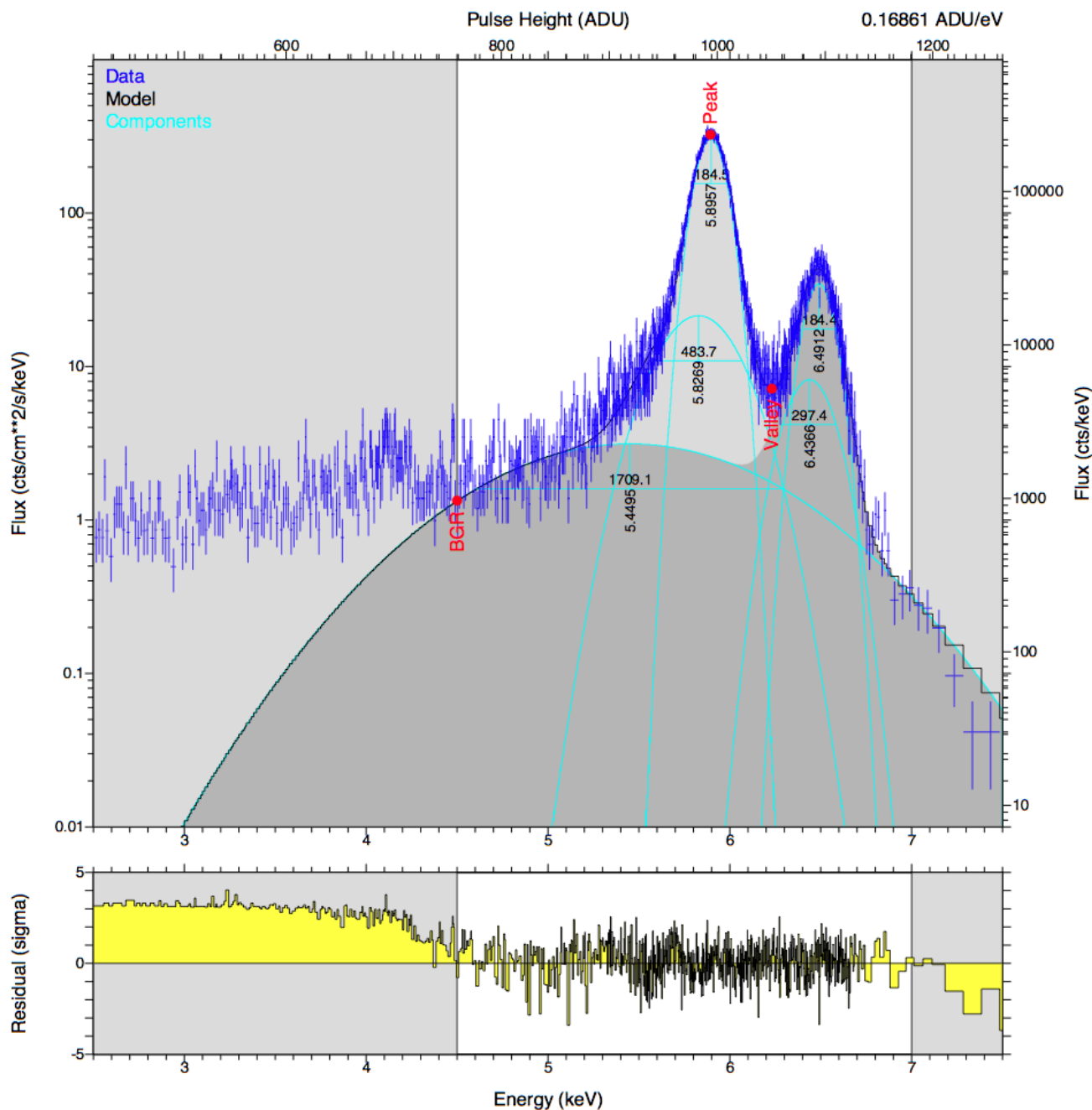


Figure 9-2 Spectral fit of an Energy Calibration Run of CAST pn-CCD detector taken on 18-07-2011 with an <sup>55</sup>Fe calibration source.

9.1. 2009

In 2009 the CCD detector covered 114 solar tracking runs out of a total of 132, summing up to a total of 167 hours and 27 minutes of Axion sensitive exposure. The following pressure settings were not covered by the CCD: 466->480, 510->5011, 558->562, 583->584, 604->614. The total detector livetime for that season was 132.47 days and an integrated full energy range exposure is presented in Figure 9-3.

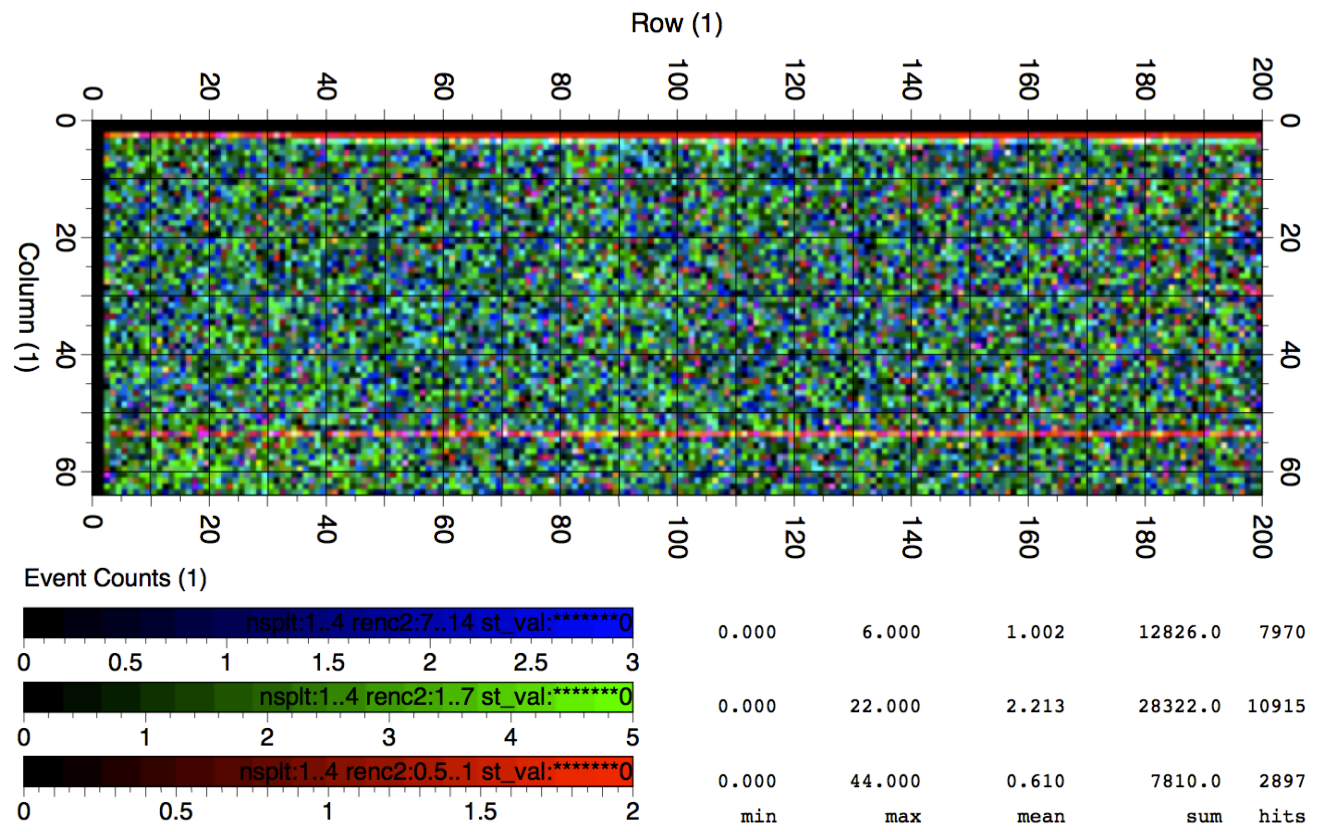


Figure 9-3 TOP - Full Energy true colour event Image of all valid events integrated over the entire detector livetime of 2009 season (13.07.2009 – 12.12.2009);  
Bottom – Energy range colour coding and statistics (red 0.5 – 1 keV, green 1 – 7 keV, blue 7 – 14 keV).

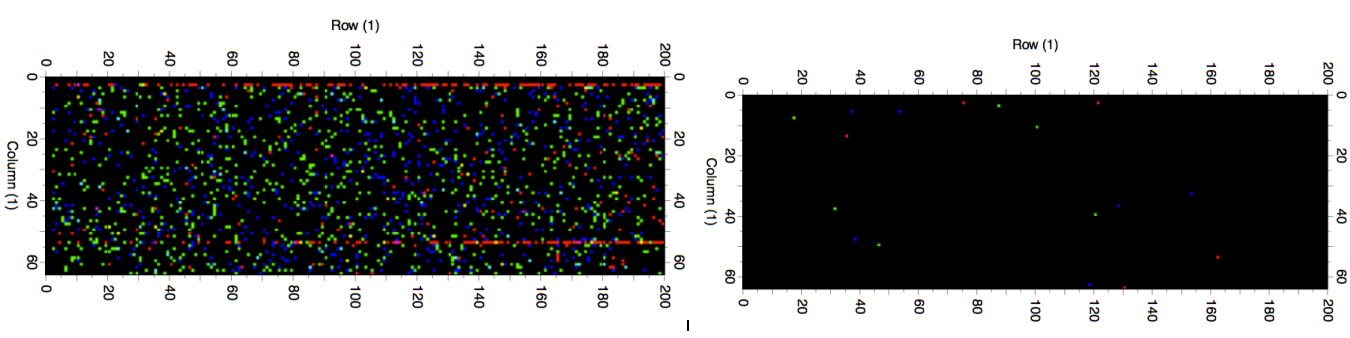


Figure 9-4 Tracking vs. Background event distribution (green for 1-7 keV scale);  
Left – Full energy range exposure for week 40 year 2009;  
Right – Event distribution from the tracking run of 02-10-2009.

2009

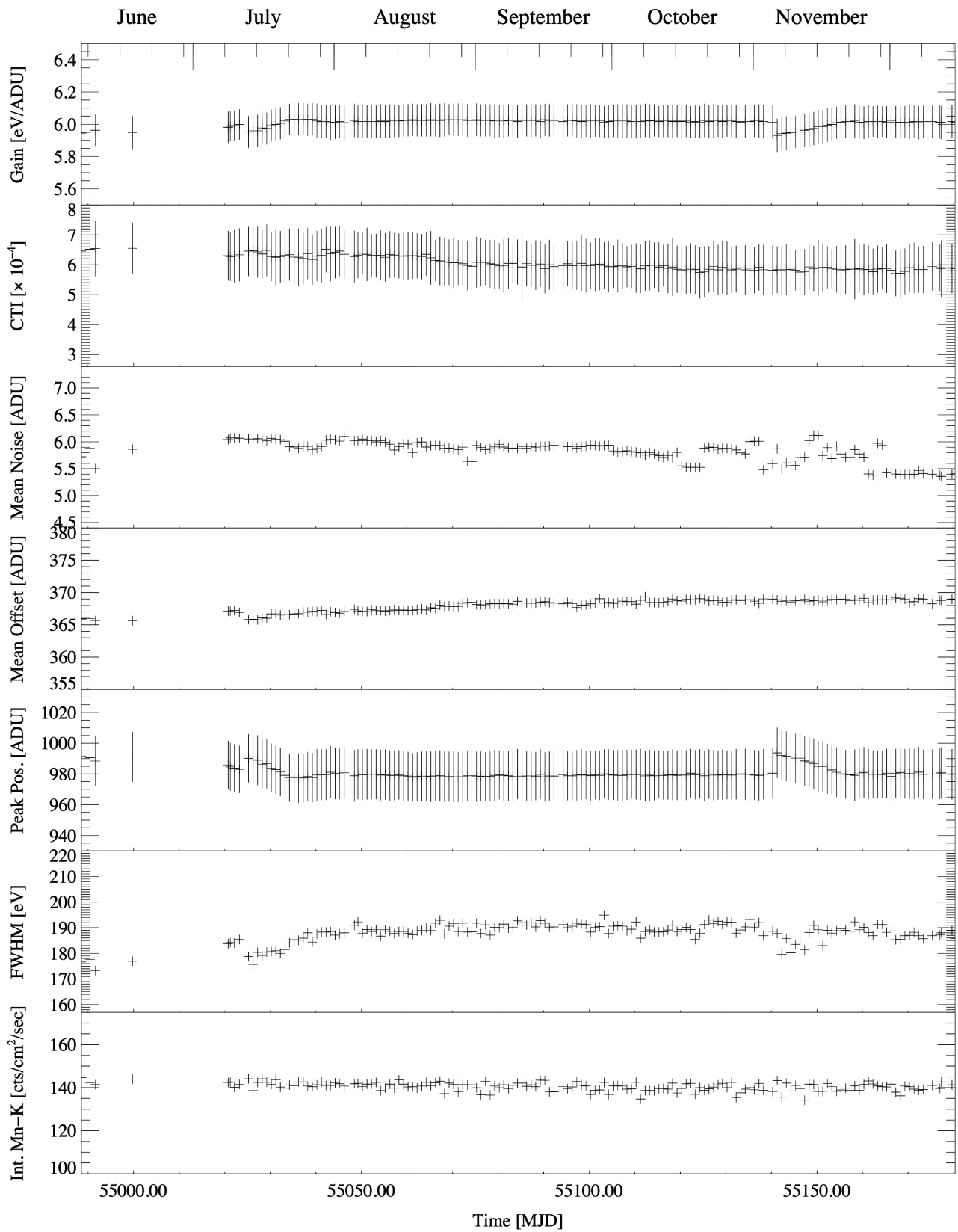


Figure 9-5 Stability of the pn-CCD detector during the 2009 data taking period based on daily <sup>55</sup>Fe calibrations.

Fit range (keV): 0.9000 15.0000  
 Number of data points: 353  
 Number of parameters: 52  
 Number of free parameters: 52  
 Chi Square (total/reduced): 432.164 1.436  
 Goodness of fit: 1.028E-06

Area: 2.88 cm\*\*2  
 Integration time: \*\*\*\*\* s

Peak Position: 1342.4 ADU / 2209.0 e1 / 8062.8 eV  
 FWHM: 45.8 ADU / 75.3 e1 / 274.9 eV ( -139.1 eV, 135.8 eV )  
 Peak-to-Valley-Ratio: 13.5 : 1  
 Peak-to-BGR-Ratio: 13.6 : 1

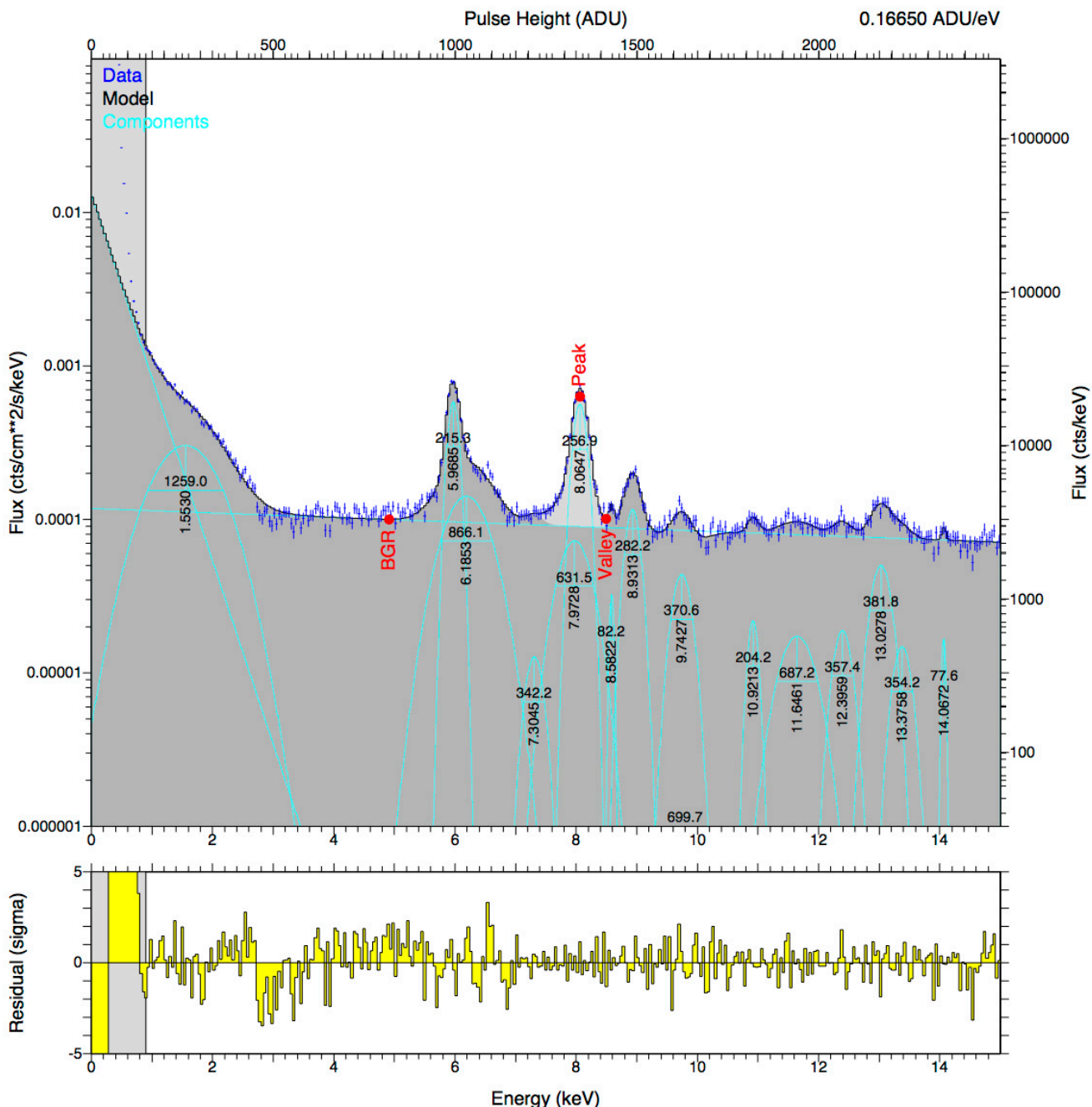
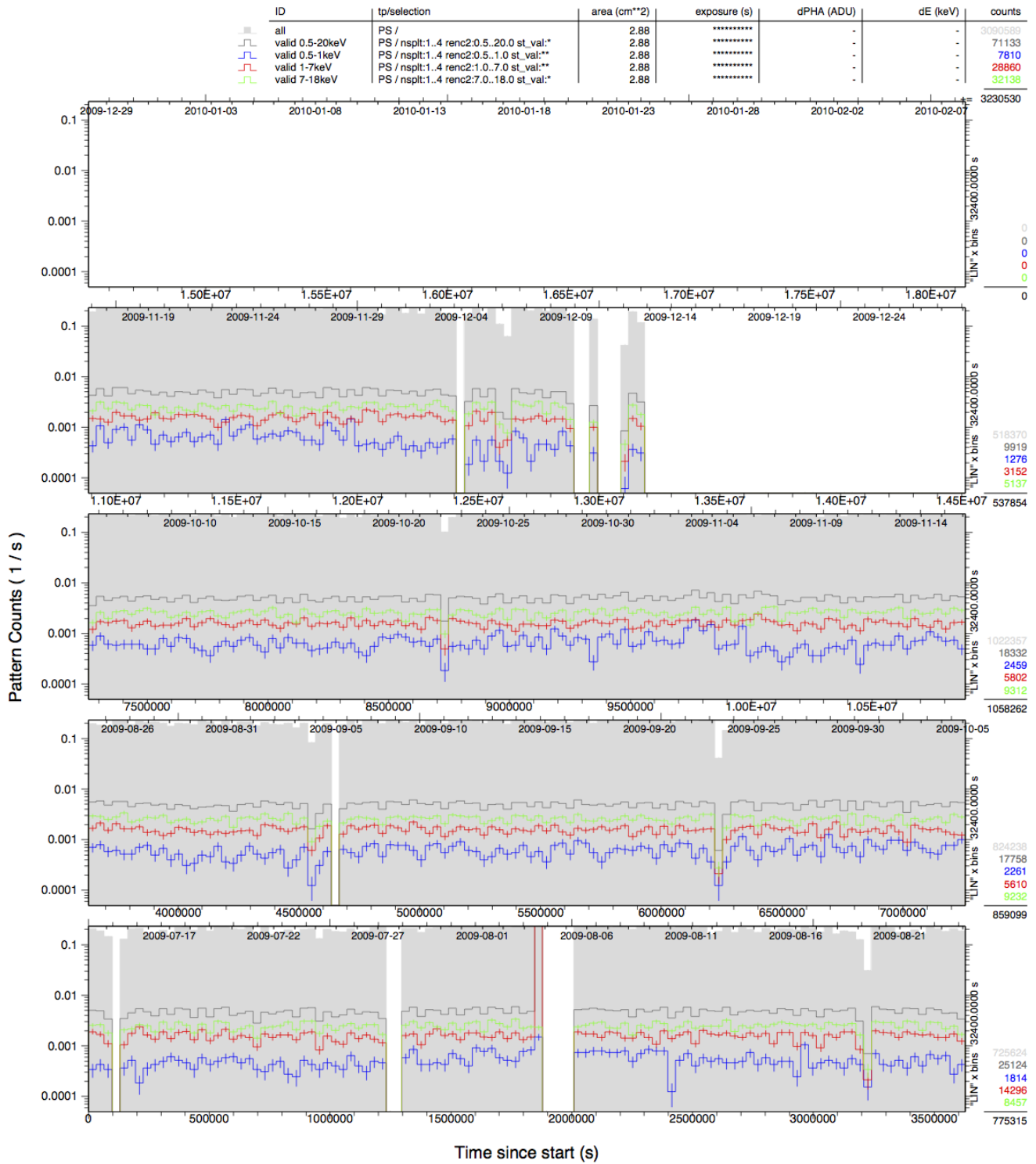


Figure 9-6 Background spectral fit of 2009 CCD data.  
 The Flux in  $\text{cts/cm}^2/\text{s/keV}$  is plotted versus energy for the range 0.9 – 15 keV



## Lightcurves

2009-07-13T03:06:41.845 .. 2009-12-12T14:09:10.656  
Event file: sel-basic.fits



---

In Figure 9-4 then the homogeneous distribution of background events can be seen in the week long exposure and on the right hand side no signal is detected in the focal spot of the telescope that has been determined to be at 35.5 and 111 with 11.5 pixels in radius (Figure 8-5).

The plot from Figure 9-5 is very important for estimating the long term performance stability of the detector. The parameters plotted there over the entire time of the data taking period are extracted from the fit of the  $^{55}\text{Fe}$  calibration runs taken each morning (see Figure 9-2). The gaps indicate times the experiment was in technical shut down and/or times when the CCD detector system was offline for maintenance.

From top to bottom are shown the detector gain, charge transfer inefficiency, the mean noise and offset both averaged over the entire chip, peak position of  $Mn - K_{\alpha}$  line, its FWHM and its intensity.

The time axis is both coded in standard Universal time and Modified Julian Day.

In Figure 9-6 the background rate of the 2009 data is plotted. Considering the energy range for Axion search 1-7 keV a typical mean normalised count rate over the hole sensitive area of the detector is  $(2.39 \pm 0.02) \times 10^{-4} \text{cts/s/keV}$  which corresponds to a mean differential flux of  $(8.66 \pm 0.06) \times 10^{-5} \text{cts cm}^{-2} \text{s}^{-1} \text{KeV}^{-1}$ . If one considers only the signal area of 23 pixels in diameter a mean background rate of 0.175 counts per hour is expected. In the 2009 data, there are 31 events in the spot registered in 167.5 hours of tracking yielding a count rate compatible with the background of 0.185 counts per hour.

In the background spectra can also be identified  $Au - M_{\alpha}$ ,  $Au - L_{\alpha}$ ,  $Au - L_{\beta}$  lines from the gold plated mask, and lead peaks from the soldering compound, namely  $Pb - L_{\alpha}$ ,  $Pb - L_{\beta}$ .

Below 7 keV a quasi-flat Compton continuum formed of mainly backscattered photons can be observed.

The lightcurve in Figure 9-7 is useful in checking the evolution of the count rate in certain energy ranges of the detector over the entire 2009 data taking period. Together with the long term stability plot based on the calibration data one can see the detector acquired good quality data over the entire 2009 run.

From 2009 data, the tracking times and events were extracted, together with the background levels in  $\text{cts/cm}^2/\text{s}$  in 0.5 keV binning. This data, which can be found in Annex 1, has been handed over to Zaragoza team for further statistical treatment and integration with the other detectors with the scope of generating a combined exclusion plot for the entire CAST experiment.

However the count rate outside the spot being compatible with the count rate inside the spot in Axion sensitive conditions I conclude that no solar Axion signal has been observed above background with the CCD detector in 2009.

The same holds true for 2010 and 2011 data for which I will show the same plots as for 2009.

2010 tracking and background data can be found in Annex 2.

2011 tracking and background data can be found in Annex 3.

## 9.2. 2010

In 2010 the CCD detector covered 110 solar tracking runs out of a total of 125, summing up to a total of 171 hours and 29 minutes of Axion sensitive exposure. The following pressure settings were not covered by the CCD: 704->728.

The total detector livetime for that season was 168.04 days and an integrated full energy range exposure is presented in Figure 9-8 .

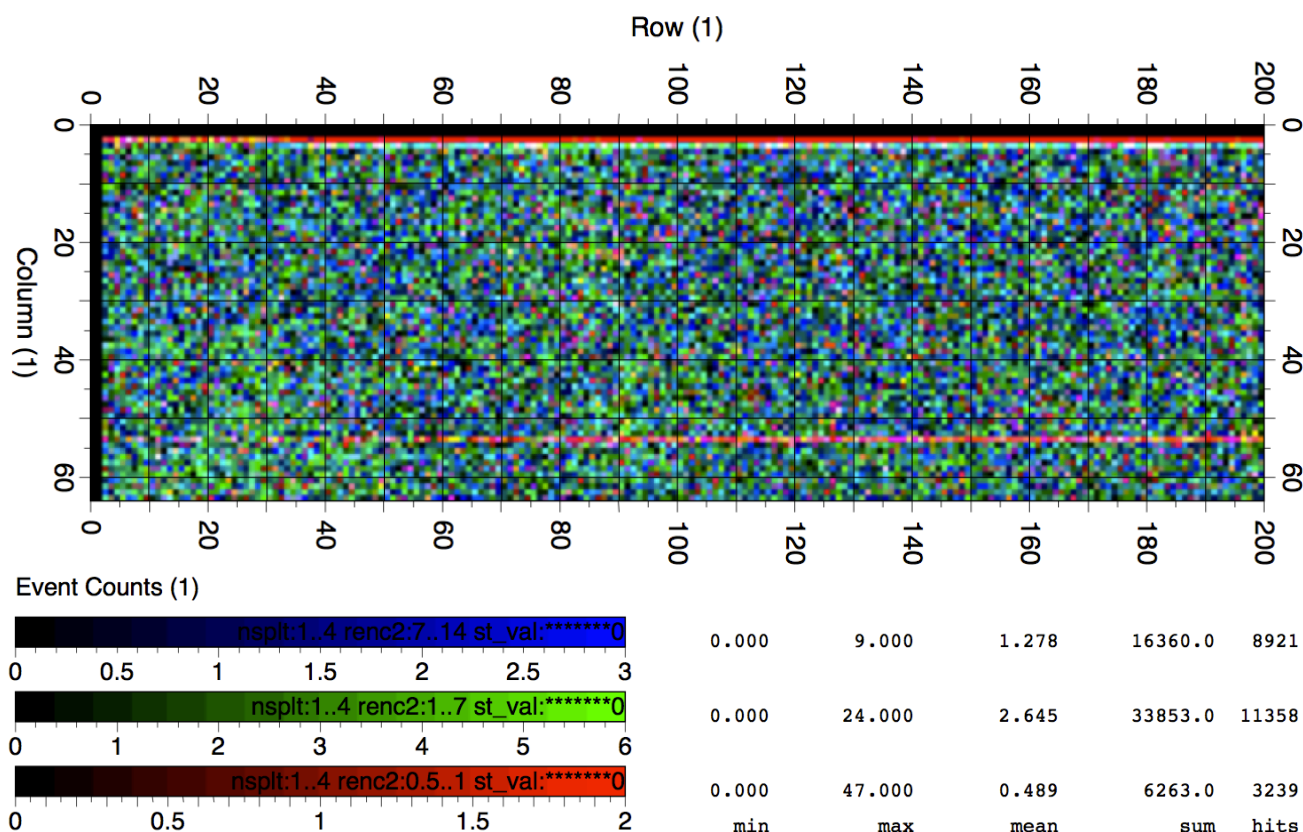


Figure 9-8 TOP - Full Energy true colour event Image of all valid events integrated over the entire detector livetime of 2010 season (03.05.2010 – 17.11.2010);  
Bottom – Energy range colour coding and statistics (red 0.5 – 1 keV, green 1 – 7 keV, blue 7 – 14 keV).

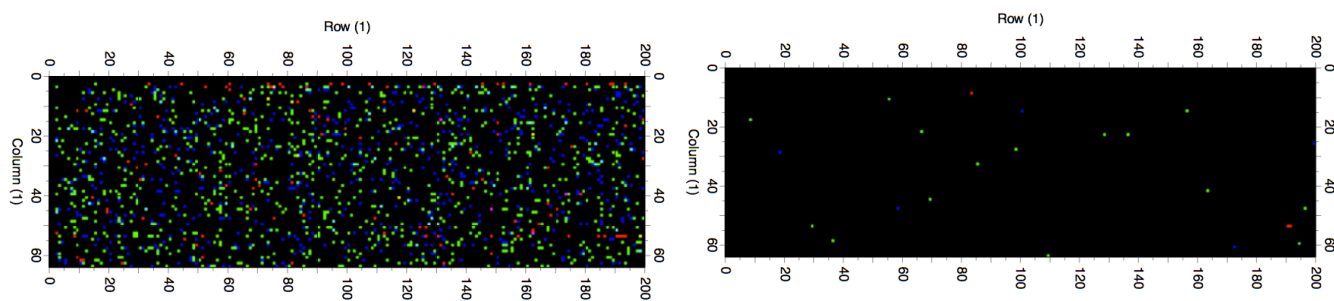


Figure 9-9 Tracking vs. Background event distribution (green for 1-7 keV scale);  
Left – Full energy range exposure for week 33 year 2010;  
Right – Event distribution from the tracking run of 21-08-2010.

2010

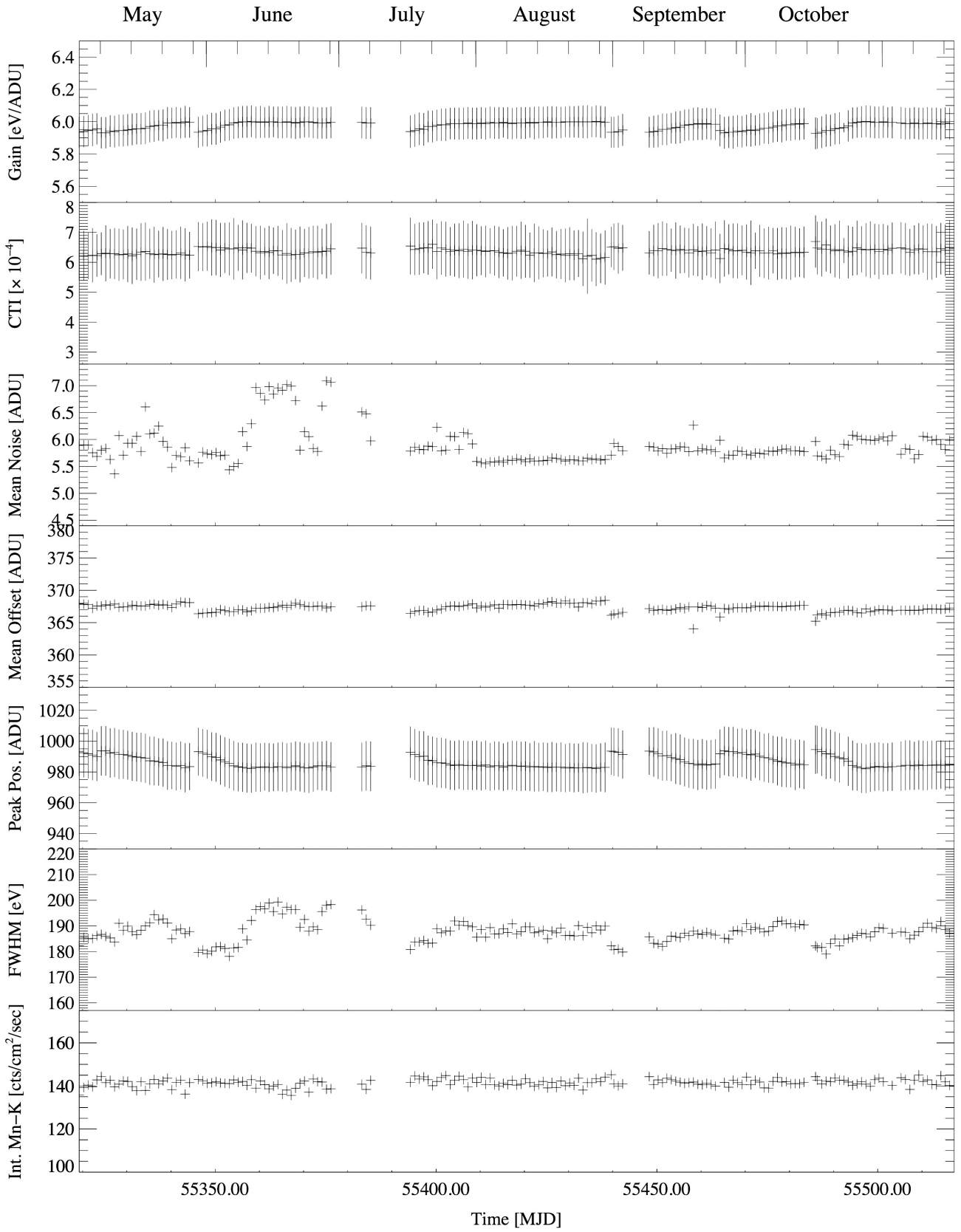


Figure 9-10 Stability of the pn-CCD detector during 2010 data taking period based on daily  $^{55}\text{Fe}$  calibrations. Blank spaces represent detector down times.

2010-05-03T03:34:06.845 .. 2010-11-17T16:41:48.518  
Event file: basic.fits

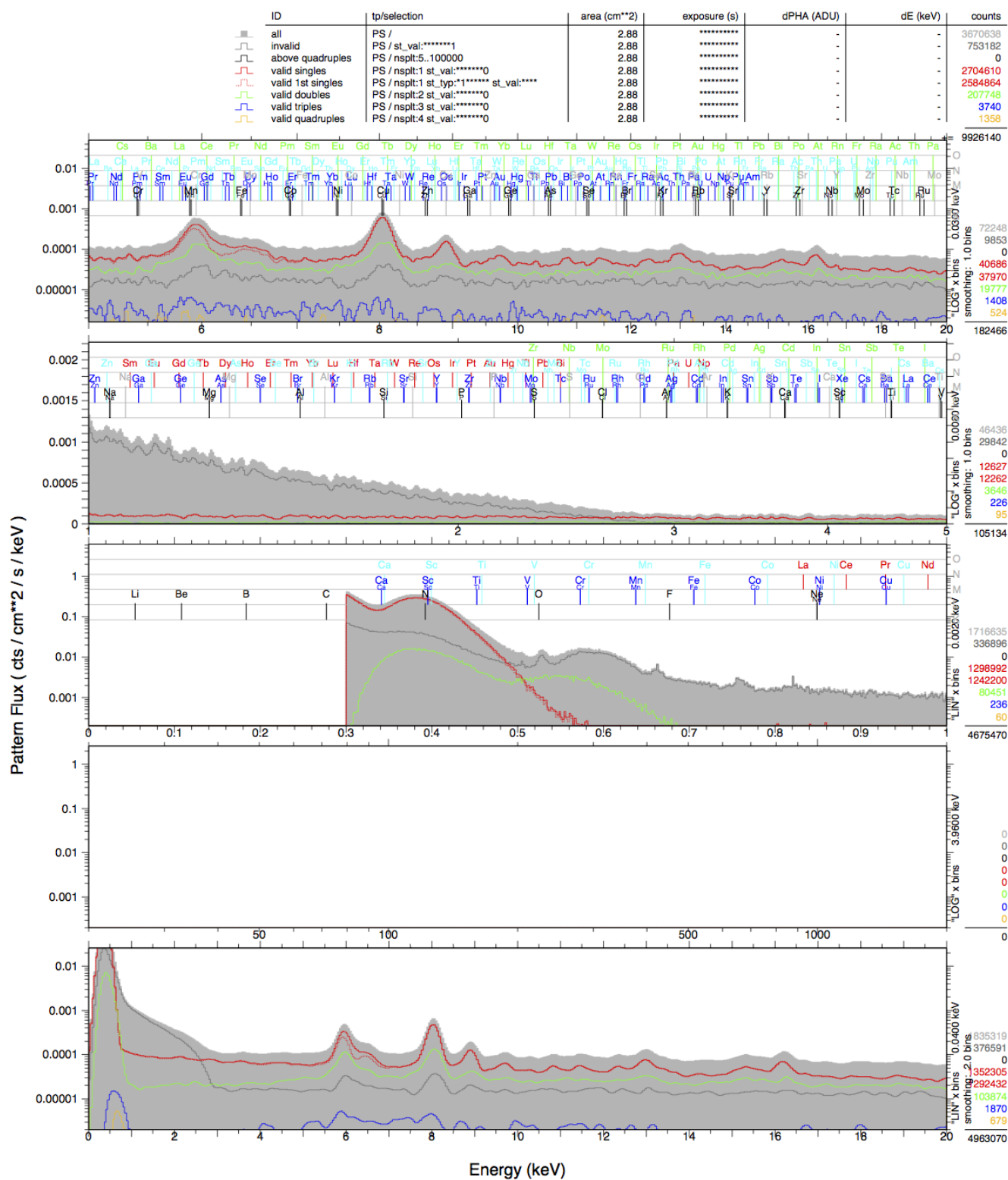


Figure 9-11 Background energy spectra for 2010 CCD data.  
The Flux in cts/cm<sup>2</sup>/s/keV is plotted versus different energy ranges 0.4 – 20 keV.



## Lightcurves

2010-05-03T03:34:06.845 .. 2010-11-17T16:41:48.518

Event file: sel-basic.fits

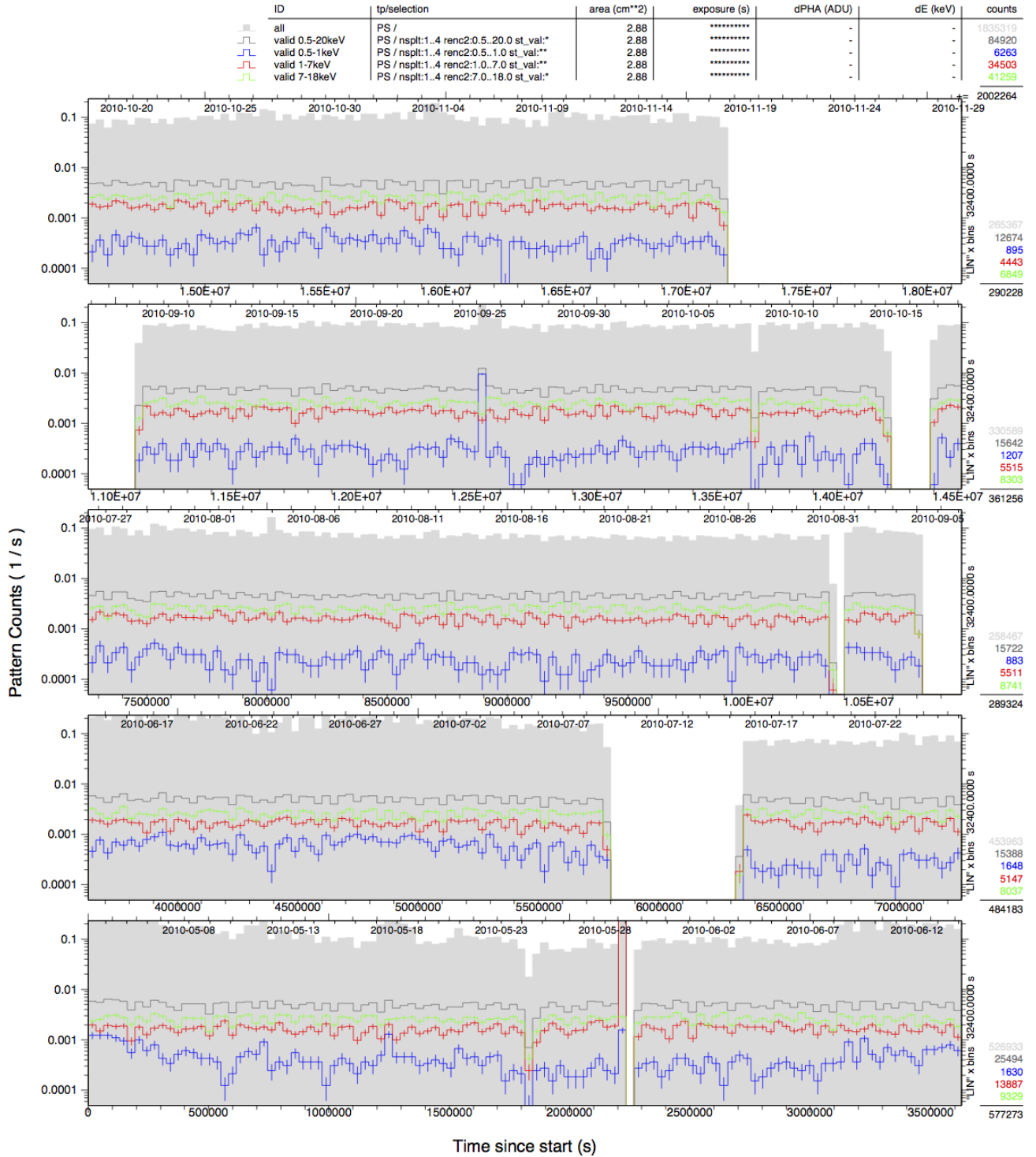


Figure 9-12 CCD lightcurves for 2010 data, pattern (counts/s), 0.5 day binning (4 weeks/panel);  
Red 0.5-1 keV, green 1-7 keV, blue 7-14 keV, grey 0.5-20 keV, solid grey all events.



### 9.3. 2011

In 2011 the CCD detector covered 50 solar tracking runs out of a total of 55, summing up to a total of 78 hours and 55 minutes of Axion sensitive exposure. The following pressure settings were not covered by the CCD: 729, 733, 737, 741, 745.

The total detector lifetime for that season was 111.85 days and an integrated full energy range exposure is presented in Figure 9-13.

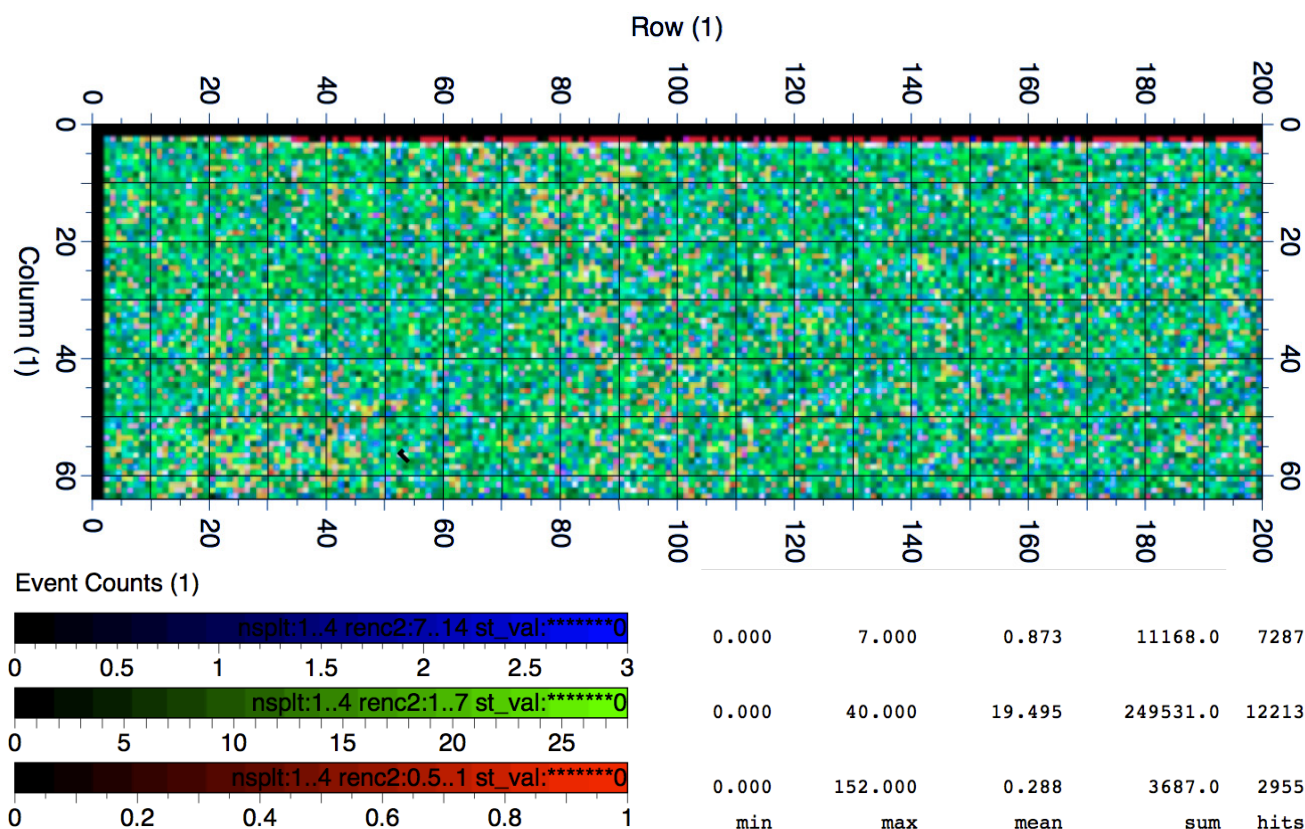


Figure 9-13 TOP - Full Energy true colour event Image of all valid events integrated over the entire detector lifetime of 2011 season (25.03.2011 – 08.08.2011);  
Bottom – Energy range colour coding and statistics (red 0.5 – 1 keV, green 1 – 7 keV, blue 7 – 14 keV).

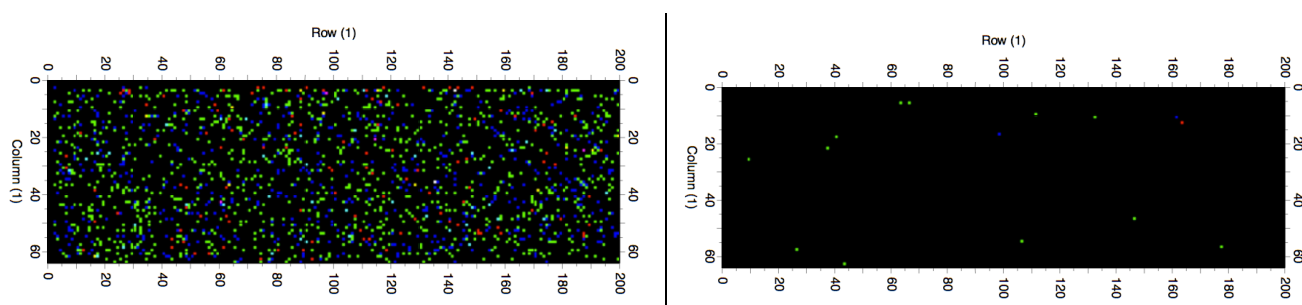


Figure 9-14 Tracking vs. Background event distribution (green for 1-7 keV scale);  
Left – Full energy range exposure for week 24 year 2011;  
Right – Event distribution from the tracking run of 11-06-2011.

2011

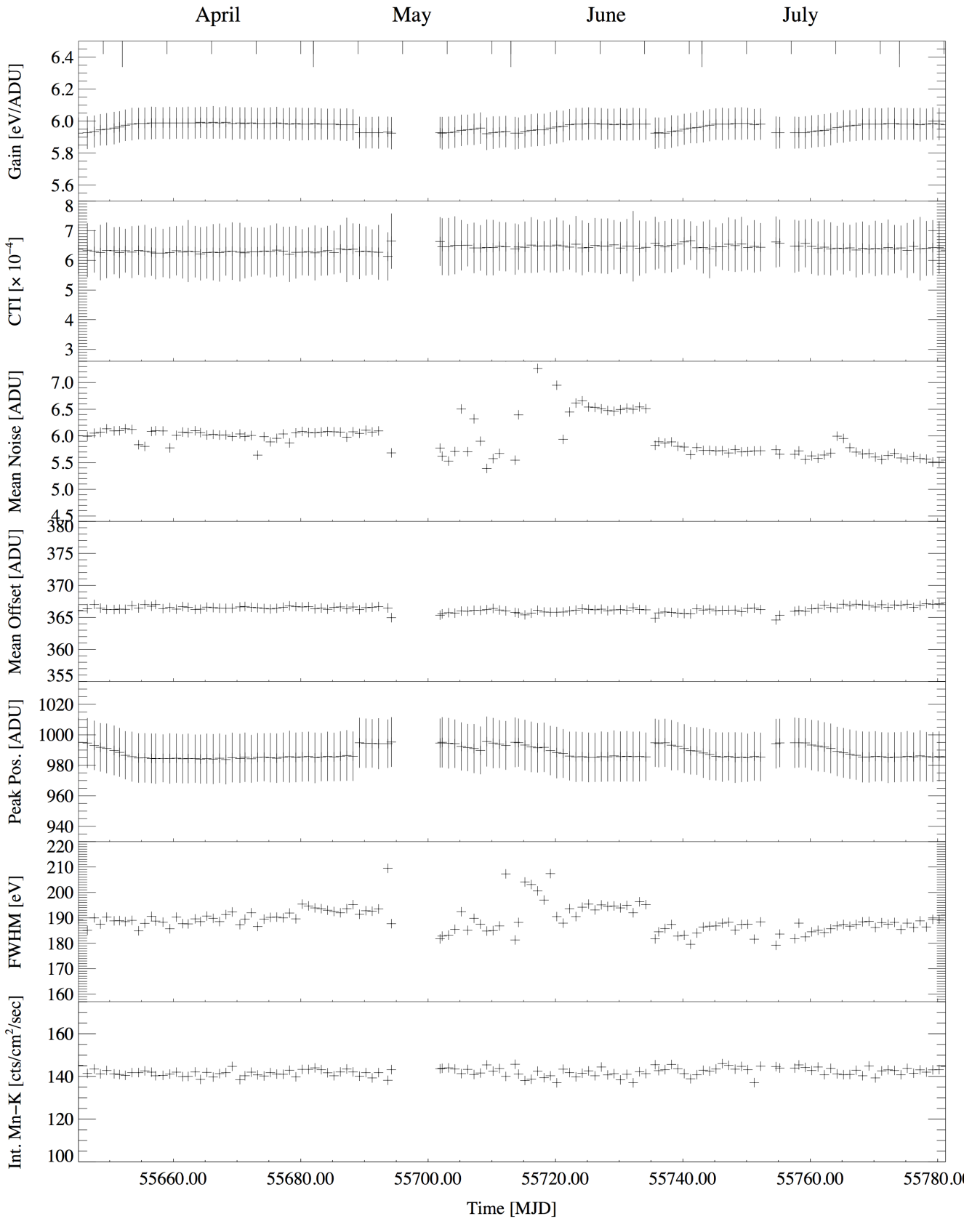


Figure 9-15 Stability of the pn-CCD detector during 2011 data taking period based on daily <sup>55</sup>Fe calibrations. Blank spaces represent detector down times.

## Energy Spectra

2011-03-25T01:47:15.280 .. 2011-08-08T01:11:17.191  
Event file: basic.fits

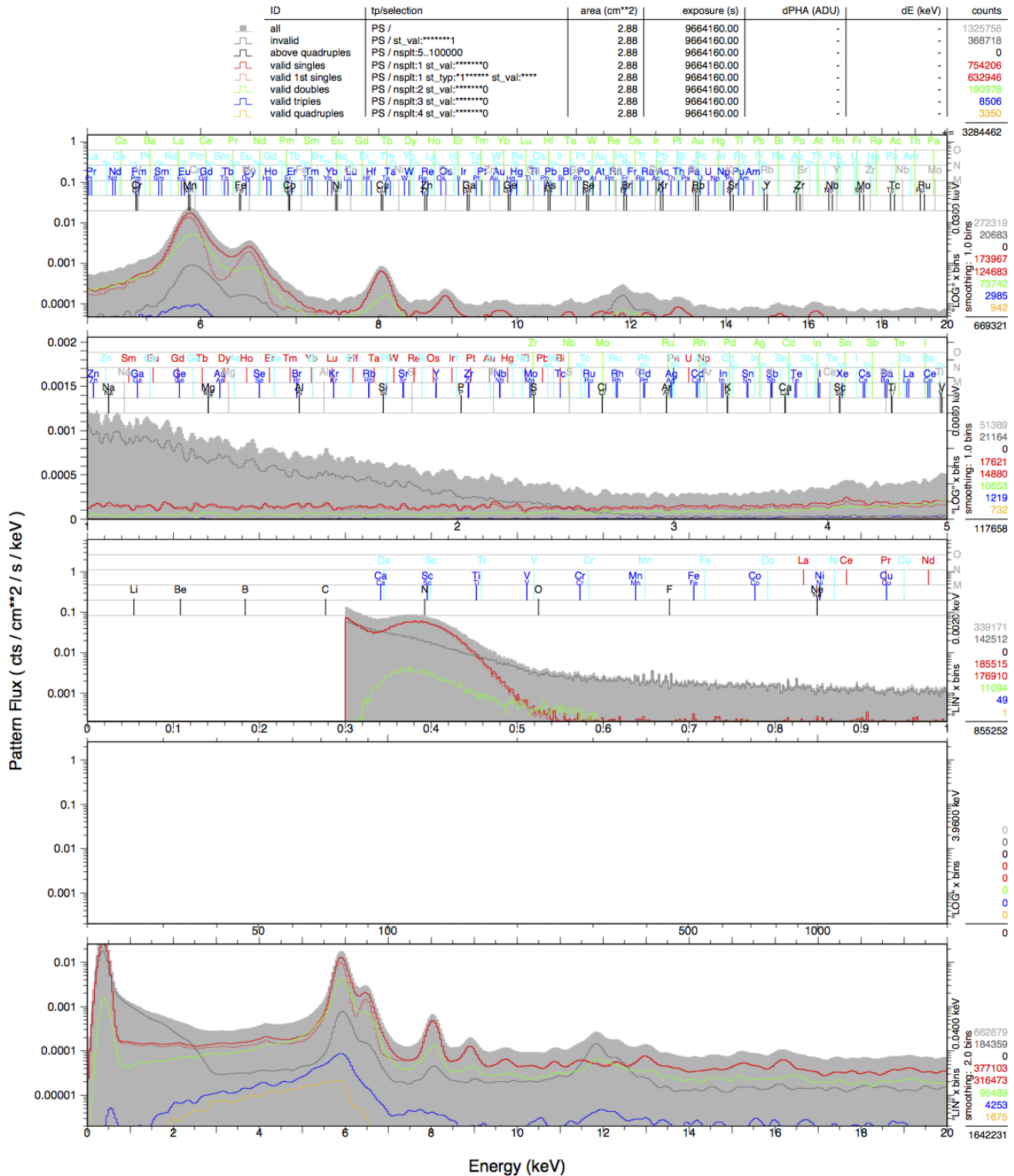


Figure 9-16 Background energy spectra for 2011 CCD data.  
The Flux in cts/cm<sup>2</sup>/s/keV is plotted versus different energy ranges 0.4 – 20 keV.

## Lightcurves

2011-03-25T01:47:15.280 .. 2011-08-08T01:11:17.191  
Event file: sel-basic.fits

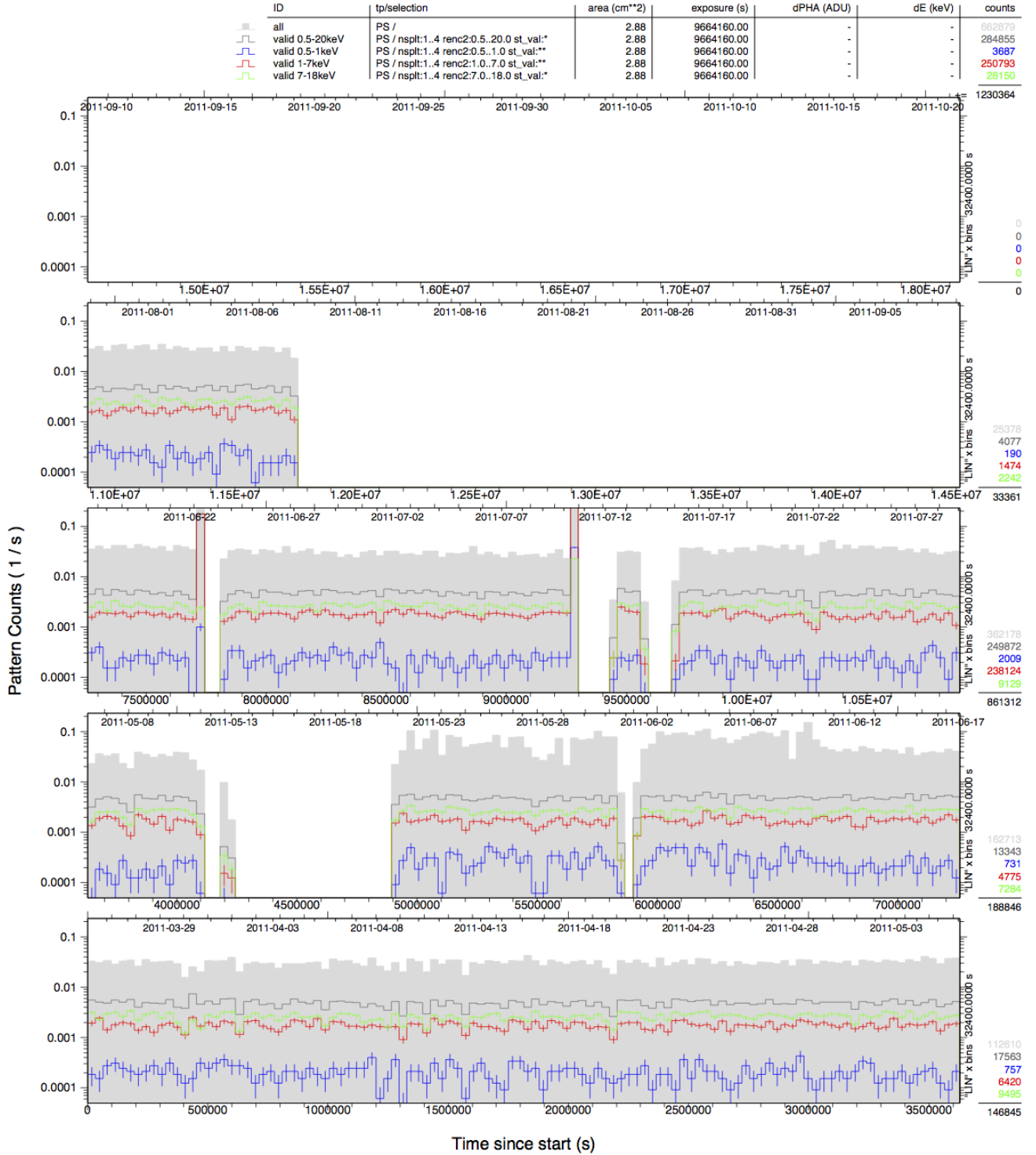


Figure 9-17 CCD lightcurves for 2011 data, pattern (counts/s), 0.5 day binning (4 weeks/panel);  
Red 0.5-1 keV, green 1-7 keV, blue 7-14 keV, grey 0.5-20 keV, solid grey all events.

---

## 10. Conclusions and outlook

---

The CAST experiment at CERN is the world's highest sensitivity Helioscope to date used for solar Axion searches working on the principle of Inverse Primakoff conversion in a strong transverse magnetic field. After the vacuum phase  $^4\text{He}$  was used as buffer gas in the conversion volume for increasing the Axion sensitivity to higher masses. To scan beyond the condensation point of this isotope at 1.8 K,  $^3\text{He}$  was used for taking data in years 2008-2011.

My experimental activity consisted in operating the detector in years 2009-2012, monitoring the quality and stability of the CCD data, aligning the X-ray telescope to the magnet axis, monitoring the long-term stability of the XRT-CCD system alignment, integrating the InGrid detector with the XRT systems in 2014, and various other tasks like Sun filming, Grid measurements etc.

In this thesis an overview of the 2009 2010 and 2011 CCD data was presented. Based on the signal and background levels extracted from the data (Annex 1, Annex 2, Annex 3), no excess X-ray photons were observed when the magnet was pointed at the Sun and the exclusion plot from Figure 10-1 was generated (Table 14-1). The analysed data will be used for improving the combined CAST upper limit thus excluding KWSZ Axions in the mass range  $0.64\text{ eV} \lesssim m_a \lesssim 1.17\text{ eV}$  at a coupling constant of  $g_{a\gamma} \lesssim 3.3 \times 10^{-10}\text{ GeV}^{-1}$  at 95% C.L. with the exact value depending on the pressure setting and the total combined exposure [105] (Figure 10-2).

This closes the gap to the cosmological hot Dark Matter limit and actually for the first time probes with this sensitivity mass regions so far unexplored, favoured by the QCD Axion models.

Besides this, X-ray telescope mirror module reflectivity checks and alignment were performed, together with long-term detector system monitoring and stability studies, spanning the interval 2009- 2014.

In 2014 CAST went through significant upgrades and it will continue to take data trying to shed some light into the hidden sector by scanning for pharaphotons and chameleons. However CAST has set the strongest limit yet on Axion-photon coupling across a wide range of Axion masses, surpassing astrophysical limits for the first time and to improve these already excellent results, and to go deeper into unexplored Axion parameter space, requires a completely new experiment.

The International Axion Observatory (IAXO) is a 4<sup>th</sup> generation proposed Axion Helioscope, currently under review/approval by CERN SPS committee [106]. It aims for a signal-to-noise ratio  $10^5$  better than CAST by using magnets, optics, platform, detectors and design optimised from the Start for detecting solar Axions or ALPs via Primakoff conversion. IAXO follows the conceptual layout of an enhanced Axion Helioscope building on the expertise and the pioneering spirit of the CAST project.

ALP community can only hope that nature has in store something just within the capabilities of IAXO, like it happened with the infamous Higgs Boson and LHC/ATLAS/CMS in 2012.

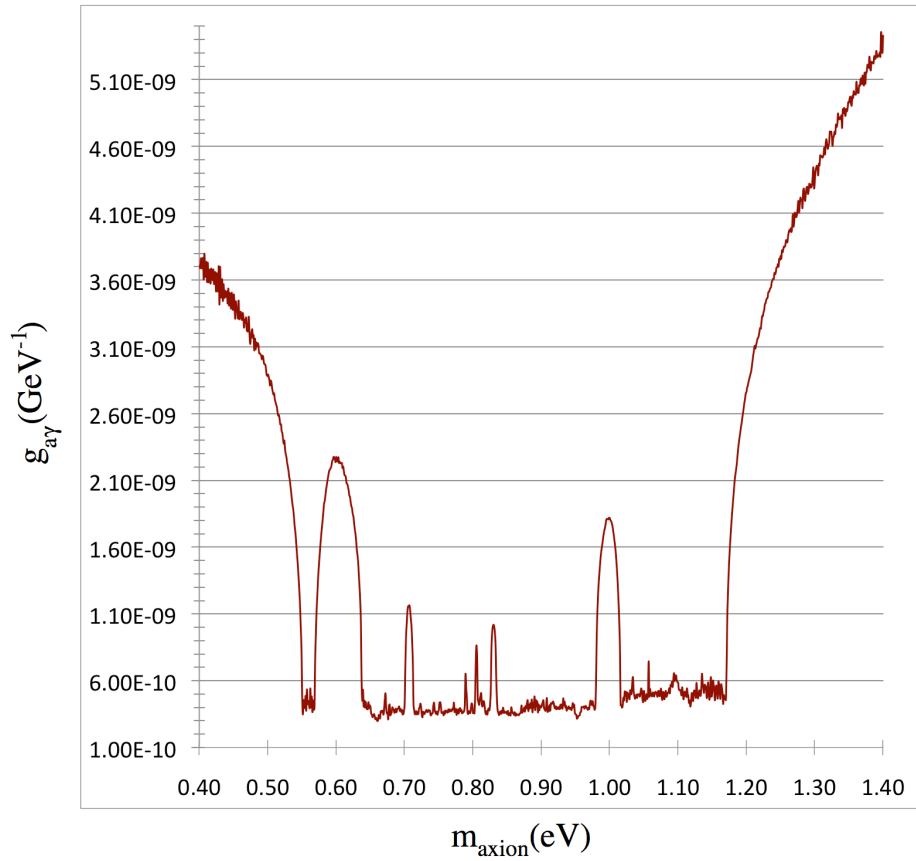


Figure 10-1 Exclusion plot for solar Axions based on the CCD-XRT detector data from 2009 2010 2011 (Annex 1,2,3,4). Some of the lower sensitivity mass domains were covered in 2008 or were not scanned due to detector technical issues.

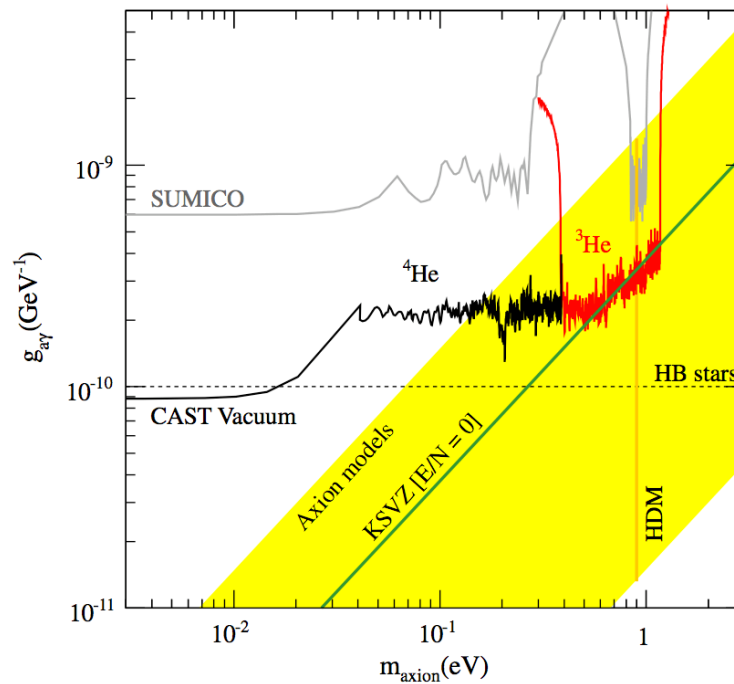


Figure 10-2 Exclusion plot achieved by CAST in Vacuum,  $^4\text{He}$  buffer gas and  $^3\text{He}$  buffer gas. Constraints from Horizontal Branch Stars with dashed line and typical Axion models in yellow band are overlaid [105]. The overall  $^3\text{He}$  sensitivity is expected to improve once the CCD data is taken into account.



## 11. Annex 1

Date	Time[UT]	X	Y	Energy[keV]
14/07/09	03:23:30.40	40.50	107.50	2.77
14/07/09	03:32:20.71	29.50	110.42	6.909
14/07/09	04:04:38.88	29.50	110.60	1.477
20/07/09	04:13:22.39	25.50	107.36	4.593
21/07/09	03:36:55.98	27.50	107.50	6.312
25/07/09	04:50:42.90	30.50	114.50	5.422
26/07/09	04:36:39.00	29.50	108.50	2.351
30/07/09	04:40:22.38	33.50	103.50	2.643
30/07/09	04:47:00.42	37.50	100.50	6.747
31/07/09	04:45:27.24	25.50	107.50	4.212
02/08/09	04:03:14.67	29.50	101.50	6.609
07/08/09	03:56:12.74	28.50	100.50	4.623
08/08/09	04:01:13.20	37.50	103.23	6.809
23/08/09	05:29:59.32	38.50	111.50	4.095
31/08/09	04:56:46.74	40.40	107.50	2.443
01/09/09	04:23:12.55	30.50	105.50	2.933
24/09/09	05:19:48.51	32.50	101.50	4.237
29/09/09	06:12:02.96	39.50	114.50	6.913
03/10/09	05:13:19.90	42.50	99.50	5.754
03/10/09	05:44:07.91	42.50	103.38	5.185
13/10/09	06:13:11.49	32.50	99.50	6.404
20/10/09	05:39:11.13	35.66	104.50	1.293
20/10/09	06:32:31.66	33.50	96.90	5.865
21/10/09	06:11:58.62	41.50	115.69	2.34
25/10/09	05:42:19.61	28.50	115.50	5.018
26/10/09	06:09:17.50	39.50	99.50	3.68
15/11/09	07:10:57.06	31.50	108.50	2.458
24/11/09	06:57:11.17	44.50	106.50	6.92
04/12/09	06:32:07.41	35.50	103.50	6.896
04/12/09	06:38:33.10	28.50	116.50	4.305

Table 11-1 CCD detector spot events for 2009 data for the energy range 1-7 keV

Cts/cm <sup>2</sup> /s	Range keV
6.47046E-05	1->1.5
5.30461E-05	1.5->2
5.36291E-05	2->2.5
4.31364E-05	2.5->3
4.48852E-05	3->3.5
4.54681E-05	3.5->4
4.48852E-05	4->4.5
4.54681E-05	4.5->5
5.07144E-05	5->5.5
5.77095E-05	5.5->6
3.90559E-05	6->6.5
6.87851E-05	6.5->7

Table 11-2 CCD background levels for 2009 data at 0.5 keV binning

Date	Start[UT]	Stop[UT]	Delta	P-Steps
2009.07.13	3:12	4:54	1:42	420-421
2009.07.14	3:13	4:53	1:40	422-423
2009.07.15	3:15	4:54	1:39	424-425
2009.07.16	3:15	4:54	1:39	426-467
2009.07.18	3:17	4:56	1:39	428-429
2009.07.19	3:19	4:58	1:39	430-431
2009.07.20	3:20	4:58	1:38	432-433
2009.07.21	3:22	4:59	1:37	434-435
2009.07.22	3:19	5:01	1:42	436-437
2009.07.23	3:27	5:00	1:33	438-439
2009.07.24	3:25	5:02	1:37	440-441
2009.07.25	3:27	5:03	1:36	442-443
2009.07.26	3:47	5:04	1:17	444-445
2009.07.27	3:29	5:06	1:37	446-447
2009.07.30	3:34	5:08	1:34	448-449
2009.07.31	3:35	5:09	1:34	450-451
2009.08.01	3:36	5:10	1:34	452-453
2009.08.02	3:37	5:11	1:34	454-455
2009.08.03	3:40	5:11	1:31	456-457
2009.08.07	3:45	5:17	1:32	458-459
2009.08.08	3:46	5:19	1:33	460-461
2009.08.09	3:47	5:20	1:33	462-463
2009.08.10	3:48	5:21	1:33	464-465
2009.08.20	4:33	5:32	0:59	481
2009.08.21	4:05	5:32	1:27	482-483
2009.08.22	4:06	5:34	1:28	484-485
2009.08.23	4:07	5:35	1:28	486-487
2009.08.24	4:09	5:35	1:26	488-489
2009.08.28	4:14	5:40	1:26	490-491
2009.08.29	4:16	5:42	1:26	492-493
2009.08.30	4:17	5:44	1:27	494-495
2009.08.31	4:19	5:44	1:25	496-497

2009.09.01	4:20	5:45	1:25	498-499
2009.09.02	4:21	5:46	1:25	500-501
2009.09.03	4:23	5:47	1:24	502-503
2009.09.04	4:23	5:48	1:25	504-505
2009.09.05	4:25	5:49	1:24	506-507
2009.09.06	4:27	5:52	1:25	508-509
2009.09.08	4:29	5:51	1:22	512-513
2009.09.09	4:30	5:55	1:25	514-515
2009.09.10	4:32	5:57	1:25	516-517
2009.09.11	4:33	5:57	1:24	518-519
2009.09.12	4:34	5:58	1:24	520-521
2009.09.13	4:36	5:58	1:22	522-523
2009.09.14	4:37	5:58	1:21	524-525
2009.09.15	4:38	6:03	1:25	526-527
2009.09.16	4:38	6:04	1:26	528-529
2009.09.17	4:41	6:04	1:23	530-531
2009.09.18	4:42	6:06	1:24	532-533
2009.09.20	4:46	6:08	1:22	534-535
2009.09.21	4:46	6:10	1:24	536-537
2009.09.22	4:47	6:11	1:24	538-539
2009.09.23	4:49	6:13	1:24	540-541
2009.09.24	4:50	5:20	0:30	542
2009.09.25	4:51	6:16	1:25	543-544
2009.09.26	4:53	6:17	1:24	545-546
2009.09.27	4:54	6:19	1:25	547-548
2009.09.28	4:55	5:23	0:28	549
2009.09.29	4:57	6:22	1:25	550-551
2009.09.30	4:58	6:23	1:25	552-553
2009.10.01	5:00	6:24	1:24	554-555
2009.10.02	5:00	6:26	1:26	556-557
2009.10.03	5:01	6:27	1:26	558-559
2009.10.04	5:03	6:27	1:24	558-559
2009.10.12	5:13	6:39	1:26	563-564
2009.10.13	5:14	6:41	1:27	565-566
2009.10.14	5:16	6:41	1:25	567-568
2009.10.15	5:18	6:44	1:26	569-570
2009.10.16	5:19	6:46	1:27	571-572
2009.10.17	5:20	6:47	1:27	573-574
2009.10.18	5:22	6:49	1:27	575-576
2009.10.19	5:23	6:50	1:27	577-578
2009.10.20	5:24	6:51	1:27	579-580
2009.10.21	5:25	6:54	1:29	581-582
2009.10.23	5:29	6:57	1:28	584-585
2009.10.24	5:30	6:58	1:28	586-587
2009.10.25	5:40	6:59	1:19	588-589
2009.10.26	5:32	6:59	1:27	590-591
2009.10.27	5:33	7:02	1:29	592-593
2009.10.28	5:35	7:04	1:29	594-595
2009.10.29	5:37	7:05	1:28	596-597
2009.10.30	5:38	7:07	1:29	598-599
2009.10.31	5:39	7:10	1:31	600-601

2009.11.01	5:40	7:12	1:32	602-603
2009.11.11	5:53	7:28	1:35	616-617
2009.11.12	5:55	7:30	1:35	618-619
2009.11.13	5:56	7:31	1:35	620-621
2009.11.14	5:57	7:32	1:35	622-623
2009.11.15	5:59	7:35	1:36	624-625
2009.11.16	6:00	7:36	1:36	626-627
2009.11.17	6:01	7:39	1:38	628-629
2009.11.18	6:04	7:40	1:36	630-631
2009.11.19	6:04	7:41	1:37	632-633
2009.11.20	6:05	7:43	1:38	634-635
2009.11.21	6:07	7:45	1:38	636-637
2009.11.22	6:08	7:46	1:38	638-639
2009.11.23	6:09	7:48	1:39	640-641
2009.11.24	6:10	7:50	1:40	642-643
2009.11.25	6:11	7:51	1:40	644-645
2009.11.26	6:12	7:50	1:38	646-647
2009.11.27	6:13	7:51	1:38	648-649
2009.11.28	6:14	7:56	1:42	650-651
2009.11.29	6:16	7:57	1:41	652-653
2009.11.30	6:17	7:58	1:41	654-655
2009.12.01	6:18	7:59	1:41	656-657
2009.12.04	6:21	8:03	1:42	658-659
2009.12.05	6:23	8:04	1:41	660-661
2009.12.06	6:24	8:06	1:42	662-663
2009.12.07	6:24	8:08	1:44	664-665
2009.12.08	6:25	8:09	1:44	666-667
2009.12.09	6:26	8:09	1:43	759
2009.12.10	6:35	8:11	1:36	850

Table 11-3 CCD tracking times and CAST pressure index for 2009 data.

## 12. Annex 2

Date	Time[UT]	X	Y	Energy[keV]
06/05/10	04:06:00.80	32.50	99.42	4.959
08/05/10	03:59:35.38	37.50	109.50	3.179
12/05/10	04:11:29.64	27.58	104.50	5.753
19/05/10	04:26:20.03	26.50	115.50	1.581
21/05/10	04:11:08.59	39.50	110.50	6.655
22/05/10	04:06:25.01	37.50	97.50	3.043
23/05/10	03:25:14.70	36.50	113.50	2.907
02/06/10	03:48:52.63	30.50	114.50	6.172
07/06/10	03:56:36.45	27.83	112.50	4.649
08/06/10	04:19:17.57	36.50	115.65	1.533
17/07/10	03:36:27.94	33.50	98.50	2.551
27/07/10	03:58:35.90	31.50	105.50	4.188
31/07/10	04:17:23.75	37.50	100.50	4.081
06/08/10	03:44:57.59	40.50	104.27	3.891
14/08/10	04:41:49.63	28.50	106.50	6.964
16/08/10	04:26:43.07	40.50	102.50	6.696
17/08/10	04:18:46.75	27.50	100.50	4.688
17/08/10	04:35:48.26	27.50	101.50	1.409
17/08/10	05:14:15.75	35.50	118.50	1.235
22/08/10	04:48:40.79	29.50	102.50	3.473
25/08/10	04:41:57.18	25.50	109.47	6.725
28/08/10	05:08:27.85	27.50	108.67	4.532
29/08/10	04:16:36.22	41.50	101.50	5.323
29/08/10	05:23:08.96	36.50	109.48	6.782
17/09/10	05:48:43.69	37.50	113.50	3.411
19/09/10	05:28:39.28	28.50	111.50	3.142
27/09/10	06:04:01.42	39.50	115.25	2.341
28/09/10	05:54:28.61	36.78	118.50	2.59
01/10/10	05:16:30.14	33.50	111.50	4.182
17/10/10	05:54:01.30	35.50	104.50	1.859
09/11/10	06:49:23.04	31.40	116.50	2.089
14/11/10	06:57:45.11	29.50	101.50	2.232
15/11/10	06:05:16.60	41.78	100.50	1.643
15/11/10	07:08:11.30	25.50	102.50	5.983
15/11/10	07:21:38.00	31.37	111.50	4.532

Table 12-1 CCD detector spot events for 2010 data for the energy range 1-7 keV

Cts/cm <sup>2</sup> /s	Range keV
5.3767E-05	1->1.5
5.5579E-05	1.5->2
5.6183E-05	2->2.5
4.3497E-05	2.5->3
4.8934E-05	3->3.5
5.2559E-05	3.5->4
4.4101E-05	4->4.5
4.4101E-05	4.5->5
4.7726E-05	5->5.5
5.6787E-05	5.5->6
4.8934E-05	6->6.5
5.7996E-05	6.5->7

Table 12-2 CCD background levels for 2010 data at 0.5 keV binning

Date	Start[UT]	Stop[UT]	Delta	P-Steps
2010.05.06	03:36:00	05:06:00	01:30:00	167
2010.05.07	03:33:00	05:06:00	01:33:00	167
2010.05.08	03:32:00	05:04:00	01:32:00	167
2010.05.09	03:30:00	05:03:00	01:33:00	168
2010.05.10	03:28:00	05:02:00	01:34:00	169
2010.05.11	03:27:00	05:00:00	01:33:00	183-184
2010.05.12	03:26:00	05:01:00	01:35:00	185-186
2010.05.13	03:23:00	04:59:00	01:36:00	187-188
2010.05.14	03:25:00	04:58:00	01:33:00	189-190
2010.05.15	03:40:00	04:56:00	01:16:00	219-220
2010.05.16	03:21:00	04:55:00	01:34:00	221-222
2010.05.17	03:19:00	04:54:00	01:35:00	223-224
2010.05.18	03:19:00	04:53:00	01:34:00	225-226
2010.05.19	03:19:00	04:53:00	01:34:00	227-228
2010.05.20	03:15:00	04:53:00	01:38:00	258-259
2010.05.21	03:15:00	04:51:00	01:36:00	260-261
2010.05.22	03:13:00	04:50:00	01:37:00	262-263
2010.05.23	03:12:00	04:50:00	01:38:00	264-265
2010.05.24	03:11:00	04:49:00	01:38:00	266-267
2010.05.25	03:11:00	04:48:00	01:37:00	268-269
2010.05.26	03:09:00	04:47:00	01:38:00	270-271
2010.05.28	03:07:00	04:46:00	01:39:00	272-273
2010.05.30	03:11:00	04:45:00	01:34:00	274-275
2010.05.31	03:05:00	04:44:00	01:39:00	276-277
2010.06.01	03:03:00	04:44:00	01:41:00	278-279
2010.06.02	03:02:00	04:28:00	01:26:00	280-281
2010.06.03	03:02:00	04:43:00	01:41:00	282-283
2010.06.04	03:01:00	04:43:00	01:42:00	284-285
2010.06.05	03:00:00	04:43:00	01:43:00	302-303
2010.06.06	02:50:00	04:41:00	01:51:00	304-305
2010.06.07	03:05:00	04:41:00	01:36:00	309-310
2010.06.08	03:05:00	04:42:00	01:37:00	311-312
2010.06.09	03:07:00	04:41:00	01:34:00	313-314



2010.06.10	03:06:00	04:40:00	01:34:00	315-316
2010.07.17	03:17:00	04:56:00	01:39:00	315-317
2010.07.18	03:18:00	04:56:00	01:38:00	318-319
2010.07.19	03:19:00	04:58:00	01:39:00	320-321
2010.07.20	03:20:00	04:58:00	01:38:00	322-323
2010.07.21	03:21:00	04:59:00	01:38:00	324-325
2010.07.22	03:22:00	05:00:00	01:38:00	327-328
2010.07.23	03:24:00	05:01:00	01:37:00	328-329
2010.07.24	03:25:00	05:02:00	01:37:00	330-331
2010.07.25	03:27:00	05:03:00	01:36:00	332-333
2010.07.26	03:28:00	05:04:00	01:36:00	334-335
2010.07.27	03:29:00	05:04:00	01:35:00	346-347
2010.07.28	03:31:00	05:06:00	01:35:00	348-349
2010.07.29	03:32:00	05:07:00	01:35:00	353-354
2010.07.30	03:33:00	05:08:00	01:35:00	355-356
2010.07.31	03:35:00	05:08:00	01:33:00	365-366
2010.08.01	03:35:00	05:09:00	01:34:00	367-368
2010.08.02	03:37:00	05:11:00	01:34:00	369-370
2010.08.03	03:39:00	05:11:00	01:32:00	371-372
2010.08.04	03:41:00	05:13:00	01:32:00	373-374
2010.08.05	03:41:00	05:14:00	01:33:00	375-376
2010.08.06	03:43:00	05:15:00	01:32:00	377-378
2010.08.07	03:45:00	05:17:00	01:32:00	379-380
2010.08.11	03:50:00	05:21:00	01:31:00	602-603
2010.08.12	03:55:00	05:22:00	01:27:00	604-605
2010.08.13	03:53:00	05:24:00	01:31:00	606-607
2010.08.14	03:54:00	05:25:00	01:31:00	608-609
2010.08.15	03:55:00	05:26:00	01:31:00	610-611
2010.08.16	03:57:00	05:27:00	01:30:00	612-613
2010.08.17	03:59:00	05:28:00	01:29:00	614-615
2010.08.18	04:00:00	05:29:00	01:29:00	616-617
2010.08.19	04:01:00	05:30:00	01:29:00	618-619
2010.08.20	04:01:00	05:31:00	01:30:00	620-621
2010.08.21	04:04:00	05:32:00	01:28:00	622-623
2010.08.22	04:05:00	05:34:00	01:29:00	624-625
2010.08.23	04:07:00	05:35:00	01:28:00	626
2010.08.24	04:08:00	05:36:00	01:28:00	627-628
2010.08.25	04:10:00	05:37:00	01:27:00	629-630
2010.08.26	04:11:00	05:38:00	01:27:00	631-632
2010.08.27	04:12:00	05:41:00	01:29:00	633-634
2010.08.28	04:14:00	05:40:00	01:26:00	635-636
2010.08.29	04:15:00	05:41:00	01:26:00	637-638
2010.09.10	04:31:00	05:56:00	01:25:00	639-640
2010.09.11	04:33:00	05:57:00	01:24:00	641-642
2010.09.12	04:34:00	05:59:00	01:25:00	643-644
2010.09.13	04:36:00	06:00:00	01:24:00	645-646
2010.09.14	04:37:00	06:01:00	01:24:00	647-648
2010.09.15	04:38:00	06:02:00	01:24:00	649-650
2010.09.16	04:40:00	06:04:00	01:24:00	651-652
2010.09.17	04:42:00	06:07:00	01:25:00	653-654

2010.09.18	04:42:00	06:06:00	01:24:00	655-656
2010.09.19	04:43:00	06:07:00	01:24:00	657-658
2010.09.20	04:44:00	06:09:00	01:25:00	659-660
2010.09.24	04:50:00	06:14:00	01:24:00	661-662
2010.09.25	04:51:00	06:14:00	01:23:00	663-664
2010.09.26	04:53:00	06:17:00	01:24:00	665-666
2010.09.27	04:54:00	06:17:00	01:23:00	667-668
2010.09.28	04:55:00	06:19:00	01:24:00	669-670
2010.09.29	04:57:00	06:21:00	01:24:00	671-672
2010.09.30	04:58:00	06:22:00	01:24:00	673-674
2010.10.01	04:59:00	06:24:00	01:25:00	675-676
2010.10.17	05:20:00	06:46:00	01:26:00	677-678
2010.10.19	05:23:00	06:50:00	01:27:00	679-680
2010.10.20	05:23:00	06:51:00	01:28:00	681-682
2010.10.30	05:38:00	07:08:00	01:30:00	677
2010.10.31	05:38:00	07:09:00	01:31:00	678
2010.11.01	05:39:00	07:11:00	01:32:00	679-680
2010.11.02	05:41:00	07:12:00	01:31:00	681-682
2010.11.03	05:43:00	07:12:00	01:29:00	683-684
2010.11.04	05:45:00	07:16:00	01:31:00	685-686
2010.11.05	05:45:00	07:18:00	01:33:00	687-688
2010.11.06	05:47:00	07:19:00	01:32:00	689-690
2010.11.07	05:48:00	07:21:00	01:33:00	691-692
2010.11.08	05:49:00	07:23:00	01:34:00	693-694
2010.11.09	05:50:00	07:24:00	01:34:00	695-696
2010.11.14	05:57:00	07:33:00	01:36:00	697-698
2010.11.15	05:59:00	07:34:00	01:35:00	699-700
2010.11.16	06:00:00	07:36:00	01:36:00	701-702
2010.11.17	06:01:00	07:38:00	01:37:00	703-704

Table 12-3 CCD tracking times and CAST pressure index for 2010 data.

## 13. Annex 3

Date	Time[UT]	X	Y	Energy[keV]
01/05/11	04:12:57.36	32.50	101.50	1.983
01/05/11	04:53:04.90	28.50	112.50	3.64
02/05/11	04:31:12.05	32.25	110.50	4.427
04/05/11	03:47:48.03	37.50	113.44	5.755
04/05/11	04:19:08.21	40.50	104.50	2.506
04/05/11	04:55:45.03	36.50	117.50	2.949
24/05/11	03:23:12.43	36.50	98.50	2.402
24/05/11	03:24:43.51	44.50	107.50	5.097
28/05/11	04:00:46.94	31.50	106.45	6.636
10/06/11	03:15:55.50	30.50	118.50	6.476
15/06/11	03:22:31.05	40.50	115.50	5.541
16/06/11	04:09:33.09	32.50	113.50	5.356
17/06/11	03:37:52.89	45.43	109.50	5.536
17/06/11	03:52:37.25	40.43	111.50	6.467
03/07/11	04:03:18.99	28.50	113.50	1.678
04/07/11	03:58:12.04	40.50	105.50	1.115
08/07/11	03:25:30.31	31.50	115.47	6.876
17/07/11	04:32:59.31	25.50	108.50	6.952

Table 13-1 CCD detector spot events for 2011 data for the energy range 1-7 keV

Cts/cm <sup>2</sup> /s	Range keV
6.64534E-05	1->1.5
4.65174E-05	1.5->2
6.51243E-05	2->2.5
5.44918E-05	2.5->3
4.25302E-05	3->3.5
4.78464E-05	3.5->4
5.18336E-05	4->4.5
5.71499E-05	4.5->5
5.05046E-05	5->5.5
5.05046E-05	5.5->6
6.51243E-05	6->6.5
6.77825E-05	6.5->7

Table 13-2 CCD background levels for 2011 data at 0.5 keV binning

Date	Start[UT]	Stop[UT]	Delta	P-Steps
20110430	3:46	5:14	1:28	304-306
20110501	3:43	5:14	1:31	308-310
20110502	3:42	5:13	1:31	312-314
20110503	3:40	5:12	1:32	316-318
20110504	3:39	5:10	1:31	382-384
20110505	3:37	5:09	1:32	386-388
20110506	3:35	5:08	1:33	390-392
20110507	3:34	5:06	1:32	394-396
20110508	3:32	5:05	1:33	398-400
20110509	3:31	5:04	1:33	402-403
20110521	3:14	4:51	1:37	749
20110522	3:13	4:50	1:37	753
20110523	3:12	4:50	1:38	757
20110524	3:11	4:50	1:39	761
20110525	3:10	4:49	1:39	765
20110526	3:09	4:47	1:38	769
20110527	3:08	4:47	1:39	773
20110528	3:06	4:46	1:40	777
20110529	3:06	4:45	1:39	781
20110530	3:06	4:45	1:39	785
20110607	3:07	4:41	1:34	789
20110608	3:07	4:41	1:34	793
20110609	3:07	4:41	1:34	797
20110610	3:07	4:42	1:35	801
20110611	3:07	4:41	1:34	805
20110612	3:07	4:41	1:34	809
20110613	3:07	4:40	1:33	813
20110614	3:08	4:40	1:32	817
20110615	3:08	4:41	1:33	821
20110616	3:10	4:40	1:30	825
20110617	3:12	4:40	1:28	829
20110618	3:10	4:41	1:31	833
20110619	3:10	4:41	1:31	837
20110620	3:10	4:41	1:31	841
20110621	3:10	4:41	1:31	845
20110622	3:10	4:41	1:31	849
20110703	3:12	4:46	1:34	849
20110704	3:12	4:47	1:35	853
20110705	3:12	4:47	1:35	857
20110706	3:12	4:48	1:36	861
20110707	3:12	4:48	1:36	865
20110708	3:12	4:49	1:37	869
20110709	3:12	4:49	1:37	873
20110716	3:15	4:55	1:40	877

20110717	3:19	4:56	1:37	881
20110718	3:18	4:57	1:39	885
20110719	3:19	4:57	1:38	889
20110720	3:20	4:58	1:38	893
20110721	3:21	4:59	1:38	897
20110722	3:22	5:00	1:38	901

Table 13-3 CCD tracking times and CAST pressure index for 2011 data.

## 14. Annex 4

$m_{\text{Axion}} \text{ (eV)}$	$g_{\text{ay}} \text{ (GeV}^{-1}\text{)}$	$m_{\text{Axion}} \text{ (eV)}$	$g_{\text{ay}} \text{ (GeV}^{-1}\text{)}$	$m_{\text{Axion}} \text{ (eV)}$	$g_{\text{ay}} \text{ (GeV}^{-1}\text{)}$	$m_{\text{Axion}} \text{ (eV)}$	$g_{\text{ay}} \text{ (GeV}^{-1}\text{)}$
0.400	3.71E-09	0.651	3.53E-10	0.902	4.39E-10	1.153	5.18E-10
0.401	3.69E-09	0.652	3.46E-10	0.903	4.53E-10	1.154	4.53E-10
0.402	3.76E-09	0.653	3.27E-10	0.904	3.92E-10	1.155	5.50E-10
0.403	3.69E-09	0.654	3.37E-10	0.905	3.87E-10	1.156	5.63E-10
0.404	3.70E-09	0.655	3.50E-10	0.906	3.75E-10	1.157	5.10E-10
0.405	3.76E-09	0.656	3.38E-10	0.907	4.07E-10	1.158	4.68E-10
0.406	3.60E-09	0.657	3.13E-10	0.908	4.70E-10	1.159	5.93E-10
0.407	3.80E-09	0.658	3.24E-10	0.909	3.68E-10	1.160	5.75E-10
0.408	3.63E-09	0.659	3.08E-10	0.910	4.04E-10	1.161	5.05E-10
0.409	3.66E-09	0.660	2.98E-10	0.911	3.72E-10	1.162	4.66E-10
0.410	3.74E-09	0.661	2.97E-10	0.912	4.17E-10	1.163	5.72E-10
0.411	3.58E-09	0.662	3.43E-10	0.913	3.76E-10	1.164	5.51E-10
0.412	3.73E-09	0.663	3.40E-10	0.914	4.32E-10	1.165	5.11E-10
0.413	3.58E-09	0.664	3.18E-10	0.915	4.24E-10	1.166	4.26E-10
0.414	3.66E-09	0.665	3.72E-10	0.916	4.34E-10	1.167	4.92E-10
0.415	3.68E-09	0.666	3.64E-10	0.917	4.44E-10	1.168	4.61E-10
0.416	3.57E-09	0.667	3.77E-10	0.918	4.34E-10	1.169	4.68E-10
0.417	3.68E-09	0.668	3.71E-10	0.919	4.06E-10	1.170	4.56E-10
0.418	3.62E-09	0.669	3.46E-10	0.920	3.92E-10	1.171	6.98E-10
0.419	3.60E-09	0.670	3.91E-10	0.921	4.09E-10	1.172	1.06E-09
0.420	3.68E-09	0.671	4.63E-10	0.922	3.86E-10	1.173	1.26E-09
0.421	3.57E-09	0.672	5.04E-10	0.923	4.02E-10	1.174	1.40E-09
0.422	3.60E-09	0.673	3.95E-10	0.924	3.89E-10	1.175	1.52E-09
0.423	3.66E-09	0.674	3.55E-10	0.925	3.90E-10	1.176	1.61E-09
0.424	3.51E-09	0.675	3.59E-10	0.926	4.04E-10	1.177	1.70E-09
0.425	3.65E-09	0.676	3.11E-10	0.927	3.87E-10	1.178	1.78E-09
0.426	3.56E-09	0.677	4.09E-10	0.928	4.21E-10	1.179	1.85E-09
0.427	3.52E-09	0.678	4.21E-10	0.929	3.97E-10	1.180	1.92E-09
0.428	3.70E-09	0.679	3.42E-10	0.930	4.22E-10	1.181	1.98E-09
0.429	3.42E-09	0.680	3.51E-10	0.931	3.92E-10	1.182	2.05E-09
0.430	3.70E-09	0.681	3.65E-10	0.932	4.68E-10	1.183	2.11E-09
0.431	3.47E-09	0.682	4.00E-10	0.933	4.17E-10	1.184	2.15E-09
0.432	3.54E-09	0.683	3.85E-10	0.934	4.44E-10	1.185	2.18E-09
0.433	3.60E-09	0.684	3.87E-10	0.935	4.01E-10	1.186	2.23E-09
0.434	3.44E-09	0.685	3.60E-10	0.936	4.13E-10	1.187	2.29E-09
0.435	3.57E-09	0.686	3.71E-10	0.937	3.76E-10	1.188	2.34E-09
0.436	3.47E-09	0.687	3.91E-10	0.938	3.97E-10	1.189	2.38E-09
0.437	3.52E-09	0.688	3.64E-10	0.939	3.92E-10	1.190	2.42E-09
0.438	3.47E-09	0.689	3.85E-10	0.940	4.08E-10	1.191	2.46E-09
0.439	3.49E-09	0.690	3.89E-10	0.941	3.99E-10	1.192	2.50E-09
0.440	3.51E-09	0.691	3.94E-10	0.942	3.88E-10	1.193	2.53E-09
0.441	3.42E-09	0.692	4.07E-10	0.943	3.97E-10	1.194	2.57E-09
0.442	3.54E-09	0.693	3.74E-10	0.944	3.80E-10	1.195	2.60E-09
0.443	3.41E-09	0.694	3.89E-10	0.945	4.01E-10	1.196	2.64E-09
0.444	3.50E-09	0.695	3.67E-10	0.946	4.32E-10	1.197	2.68E-09
0.445	3.45E-09	0.696	3.82E-10	0.947	4.00E-10	1.198	2.71E-09
0.446	3.39E-09	0.697	3.47E-10	0.948	4.21E-10	1.199	2.75E-09
0.447	3.50E-09	0.698	3.51E-10	0.949	3.61E-10	1.200	2.76E-09
0.448	3.43E-09	0.699	3.74E-10	0.950	3.48E-10	1.201	2.79E-09
0.449	3.38E-09	0.700	4.26E-10	0.951	3.45E-10	1.202	2.81E-09
0.450	3.49E-09	0.701	7.10E-10	0.952	3.15E-10	1.203	2.83E-09
0.451	3.42E-09	0.702	9.26E-10	0.953	3.22E-10	1.204	2.86E-09
0.452	3.31E-09	0.703	1.03E-09	0.954	3.35E-10	1.205	2.88E-09
0.453	3.44E-09	0.704	1.12E-09	0.955	3.39E-10	1.206	2.90E-09



$m_{\text{Axion}} \text{ (eV)}$	$g_{\text{ay}} \text{ (GeV}^{-1}\text{)}$	$m_{\text{Axion}} \text{ (eV)}$	$g_{\text{ay}} \text{ (GeV}^{-1}\text{)}$	$m_{\text{Axion}} \text{ (eV)}$	$g_{\text{ay}} \text{ (GeV}^{-1}\text{)}$	$m_{\text{Axion}} \text{ (eV)}$	$g_{\text{ay}} \text{ (GeV}^{-1}\text{)}$
0.454	3.39E-09	0.705	1.16E-09	0.956	3.43E-10	1.207	2.92E-09
0.455	3.37E-09	0.706	1.15E-09	0.957	3.64E-10	1.208	2.95E-09
0.456	3.31E-09	0.707	1.16E-09	0.958	3.68E-10	1.209	3.00E-09
0.457	3.45E-09	0.708	1.13E-09	0.959	4.04E-10	1.210	3.04E-09
0.458	3.31E-09	0.709	1.07E-09	0.960	4.04E-10	1.211	3.07E-09
0.459	3.32E-09	0.710	1.00E-09	0.961	4.01E-10	1.212	3.11E-09
0.460	3.36E-09	0.711	8.86E-10	0.962	4.06E-10	1.213	3.09E-09
0.461	3.32E-09	0.712	7.21E-10	0.963	3.91E-10	1.214	3.11E-09
0.462	3.30E-09	0.713	4.14E-10	0.964	4.04E-10	1.215	3.13E-09
0.463	3.35E-09	0.714	3.79E-10	0.965	4.10E-10	1.216	3.16E-09
0.464	3.32E-09	0.715	3.48E-10	0.966	4.02E-10	1.217	3.17E-09
0.465	3.24E-09	0.716	3.56E-10	0.967	3.94E-10	1.218	3.18E-09
0.466	3.30E-09	0.717	3.72E-10	0.968	3.82E-10	1.219	3.21E-09
0.467	3.28E-09	0.718	3.47E-10	0.969	3.99E-10	1.220	3.24E-09
0.468	3.32E-09	0.719	3.65E-10	0.970	3.87E-10	1.221	3.24E-09
0.469	3.22E-09	0.720	3.51E-10	0.971	4.27E-10	1.222	3.28E-09
0.470	3.21E-09	0.721	3.91E-10	0.972	4.52E-10	1.223	3.33E-09
0.471	3.26E-09	0.722	4.02E-10	0.973	4.22E-10	1.224	3.33E-09
0.472	3.32E-09	0.723	4.29E-10	0.974	4.17E-10	1.225	3.36E-09
0.473	3.19E-09	0.724	4.05E-10	0.975	4.47E-10	1.226	3.38E-09
0.474	3.12E-09	0.725	3.48E-10	0.976	4.16E-10	1.227	3.42E-09
0.475	3.17E-09	0.726	3.27E-10	0.977	4.02E-10	1.228	3.43E-09
0.476	3.21E-09	0.727	3.67E-10	0.978	3.82E-10	1.229	3.45E-09
0.477	3.23E-09	0.728	3.53E-10	0.979	3.88E-10	1.230	3.46E-09
0.478	3.17E-09	0.729	3.52E-10	0.980	5.91E-10	1.231	3.46E-09
0.479	3.19E-09	0.730	3.64E-10	0.981	9.33E-10	1.232	3.51E-09
0.480	3.07E-09	0.731	3.74E-10	0.982	1.12E-09	1.233	3.51E-09
0.481	3.16E-09	0.732	3.81E-10	0.983	1.25E-09	1.234	3.53E-09
0.482	3.08E-09	0.733	3.65E-10	0.984	1.34E-09	1.235	3.54E-09
0.483	3.13E-09	0.734	3.67E-10	0.985	1.41E-09	1.236	3.54E-09
0.484	3.10E-09	0.735	3.82E-10	0.986	1.48E-09	1.237	3.58E-09
0.485	3.13E-09	0.736	3.77E-10	0.987	1.54E-09	1.238	3.59E-09
0.486	3.11E-09	0.737	3.77E-10	0.988	1.58E-09	1.239	3.61E-09
0.487	3.05E-09	0.738	3.41E-10	0.989	1.62E-09	1.240	3.61E-09
0.488	3.05E-09	0.739	3.40E-10	0.990	1.65E-09	1.241	3.65E-09
0.489	3.04E-09	0.740	3.56E-10	0.991	1.69E-09	1.242	3.64E-09
0.490	3.04E-09	0.741	3.59E-10	0.992	1.72E-09	1.243	3.66E-09
0.491	3.01E-09	0.742	4.15E-10	0.993	1.74E-09	1.244	3.69E-09
0.492	3.03E-09	0.743	4.35E-10	0.994	1.77E-09	1.245	3.70E-09
0.493	3.02E-09	0.744	3.81E-10	0.995	1.80E-09	1.246	3.72E-09
0.494	2.98E-09	0.745	3.64E-10	0.996	1.81E-09	1.247	3.70E-09
0.495	2.97E-09	0.746	3.52E-10	0.997	1.81E-09	1.248	3.76E-09
0.496	2.97E-09	0.747	3.68E-10	0.998	1.81E-09	1.249	3.75E-09
0.497	2.94E-09	0.748	3.46E-10	0.999	1.82E-09	1.250	3.78E-09
0.498	2.89E-09	0.749	3.67E-10	1.000	1.82E-09	1.251	3.76E-09
0.499	2.88E-09	0.750	3.76E-10	1.001	1.80E-09	1.252	3.82E-09
0.500	2.89E-09	0.751	4.38E-10	1.002	1.80E-09	1.253	3.81E-09
0.501	2.88E-09	0.752	4.40E-10	1.003	1.78E-09	1.254	3.83E-09
0.502	2.85E-09	0.753	4.10E-10	1.004	1.76E-09	1.255	3.85E-09
0.503	2.81E-09	0.754	3.58E-10	1.005	1.72E-09	1.256	3.85E-09
0.504	2.85E-09	0.755	3.63E-10	1.006	1.69E-09	1.257	3.86E-09
0.505	2.83E-09	0.756	3.63E-10	1.007	1.65E-09	1.258	3.90E-09
0.506	2.79E-09	0.757	3.41E-10	1.008	1.60E-09	1.259	3.89E-09
0.507	2.76E-09	0.758	3.72E-10	1.009	1.55E-09	1.260	3.88E-09
0.508	2.74E-09	0.759	3.53E-10	1.010	1.48E-09	1.261	3.93E-09
0.509	2.75E-09	0.760	3.77E-10	1.011	1.40E-09	1.262	3.96E-09

$m_{\text{Axion}} \text{ (eV)}$	$g_{\text{ay}} \text{ (GeV}^{-1}\text{)}$	$m_{\text{Axion}} \text{ (eV)}$	$g_{\text{ay}} \text{ (GeV}^{-1}\text{)}$	$m_{\text{Axion}} \text{ (eV)}$	$g_{\text{ay}} \text{ (GeV}^{-1}\text{)}$	$m_{\text{Axion}} \text{ (eV)}$	$g_{\text{ay}} \text{ (GeV}^{-1}\text{)}$
0.510	2.71E-09	0.761	3.66E-10	1.012	1.29E-09	1.263	3.97E-09
0.511	2.69E-09	0.762	3.74E-10	1.013	1.18E-09	1.264	3.96E-09
0.512	2.67E-09	0.763	3.61E-10	1.014	1.03E-09	1.265	3.99E-09
0.513	2.65E-09	0.764	3.85E-10	1.015	8.26E-10	1.266	3.96E-09
0.514	2.61E-09	0.765	3.68E-10	1.016	4.17E-10	1.267	4.00E-09
0.515	2.58E-09	0.766	3.85E-10	1.017	4.18E-10	1.268	4.09E-09
0.516	2.59E-09	0.767	3.71E-10	1.018	3.98E-10	1.269	4.00E-09
0.517	2.56E-09	0.768	3.80E-10	1.019	4.15E-10	1.270	4.04E-09
0.518	2.52E-09	0.769	3.73E-10	1.020	4.73E-10	1.271	4.10E-09
0.519	2.52E-09	0.770	3.92E-10	1.021	4.52E-10	1.272	4.10E-09
0.520	2.47E-09	0.771	3.86E-10	1.022	5.20E-10	1.273	4.07E-09
0.521	2.45E-09	0.772	4.36E-10	1.023	4.86E-10	1.274	4.09E-09
0.522	2.41E-09	0.773	3.65E-10	1.024	5.15E-10	1.275	4.14E-09
0.523	2.37E-09	0.774	3.69E-10	1.025	4.41E-10	1.276	4.19E-09
0.524	2.40E-09	0.775	3.89E-10	1.026	5.09E-10	1.277	4.10E-09
0.525	2.33E-09	0.776	3.44E-10	1.027	4.96E-10	1.278	4.16E-09
0.526	2.30E-09	0.777	3.78E-10	1.028	4.81E-10	1.279	4.22E-09
0.527	2.27E-09	0.778	3.83E-10	1.029	4.63E-10	1.280	4.20E-09
0.528	2.23E-09	0.779	3.55E-10	1.030	5.29E-10	1.281	4.20E-09
0.529	2.20E-09	0.780	3.82E-10	1.031	4.97E-10	1.282	4.14E-09
0.530	2.17E-09	0.781	3.95E-10	1.032	5.02E-10	1.283	4.27E-09
0.531	2.13E-09	0.782	3.71E-10	1.033	5.82E-10	1.284	4.28E-09
0.532	2.10E-09	0.783	3.82E-10	1.034	6.26E-10	1.285	4.22E-09
0.533	2.05E-09	0.784	3.55E-10	1.035	5.22E-10	1.286	4.19E-09
0.534	2.01E-09	0.785	3.58E-10	1.036	4.88E-10	1.287	4.25E-09
0.535	1.96E-09	0.786	3.68E-10	1.037	4.65E-10	1.288	4.29E-09
0.536	1.91E-09	0.787	3.68E-10	1.038	4.73E-10	1.289	4.30E-09
0.537	1.88E-09	0.788	4.18E-10	1.039	4.96E-10	1.290	4.24E-09
0.538	1.83E-09	0.789	6.50E-10	1.040	4.72E-10	1.291	4.26E-09
0.539	1.76E-09	0.790	5.46E-10	1.041	4.98E-10	1.292	4.32E-09
0.540	1.71E-09	0.791	4.74E-10	1.042	4.94E-10	1.293	4.32E-09
0.541	1.65E-09	0.792	3.59E-10	1.043	5.00E-10	1.294	4.29E-09
0.542	1.58E-09	0.793	3.50E-10	1.044	4.81E-10	1.295	4.29E-09
0.543	1.51E-09	0.794	3.73E-10	1.045	5.08E-10	1.296	4.31E-09
0.544	1.44E-09	0.795	3.69E-10	1.046	5.42E-10	1.297	4.37E-09
0.545	1.35E-09	0.796	3.58E-10	1.047	5.25E-10	1.298	4.44E-09
0.546	1.26E-09	0.797	3.97E-10	1.048	4.60E-10	1.299	4.29E-09
0.547	1.15E-09	0.798	4.30E-10	1.049	4.41E-10	1.300	4.33E-09
0.548	9.95E-10	0.799	4.20E-10	1.050	5.22E-10	1.301	4.41E-09
0.549	8.45E-10	0.800	3.57E-10	1.051	4.83E-10	1.302	4.44E-09
0.550	5.01E-10	0.801	3.59E-10	1.052	4.49E-10	1.303	4.46E-09
0.551	3.48E-10	0.802	3.56E-10	1.053	4.69E-10	1.304	4.45E-09
0.552	4.53E-10	0.803	4.57E-10	1.054	5.00E-10	1.305	4.38E-09
0.553	4.31E-10	0.804	7.24E-10	1.055	4.64E-10	1.306	4.47E-09
0.554	3.96E-10	0.805	8.64E-10	1.056	4.97E-10	1.307	4.46E-09
0.555	4.87E-10	0.806	7.81E-10	1.057	7.45E-10	1.308	4.53E-09
0.556	3.75E-10	0.807	4.62E-10	1.058	4.85E-10	1.309	4.53E-09
0.557	5.35E-10	0.808	4.40E-10	1.059	5.38E-10	1.310	4.53E-09
0.558	4.26E-10	0.809	4.19E-10	1.060	5.01E-10	1.311	4.52E-09
0.559	4.48E-10	0.810	4.59E-10	1.061	4.90E-10	1.312	4.52E-09
0.560	4.34E-10	0.811	4.88E-10	1.062	4.84E-10	1.313	4.55E-09
0.561	3.97E-10	0.812	5.06E-10	1.063	5.12E-10	1.314	4.59E-09
0.562	5.42E-10	0.813	4.18E-10	1.064	5.08E-10	1.315	4.54E-09
0.563	4.01E-10	0.814	4.07E-10	1.065	4.82E-10	1.316	4.62E-09
0.564	4.82E-10	0.815	4.47E-10	1.066	5.09E-10	1.317	4.65E-09
0.565	3.64E-10	0.816	4.46E-10	1.067	5.16E-10	1.318	4.62E-09

$m_{\text{Axion}} \text{ (eV)}$	$g_{\text{ay}} \text{ (GeV}^{-1}\text{)}$	$m_{\text{Axion}} \text{ (eV)}$	$g_{\text{ay}} \text{ (GeV}^{-1}\text{)}$	$m_{\text{Axion}} \text{ (eV)}$	$g_{\text{ay}} \text{ (GeV}^{-1}\text{)}$	$m_{\text{Axion}} \text{ (eV)}$	$g_{\text{ay}} \text{ (GeV}^{-1}\text{)}$
0.566	4.53E-10	0.817	4.11E-10	1.068	5.15E-10	1.319	4.58E-09
0.567	3.81E-10	0.818	3.64E-10	1.069	4.94E-10	1.320	4.61E-09
0.568	3.89E-10	0.819	3.49E-10	1.070	4.81E-10	1.321	4.62E-09
0.569	7.45E-10	0.820	3.72E-10	1.071	5.24E-10	1.322	4.71E-09
0.570	9.37E-10	0.821	3.46E-10	1.072	5.21E-10	1.323	4.71E-09
0.571	1.11E-09	0.822	3.83E-10	1.073	4.85E-10	1.324	4.71E-09
0.572	1.22E-09	0.823	3.92E-10	1.074	4.98E-10	1.325	4.67E-09
0.573	1.34E-09	0.824	3.78E-10	1.075	5.41E-10	1.326	4.60E-09
0.574	1.42E-09	0.825	4.25E-10	1.076	4.78E-10	1.327	4.66E-09
0.575	1.50E-09	0.826	5.33E-10	1.077	4.57E-10	1.328	4.68E-09
0.576	1.57E-09	0.827	8.50E-10	1.078	5.15E-10	1.329	4.71E-09
0.577	1.64E-09	0.828	9.60E-10	1.079	5.02E-10	1.330	4.69E-09
0.578	1.70E-09	0.829	1.01E-09	1.080	4.61E-10	1.331	4.76E-09
0.579	1.75E-09	0.830	1.02E-09	1.081	4.96E-10	1.332	4.75E-09
0.580	1.80E-09	0.831	1.00E-09	1.082	5.23E-10	1.333	4.77E-09
0.581	1.86E-09	0.832	9.61E-10	1.083	4.81E-10	1.334	4.85E-09
0.582	1.92E-09	0.833	8.67E-10	1.084	4.92E-10	1.335	4.80E-09
0.583	1.95E-09	0.834	6.20E-10	1.085	5.11E-10	1.336	4.82E-09
0.584	1.98E-09	0.835	4.64E-10	1.086	5.12E-10	1.337	4.80E-09
0.585	2.03E-09	0.836	3.79E-10	1.087	5.43E-10	1.338	4.80E-09
0.586	2.06E-09	0.837	3.61E-10	1.088	5.05E-10	1.339	4.83E-09
0.587	2.10E-09	0.838	3.43E-10	1.089	5.67E-10	1.340	4.74E-09
0.588	2.13E-09	0.839	3.60E-10	1.090	5.57E-10	1.341	4.88E-09
0.589	2.16E-09	0.840	3.70E-10	1.091	5.91E-10	1.342	4.85E-09
0.590	2.18E-09	0.841	3.51E-10	1.092	5.52E-10	1.343	4.89E-09
0.591	2.18E-09	0.842	3.76E-10	1.093	6.03E-10	1.344	4.84E-09
0.592	2.19E-09	0.843	3.60E-10	1.094	6.56E-10	1.345	4.83E-09
0.593	2.21E-09	0.844	3.99E-10	1.095	5.98E-10	1.346	4.88E-09
0.594	2.25E-09	0.845	3.59E-10	1.096	6.04E-10	1.347	4.86E-09
0.595	2.25E-09	0.846	3.71E-10	1.097	6.41E-10	1.348	4.88E-09
0.596	2.28E-09	0.847	3.60E-10	1.098	6.04E-10	1.349	4.93E-09
0.597	2.28E-09	0.848	3.63E-10	1.099	5.91E-10	1.350	4.93E-09
0.598	2.26E-09	0.849	3.69E-10	1.100	5.85E-10	1.351	4.96E-09
0.599	2.24E-09	0.850	3.50E-10	1.101	5.39E-10	1.352	4.97E-09
0.600	2.27E-09	0.851	3.74E-10	1.102	5.28E-10	1.353	4.93E-09
0.601	2.27E-09	0.852	3.41E-10	1.103	5.29E-10	1.354	4.91E-09
0.602	2.24E-09	0.853	3.55E-10	1.104	5.21E-10	1.355	4.98E-09
0.603	2.27E-09	0.854	3.59E-10	1.105	4.91E-10	1.356	4.96E-09
0.604	2.23E-09	0.855	3.40E-10	1.106	5.50E-10	1.357	5.01E-09
0.605	2.24E-09	0.856	4.00E-10	1.107	5.08E-10	1.358	4.99E-09
0.606	2.23E-09	0.857	3.75E-10	1.108	4.61E-10	1.359	4.99E-09
0.607	2.23E-09	0.858	3.61E-10	1.109	5.05E-10	1.360	4.99E-09
0.608	2.23E-09	0.859	3.57E-10	1.110	5.18E-10	1.361	5.08E-09
0.609	2.19E-09	0.860	3.45E-10	1.111	4.87E-10	1.362	5.00E-09
0.610	2.20E-09	0.861	3.64E-10	1.112	4.80E-10	1.363	5.03E-09
0.611	2.17E-09	0.862	3.38E-10	1.113	5.43E-10	1.364	5.00E-09
0.612	2.14E-09	0.863	3.55E-10	1.114	5.01E-10	1.365	5.06E-09
0.613	2.14E-09	0.864	3.41E-10	1.115	4.86E-10	1.366	5.05E-09
0.614	2.12E-09	0.865	3.48E-10	1.116	4.33E-10	1.367	5.10E-09
0.615	2.08E-09	0.866	3.45E-10	1.117	4.52E-10	1.368	5.11E-09
0.616	2.07E-09	0.867	3.41E-10	1.118	4.07E-10	1.369	5.07E-09
0.617	2.05E-09	0.868	3.53E-10	1.119	4.42E-10	1.370	5.13E-09
0.618	2.03E-09	0.869	3.53E-10	1.120	5.08E-10	1.371	5.09E-09
0.619	1.99E-09	0.870	3.67E-10	1.121	5.05E-10	1.372	5.06E-09
0.620	1.98E-09	0.871	4.15E-10	1.122	4.47E-10	1.373	5.15E-09
0.621	1.94E-09	0.872	3.61E-10	1.123	5.18E-10	1.374	5.07E-09

$m_{\text{Axion}} \text{ (eV)}$	$g_{\text{ay}} \text{ (GeV}^{-1}\text{)}$	$m_{\text{Axion}} \text{ (eV)}$	$g_{\text{ay}} \text{ (GeV}^{-1}\text{)}$	$m_{\text{Axion}} \text{ (eV)}$	$g_{\text{ay}} \text{ (GeV}^{-1}\text{)}$	$m_{\text{Axion}} \text{ (eV)}$	$g_{\text{ay}} \text{ (GeV}^{-1}\text{)}$
0.622	1.91E-09	0.873	3.80E-10	1.124	5.27E-10	1.375	5.16E-09
0.623	1.89E-09	0.874	3.71E-10	1.125	5.10E-10	1.376	5.15E-09
0.624	1.85E-09	0.875	3.99E-10	1.126	4.74E-10	1.377	5.21E-09
0.625	1.83E-09	0.876	3.68E-10	1.127	5.84E-10	1.378	5.20E-09
0.626	1.78E-09	0.877	4.11E-10	1.128	4.97E-10	1.379	5.19E-09
0.627	1.74E-09	0.878	3.91E-10	1.129	4.68E-10	1.380	5.27E-09
0.628	1.70E-09	0.879	4.29E-10	1.130	4.90E-10	1.381	5.19E-09
0.629	1.65E-09	0.880	4.53E-10	1.131	5.27E-10	1.382	5.17E-09
0.630	1.58E-09	0.881	3.73E-10	1.132	5.17E-10	1.383	5.23E-09
0.631	1.54E-09	0.882	4.21E-10	1.133	4.87E-10	1.384	5.23E-09
0.632	1.48E-09	0.883	3.91E-10	1.134	5.48E-10	1.385	5.23E-09
0.633	1.39E-09	0.884	4.32E-10	1.135	6.53E-10	1.386	5.22E-09
0.634	1.30E-09	0.885	3.98E-10	1.136	5.82E-10	1.387	5.28E-09
0.635	1.19E-09	0.886	4.60E-10	1.137	5.41E-10	1.388	5.27E-09
0.636	1.02E-09	0.887	3.64E-10	1.138	5.10E-10	1.389	5.26E-09
0.637	5.90E-10	0.888	4.32E-10	1.139	5.70E-10	1.390	5.31E-09
0.638	4.49E-10	0.889	4.02E-10	1.140	5.65E-10	1.391	5.29E-09
0.639	5.33E-10	0.890	4.83E-10	1.141	5.46E-10	1.392	5.27E-09
0.640	4.08E-10	0.891	3.80E-10	1.142	4.70E-10	1.393	5.28E-09
0.641	4.52E-10	0.892	4.55E-10	1.143	5.25E-10	1.394	5.28E-09
0.642	3.99E-10	0.893	4.09E-10	1.144	5.87E-10	1.395	5.30E-09
0.643	4.41E-10	0.894	4.45E-10	1.145	4.96E-10	1.396	5.27E-09
0.644	3.99E-10	0.895	3.63E-10	1.146	4.58E-10	1.397	5.45E-09
0.645	3.86E-10	0.896	4.22E-10	1.147	5.30E-10	1.398	5.37E-09
0.646	3.85E-10	0.897	3.79E-10	1.148	6.27E-10	1.399	5.30E-09
0.647	4.39E-10	0.898	4.07E-10	1.149	4.84E-10	1.400	5.43E-09
0.648	3.96E-10	0.899	4.12E-10	1.150	5.14E-10	1.153	5.18E-10
0.649	4.16E-10	0.900	4.01E-10	1.151	6.00E-10	1.154	4.53E-10
0.650	4.03E-10	0.901	4.24E-10	1.152	5.74E-10	1.155	5.50E-10

Table 14-1 Axion mass vs. Coupling Constant for 2009 2010 2011 CCD-XRT data (preliminary)

---

---

## 15. List of Equations

---

Equation 2-1 .....	4
Equation 2-2 .....	5
Equation 2-3 .....	5
Equation 2-4 .....	7
Equation 2-5 .....	7
Equation 2-6 .....	7
Equation 2-7 CKM matrix.....	8
Equation 2-8 .....	9
Equation 2-9 .....	9
Equation 2-10 .....	9
Equation 2-11 .....	10
Equation 2-12 .....	10
Equation 2-13 .....	10
Equation 2-14 .....	10
Equation 2-15 .....	10
Equation 2-16 .....	10
Equation 2-17 .....	11
Equation 2-18 .....	11
Equation 2-19 .....	11
Equation 2-20 .....	11
Equation 2-21 .....	11
Equation 2-22 .....	11
Equation 2-23 .....	11
Equation 2-24 .....	12
Equation 2-25 .....	12
Equation 2-26 .....	12
Equation 2-27 .....	12
Equation 2-28 .....	12
Equation 3-1 .....	13
Equation 3-2 .....	13
Equation 3-3 .....	14
Equation 3-4 .....	14
Equation 3-5 .....	14
Equation 3-6 .....	15
Equation 3-7 fermion coupling constant .....	15
Equation 3-8 .....	15
Equation 3-9 .....	17
Equation 3-10 .....	18
Equation 3-11 .....	18
Equation 3-12 .....	19
Equation 3-13 .....	19
Equation 3-14 .....	19
Equation 3-15 .....	22
Equation 3-16 The solar mass .....	25
Equation 3-17 .....	25
Equation 3-18 energy loss ratio.....	25
Equation 3-19 coupling constant upper limit .....	25
Equation 3-20 Axion mass upper limit .....	25
Equation 3-21 .....	26
Equation 3-22 White Dwarf limit .....	26

---

Equation 3-23 ZZ Ceti limit .....	26
Equation 3-24 SN1987A limit.....	28
Equation 3-25 Telescope bound .....	31
Equation 3-26.....	31
Equation 3-27 SOLAX.....	33
Equation 3-28 COSME.....	33
Equation 3-29 DAMA.....	33
Equation 3-30.....	33
Equation 4-1.....	36
Equation 4-2.....	36
Equation 4-3.....	37
Equation 4-4.....	38
Equation 4-5.....	38
Equation 4-6 The wave equation for particles propagating in the $z$ axis through a perpendicular magnetic field .....	39
Equation 4-7 Conversion Probability .....	39
Equation 4-8 Momentum Transfer .....	39
Equation 4-9 Axion Momentum .....	39
Equation 4-10 Photon-Axion Momentum transfer .....	39
Equation 4-11.....	40
Equation 4-12.....	40
Equation 4-13 Conversion Probability in Vacuum .....	40
Equation 4-14 Effective photon mass in Helium.....	41
Equation 4-15.....	42
Equation 4-16 Absorption length.....	42
Equation 4-17.....	42
Equation 4-18.....	43
Equation 5-1 FOV of the magnet .....	53
Equation 6-1.....	59
Equation 6-2.....	63
Equation 6-3.....	68
Equation 6-4.....	68
Equation 6-5.....	72
Equation 6-6.....	77



---

## 16. List of Figures

---

Figure 2-1 Box diagram for neutral kaon oscillations.....	7
Figure 2-2 Updated diagram of the Standard Model - elementary particles with three generations of fermions, gauge Bosons on the fourth column, and the Higgs Boson in the fifth [17] .....	10
Figure 3-1 Triangle loop diagram for the Axion-to-gluon coupling. ....	13
Figure 3-2 Additional contribution to the coupling of Axions to photons via a triangle loop through fermions carrying both PQ and electric charges. ....	14
Figure 3-3 Axion-electron coupling. Left: Contributing Feynman diagram for direct Axion-electron coupling which is possible only in models in which fermions carry PQ-charge (see DFSZ Model). Right: Radiatively induced coupling of Axions to electrons at a one-loop level. This coupling is present even in models in which fermions do not carry PQ-charge (see KSVZ Model). ....	15
Figure 3-4 Feynman Diagram of direct Axion to nucleon coupling. Even Axions which do not couple to light quarks at tree-level still have a coupling to nucleons since the Axion nucleon coupling partly results from Axion-pion mixing and partly from the shown direct coupling of Axions to nucleons. ....	16
Figure 3-5 Upper image: Compton-like process for Axion models with Axion-electron coupling at tree-level. Together with the bremsstrahlung process shown in the lower part of this figure, Compton scattering is the main Axion emission process in main sequence Stars, white dwarfs and red giants. Lower image: Electron bremsstrahlung process for Axion models with Axion electron coupling at tree-level. ....	16
Figure 3-6 The Primakoff effect - the dominant Axion emission process in hadronic models for main sequence Stars, horizontal branch Stars, red giants and white dwarfs.....	17
Figure 3-7 Axion Nucleon bremsstrahlung is the most important Axion emission process in neutron Stars. ....	17
Figure 3-8 Plotted the two most common invisible Axion models KSVZ and DFSZ . The inserted plot shows the same plot but in linear scale. The error bars are inserted here under the form of black dashed lines. ....	18
Figure 3-9 Axion mass versus coupling constant, $E/N$ dependence for DFSZ Model.....	20
Figure 3-10 CMB as observed by Planck in 9 frequency channels – 12.2014 .....	21
Figure 3-11 Astrophysical and cosmological exclusion ranges together with experimentally reachable mass-ranges. The orange bars indicate a strong model dependence. [51] .....	23
Figure 3-12 The Hertzsprung-Russell diagram for the globular Star cluster M5 - it is a good representative for a typical globular cluster of the same generation. Here the visual magnitude is plotted as a function of the colour index. ....	24
Figure 3-13 SN1987A before (left) and after. ....	27
Figure 3-14 The duration of Neutrino cooling function of $g_{aN}$ for SN 1987A [26] .....	28
Figure 3-15 The Axion parameter space regions excluded by different experiments. [59].....	30
Figure 3-16 Left – the results of first generation ADMX , Right – recent results of ADMX.....	31
Figure 3-17 Combined exclusion plot for most important Haloscope experiments: .....	32
Figure 3-18 The principle of detection for an Helioscope.....	32
Figure 3-19 Principle of operation for “Shining light through the wall” or “Photon regeneration” experiments .....	34
Figure 3-20 Top – the principle of dichroism, Bottom – the principle of birefringence. ....	34
Figure 4-1 Feynman diagram of the direct and indirect Primakoff effect.....	36
Figure 4-2 Differential Axion flux at Earth comparison for the old and revised model. [77].....	37
Figure 4-3 Axion surface luminosity of the Sun for different energies and radial coordinates. [59] .....	37
Figure 4-4 Solar surface Axion luminosity as a function of energy and dimensionless radial coordinate. The colour scale represents the flux in Axions/cm <sup>2</sup> s keV for unit surface area on the solar disk. [59] .....	38
Figure 4-5 The function that dictates the conversion probability .....	40

Figure 4-6 Colour coded plot of the momentum transfer in eV superimposed over Axion mass and energy dependence for a pressure of 5.5 mbar at 1.8K. [59] .....	42
Figure 4-7 Best fit of the NIST data on $\text{He}^3$ mass attenuation coefficient .....	43
Figure 4-8 Black line – expected number of photons with vacuum in the conversion volume, Red line – coherence restored for a small Axion mass range with 6.08 mbar $\text{He}^4$ in the conversion volume. [59].....	43
Figure 5-1 CERN’s accelerator complex, experimental areas and test facilities [82].....	44
Figure 5-2 CAST experiment tracking the Sun in the morning run.....	45
Figure 5-3 Schematic drawing explaining the principle of operation for the CERN Axion Solar Telescope. [83] .....	45
Figure 5-4 The magnetic field structure of the CAST dipole magnet at a maximum of 2.4T [83]. .....	47
Figure 5-5 Standard cross section of a twin aperture LHC dipole prototype magnet [83].....	47
Figure 5-6 Cryo flexibles condensing atmospheric oxygen and water during a Quench. ....	48
Figure 5-7 Safety release of cryogenic hydrogen during a Magnet Quench in 2010.....	49
Figure 5-8 Driving mechanisms: Left – horizontal motor encoder and a driving wheel; Right – vertical motor encoder, with the transmission system and lifting jacks. ....	50
Figure 5-9 Deviation from standard linear interpolation in the encoder-angle relation.....	51
Figure 5-10 Cumulative tracking coverage of the grid coordinate space for 2005-2011.....	51
Figure 5-11 User Interface of the tracking program displaying the trajectory of the Sun, position of the magnet, precision of the tracking, atmospheric conditions and many other parameters .....	52
Figure 5-12 Sun filming in March 2014 with aligned DSLR camera.....	53
Figure 5-13 The FOV $\alpha$ of the magnet. FOV1 is the fully illuminated view, while FOV2 is what actually the detectors see due to the distance between the bore and the sensitive part.....	53
Figure 5-14 Atmospheric refraction scheme .....	54
Figure 5-15 Solar filming campaign of March 2014. ....	54
Figure 5-16 CAST Slow Control snapshot.....	55
Figure 5-17 Subsystems of the magnet. Cold windows are used for separating the buffer gas in the conversion volume [83] .....	56
Figure 5-18 Left – cross section of a cold window , Right – Cold window mounted on a CF63 flange .	57
Figure 5-19 Schematic drawing of the $\text{He}^3$ gas system. With green arrows is indicated the standard filling procedure. With red arrows is represented the recovery procedure in the storage volume. [88].....	58
Figure 6-1 CAST TPC schematics.....	60
Figure 6-2 CAST X-ray Telescope Mirror System mounted on Sun-Rise platform with vacuum and electro-pneumatic systems disconnected. Survey targets are visible. ....	62
Figure 6-3 Left: Front view of ABRIXAS mirror system showing the 27 nested mirrors in 6 sectors. CAST magnet bore aperture is marked in one of the sectors justifying the off-axis use of the module. Right: Logarithmic intensity image of the Point Spread Function obtained at PANTER X-ray test facility in Munich by illuminating one sector with a beam of 1.5 keV. The red circle depicts the expected solar Axion image, and the top right reflexion is explained by single reflections on the shells due to finite distance to the source. [94].....	63
Figure 6-4 Wolter-type I optics schematics [95] .....	64
Figure 6-5 Left: Effective area – general view with all 6 sectors of the CAST Telescope with the out of focus transmitted intensity (shadowing effect of the support structure visible); Right: Point Spread Function of the CAST Telescope measured at 1.49 keV, HEW: 33.4”, W90: 123”.....	65
Figure 6-6 Left: Effective area of CAST Telescope measured at PANTER, extended for the first time below 2 keV with TRoPIC setup also for other energies beside the characteristic emission lines; Right: Comparison with 2008 measurements done in PSPC setup. ....	65
Figure 6-7 Left: Effective area of Sector nr. 4 of the CAST Telescope taking into account the magnet bore aperture of $d=43\text{mm}$ , and the quantum efficiency of pn-CCD detector in three cases: Blue line – point source case, Black line – point source located at infinity, Red line – for a source of	

roughly the same angular size as the Axion image of the Sun; Right: Off-axis dependence of effective area for Sector nr. 4 shown for radial angles with triangles and tangential angles with diamonds. [97].....	66
Figure 6-8 Left: Off-axis transmission penalty due to the geometric vignetting effects of the CAST setup plotted with triangles for the case of radial off-axis angles and with diamonds for the tangential off-axis angles; Right: The off-axis transmission dependence of individual components of radial off-axis angles: Rectangles – vignetting losses due to the magnet bore, Triangles – transmission of the mirror module, Diamonds – The total transmission of the system (Mirror Module coupled with the Magnetic Bore.) [97] .....	66
Figure 6-9 Schematic of a pn-Junction [59].....	67
Figure 6-10 Energy dependence of absorption length in Si and SiO <sub>2</sub> [99].....	69
Figure 6-11 The Principle of sideward depletion [99].....	69
Figure 6-12 Cross section along a transfer channel trough a pn-CCD [99] .....	70
Figure 6-13 Pixel structure formed from the shift registers each of 50 $\mu\text{m}$ resulting a pixel of 150 $\times$ 150 $\mu\text{m}^2$ [99].....	70
Figure 6-14 Schematics of the pn-CCD readout (64x200 pixels) [99].....	71
Figure 6-15 Examples of signal patterns for split events in a pn-CCD detector .....	72
Figure 6-16 The pn-CCD chip implementation in CAST with the cooling system. Individual components are presented as they were modelled in GEANT4 during the implementation phase.	73
Figure 6-17 The Vacuum Control and Monitoring interface for the X-ray telescope – CCD detector system.....	74
Figure 6-18 Quantum Efficiency of the pn-CCD chip used in CAST and in XMM-Newton function of incident photon energy [100] .....	75
Figure 6-19 Left – Dependence ADU and the incident photon energy in keV based on calibration data. Red line is a linear fit and blue is a third order polynomial. Below is the deviation from the literature values in units of $\chi^2$ ; Right – The same plot but with the axis inverted. [101].....	76
Figure 6-20 CAST pc-CCD detector Response Matrix in logarithmic grey scale. The width of the distribution correlates with the energy resolution. [100].....	76
Figure 6-21 Energy Resolution of the CAST pn-CCD detector versus the incident photon energy.....	77
Figure 6-22 CAST CCD detector spectrum of <sup>55</sup> Fe calibration source. ....	77
Figure 7-1 Schematic representation of the experimental setup for the XRT alignment.....	78
Figure 7-2 Left – View trough the V1 Magnet bore from the point of view of the X-ray telescope dismantled at that time. The two mounting supports are visible in the lower part. Right – Zoomed view of the alignment crosshair found inside the V1 beam line of the magnet. ....	79
Figure 7-3 Left – The alignment tube used for aligning the XRT with the V1 beam line; Right – Plexiglas target found in the focal (detector) plane of the telescope, with mm paper for better reference.....	79
Figure 7-4 X-ray telescope laser alignment spot on the Plexiglas target overlaid with mm paper; Left – Spot before platform tilt; Right – Spot after the platform tilt.....	80
Figure 7-5 Principle of XRT alignment from 2014.....	80
Figure 7-6 XRT survey targets for long-term alignment checks. ....	81
Figure 7-7 Z Coordinate variations of the SCOTCH1B survey target in mm. Measurements 8 and 9 correspond to 12-02-2012 with the CCD-XRT vacuum system at atmospheric pressure and MRB side loaded with 450 kg of additional lead. A negative deflection in Z axis corresponds to a deformation in the platform towards the floor. ....	81
Figure 8-1 Laser run spot on the CCD chip; Spot coordinates must coincide with the X-ray finger runs. ....	82
Figure 8-2 X-ray finger source from Amptek Left- Cooling phase spectrum; Right- The output flux in cyclic emission during heating and cooling. [103].....	83
Figure 8-3 Left – CCD spot image of the X-ray Finger Run (05) from 03.12.2009; Right – Gaussian fit of the circular envelope of the intensity distribution for determining the spot coordinates. ....	84

Figure 8-4 Typical demonstration of analysis for determining the centre coordinated of the Signal Area [102] by overlaying the laser alignment data (green crosses) and the X-ray finger data (red crosses for intensities higher than 7% of the maximum value). Blue lines indicate the circular envelope of the signal area.....	84
Figure 8-5 Coordinate stability of the Signal Area for 2009-2012. Red cross is the coordinate considered in the Data Analysis and it was stable within the tolerance of one pixel. ....	85
Figure 9-1 Left – Example of pn-CCD detector light contamination due to the angle the magnet did with the Sun light; Right – Examples of electrical noise from May 2010. ....	87
Figure 9-2 Spectral fit of an Energy Calibration Run of CAST pn-CCD detector taken on 18-07-2011 with an $^{55}\text{Fe}$ calibration source.....	88
Figure 9-3 TOP - Full Energy true colour event Image of all valid events integrated over the entire detector livetime of 2009 season (13.07.2009 – 12.12.2009); Bottom – Energy range colour coding and statistics (red 0.5 – 1 keV, green 1 – 7 keV, blue 7 – 14 keV). ....	89
Figure 9-4 Tracking vs. Background event distribution (green for 1-7 keV scale); Left – Full energy range exposure for week 40 year 2009; Right – Event distribution from the tracking run of 02-10-2009.....	89
Figure 9-5 Stability of the pn-CCD detector during the 2009 data taking period based on daily $^{55}\text{Fe}$ calibrations. ....	90
Figure 9-6 Background spectral fit of 2009 CCD data. The Flux in $\text{cts}/\text{cm}^2/\text{s}/\text{keV}$ is plotted versus energy for the range 0.9 – 15 keV.....	91
Figure 9-7 CCD lightcurves for 2009 data, pattern (counts/s), 0.5 day binning (4 weeks/panel); Red 0.5-1 keV, green 1-7 keV, blue 7-14 keV, grey 0.5-20 keV, solid grey all events. ....	92
Figure 9-8 TOP - Full Energy true colour event Image of all valid events integrated over the entire detector livetime of 2010 season (03.05.2010 – 17.11.2010); Bottom – Energy range colour coding and statistics (red 0.5 – 1 keV, green 1 – 7 keV, blue 7 – 14 keV). ....	94
Figure 9-9 Tracking vs. Background event distribution (green for 1-7 keV scale); Left – Full energy range exposure for week 33 year 2010; Right – Event distribution from the tracking run of 21-08-2010.....	94
Figure 9-10 Stability of the pn-CCD detector during 2010 data taking period based on daily $^{55}\text{Fe}$ calibrations. Blank spaces represent detector down times.....	95
Figure 9-11 Background energy spectra for 2010 CCD data. The Flux in $\text{cts}/\text{cm}^2/\text{s}/\text{keV}$ is plotted versus different energy ranges 0.4 – 20 keV.....	96
Figure 9-12 CCD lightcurves for 2010 data, pattern (counts/s), 0.5 day binning (4 weeks/panel); Red 0.5-1 keV, green 1-7 keV, blue 7-14 keV, grey 0.5-20 keV, solid grey all events. ....	97
Figure 9-13 TOP - Full Energy true colour event Image of all valid events integrated over the entire detector livetime of 2011 season (25.03.2011 – 08.08.2011); Bottom – Energy range colour coding and statistics (red 0.5 – 1 keV, green 1 – 7 keV, blue 7 – 14 keV). ....	98
Figure 9-14 Tracking vs. Background event distribution (green for 1-7 keV scale); Left – Full energy range exposure for week 24 year 2011; Right – Event distribution from the tracking run of 11-06-2011.....	98
Figure 9-15 Stability of the pn-CCD detector during 2011 data taking period based on daily $^{55}\text{Fe}$ calibrations. Blank spaces represent detector down times.....	99
Figure 9-16 Background energy spectra for 2011 CCD data. The Flux in $\text{cts}/\text{cm}^2/\text{s}/\text{keV}$ is plotted versus different energy ranges 0.4 – 20 keV.....	100
Figure 9-17 CCD lightcurves for 2011 data, pattern (counts/s), 0.5 day binning (4 weeks/panel); Red 0.5-1 keV, green 1-7 keV, blue 7-14 keV, grey 0.5-20 keV, solid grey all events. ....	101
Figure 10-1 Exclusion plot for solar Axions based on the CCD-XRT detector data from 2009 2010 2011 (Annex 1.2,3,4). Some of the lower sensitivity mass domains were covered in 2008 or were not scanned due to detector technical issues. ....	103
Figure 10-2 Exclusion plot achieved by CAST in Vacuum, $^4\text{He}$ buffer gas and $^3\text{He}$ buffer gas. Constraints from Horizontal Branch Stars with dashed line and typical Axion models in yellow	

band are overlaid [105]. The overall $^3\text{He}$ sensitivity is expected to improve once the CCD data is taken into account. ....	103
---	-----

---

## 17. List of Tables

---

Table 5-1 Run History of CAST. ....	46
Table 5-2 Current – Magnetic Field dependence for the CAST magnet.....	48
Table 5-3 Error sources in the Sun Tracking System.....	52
Table 6-1 Effective area measurement for all the sectors of CAST telescope at PANTER, sector nr. 4 had the best performances and is used at CAST. ....	64
Table 6-2 Approximate distribution of split events for a pixel size of $150 \times 150 \mu\text{m}^2$ . ....	71
Table 6-3 The relevant parameters of the response function. The linear fit function was chosen of the form $f(x) = a \cdot x$ .....	76
Table 11-1 CCD detector spot events for 2009 data for the energy range 1-7 keV .....	104
Table 11-2 CCD background levels for 2009 data at 0.5 keV binning .....	105
Table 11-3 CCD tracking times and CAST pressure index for 2009 data.....	107
Table 12-1 CCD detector spot events for 2010 data for the energy range 1-7 keV .....	108
Table 12-2 CCD background levels for 2010 data at 0.5 keV binning .....	109
Table 12-3 CCD tracking times and CAST pressure index for 2010 data.....	111
Table 13-1 CCD detector spot events for 2011 data for the energy range 1-7 keV .....	112
Table 13-2 CCD background levels for 2011 data at 0.5 keV binning .....	112
Table 13-3 CCD tracking times and CAST pressure index for 2011 data.....	114
Table 14-1 Axion mass vs. Coupling Constant for 2009 2010 2011 CCD-XRT data (preliminary) .....	119



---

## 18. Bibliography

---

- [1] NASA/WMAP Science Team. CMB Timeline300 no WMAP.
- [2] R. D. Peccei and Helen R. Quinn, "CP Conservation in the Presence of Pseudoparticles," *Phys. Rev. Lett.*, pp. 38(25):1440–1443, Jun 1977.
- [3] G.'t Hooft, "Symmetry Breaking through Bell-Jackiw Anomalies ," *Phys. Rev. Lett* , pp. 37(1):8 , Jul 1976.
- [4] G.'t Hooft, "Computation of the quantum effects due to a four-dimensional pseudoparticle ," *Phys. Rev. D* , pp. 14(12):3432–3450 , Dec 1976.
- [5] E.Noether, "Invariante Variationsprobleme ," *Nachr.d.König.Gesellsch.d.Wiss.zuGöttingen, Math-phys. Klasse* , pp. 235-257, 1918.
- [6] D. Perkins, "Particle Astrophysics ," *Oxford Master Series in Particle Physics, Astrophysics, and Cosmology, Oxford University Press, Ney York* , 2003.
- [7] G. Lüders, "Proof of the TCP Theorem ," *Ann. Phys. 2 (1957), Issue 1, 1. W. Pauli, Niels Bohr and the development of Physics, ed. W Pauli, L Rosenfeld and V Weis- skopf, New York:McGraw Hill* , p. 30, 1955.
- [8] K. Lande et al., "Observation of Long-Lived Neutral V Particles ," *Phys. Rev. 103* , 1956.
- [9] J. W. Cronin, V. L. Fitch, and R. Turlay J. H. Christenson, "Evidence for the 2 pi Decay of the K02 Meson ," *Phys. Rev. Lett. 13* , pp. 138-140 , 1964.
- [10] C. Amsler et al. (Particle Data Group), "The Review of Particle Physics ," *PL B 667* , p. 1, 2008.
- [11] B. Aubert et al. (BABAR Collaboration), "Observation of CP Violation in the B0 Meson Sys- tem ," *Phys. Rev. Lett. 87* , . 2001.
- [12] K. Abe et al. (BELLE Collaboration), "Observation of Large CP Violation in the Neutral B Meson System ," *Phys. Rev. Lett. 87* , 2001.
- [13] J. R. Fry, "CP violation and the Standard Model ," *Rep. Prog. Phys. 63* , p. 117, 2000.
- [14] R. D. Peccei, "QCD, strong CP and axions ," *J. Korean Phys. Soc. 29* , p. S199 , 1996.
- [15] S. Weinberg, "The U (1)A – P roblem ," *Phys. Rev. D. 11* , p. 3583 , 1975.
- [16] J. E. Kim, "Light Pseudoscalars, Particle Physics and Cosmology ," *Phys. Rep.150* , p. 1, 1987.
- [17] Office of Science, United States Department of Energy, Particle Data Group Fermilab. The Standard Model of elementary particles (more schematic depiction), with the three generations of matter, gauge bosons in the fourth column, and the Higgs boson in the fifth.
- [18] V. Baluni, "CP-nonconserving effects in quantum chromodynamics ," *Phys. Rev. D 19* , p. 2227, 1979.
- [19] N.F.Ramsey, "ElectricDipoleMomentOfTheNeutron ," *Ann.Rev.Nucl.Part.Phys.40* , 1990.
- [20] J. M. Pendlebury, "Fundamental Physics With Ultracold Neutrons ," *Ann. Rev. Nucl. Part. Phys. 43* , p. 687, 1993.
- [21] C. A. Baker et al., "Improved Experimental Limit on the Electric Dipol Moment of the Neutron ," *Phys. Rev. Lett. 97* , p. 131801 , 2006.
- [22] R. D. Peccei and H. R. Quinn, "CP Conservation In The Presence Of Pseudoparticles," *Phys. Rev. Lett. 38* , 1977.
- [23] R. D. Peccei and H. R. Quinn, "Constraints imposed by CP conservation in the presence of pseudoparticles ," *Phys. Rev. D 16* , 1977.
- [24] S. Weinberg, "A New Light Boson? ," *Phys. Rev. Lett. 40* , p. 223, 1978.
- [25] F. Wilczek, "Problem Of Strong P And T Invariance In The Presence Of Instantons ," *Phys. Rev. Lett. 40* , vol. 279, 1978.
- [26] G. G. Raffelt, "Stars as Laboratories for Fundamental Physics," *University of Chicago Press*,



---

*Chicago/London*, 1996.

- [27] W. A. Bardeen and S.-H. H. Tye, "Current Algebra Applied To Properties Of The Light Higgs Boson," *Phys. Lett. B* 74, p. 229, 1978.
- [28] H. Primakoff, "Photo-Production of Neutral Mesons in Nuclear Electric Fields and the Mean Life of Neutral Meson," *Phys. Rev.* 81, 1951.
- [29] I. and T. N. Truong Antoniadis, *Physics Letters B*, vol. Vol. 109, pp. 67-72, 1982.
- [30] T. W. Donnelly et al., "Do axions exist?," *Phys. Lett. D* 18, 1978.
- [31] A. I. Vainshtein, V. I. Zakharov M. A. Shifman, "Can Confinement Ensure Natural CP Invariance of Strong Interactions?," *Nucl. Phys. B* 166, 1980.
- [32] J. E. Kim, "Weak Interaction Singlet and CP Invariance," *Phys. Rev. Lett.* 43, 1979.
- [33] D. B. Kaplan, "Opening the Axion Window," *Nucl. Phys. B* 260, 1985.
- [34] M. Srednicki, "Axion Couplings to Matter. I. CP-conserving parts," *Nucl. Phys. B* 260, p. 689, 1985.
- [35] C. Q. Geng and W.-T. Ni S. L. Cheng, "Axion-photon Couplings in Invisible Axion Models," *Phys. Rev. D* 52, 1995, arXiv:hep-ph/9506295.
- [36] W. Fischler and M. Srednicki M. Dine, "A simple solution to the strong CP problem with a harmless axion," *Phys. Lett. B* 104, 1981, 199.
- [37] J. E. Kim, "Light pseudoscalars, particle physics and cosmology," *Phys. Rept.* 150, 1987.
- [38] M. Ahlers et al, "Light from the hidden sector: Experimental signatures of paraphotons," *Phys. Rev. D* 76, 2007, 115005.
- [39] A. Ringwald et al., "Proceedings of the 4th PatrasWorkshop on Axions," *WIMPs and WISPs, DESY, Hamburg, Germany*, 2008.
- [40] L. F. Abbott and P. Sikivie, "A cosmological bound on the invisible axion," *Phys. Lett., B* 120:133–136, 1983.
- [41] M. B. Wise, and F. Wilczek J. Preskill, "Cosmology of the Invisible Axion," *Phys. Lett., B* 120:127–132, 1983.
- [42] M. Dine and W. Fischler, "The not-so-harmless axion," *Phys. Lett., B* 120:137–141, 1983.
- [43] A. Dabholkar and J. M. Quashnock, "Pinning down the axion," *Nucl. Phys., B* 333:815, 1990.
- [44] R. A. Battye and E. P. S. Shellard, "Global string radiation," *Nucl. Phys., B* 423:260–304, 1994.
- [45] R. A. Battye and E. P. S. Shellard, "Axion String Constraints," *Phys. Rev. Lett.,* 73:2954–2957, 1994.
- [46] C. Hagmann, and P. Sikivie S. Chang, "Studies of the motion and decay of axionwalls bounded by strings," *Phys. Rev., D* 59:023505, 1999.
- [47] D. H. Lyth, "Estimates of the cosmological axion density," *Phys. Lett., B* 275:279–283, 1992.
- [48] M. Nagasawa and M. Kawasaki, "Collapse of axionic domain wall and axion emission," *Phys. Rev., D* 50:4821–4826, 1994.
- [49] "Cosmological Constraints On Neutrino Plus Axion Hot Dark Matter: Update After WMAP-5," *Journal of Cosmology and Astroparticle Physics*, 2008.
- [50] Xue-Lei Chen and Marc Kamionkowski, "Particle decays during the cosmic dark ages," *Phys. Rev., D* 70:043502, 2004.
- [51] G. G. Raffelt, "Astrophysical axion bounds," *Lect. Notes Phys.* 741, 2008, arXiv:hep-ph/0611350.
- [52] *Astrophysical Journal* 135, 1962, 311.
- [53] G. G. Raffelt, "Particle Physics from Stars," *Annu. Rev. Nucl. Part. Sci.* 49, 1999, arXiv:hep-ph/9903472.
- [54] Mitchell Begelman and Martin Rees, "Gravity's Fatal Attraction: Black Holes in the Universe,"

- Cambridge University Press, 2009, ISBN-13: 978-0521717939.
- [55] A. Buzzoni et al, "Helium abundance in globular clusters: the R-method," *Astron. Astrophys.* **128**, 1983.
  - [56] M. S. Turner, "Early-Universe Thermal Production of Not-So-Invisible Axions," *Phys.Rev.Lett.* **59**, 1987.
  - [57] A. Mirizzi, G. G. Raffelt and Y. Y. Y. Wong S. Hannestad, "Cosmological constraints on neutrino plus axion hot dark matter: Update after WMAP-5, JCAP," 2008, arXiv:astro-ph/0803.1585.
  - [58] P. Sikivie, "Experimental Tests of the "invisible" Axion," *Phys. Rev. Lett.* **51**, 1983.
  - [59] Julia Katharina Vogel, "Searching for Solar Axions in the eV-Mass Region with the CCD Detector at CAST ," FAKULTÄT FÜR MATHEMATIK UND PHYSIK ALBERT-LUDWIGS-UNIVERSITÄT FREIBURG , 2009.
  - [60] M. T. Ressell, "Limits to the radiative decay of the axion," *Phys. Rev. D* **44**, 1991.
  - [61] W.Wuensch et al., "Results of a laboratory search for cosmic axions and other weakly coupled light particles," *Phys. Rev. D* **40**, 1989.
  - [62] "Results from A High-Sensitivity Search For Cosmic Axions," *Physical Review Letters*, Vol. **80**, No. **1**, p. 2043
  - [63] S. J., G. Carosi, C. Hagmann, D. Kinion, K. van Bibber, M. Hotz, L. Rosenberg, G. Rybka, J. Hoskins, J. Hwang, P. Sikivie, D. B. Tanner, R. Bradley and J. Clarke Asztalos, "A SQUID-Based Microwave Cavity Search For Dark-Matter Axions," *Physical Review Letters*, vol. **104**, pp. 1301-1305, 2010.
  - [64] W.Wuensch et al., "Results of a laboratory search for cosmic axions and other weakly coupled light particles," *Phys. Rev. D* **40**, 1989.
  - [65] C. Hagmann et al., "Results from a search for cosmic axions," *Phys. Rev. D* **42**, 1990.
  - [66] L. D. Duffy et al, "A High Resolution Search for Dark-Matter Axions," *Phys. Rev.D* **74**, 2006, arXiv:astro-ph/0603108.
  - [67] K. Yamamoto et al., "The Rydberg atom cavity axion search," Invited talk presented at the Dark2000, Heidelberg, Germany, 10-15 July, (2000).
  - [68] G. C. Smith, R. Cameron, A. C. Melissinos, G. Ruoso, Y. K. Semertzidis and F. A. Nezrick D. M. Lazarus, "A Search for solar axions," *Phys. Rev. Lett.* **69**, p. 2333, 1992.
  - [69] M. Minowa, T. Namba, Y. Inoue, Y. Takasu and A. Yamamoto S. Moriyama, "Direct search for solar axions by using strong magnetic field and X-ray detectors," *Phys. Lett. B* **434**, p. 147, 1998.
  - [70] E. A. Paschos and K. Zioutas, "A Proposal for solar axion detection via Bragg scattering," *Phys. Lett. B* **323**, p. 367, 1994.
  - [71] F. T. Avignone III et al. (SOLAX Collaboration), "Experimental Search for Solar Axions via Coherent Primakoff Conversion in a Germanium Spectrometer," *Phys. Rev. Lett.* **81**, 1998, arXiv:astro-ph/9708008.
  - [72] A. Morales et al. (COSME Collaboration), "Particle Dark Matter and Solar Axion Searches with a Small Germanium Detector at the Canfranc Underground Laboratory," *Astropart. Phys.* **16**, 2002, arXiv:hep-ex/0101037.
  - [73] R. Bernabei et al., "Search for Solar Axions by Primakoff Effect in NaI Crystals," *Phys. Lett. B* **515**, 2001.
  - [74] G. Ruoso et al., "Search for photon regeneration in a magnetic field," *Z. Phys.* **56**, 1992.
  - [75] G. Cantatore, A. C. Melissinos, G. Ruoso, Y. Semertzidis, H. J. Halama, D. M. Lazarus, A. G. Prodel, F. Nezrick, C. Rizzo, and E. Zavattini R. Cameron, "Search for nearly massless, weakly coupled particles by optical techniques," *Phys. Rev. D*, **47(9)**:3707–3725, 1993.
  - [76] E. Zavattini et al. (PVLAS Collaboration), "New PVLAS results and limits on magnetically

- induced optical rotation and ellipticity in vacuum," *Phys. Rev. D.* 77, 2008.
- [77] J. N. Bahcall and M. H. Pinsonneault, "What do we (not) know theoretically about solar neutrino fluxes?," *Phys. Rev. Lett.* 92 (2004) 121301, arXiv:astro-ph/0402114.
- [78] A. Weiss, and G. G. Raffelt H. Schlattl, "Helioseismological constraint on solar axion emission," *Astropart. Phys.* 10, 1999, arXiv:hep-ph/9807476.
- [79] G. G. Raffelt and L. Stodolsky, "Mixing of the Photon with Low-Mass Particles," *Phys.Rev.D* 37, 1988.
- [80] F. S. Crawford, "Waves - Berkley Physics Course Volume 3," 1968, McGraw-Hill College, Newton, Massachusetts, USA.
- [81] J.H., and S. M. Seltzer Hubbell, , 1996, <http://www.nist.gov/pml/data/xraycoef/index.cfm>.
- [82] CERN TE-EPC division. CERN's accelerator complex, experimental areas and test facilities.
- [83] <http://cdsweb.cern.ch/collection/Photos..>
- [84] "Proposal To The SPSC: A Solar Axion Search Using A Decommissioned LHC Test Magnet," *SPS-PS Experiments Committee*, 1999, CERN-SPSC-99-21.
- [85] A K Peters, Wellesey Spath H., "Two Dimensional Spline Interpolation Algorithms," 1993.
- [86] NOVAS (Naval Observatory Vector Astrometry Subroutines), , <http://www.usno.navy.mil/>, <http://aa.usno.navy.mil/software/>.
- [87] B. Bellanger, M. Davenport, N. Elias, S. Aune, J. Franz T.O. Niinikoski, "THIN CRYOGENIC X-RAY WINDOWS," *Departmental Report CERN-AT-2008-034*.
- [88] N. A. Rio Duarte Elias et al., "Technical Design Report of the CAST 3He Gas System ,," *CERN-SPSC-2006-029, SPSC-TDR-001, CAST TDR 1, (2006)*.
- [89] K Zioutas et al., "An improved limit on the axion-photon coupling from the CAST experiment," *Journal of Cosmology and Astroparticle Physics*, 2007.
- [90] E. Arik et al [CAST Collaboration], "Probing ev-scale axions with CAST," *Journal of Cosmology and Astroparticle Physics*, 2009.
- [91] CAST Collaboration, "CAST search for sub-eV mass solar axions with He3 buffer gas," *Physical Review Letters*, 2011, arXiv:1106.3919.
- [92] S Andriamonje et al., "Development and performance of Microbulk Micromegas detectors," *JINST*, 2010.
- [93] J. Altmann et al., "Mirror System for the German X-ray Satellite ABRIXAS: I. Flight Mirror Fabrication, Integration, and Testing," in *X-Ray Optics, Instruments, and Missions II, Proc. SPIE 3444*, ed. R. B. Hoover and A. B. Walker (Bellingham, WA: SPIE) (1998) 350. W. J. Egle et al., *Mirror System for the German X-ray Satellite ABRIXAS: II. Design and Mirror Development*, in *X-Ray Optics, Instruments, and Missions II, Proc. SPIE 3444*, ed. R. B. Hoover and A. B. Walker (Bellingham, WA: SPIE) (1998) 359.
- [94] M. Kuster et al., "The X-Ray Telescope of CAST ,," *New Journal of Phys.* 9 , 2007.
- [95] Dr. Markus Kuster,.
- [96] M. J. Freyberg et al., "The MPE X-Ray Test Facility PANTER: Calibration of Hard X-Ray (15 – 50 keV) Optics," *Exp.Astron* 20, p. 405, 2005.
- [97] M. Kuster et al., "The X-Ray Telescope of CAST," *New Journal of Phys*, vol. 9, p. 169, 2007, [arXiv:physics/0702188].
- [98] G. Lutz, "Semiconductor Radiation Detectors," 1999.
- [99] L. Strüder, "High-Resolution Imaging X-Ray Spectrometers," *Nucl. Instr. and Meth. A*, vol. 454, p. 73, 2000.
- [100] L. Strüder, "High-Resolution Imaging X-Ray Spectrometers," *Nucl. Instr. and Meth*, 2000.

- 
- 
- 
- [101] Philipp-Michael Lang, "Energiekalibration des pn-CCD-Detektors des CERN Axion Solar Telescope (CAST)," *Bachelor-Thesis*, Aug. 2008.
- [102] A. Nordt and J. Vogel M. Kuster, "X-ray-finger Measurement Report," *Internal CASTReport*, vol. CSTR-06-001, 2006.
- [103] J.D. Brownridge and S. Raboy, "Investigations of pyroelectric generation of X-rays," *Journal of Applied Physics*, vol. 86, no. 1, July 1999.
- [104] I. G. Irastorza, "Some Considerations towards a Protocol to deal with Candidate Events in CAST Phase II," *Internal CAST Report*.
- [105] M. Arik et al. (CAST Collaboration), "Search for Solar Axions by the CERN Axion Solar Telescope with He3 Buffer Gas: Closing the Hot Dark Matter Gap," *Phys. Rev. Lett.*, vol. 112, no. 091302, Mar. 2014.
- [106] Irastorza Igor, "The International Axion Observatory IAXO. Letter of Intent to the CERN SPS committee," *CERN-SPSC-2013-022 ; SPSC-I-242*.
- [107] K. Ehret et al., "Production and Detection of Axion-Like Particles in a HERA Dipole Magnet - Letter-of-Intent for the ALPS experiment," 2007, arXiv:hep-ex/0702023v1s.
- [108] P. Sikivie, "Axion Searches," *Nucl. Phys. Proc. Suppl.* 87, 2000, arXiv:hep-ph/0002154.
- [109] G.G. Raffelt, "Astrophysics probes of particle physics," *Physics Reports* 333-334, 2000.
- [110] R.A. Battye E.P.S. Shellard, "Cosmic axions," *astro-ph - 9802216*.
- [111] R. A. Battye and E. P. S. Shellard, "Axion string constraints," *Phys. Rev. Lett.* 73, 1994.
- [112] D. Harari and P. Sikivie, "On the evolution of global strings in the early Universe," *Phys. Lett. B* 195, 1987.
- [113] C. Hagmann and P. Sikivie, "Computer simulations of the motion and decay of global strings," *Nucl. Phys. B* 363, 1991.
- [114] M. Kuster et al. (Eds.), *Axions: Theory, Cosmology, and Experimental Searches*, Lect. Notes Phys. 741 (Springer, Berlin Heidelberg 2008), DOI 10.1007/ 978-3-540-73518-2
- [115] P. D. Serpico and G. G. Raffelt, "New Calculations of Solar Axion FluxInternal CAST Report," 2005.

---

## 19. Acknowledgements

---

First and foremost I would like to thank Prof. Dr. Dr./RUS Dieter H.H Hoffmann for giving me the opportunity to perform my PhD research work within the Astroparticle Physics group from IKP and the experimental work in the CAST experiment at CERN. His continuous support, advice, wisdom and guiding were invaluable to me.

Secondly I am sincerely indebted to Dr. Serban Udrea for his never-ending good spirit, kind words and moral support that he never hesitated to impart in the twinkling of an eye.

I would also like to show my consideration to Prof. Dr Konstantin Zioutas for the numerous enlightening and interesting discussions we had together at CERN. He was the main person I could count on with any problem and question scientific or logistic that I had during my long stay at CERN. His wisdom is something I always put great value on. Not only he is the one who brought CAST into being, but he is also the one that keeps its spirit alive.

Another person I consider myself lucky to have had the opportunity to work and learn from is Martyn Davenport, the technical coordinator of CAST. The depth of his thought process and the level of understanding of every single technical and scientific aspect of the experiment is something that has never ceased to amaze me, even after 5 years around him. I came to realise that thanks to his level of understanding the hardware, CAST is actually running.

Furthermore I would like to express my gratitude to the group of excellent scientists and friends that are running CAST. I will not explicitly mention names but I assure them I thoroughly enjoyed all the discussions, barbecues and things we discovered and learned together during these years. We went together both through fun times and excruciating many long/early/late shifts. CAST is one of the “coolest” places in the Universe for a young scientist to work at and I say that not just because of the Cryogenics, you guys have an important role in this also.

The same holds for the IKP colleagues that were always there for maintaining the Server cluster, when the code crashed and also having good times afterwards. There were moments I will always replay in my memory with a smile on my face and a happy heart.

A special thanks to Dr. Marian Ristici, Dr. Dan Apostol and Dr. Catalin Logofatu from the National Institute for Laser Plasma and Radiation Physics and University of Bucharest for paving my way into the scientific research.

Last but not least I am thinking of all my friends and family back at home and elsewhere that have made this incredible journey possible. I wish you would all knew how much I praise you all and how lucky I consider myself to have had you beside me.





---

## Curriculum Vitae

---

<i>Name</i>	Madalin-Mihai Rosu
<i>Birth day / Place</i>	12.05.1985 / Roman, Romania
<i>Citizenship</i>	Romanian

---

### Educational profile

<i>1992-2000</i>	Primary and secondary school in Roman, Romania
<i>2000-2004</i>	Highschool “National College Roman-Voda”, class natural sciences, Roman
<i>2004-2009</i>	Diploma at University of Bucharest, Physics Faculty, class physics-informatics. <b>Thesis:</b> Shack Hartmann Wavefront Sensor coupled with Deformable Mirror – Adaptive Optics.
<i>Since August 2009</i>	PhD student at Technical University of Darmstadt, and IKP Darmstadt, Germany. Experimental work (60% of the time) conducted in CAST experiment at CERN, CCD-XRT detector.

---

## **Erklärung zur Dissertation**

---

Hiermit versichere ich, die vorliegende Dissertation ohne Hilfe Dritter nur mit den angegebenen Quellen und Hilfsmitteln angefertigt zu haben. Alle Stellen, die aus Quellen entnommen wurden, sind als solche kenntlich gemacht. Diese Arbeit hat in gleicher oder ähnlicher Form noch keiner Prüfungsbehörde vorgelegen.

Darmstadt, den 13. April 2015

---

(Madalin-Mihai Rosu)